Search for chargino and neutralino production using final states with two soft leptons in pp collisions at $\sqrt{s} = 13$ TeV

Shunichi Akatsuka

May, 2020

Abstract

The Standard Model (SM) of particle physics successfully explains most of the experimental results. Yet, there are some phenomena that cannot be described by the SM, and that implies a new physics beyond the SM. Supersymmetry (SUSY) is one of the natural extensions of the SM, based on boson–fermion symmetry, which predicts existence of a supersymmetric partner for each SM particle. The Minimal Supersymmetric Standard Model (MSSM) with the R-parity conservation is expected to solve several problems in the SM. The masses of the SUSY particles depend on the parameters in the MSSM Lagrangian, which provides various scenarios with different mass spectra. Many scenarios in the MSSM favor the SUSY particles lighter than $O(\text{TeV})$, thus they can be probed by the experiments at the Large Hadron Collider (LHC). The naturalness argument on the Higgs boson mass supports the "Higgsino scenario", whereas the compatibility of the SUSY particle with the dark matter motivates the "Wino/Bino scenario". Both of the scenarios predict compressed mass spectra, where the mass of the lightest neutralino $\widetilde{\chi}_1^0$ is close to the masses of the chargino $\widetilde{\chi}_1^\pm$ and the second-to-lightest neutralino $\widetilde{\chi}_2^0$. In those scenarios, only low-momentum particles are kinematically allowed to appear in the decay of $\widetilde{\chi}_2^0/\widetilde{\chi}_1^\pm$ into $\widetilde{\chi}_1^0$.

This thesis presents results of search for electroweak production of $\widetilde{\chi}_1^\pm$, $\widetilde{\chi}_2^0$ and $\widetilde{\chi}_1^0$ with compressed mass spectra. The search uses 139 fb^{-1} of $\sqrt{s}$ = 13 TeV proton–proton collision data at the LHC collected by the ATLAS detector. The search assumes pair production of SUSY particles via electroweak interactions, which decay into the lightest neutralinos $\widetilde{\chi}_1^0$ and SM particles. The lightest neutralinos are invisible in the detector, thus are observed as missing momentum in the transverse direction. The decay process $\widetilde{\chi}_2^0 \to Z^*\widetilde{\chi}_1^0$ followed by $Z^* \to \ell\ell$ leads to a characteristic kinematic edge in the spectrum of the invariant mass of the two leptons, at $\Delta m = m(\widetilde{\chi}_2^0) - m(\widetilde{\chi}_1^0)$. The search exploits this feature, using events with two leptons that form a small invariant mass. Events with missing transverse momentum and two same-flavor, oppositely charged leptons are selected, with presence of hadronic activity from initial-state radiation. The compressed mass spectrum expected in the Higgsino and the Wino/Bino scenarios leads to small transverse momentum (p_T) of the two leptons. Various new techniques to efficiently reconstruct low-p_T leptons, as well as data-driven methods to estimate the backgrounds are applied in the search to enhance the sensitivity for the compressed scenarios.

Finally no signals from the MSSM are observed in this search. The data are consistent with predictions from the SM, and the 95% C.L. exclusion limits on the mass of the second-to-lightest neutralino $m(\widetilde{\chi}_2^0)$ are set as functions of the mass difference $\Delta m = m(\widetilde{\chi}_2^0) - m(\widetilde{\chi}_1^0)$, for the Higgsino and the Wino/Bino scenarios. For the Higgsino scenario, the lower limits on $m(\widetilde{\chi}_2^0)$ is set at 193 GeV for Δm = 9.3 GeV, and 92.4 GeV for Δm = 2.3 GeV. For the Wino/Bino scenario, two different parameters that produce the same mass spectra are considered. In the first parameter set, the lower limits on $m(\widetilde{\chi}_2^0)$ is set at 240 GeV for Δm = 7.0 GeV and 92.4 GeV for Δm = 1.5 GeV. In the second parameter set, the lower limits on $m(\widetilde{\chi}_2^0)$ is set at 241 GeV for Δm = 9.0 GeV and 92.4 GeV for Δm = 1.7 GeV.

Studies using multi-variate analysis techniques for lepton reconstruction are also presented. With including this method, the expected lower limits on $m(\widetilde{\chi}_2^0)$ are found to improve by about 15 GeV in the regions with Δm larger than 10 GeV, for both parameters sets in the Wino/Bino scenarios.

Acknowledgements

It has been an extremely intense and exciting five years of doctor course in Kyoto and CERN. This thesis would not have been completed without supports from many people.

I appreciate Prof. Tsuyoshi Nakaya for all the comments and suggestions for putting together the work into the thesis. I would also like to thank Dr. Toshi Sumida, for the supervision and discussion during the master and doctor course. I must also express my gratitude to Prof. Masaya Ishino for offering me a great opportunity to start my first step as a researcher in the ATLAS experiment.

The analysis presented in this thesis would not have been complete without any of the efforts from my colleagues in the compressed electroweak SUSY analysis team. I would like to express my deepest gratitude and respect to Joana Machado Miguens, Stefano Zambito and Mike Hance for the coordination of this extremely complicated analysis and putting together all the efforts into a piece of beautiful paper. I would also like to thank all the members of the team, including Michael Holzbock, Julia Lynne Gonski, Jeffrey David Shahinian, Lorenzo Rossini, and Andrew Todd Aukerman, for the great work and insightful discussions.

My special thanks go to Dr. Shion Chen, who has been a good advisor, a roommate, and a Senpai that I respect. His advice on almost every part of the analysis, from the usage of the ATLAS SUSY analysis tools to the detailed discussion on the Prompt Lepton Tagging method, has been essential to push my work forward.

The days in CERN has been tough but lively, thanks to the roommates in Nagoyatei. I would like to thank Dr. Kouta Onogi for the supports in my early days at CERN, as well as for the very nice dishes he used to cook. I would also like to thank Dr. Masahiro Morinaga for the discussion on the analysis strategies, as well as the Japanese animes he showed to me; it has always been a good refresh during the days in CERN.

I greatly appreciate my friends in Kyoto High-energy Physics Lab, Yosuke Ashida, Yohei Noguchi, Ayami Hiramoto, Shunsuke Tanaka, and Yoshie Nakanishi (Kageyama), for many interesting discussions as well as for a lot more fun stuff (nomikai, coffee, etc.). Special thanks to Yosuke Ashida for the gasshuku style working - it has significantly speeded up my thesis. Special thanks to Yohei Noguchi as well, for great discussion throughout the whole master and doctor courses - it has always been inspiring and interesting.

I would like to thank all the friends in CERN, for sharing both good and tough times. I especially thank Kenta Uno for discussing a variety of things, from technical issues to physics models, and for being a good friend; going for a drive, climbing mountains, playing tennis and a lot of drinks! I also appreciate Atsushi Mizukami, Tomomi Kawaguchi, and Kosuke Takeda, for the nice collaboration work on muon triggers since the master course.

I am grateful to members of the ATLAS Japan SUSY working group, for interesting discussion and technical assistance; especially to Dr. Koji Terashi, Dr.Tomoyuki Saito and Dr. Takuya Nobe. I appreciate the members of the Kyoto ATLAS group, including the former members, for thorough discussion at the

early stage of the study; Dr. Takuya Tashiro, Dr. Takuto Kunigo, Yuta Okazaki, Yuya Mino, Masayuki Hatano, Koichiro Kuniyoshi, Toshiaki Tsujikawa and Ren Kobayashi.

I would like to thank my parents for allowing me to challenge anything I wished to do. Their moral supports have always encouraged me to overcome difficult times.

Finally, I thank my wife, Megu, for the patience and support at any time. Without your love and supports, this thesis would not have been completed.

Contents

List of Tables

List of Figures

Chapter 1

Introduction

The Standard Model of particle physics (SM) successfully offers a very good and systematic descriptions of our universe. However, we have some clear evidences that the SM is not a perfect theory; the gravity is not included in the theory, it does not address to the finite neutrino masses, realistic candidates of the dark matter is absent, the dark energy is not addressed, the mass of the Higgs boson cannot be naturally explained, etc. A new framework is certainly necessary at a higher energy scale, to give solutions to phenomena that can not be explained in the SM.

Supersymmetry (SUSY) [1–3] is one of the natural extensions of the SM, which assumes a hypothetical symmetry between fermions and bosons. New particles with identical quantum numbers to their SM partners except for their spins are introduced in the SUSY models. In this chapter, the theoretical background of this thesis is presented. In Section 1.1, a brief introduction to the SUSY models is presented. We particularly focus on the Minimal Supersymmetric Standard Model (MSSM), where the SM is extended in a minimal way into the SUSY model. The scenarios in the MSSM with "compressed" mass spectra, considered in this thesis, are explained in Section 1.2. An overview of the strategy of search for SUSY particles with compressed mass spectra is explained in Section 1.3. Finally, the outline of this thesis is shown in Section 1.4.

1.1 Supersymmetry

Supersymmetry transforms each particle of the SM to a partner whose spin differs by 1/2. An operator Q that generates the transformations is introduced;

$$Q|\text{Boson}\rangle = |\text{Fermion}\rangle, \qquad Q|\text{Fermion}\rangle = |\text{Boson}\rangle. \tag{1.1}$$

The fermionic (bosonic) partner of the boson (fermion) is referred to as a "superpartner". The SM particles and their superpartners are placed into a irreducible representations of the supersymmetry algebra, called "supermultiplet". A supermultiplet contains both fermionic and bosonic states. The supersymmetric generators $Q, Q^\dagger$ are defined to commute with the squared-mass operator $-P^2$ and also with the gauge symmetry generators, therefore the masses and the quantum numbers of the particles in the same supermultiplet are identical, except for their spins.

1.1.1 The Minimal Supersymmetric Standard Model

In the minimal extention of the SM, referred to as the Minimal Supersymmetric Standard Model (MSSM) [4, 5], only the minimal supersymmetric particles are added to extend the SM.

Table 1.1: Chiral supermultiplets in the Minimal Supersymmetric Standard Model. The spin-0 fields are complex scalars, and the spin-1/2 fields are left-handed two-component Weyl fermions [6].

Names		spin 0	spin 1/2	$SU(3)_C,\ SU(2)_L,\ U(1)_Y$
squarks, quarks	Q_i	$(\widetilde{u}_L\ \ \widetilde{d}_L)$	$(u_L\ \ d_L)$	$(\mathbf{3},\ \mathbf{2},\ \frac{1}{6})$
(×3 families)	$\overline{u}_i$	$\widetilde{u}^*_R$	$u^\dagger_R$	$(\overline{\mathbf{3}},\ \mathbf{1},\ -\frac{2}{3})$
	$\overline{d}_i$	$\widetilde{d}^*_R$	$d^\dagger_R$	$(\overline{\mathbf{3}},\ \mathbf{1},\ \frac{1}{3})$
sleptons, leptons	L_i	$(\widetilde{\nu}\ \ \widetilde{e}_L)$	$(\nu\ \ e_L)$	$(\mathbf{1},\ \mathbf{2},\ -\frac{1}{2})$
(×3 families)	$\overline{e}_i$	$\widetilde{e}^*_R$	$e^\dagger_R$	$(\mathbf{1},\ \mathbf{1},\ 1)$
Higgs, Higgsinos	H_u	$(H^+_u\ \ H^0_u)$	$(\widetilde{H}^+_u\ \ \widetilde{H}^0_u)$	$(\mathbf{1},\ \mathbf{2},\ +\frac{1}{2})$
	H_d	$(H^0_d\ \ H^-_d)$	$(\widetilde{H}^0_d\ \ \widetilde{H}^-_d)$	$(\mathbf{1},\ \mathbf{2},\ -\frac{1}{2})$

Table 1.2: Gauge supermultiplets in the Minimal Supersymmetric Standard Model [6].

Names	spin 1/2	spin 1	$SU(3)_C,\ SU(2)_L,\ U(1)_Y$
gluino, gluon	$\widetilde{g}$	g	$(\mathbf{8},\ \mathbf{1}\ ,\ 0)$
Winos, W bosons	$\widetilde{W}^\pm\ \ \widetilde{W}^0$	$W^\pm\ \ W^0$	$(\mathbf{1},\ \mathbf{3}\ ,\ 0)$
Bino, B boson	$\widetilde{B}^0$	B^0	$(\mathbf{1},\ \mathbf{1}\ ,\ 0)$

Particles in the MSSM

There are two types of supermultiplets in the MSSM, the "chiral supermultiplets", composed of spin-0 bosons and spin-1/2 fermions, and the "gauge supermultiplets", composed of spin-1 bosons and spin-1/2 fermions. The chiral supermultiplets in the MSSM is summarized in Table 1.1, classified according to their transformation properties under the SM gauge group $SU(3)_C \times SU(2)_L \times U(1)_Y$. The gauge supermultiplets in the MSSM is summarized in Table 1.2.

The fermions in the SM and their spin-0 superpartners, referred to as "sfermions", are formed into the chiral multiplets. The superpartners of the quarks and leptons are also referred to as "squarks" or "sleptons". Since the left-handed quarks and leptons transform as $SU(2)_L$ doublets and the right-handed parts transform as singlets, they must reside in different chiral supermultiplet. Thus each left- and right-handed part has its own complex scalar partner. The superpartner of the left-handed and right-handed fermions are denoted as $\widetilde{f}_L$ and $\widetilde{f}_R$.

The Higgs boson, with spin-0, is included in the chiral supermultiplets. While the SM contains one Higgs doublet, in the MSSM two Higgs doublets are introduced, denoted by (H^0_u, H^+_u) and (H^0_d, H^-_d), which provide masses to up-type and down-type fermions, respectively. These two doublets mix to form four mass eigenstates, h^0, H^0, A^0 and $H^\pm$. "Higgsinos", the superpartners of the Higgs doublets, are $SU(2)_L$ doublet left-handed Weyl spinor fields, denoted by $(\widetilde{H}^0_u, \widetilde{H}^+_u)$ and $(\widetilde{H}^0_d, \widetilde{H}^-_d)$.

The gauge bosons in the SM are arranged into gauge supermultiplets. The spin 1/2 partners of these bosons are referred to as "gauginos", or more specifically with an "-ino" suffix at the end of the name of the SM bosons. The superpartner of the gluon is called "gluino", and the superpartners of the electroweak gauge bosons $W^\pm$, W^0 and B^0 are referred to as "Wino" and "Bino", denoted by $\widetilde{W}^\pm$, $\widetilde{W}^0$ and $\widetilde{B}^0$.

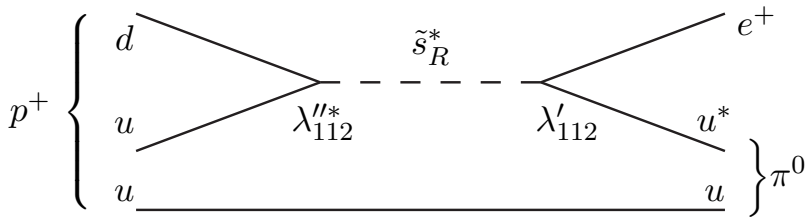

Figure 1.1: A diagram with a squark mediating proton decay $p \to e^+\pi^0$. This process is possible when the R-parity is violated by both $\Delta B = 1$ and $\Delta L = 1$ interactions.

R-parity

In this thesis, a parity called "R-parity" is assumed to be conserved. The R-parity is defined as

$$R = (-1)^{3(B-L)+2s}, \tag{1.2}$$

where B is the baryon number, L is the lepton number, and s is the spin. The chiral supermultiplets carry baryon number assignments $B = +1/3$ for Q_i; $B = -1/3$ for $\overline{u}_i, \overline{d}_i$; and $B = 0$ for all the others. The lepton number assignments are $L = +1$ for L_i, $L = -1$ for $\overline{e}_i$, and $L = 0$ for all the others. If the R-parity is violated, a B- or L-violating process can take place at a reasonable rate. An example is given in Figure 1.1, where the proton decay occurs via squark mediation. Given that such process is not yet observed, we assume that the R-parity is conserved.

The consequence of the R-parity conservation is that the SUSY particle cannot decay into the SM particles. Thus, a SUSY particle can only decay into another lighter SUSY particle and some SM particles. The lightest SUSY particle (LSP) does not have a decay channel, and are stable.

Soft SUSY breaking

If the supersymmetry were an unbroken symmetry, it would require the masses of the superpartner particles to be the same as those of the SM particles. For example, the superpartners of the electron $\widetilde{e}_L$ and $\widetilde{e}_R$ would have the same masses as the electron, $m_{\widetilde{e}} = 511\text{keV}$, which would make the particle have been observed already if they exist. This leads to a conclusion that the supersymmetry must be a broken symmetry. The Lagrangian of the MSSM can be divided into the SUSY conserving part, $\mathcal{L}_{\text{SUSY}}$, and the SUSY breaking part, $\mathcal{L}_{\text{soft}}$. The SUSY conserving part of the Lagrangian (explained for example in Ref. [6]) extends the SM in a way that they are invariant under the supersymmetric transformation.

The SUSY breaking part is introduced to explicitly break the symmetry with keeping the ideal behavior of the theory. The allowed form of the supersymmetry breaking part of the Lagrangian is strongly related with the fine-tuning problem explained in Section 1.1.2. If we assume that the MSSM gives a solution to the fine-tuning problem, the SUSY breaking must be "soft", i.e. it should not include terms with dimensionless couplings. The most general form of the soft SUSY-breaking Lagrangian in the MSSM, which includes mass terms of gauginos, higgsinos and sfermions, is written as

$$
\begin{aligned}
\mathcal{L}_{\text{soft}} \;=\; & -\frac{1}{2}\left(M_3\tilde{g}\tilde{g} + M_2\widetilde{W}\widetilde{W} + M_1\widetilde{B}\widetilde{B} + \text{c.c.}\right) \\
& -\left(\mathbf{a_u}\widetilde{u}^{\dagger}H_u\widetilde{Q} + \mathbf{a_d}\widetilde{d}^{\dagger}H_d\widetilde{Q} + \mathbf{a_e}\widetilde{e}^{\dagger}H_d\widetilde{L} + \text{c.c.}\right) \\
& -\widetilde{Q}^{\dagger}\mathbf{m_Q^2}\widetilde{Q} - \widetilde{L}^{\dagger}\mathbf{m_L^2}\widetilde{L} - \widetilde{\overline{u}}^{\dagger}\mathbf{m_{\overline{u}}^2}\widetilde{\overline{u}} - \widetilde{\overline{d}}^{\dagger}\mathbf{m_{\overline{d}}^2}\widetilde{\overline{d}} - \widetilde{\overline{e}}^{\dagger}\mathbf{m_{\overline{e}}^2}\widetilde{\overline{e}} \\
& -m_{H_u}^2 H_u^* H_u - m_{H_d}^2 H_d^* H_d - (bH_uH_d + \text{c.c.}) \;, \qquad (1.3)
\end{aligned}
$$

where M_1 is the mass of the Bino, M_2 of the Wino, and M_3 of the gluino. The matrices $\mathbf{m_i^2}$ ($i = Q, L, \overline{u}, \overline{d}, \overline{e}$), $\mathbf{a_i}$ ($i = \overline{u}, \overline{d}, \overline{e}$) and b, stand for mass squared, trilinear, and bilinear coefficients for the scalar fields, respectively. A total of 105 additional masses, phases and mixing angles are introduced [7], and this makes the MSSM highly arbitrary. Many of these parameters can not be constrained by experiments and therefore is constrained by imposing some reasonable theoretical assumptions.

MSSM mass eigenstates

The squarks and sleptons with the same electric charge, R-parity, and color quantum numbers can mix with each other to form mass eigenstates. However, we often assume

$$
\mathbf{m}_i^2 = m_i^2\mathbf{1}, \qquad i = Q, L, \overline{u}, \overline{d}, \overline{e}, \qquad (1.4)
$$

to avoid large flavor-changing and CP-violating effects, which are highly disfavored by experiments. The non-diagonal component in $\mathbf{a_i}$ should also be small, to suppress the flavor-changing effect. The diagonal components correspond to the scalar three-point couplings, and are often assumed that they are proportional to the corresponding Yukawa coupling matrices,

$$
\mathbf{a_u} = A_{u0}\,\mathbf{y_u}, \qquad \mathbf{a_d} = A_{d0}\,\mathbf{y_d}, \qquad \mathbf{a_e} = A_{e0}\,\mathbf{y_e}, \qquad (1.5)
$$

where A_{u0}, A_{d0} and A_{e0} are assumed to be real, in order to avoid adding extra CP-violation phases. Mixing between the left-handed sfermion $\widetilde{f_L}$ and the right-handed sfermion $\widetilde{f_R}$ is induced by the term proportional to a_i, and also by the term in supersymmetric part Lagrangian that are proportional to Yukawa coupling. The mixing forms the mass eigenstates $\widetilde{f_1}$ and $\widetilde{f_2}$, where $m(\widetilde{f_1})$ is smaller than $m(\widetilde{f_2})$. Because the mixing is proportional to the Yukawa coupling, the mass of $\widetilde{f_1}$ can become significantly smaller than the masses of $\widetilde{f_L}/\widetilde{f_R}$ for the third generation of the sfermions. Thus, in the MSSM, it is often assumed that the stop ($\widetilde{t_1}$), sbottom ($\widetilde{b_1}$) and stau ($\widetilde{\tau_1}$) are much lighter than the other generation of the sfermions.

The neutral electroweak gauginos mix with the neutral Higgsinos to form four mass eigenstates called "neutralinos", denoted by $\widetilde{\chi}_{1-4}^0$, ordered by their masses. The mass eigenstates are obtained by diagonalizing the mass matrix $M_{\widetilde{N}}$, which are

$$
\mathbf{M}_{\widetilde{N}} = \begin{bmatrix}
M_1 & 0 & -c_\beta\, s_W\, m_Z & s_\beta\, s_W\, m_Z \\
0 & M_2 & c_\beta\, c_W\, m_Z & -s_\beta\, c_W\, m_Z \\
-c_\beta\, s_W\, m_Z & c_\beta\, c_W\, m_Z & 0 & -\mu \\
s_\beta\, s_W\, m_Z & -s_\beta\, c_W\, m_Z & -\mu & 0
\end{bmatrix}. \qquad (1.6)
$$

Here we have introduced abbreviations $s_\beta = \sin\beta$, $c_\beta = \cos\beta$, $s_W = \sin\theta_W$, and $c_W = \cos\theta_W$, where θ_W is the Weinberg angle, and β is a parameter defined by the ratio of the two vacuum expectation values

$$\tan\beta \equiv \langle H_u^0\rangle / \langle H_d^0\rangle, \tag{1.7}$$

where $\langle H_u^0\rangle$ and $\langle H_d^0\rangle$ are the vacuum expectation values of the two Higgs doublets.

The parameters M_1, M_2 are chosen to be real and positive, by re-definition of the phases of the $\widetilde{B}$ and $\widetilde{W}$. The Higgsino mass parameter μ is assumed to be real, however the sign of μ can be either positive or negative. In the limit of $m_Z \ll |\mu \pm M_1|, |\mu \pm M_2|$, the mass eigenvalues are

$$m_{\widetilde{N}_1} = M_1 - \frac{m_Z^2 s_W^2 (M_1 + \mu \sin 2\beta)}{\mu^2 - M_1^2} + \ldots \quad , \tag{1.8}$$

$$m_{\widetilde{N}_2} = M_2 - \frac{m_W^2 (M_2 + \mu \sin 2\beta)}{\mu^2 - M_2^2} + \ldots \quad , \tag{1.9}$$

$$m_{\widetilde{N}_3}, m_{\widetilde{N}_4} = |\mu| + \frac{m_Z^2 (I - \sin 2\beta)(\mu + M_1 c_W^2 + M_2 s_W^2)}{2(\mu + M_1)(\mu + M_2)} + \ldots \quad , \text{and} \tag{1.10}$$

$$|\mu| + \frac{m_Z^2 (I + \sin 2\beta)(\mu - M_1 c_W^2 - M_2 s_W^2)}{2(\mu - M_1)(\mu - M_2)} + \ldots \quad . \tag{1.11}$$

where we have taken M_1 and M_2 real and positive by convention, and assumed μ is real with sign $I = \pm 1$.

The chargino spectrum can be analyzed in a similar way. The chargino mass eigenstates consist of a Wino-like $\widetilde{C}_1^\pm$ and and a Higgsino-like $\widetilde{C}_2^\pm$, with masses

$$m_{\widetilde{C}_1} = M_2 - \frac{m_W^2 (M_2 + \mu \sin 2\beta)}{\mu^2 - M_2^2} + \ldots \quad \text{and} \tag{1.12}$$

$$m_{\widetilde{C}_2} = |\mu| + \frac{I m_W^2 (\mu + M_2 \sin 2\beta)}{\mu^2 - M_2^2} + \ldots \quad . \tag{1.13}$$

The neutralinos are assumed to be the lightest SUSY particles (LSP) in many scenarios, as they provide a good dark matter candidate, as explained in Section 1.1.2. Depending on the M_1, M_2 and μ values, three types of LSP, each dominated by one of the three components (Bino, Wino, or Higgsino), can be considered. Figure 1.2 illustrates the mass spectra of the lightest neutralino-chargino sector, for the Bino, Wino and Higgsino dominated cases. If $M_1 \ll M_2, |\mu|$, the lightest neutralino $\widetilde{\chi}_1^0$ would be dominated by the Bino component. The mass of the Bino-dominant $\widetilde{\chi}_1^0$ will be $m_{\widetilde{N}_1} \sim M_1$. If $M_2 \ll M_1, |\mu|$, then the lightest neutralino $\widetilde{\chi}_1^0$ and the lightest chargino $\widetilde{\chi}_1^\pm$ are dominated by the Wino component. Then, the $\widetilde{\chi}_1^0$ and the $\widetilde{\chi}_1^\pm$ are nearly mass-degenerate, with $m_{\widetilde{N}_2} \simeq m_{\widetilde{C}_1} \sim M_2$. Finally, if $|\mu| \ll M_1, M_2$, two lightest neutralinos $\widetilde{\chi}_1^0, \widetilde{\chi}_2^0$ and the lightest chargino $\widetilde{\chi}_1^\pm$ mostly consist of the Higgsino components. With the approximation that $|\mu| \ll \min(M_1, M_2)$ and $\sin 2\beta \ll 1$ (i.e. $\tan\beta$ is sufficiently large), the neutralino and chargino masses become $m_{\widetilde{N}_3}, m_{\widetilde{N}_4} \sim |\mu| \pm I m_Z^2 / 2M_1$ and $m_{\widetilde{C}_2} \sim |\mu|$.

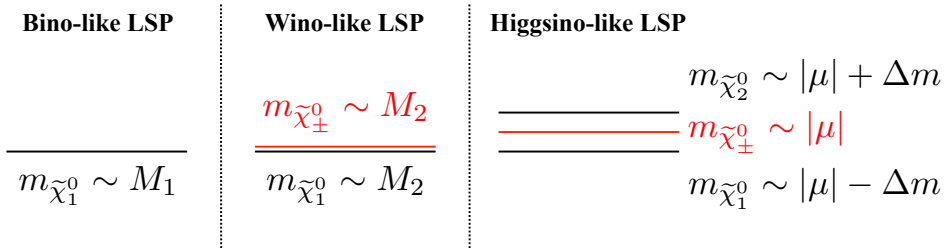

Figure 1.2: Illustration of the neutralino and chargino mass spectra, for Bino-dominated (left), Wino-dominated (middle) and Higgsino dominated (right) lightest supersymmetric particle (LSP).

Figure 1.3: The diagrams for one-loop quantum corrections to the Higgs squared mass parameter m_H^2, due to a Dirac fermion f (left), and a scalar S (right).

1.1.2 Benefit of introducing SUSY

The fine-tuning problem

One of the promising motivation of introducing supersymmetry is that it can solve so called the "fine-tuning problem" in the Higgs boson mass. The Higgs boson was discovered by ATLAS and CMS Collaborations [8][9] in 2012, with its mass of 125 GeV. The bare mass of the Higgs boson receives quantum corrections by the virtual contribution from all the particles that the Higgs couples to. All the contributions are summed up, and yield the observed mass of 125 GeV. The quantum correction from one-loop diagram (Figure 1.3, left) yields

$$\Delta m_H^2 = -\frac{|\lambda_f|^2}{8\pi^2}\Lambda_{\rm UV}^2 + O(\log\Lambda_{\rm UV}). \tag{1.14}$$

Here, we assume a Dirac fermion f with mass m_f, which couples to the Higgs field with a term in the Lagrangian $-\lambda_f H\bar{f}f$. The Λ_{UV} is the ultraviolet cutoff energy scale, which can be understood as the energy scale where the contribution of a new physics changes the structure of the theory. We may assume that the SM is an effective theory that holds up to the Planck scale ($M_{\rm P}$) of $O(10^{18})$ GeV, and set $\Lambda_{UV} = M_{\rm P}$. The problem is that the quantum correction to m_H^2 is more than 30 orders of magnitude larger than the observed mass of $O(100)$ GeV. A precise fine-tuning of the parameters is required, for all orders of the perturbation, and for every particle that couples to the Higgs boson, to reproduce the electroweak scale mass. This problem is known as the "fine-tuning problem" or the "hierarchy problem".

Supersymmetry gives a solution to this problem. A scalar particle with a mass m_S that couples to Higgs in a form of $-\lambda_S|H|^2|S|^2$ gives a correction

$$\Delta m_H^2 = \frac{|\lambda_S|}{16\pi^2}\Lambda_{\rm UV}^2 + O(\log\Lambda_{\rm UV}), \tag{1.15}$$

via the diagram in Figure 1.3 right. In the MSSM, two scalar partners ($\widetilde{f_L}$ and $\widetilde{f_R}$) are added for one SM fermion, therefore by comparing Eqs. 1.14 and 1.15, the quadratic divergence cancels and only leaves the terms with $O(\log \Lambda_{UV})$. The soft-breaking part of the Lagrangian can not include terms with dimensionless couplings because such terms would bring up the quadratic divergence again.

Grand Unification

Another benefit of introducing SUSY is that we can obtain unification of the couplings of three interactions (electromagnetic, weak, and strong) at a high-energy scale. As a consequence of renormalization, the SM couplings have to evolve against the energy scale according to the renormalization group equation (RGE). This is known as "running coupling constants" [10][11]. The RGEs for one-loop are

$$\frac{d}{dt}\alpha_a^{-1} = -\frac{b_a}{2\pi} \qquad (a = 1, 2, 3), \tag{1.16}$$

where α_a are the coupling constants for the strong, weak and electro-magnetic interactions, b_a are the coefficients determined by the gauge group and the particle multiplets, to which the gauge bosons couple. For the SM and the MSSM, they are

$$(b_1, b_2, b_3) = \begin{cases} (41/10,\ -19/6,\ -7) & : \text{Standard Model} \\ (33/5,\ 1,\ -3) & : \text{MSSM} \end{cases} \tag{1.17}$$

The MSSM coefficients are larger because of the extra MSSM particles. Figure 1.4 shows the running of the gauge couplings, including the two-loop effects, in the SM and the MSSM. In the MSSM, the gauge couplings unify at a scale of $M_U \sim 1.5 \times 10^{16}$ GeV, with the SUSY particles with the mass scale of $O(\text{TeV})$.

Dark Matter

The existence of the dark matter has been strongly suggested by many different experiments, for example from the galaxy rotation curves measurements [12][13], gravitational lensing [14], and Bullet Cluster measurements [15]. The Λ-CDM model assumes that the dark matter is massive "cold" particles, which have average kinetic energy much lower than their mass. Dark matter candidates must be electrically neutral, and also should interact with ordinary matter only weakly. The most commonly considered mechanism for generating such dark matter is the "freeze-out" mechanism, where in the early universe the SM particles and the dark matter were in thermal equilibrium, until at a freeze-out temperature when the dark matter annihilation rate is lower than the rate of the cosmic expansion. The dark matter density at the freeze-out temperature remains unchanged, which is called "the relic density". The current experimental results are consistent with the Λ-CDM model, however, there are no dark matter candidate in the SM. This is considered as a clear evidence that beyond-SM particles exist.

The dark matter abundance can be measured via cosmic microwave background radiations. Assuming the Λ-CDM model, the latest result from Planck [16] reports

$$\Omega_c h^2 = 0.1200 \pm 0.0012, \tag{1.18}$$

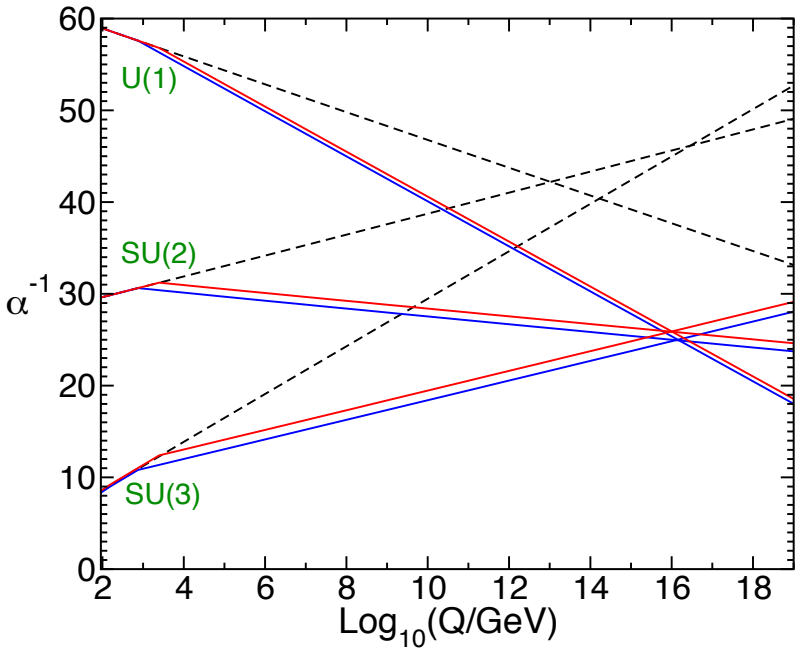

Figure 1.4: Inverse gauge couplings $\alpha_a^{-1}(Q)$ in the Standard Model (dashed lines) and the MSSM (solid lines) [6]. In the MSSM case, the sparticle masses are treated as a common threshold varied between 750 GeV (blue) and 2.5 TeV (red), and α_3 is varied between 0.117 and 0.120, accordingly.

where h is the reduced Hubble constant and Ω_c is the dark matter density relative to the "critical density". The critical density is about 10^{26} kg/m^3, defined as the average density of matter in the universe assuming that the universe will stop its expansion after an infinite time. The dark matter candidate must have annihilation cross section that matches with this observation. If the cross section is too high, the dark matter annihilates too rapidly before the freeze-out temperature, and leads to too small dark matter relic density. On the contrary, if the annihilation cross section is too low, the dark matter relic density becomes too large.

The MSSM can provide good dark matter candidates. When the R-parity is conserved, the lightest SUSY particle (LSP), which is often considered to be the lightest neutralino $\widetilde{\chi}_1^0$, is stable, massive and weakly interacting with SM particles, therefore is a good candidate of the dark matter. The $\widetilde{\chi}_1^0$ with its mass smaller than a few TeV, depending on the composition of the $\widetilde{\chi}_1^0$, gives a correct dark matter density. More detailed discussion is in Section 1.2.2.

1.2 MSSM scenarios with compressed mass spectra

In this thesis, two main MSSM scenarios are discussed. The first one is "Higgsino" scenario, which is motivated by the naturalness argument, and is explained in Section 1.2.1. The second one is "Wino/Bino" scenario, motivated by the SUSY LSP dark matter and is discussed in Section 1.2.2. Both scenarios give characteristic compressed mass spectra, where $\Delta m = m(\widetilde{\chi}_1^0) - m(\widetilde{\chi}_2^0)$ is small.

1.2.1 Naturalness motivated scenarios

After the discovery of the 125 GeV Higgs boson, natural SUSY mass spectra have been discussed extensively in many ways. As described in Section 1.1.2, the MSSM cancels the quadratic divergence of the Higgs mass correction. However, because the bare mass of the Higgs boson is limited to $m_{h^0} < m_Z|\cos 2\beta|$, a total radiative correction of a few tens of GeV is required to produce Higgs mass of 125 GeV [6]. The correction would be the sum of the $\log \Lambda_{UV}$ parts for all the fermions/scalars, and the contributions to the mass correction is dominated by the top quark and its supersymmetric partner (stop). Their one-loop corrections are given as [17]

$$m_h^2 \approx m_Z^2 \cos^2 2\beta + \frac{3}{(4\pi)^2}\frac{m_t^4}{v^2}\left[\ln\frac{m_{\tilde{t}}^2}{m_t^2} + \frac{X_t^2}{m_{\tilde{t}}^2}\left(1 - \frac{X_t^2}{12m_{\tilde{t}}^2}\right)\right], \tag{1.19}$$

where X_t is a mixing parameter defined in Ref. [17], responsible for the magnitude of mixing between $\tilde{t}_L$ and $\tilde{t}_R$. The $m_{\tilde{t}}^2 = m_{\tilde{t}_L} m_{\tilde{t}_R}$ is the geometric mean of the stop masses, and the v is the vacuum expectation value at 174 GeV. The size of the correction for a given $m_{\tilde{t}}$ is maximized at $X_t = \sqrt{6}m_{\tilde{t}}$. Figure 1.5 shows the Higgs mass as a function of $m_{\tilde{t}_1}$ for minimum and maximum mixing. For the minimum mixing, the mass of the lightest stop needs to be larger than 3 TeV, while for the maximum mixing, it can be lighter than 1 TeV. If the stop mass is large, the size of the quantum correction becomes very sensitive to the mass itself, leading to another fine-tuning of the stop mass parameter. To suppress the fine-tuning of the parameters to be $O(10)\%$ level, the $m_{\tilde{t}}$ is required to be at $O(1)$ TeV, which favors relatively large mixing. Similar discussion can be applied to masses of the Higgsino ($|\mu|$) and the gluino ($M_3 = m(\tilde{g})$), although the gluino contributes to the correction of the Higgs mass indirectly via correction to the stop mass. A "natural" SUSY scenario thus requires a small $m_{\tilde{t}_1}$, $|\mu|$, and M_3, to be typically $O(\text{TeV})$ or less.

Recent LHC searches set strict exclusion limits on the masses of stop ($m(\tilde{t}_1)$) and gluino ($m(\tilde{g})$). Figure 1.6 shows latest results for stop and gluino searches in ATLAS [20]. The lightest stop is excluded up to 1 TeV for $m(\tilde{\chi}_1^0)$ smaller than 400 GeV. The gluino is excluded up to 2 TeV for $m(\tilde{\chi}_1^0)$ smaller than 1 TeV [1]. These exclusion limits are extracted using a "simplified" scenario [22–24], where all the SUSY particles that do not directly contribute to the decay of the stop/gluino are assumed to be decoupled, i.e. heavier than a few TeV. In the simplified scenarios, it is also assumed that the branching ratio of a particular decay chain is 100%. For example, in the stop search, the branching ratio of $\tilde{t}_1 \to t\tilde{\chi}_1^0$ is assumed to be 100% if it is kinematically allowed, i.e. $m(\tilde{t}_1) > m(t) + m(\tilde{\chi}_1^0)$. The CMS experiment also sets exclusion limits to the stop and gluino mass in the simplified scenario, which impose similar constraints. Although these constraints assume the simplified scenario and do not immediately exclude all the stop/gluino in this mass region, the "standard" naturalness in the MSSM is constrained by these limits. An exception is phase space difficult to have good physics sensitivity, for example regions where the mass splitting between $m(\tilde{t}_1)$ and $m(\tilde{\chi}_1^0)$ is small.

However, a discussion in Ref. [25] argues that 125 GeV Higgs can be obtained with larger $m(\tilde{t}_1)$ or $m(\tilde{g})$ with keeping the level of fine-tuning to a reasonable level. The main idea of this study is to re-consider the measure of "naturalness", by taking into account various potential fine-tuning of the intermediate parameters, such as $\tan\beta$. Also, this study uses a likelihood approach to take into account the effect of all the parameters, as well as the correlations among them. As a result, $m(\tilde{t}_1)$ or $m(\tilde{g})$ can be heavier than a

[1] The yellow exclusion contour shown in the right plot of Figure 1.6, labeled as "$\tilde{g} \to qq(\gamma/Z)\tilde{G}$ via $\tilde{\chi}_1^0$" assumes the "General Gauge Mediated" [21] scenario, which has a significantly different structure to the nominal MSSM scenarios, and is not considered in this context.

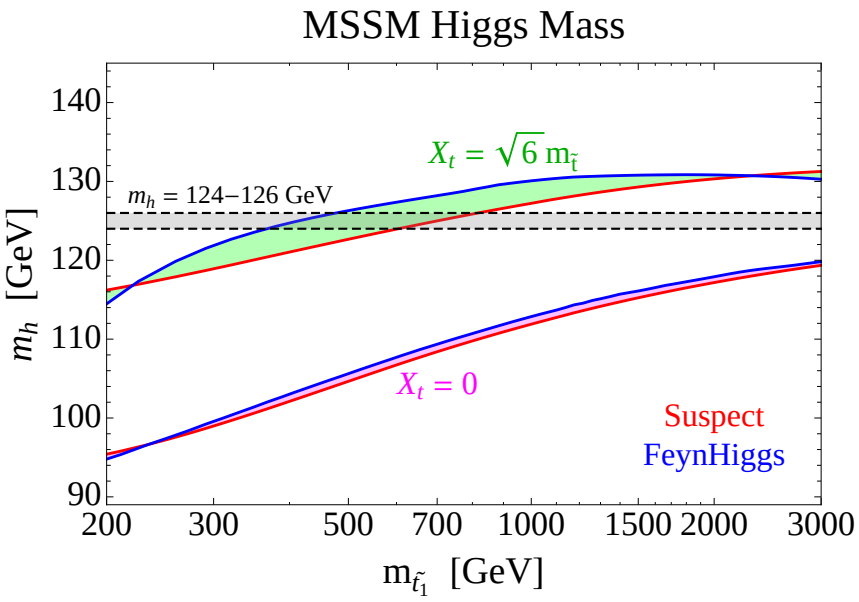

Figure 1.5: The Higgs mass in the MSSM as a function of the lightest top squark mass, $m_{\tilde{t}_1}$ [17]. The red and blue solid lines are computed using Suspect [18] and FeynHiggs [19]. The two upper lines are for the maximal top squark mixing assuming degenerate stop soft masses and yield a 124 (126) GeV Higgs mass for $m_{\tilde{t}_1}$ in the range of 350–600 (500–800) GeV. The two lower lines are for zero top squark mixing and do not yield the 124 GeV Higgs mass for $m_{\tilde{t}_1}$ below 3 TeV. The tan β is set to 20.

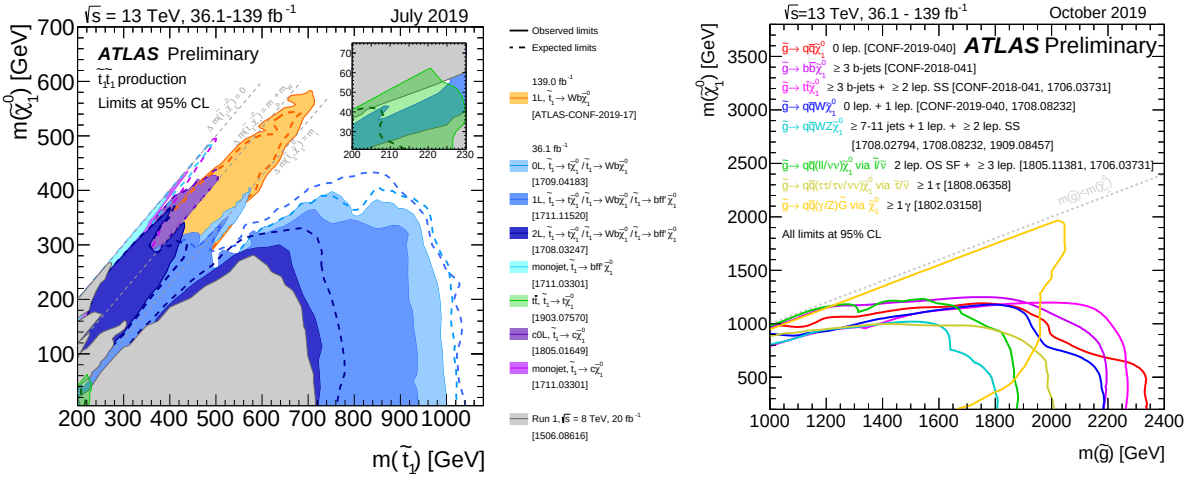

Figure 1.6: The exclusion limits at 95% C.L. for stop (left) and gluino (right), obtained using 36.1–139 fb^{-1}of pp-collision data in Run-2 in ATLAS [20]. The limits are set on a 2D plane, with the mass of the lightest stop ($m(\tilde{t}_1)$) or gluino ($\tilde{g}$) in the horizontal axis and the mass of the lightest neutralino ($m(\tilde{\chi}_1^0)$) in the vertical axis. The colored regions are excluded in the left plot, and the regions inside (lower left side of) the contours are excluded in the right plot.

few TeV if we allow 1% fine-tuning. It is interesting that the Higgsino mass parameter μ still needs to be $\lesssim 700$ GeV. The Higgsino-dominant LSP below 1 TeV is motivative in this context. This scenario, referred to as the Higgsino scenario in this thesis, is also supported by other arguments on the naturalness [26, 27] which suggest that $|\mu|$ should be near the electroweak scale [28–31] while M_1 and/or M_2 can be larger. It is also worth pointing out that a pure-Higgsino LSP is a good candidate of dark matter when its mass is about 1 TeV, which is not far from this limit. The masses of the Higgsino-dominant neutralinos are nearly degenerate from Eq. 1.10 and Eq. 1.11 when $|\mu| \ll M_1, M_2$. Assuming nearly pure-Higgsino LSP, the mass difference $\Delta m = m(\widetilde{\chi}_1^0) - m(\widetilde{\chi}_2^0)$ is at $O(100)$ MeV, which are generated by radiative corrections [32]. However, when M_1 or M_2 is larger than $|\mu|$ but smaller than about 1 TeV, the mass difference can be as large as a few tens of GeV. In this thesis, we consider Higgsino-dominant LSP with moderate Wino and Bino mixing, to create Δm larger than a few GeV.

1.2.2 Dark Matter motivated scenarios

As discussed in Section 1.1.2, the lightest neutralino is a good candidate of dark matter, assuming that the R-parity is conserved in the MSSM. The component of the lightest neutralino, whether it is dominated by Bino, Wino or Higgsino, is important to predict the mass of the neutralino that gives the correct dark matter density. A phenomenological MSSM (pMSSM) [33] is introduced by constraining some of the free parameters in the MSSM based on reasonable phenomenological assumptions. In Figure 1.7, the pMSSM is further constrained to produce the correct dark matter relic density, and are scanned over the $(m_\chi, \sigma_p^{\mathrm{SI}})$ plane by varying the remaining free parameters in the MSSM, for example M_1, M_2 and μ. Here, the m_χ denotes the mass of the dark matter, and the σ_p^{SI} denotes the spin-independent scattering cross section of the dark matter and the proton. Colors of the points in Figure 1.7 indicate the difference of the composition of the lightest neutralino.

Generally, a promising dark-matter candidate is either a Higgsino-dominant LSP at $m_\chi \sim 1$ TeV, or a Wino-dominant LSP at $m_\chi \sim 3$ TeV, which is outside the reach of LHC searches. However, for mixed states there are some scenarios that lowers the neutralino mass to $O(100)$ GeV with reproducing the dark matter relic density. Such scenarios are referred to as "well-tempered neutralino" [37, 38]. The lightest two of the three mass parameters need to be precisely controlled to make the mass of the LSP degenerate or maximally mixed, and produce the correct dark matter density.

The "Wino/Bino scenario" in this thesis refer to the case with $M_1 \lesssim M_2 \ll |\mu|$, where the Bino-dominant neutralino is the LSP and the Wino-dominant neutralino and charginos have masses just above the LSP mass. In Ref. [38], the compatibility of such scenario with the dark matter relic density, as well as the constraints set by experiments, is discussed. Figure 1.8 shows the experimental limits on the Wino/Bino scenario, projected onto $M_2 \times (M_2 - M_1)$ plane. Different MSSM parameters are assumed in the two plots; $\mu = 750$ GeV is assumed in the plot on the left, and $\mu = 2.5$ TeV is assumed in the plot on the right. Other parameters in the MSSM are set to $\tan\beta = 10$ and pseudoscalar Higgs mass $M_A = 500$ GeV in both plots. The constraints from two dark matter experiments, the XENON1T [36] and the Fermi-LAT [39], are shaded with purple and magenta, respectively. The constraints from the collider experiments, the LEP [40] and the CMS [41, 42], are shown with green and orange regions, respectively. A brief overview of the constraints set by each of the experiments is given below.

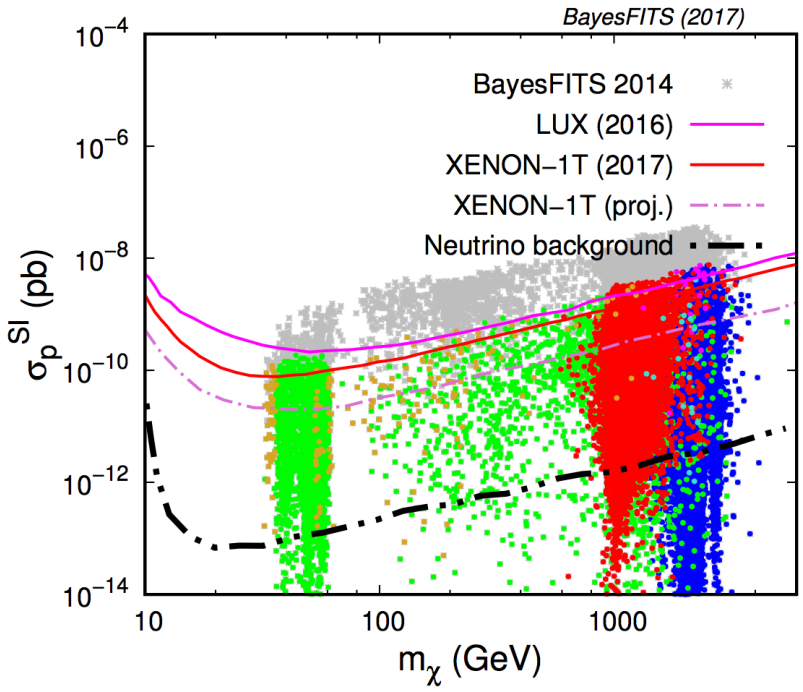

Figure 1.7: Current and projected limits on dark matter spin-independent cross section with a proton ($\sigma_p^{\rm SI}$), as a function of the mass of the dark matter (m_χ) [34]. The results from LUX [35] and XENON1T [36] are shown with magenta and red solid lines, respectively. The m_χ and $\sigma_p^{\rm SI}$ of the LSPs in various scenarios in the pMSSM that reproduce the dark matter abundance $\Omega_\chi h^2 \approx 0.12$ are shown with colored points. Points in green are characterized by a 90% or more Bino composition of the neutralino; points in red are > 90% Higgsino; and points in blue are > 90% Wino. Bino/Higgsino admixtures are shown in gold, Wino/Higgsino in magenta, and Wino/Bino in cyan.

Limits by XENON1T The XENON1T is a dark matter direct detection experiment, which searches for the scattering of the dark matter with the xenon nuclei. The results shown in Figure 1.8 are derived from 34 days of data collected with 1000 kg fiducial xenon mass [36]. With no significant excess over the background expectation, a limit on the cross section of the dark matter-nucleon scattering is set as a function of dark matter mass. The XENON1T results are overlayed on $M_2 \times (M_2 - M_1)$ plane and are shown with regions shaded with purple, which exclude regions with large values of $(M_2 - M_1)$. The light purple areas show the projected exclusion limits by the XENON1T, assuming a factor 2 improvement in the left plot, and factors 25 and 50 improvements in the right plot.

Limits by Fermi-LAT The Fermi-LAT is an indirect search experiment for dark matter, which measures the energy spectrum of the gamma rays to detect the dark matter annihilation processes, $\chi\chi \to \gamma\gamma/Z\gamma$ in the universe. The results shown in Figure 1.8 are derived from six years of measurement of the gamma rays from dwarf spheroidal galaxies [39]. The constraints from the Fermi-LAT results are overlaid on $M_2 \times (M_2 - M_1)$ plane, and are shown with the magenta areas. The light magenta areas show the projected limit by the Fermi-LAT, assuming an improvement by two and three orders of magnitude from high to low opacity.

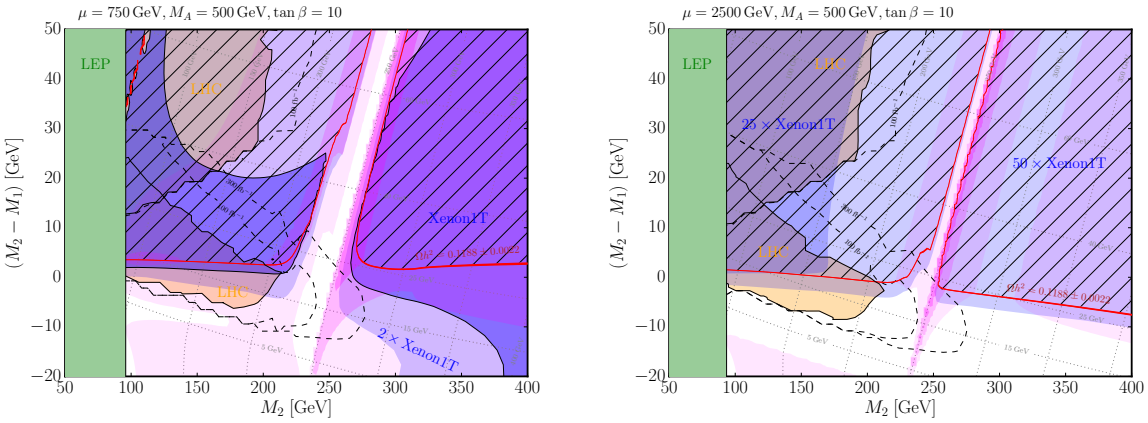

Figure 1.8: The allowed parameter space for the the well-tempered Wino-Bino neutralino dark matter scenario in the $(M_2, M_2 - M_1)$ plane for $\mu = 750$ GeV (left) and 2.5 TeV (right). The roughly horizontal gray dotted grid lines give values for the mass splitting $\Delta m = m(\widetilde{\chi}_1^{\pm}) - m(\widetilde{\chi}_1^0)$. The roughly vertical gray dotted grid lines give the dark matter mass, $m(\widetilde{\chi}_1^0)$. Other parameters in the MSSM are set to $\tan\beta = 10$ and the pseudoscalar Higgs mass $M_A = 500$ GeV. Constraints from the Xenon1T [36] experiments are shaded with purple, and the constraints from the Fermi-LAT [39] measurements are shaded with magenta. The regions shaded with lower opacity correspond to future expected limits by each experiment. The orange regions are excluded by two different LHC searches for $pp \to \widetilde{\chi}_1^{\pm}\widetilde{\chi}_2^0 \to W^{\pm}Z\widetilde{\chi}_1^0\widetilde{\chi}_1^0$ in the CMS experiment [41, 42]. The red solid line shows the parameter which makes the dark matter relic abundance match the observed dark matter density. The green area is excluded by the experiments at LEP [40].

Limits by LEP The region colored with green in Figure 1.8 is excluded by the experiments at the Large Electron-Positron (LEP) collider. The results from the four experiments at the LEP (ALEPH, DELPHI, L3, and OPAL) are combined to derive limits on chargino mass $m(\widetilde{\chi}_1^{\pm})$. The electron-positron collision data at $\sqrt{s} = 189 - 208$ GeV are used to search for the excess of events. No excess is observed in any of the four experiments, and the exclusion limit on $m(\widetilde{\chi}_1^{\pm})$ is derived as a function of $\Delta m = m(\widetilde{\chi}_1^{\pm}) - m(\widetilde{\chi}_1^0)$. The lower bound on Wino-dominant $m(\widetilde{\chi}_1^{\pm})$ ranges from 91.9 GeV at $\Delta M = 200$ MeV, to 103.5 GeV at $\Delta M > 10$ GeV.

Limits by CMS The regions colored with orange are excluded by results from two searches at the CMS experiment. The searches use 35.9 fb^{-1}of proton–proton collision data at $\sqrt{s} = 13$ TeV in the LHC. The regions with small $(M_2 - M_1)$ values are excluded by the search using two leptons presented in Ref. [42]. The regions with larger $(M_2 - M_1)$ values are excluded by the search using multiple leptons, presented in Ref. [41].

The red solid lines show the parameters that reproduce the dark matter density. The hatched regions above the red lines are where the dark matter density is higher than the observed one. The gap in the middle, at $M_2 \sim 250$ GeV is so called a "funnel" region, where the LSP mass is approximately half of the pseudoscalar Higgs mass M_A. In this region, neutralinos can annihilate via s-channel A^0 exchange, which significantly reduces the dark matter abundance. The sensitivity of the dark matter direct/indirect searches degrade at regions with small $(M_2 - M_1)$, as the dark matter relic density becomes smaller. The actual mass of the dark matter, and the mass difference between the lightest two neutralinos $\Delta m = m(\widetilde{\chi}_1^{\pm}) - m(\widetilde{\chi}_1^0)$ are shown with the dotted grids in Figure 1.8.

The main conclusion of the study in Ref. [38] is that a correct dark matter relic density can be obtained for $M_2 - M_1 < 5$ GeV, which corresponds to $\Delta m \sim$ 15-25 GeV. For higher $|\mu|$ values, the direct and indirect searches of the dark matter quickly become ineffective, as neutralino couplings to Higgs and Z-boson are driven by the Higgsino mixing to the gaugino [38]. Only LHC searches or a future dark matter searches can probe this parameter space. For $\Delta m < 15$ GeV, the predicted thermal neutralino density will be smaller than the dark matter density, which means that only a part of the dark matter is composed of the LSP. Although this requires another source of dark matter, it is still viable and even less explored by experiments so far.

1.3 Search strategy

A search for the production of neutralinos and charginos with compressed mass spectra in proton–proton collision at LHC is presented in this thesis. The strategy of the search is summarized in this section. The assumptions imposed to simplify the Higgsino and Wino/Bino scenarios are shown in the first paragraph. In the next two paragraphs, the production modes and the decay modes that are targeted in this thesis are explained. The search strategy, and the constraints from the previous searches are presented in the last part of this section.

Simplified signal scenarios The Higgsino and Wino/Bino scenarios, introduced in the previous sections, are the main target of the search. We use the simplified Higgsino and Wino/Bino scenarios, where we assume the masses of all the SUSY particles except for $\widetilde{\chi}_1^0$, $\widetilde{\chi}_2^0$ and $\widetilde{\chi}_1^\pm$ are decoupled ($m \gg 1$ TeV), so that they do not affect the production cross section or the branching ratio in the decay process. The branching ratios for the processes $\widetilde{\chi}_2^0 \to Z^* \widetilde{\chi}_1^0$ and $\widetilde{\chi}_1^\pm \to W^* \widetilde{\chi}_1^0$ are assumed to be 100%. For the Higgsino scenario, we set $|\mu| \ll M_1, M_2$, and therefore get Higgsino-dominant chargino and neutralinos. The mass spectrum is assumed to be $m(\widetilde{\chi}_1^\pm) = \frac{1}{2}\left[m(\widetilde{\chi}_1^0) + m(\widetilde{\chi}_2^0)\right]$ from Eqs. 1.10, 1.11 and 1.13. For the Wino/Bino scenario, we set $M_1 \lesssim M_2 \ll |\mu|$, and get Wino-dominant $\widetilde{\chi}_2^0$ and $\widetilde{\chi}_1^\pm$ with $m(\widetilde{\chi}_1^\pm) = m(\widetilde{\chi}_2^0)$, and a Bino-dominant LSP. The mass splitting Δm and the mass of the neutralino $m(\widetilde{\chi}_1^0)$ are controlled by varying the M_1, M_2 and μ parameters.

Production mode For both of the Higgsino and Wino/Bino scenarios, we search for direct production of charginos and/or neutralinos via electroweak interactions. For the Higgsino scenario, production cross sections are calculated assuming pure Higgsino neutralino/chargino. For the Wino/Bino scenario, production cross sections are calculated for pure Wino neutralino/chargino. Figure 1.9 shows the calculated cross sections for Higgsino and Wino neutralino/chargino production, as a function of the particle mass, assuming that Higgsino/Wino masses are degenerate.

Decay modes and signal topology In both of the Higgsino and Wino/Bino scenarios, the $\widetilde{\chi}_2^0$ can decay into a dilepton pair and a $\widetilde{\chi}_1^0$, via an off-shell Z boson (Z^*). The invariant mass of the dilepton system, $m_{\ell\ell}$, is kinematically restricted to be smaller than the mass splitting between the $\widetilde{\chi}_2^0$ and $\widetilde{\chi}_1^0$. Thus $m_{\ell\ell}$ of the dilepton system is sensitive to the original mass splitting, which makes a characteristic peak in the $m_{\ell\ell}$ distribution. This topology is useful to distinguish the signal events from the SM backgrounds, therefore the final states with two leptons are used in the analysis.

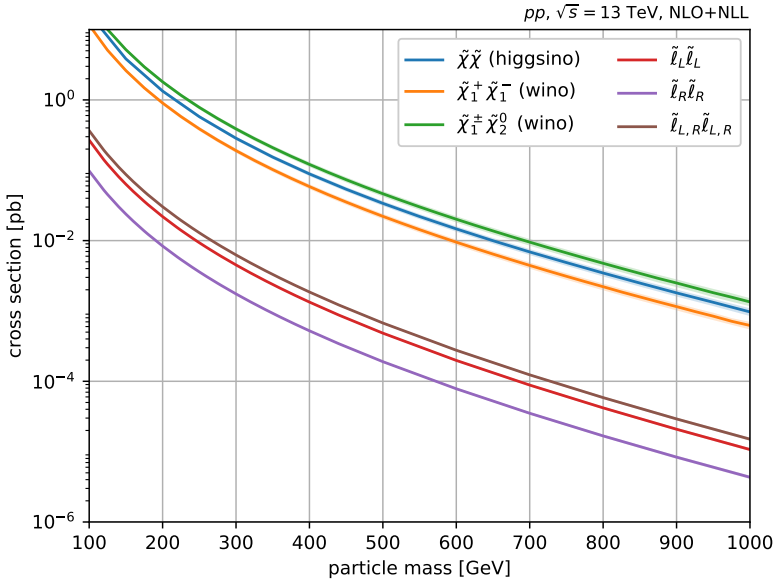

Figure 1.9: Production cross sections as functions of particle mass, for pure Higgsino and Wino neutralino and chargino. The cross sections for sleptons are also shown.

Search strategy A diagram representing the signal process with two leptons in the final state is shown in Figure 1.10. The two $\widetilde{\chi}_1^0$ in the final state are invisible in the detector, and therefore are observed as missing energy, which is explained in Chapter 4. The final state in the leading order includes missing energy from the $\widetilde{\chi}_1^0$, two leptons with low momentum from the Z^* decay, and quarks from W^* decay observed as jets with low momentum. Although the characteristic $m_{\ell\ell}$ shape is useful to reject the SM backgrounds, it is generally difficult to distinguish events with no visible particles with high momentum from enormous amount of background from QCD interactions. A hadronic initial-state radiation (ISR) is required to enhance the sensitivity of the search, with boosting the SUSY system in the opposite direction of the ISR. This creates a large missing energy by the boosted $\widetilde{\chi}_1^0$ s. In conclusion, we search for events with high momentum jet, a significantly large missing energy in the opposite direction to the jet, and two soft leptons with small $m_{\ell\ell}$. Additional jets from W^* decay is allowed but not explicitly required, as they have very small momentum and thus are not always detected as jets.

Current limits from collider experiments Previous ATLAS limits for the simplified Higgsino and Wino/Bino scenarios are shown in Figure 1.11. Similar results by CMS are shown in Figure 1.12. The limits are set in a 2D plane, with the $m(\widetilde{\chi}_2^0)$ in the horizontal axis and the mass splitting $\Delta m = m(\widetilde{\chi}_2^0) - m(\widetilde{\chi}_1^0)$ in the vertical axis. Both of them use similar strategies as the analysis presented in this thesis. The LEP limits [40] shown with gray regions in Figure 1.11 come from the limits on chargino as described in Section 1.2.2. It had been the most strict limit in the compressed regions, until being updated by the two results from ATLAS and CMS, shown in Figures 1.11 and 1.12. Limits for the Higgsino scenario are shown in left plots of Figures 1.11 and 1.12. The search by ATLAS uses 36.1 fb^{-1}of data, and the exclusion limit extends to $m(\widetilde{\chi}_2^0) = 145$ GeV at $\Delta m \sim 6$ GeV, whereas the search by CMS uses 33.2–35.9 fb^{-1}of data and excludes up to $m(\widetilde{\chi}_2^0) = 168$ GeV at $\Delta m \sim 20$ GeV. For the Wino/Bino scenario, ATLAS excludes $m(\widetilde{\chi}_2^0) = 175$ GeV at $\Delta m \sim 10$ GeV, and CMS $m(\widetilde{\chi}_2^0) = 230$ GeV at $\Delta m \sim 20$ GeV. The searches by

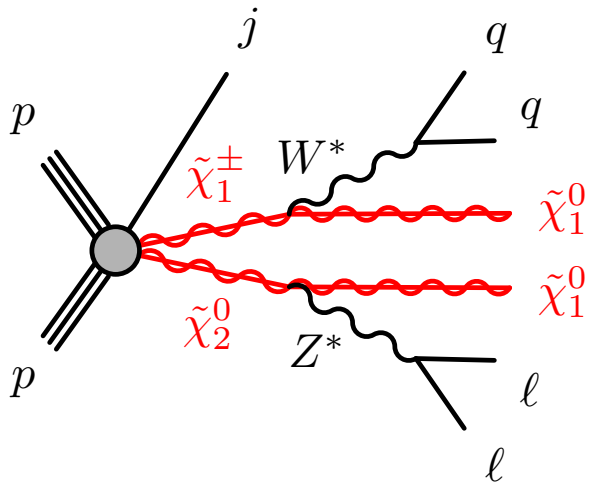

Figure 1.10: A diagram representing the two-lepton final state of production of electroweakino $\widetilde{\chi}_2^0\widetilde{\chi}_1^{\pm}$ with initial-state radiation (j). The Higgsino simplified model also considers $\widetilde{\chi}_2^0\ \widetilde{\chi}_1^0$ and $\widetilde{\chi}_1^+\ \widetilde{\chi}_1^-$ productions.

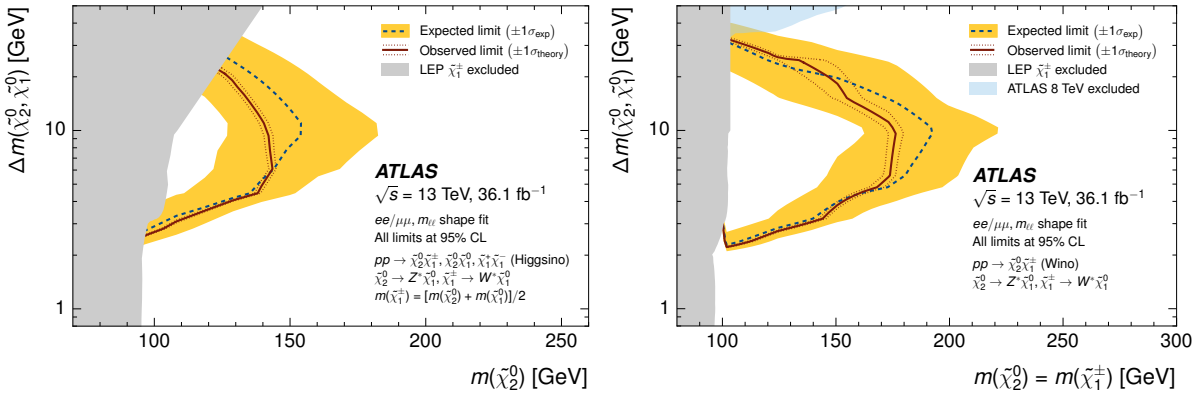

Figure 1.11: Expected 95% CL exclusion sensitivity (blue dashed line) and observed limits (red solid line) for simplified models of direct Higgsino (left) and Wino (right) production [43]. The yellow band shows the $\pm 1\sigma_{\text{exp}}$ region from experimental systematic uncertainties. The dotted red line shows the $\pm 1\sigma_{\text{theory}}$ limits from signal cross-section uncertainties. The gray regions denote the lower chargino mass limit from LEP [40]. The blue region in the right plot indicates the limit from the $2\ell + 3\ell$ combination of ATLAS Run 1 [44, 45].

ATLAS focuses on more compressed scenarios, whereas the CMS searches are optimized for larger mass splittings. In this thesis, we aim to further extend the search region to find supersymmetric particles with compressed mass spectra.

1.4 Outline of this thesis

In this thesis, a search for production of chargino and neutralino with compressed mass spectra is presented. The search uses 139 fb^{-1} of $\sqrt{s}$ = 13 TeV proton–proton collision data at the LHC collected by the ATLAS detector. The outline of this thesis is summarized in this section.

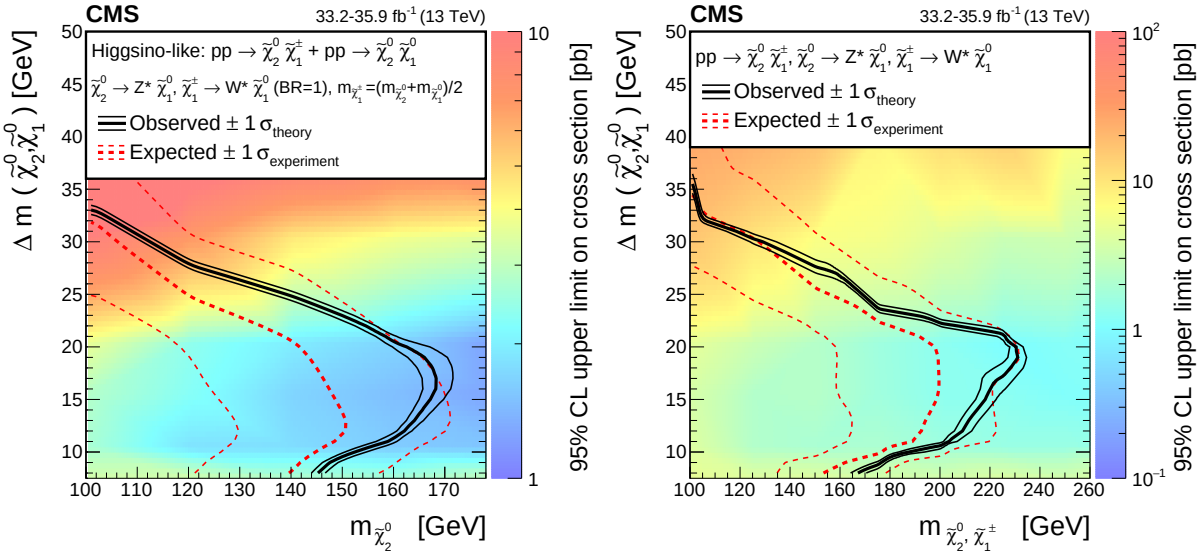

Figure 1.12: Expected 95% CL exclusion sensitivity (red dashed line) with $\pm 1\sigma_{\text{exp}}$ and observed limits (black solid line) with $\pm 1\sigma_{\text{theory}}$ for simplified models of direct Higgsino (left) and Wino (right) production [42].

In Chapter 2, an overview of the experimental setup are presented. In Chapter 3, the details of the collision data and the generation steps of Monte Carlo samples are explained. In Chapter 4, algorithms to reconstruct particles in the ATLAS detector are discussed in detail. Descriptions of dedicated reconstruction methods for low-p_{T} particles are explained in Chapter 5. The event selection criteria to separate the signal events from backgrounds are defined in Chapter 6. In Chapter 7, the background estimation method is introduced, where the "fake/non-prompt" lepton background plays an important role. The systematic uncertainties assigned to the background and signal modeling are explained in Chapter 8, and the statistical treatments used derive the final results are discussed in Chapter 9. The final results of the search are presented in Chapter 10, and are further discussed in Chapter 11. Finally, the conclusion of this thesis is displayed in Chapter 12.

Chapter 2

The ATLAS Experiment at the LHC

The ATLAS experiment [46] is one of the four major experiments at the Large Hadron Collider (LHC) [47], located at CERN, the European Organisation for Nuclear Research, in Geneva. The LHC is a proton-proton collider with the highest center-of-mass energy in the world. The ATLAS detector is designed to explore wide range of physics, by precisely measuring the particles from the proton-proton collisions and reconstructing the initial interaction of the partons. A brief overview of the experimental setup is presented in this chapter. The design of the LHC, as well as the accelerating system in CERN used as an injector, are explained in Section 2.1. The design and the performance of the ATLAS detector are introduced in Section 2.2. An overview of the data recording system is also shown in this section.

2.1 Large Hadron Collider

The Large Hadron Collider (LHC) is the largest circular proton accelerator in the world, with the circumference of 27 km. The primary goal of the LHC is to provide high-energy and high-intensity proton–proton collisions to the experiments. The LHC has two circular beam pipes, each to accelerate proton beam in different direction, up to the design energy of 7 TeV. At the collision points, the two proton beams are made to collide, where head-on collisions of the protons at center-of-mass energy ($\sqrt{s}$) of 14 TeV take place. The proton beam in the LHC has a bunch structure, and each bunch contains about 10^{11} protons. Total of 2808 proton bunches can be stored in the LHC, and the time difference between the bunches are 25 ns . This corresponds to the maximum proton bunch collision rate of 40 MHz. The design value of the peak luminosity is $10^{34}\,\mathrm{cm}^{-2}\,\mathrm{s}^{-1}$.

The LHC is constructed in a circular tunnel built underground of the area close to the city of Geneva. Figure 2.1 shows the schematic layout of the LHC main ring. It consists of eight arcs of 2450 m long, where dipole magnets are placed to bend the proton trajectory, and eight straight sections of 545 m long. 1232 superconducting dipole magnets in total are used to bend the trajectory of the protons, and 858 quadrupole magnets are used to focus the proton beam. In one of the straight sections, radio-frequency cavities are placed to accelerate the particles. Four different detectors are placed at four collision points in the straight sections; ATLAS, CMS [48], LHCb [49] and ALICE [50]. The remaining three straight sections are used for beam dump and beam cleaning.

The first operation period of the LHC for the physics experiment is referred to as “Run1”, which started in 2010. The LHC operated at $\sqrt{s}$ = 7 TeV and 8 TeV until 2012, and provided rich statistics of high-energy proton–proton collisions to the experiments. The ATLAS experiment collected 4.7 $\mathrm{fb}^{-1}$and 20.3 $\mathrm{fb}^{-1}$of collision data at $\sqrt{s}$ = 7 TeV and 8 TeV, respectively. The second physics run (Run2) took place in 2015–2018, where the center-of-energy is raised to $\sqrt{s}$ = 13 TeV. The ATLAS collected 139 $\mathrm{fb}^{-1}$of collision data, which is used for the analysis presented in this thesis.

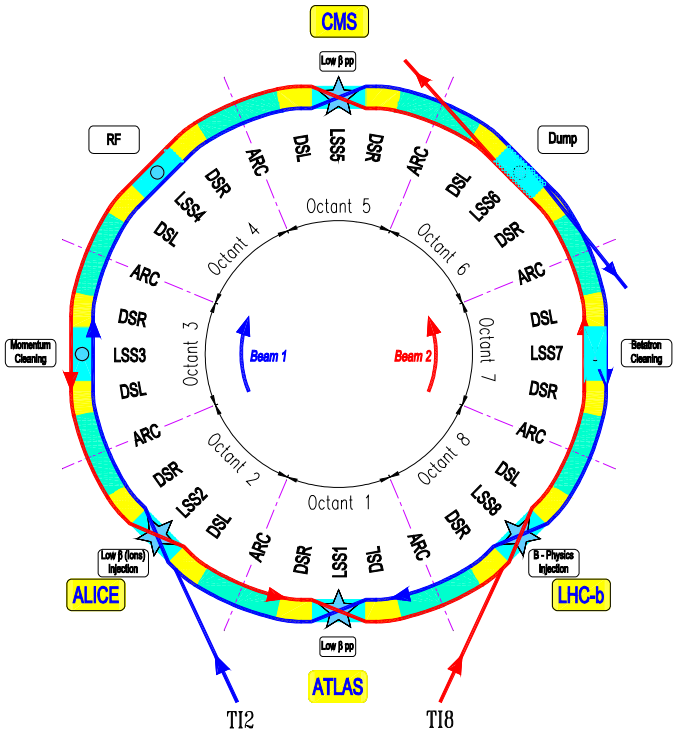

Figure 2.1: Schematic layout of the LHC main ring [47]. The main ring is divided into eight octants, each containing one straight section. Two proton beams of different direction are injected to the LHC at Octant 2 and 8. Four main detectors are placed at Octant 1, 2, 5 and 8.

Figure 2.2 shows the accelerator system at CERN. The acceleration of the protons starts at LINAC2 accelerator, where the protons are taken from the hydrogen gas and are accelerated to 50 MeV. The protons are injected to the Proton Synchrotron Booster and further accelerated to 1.4 GeV before being passed to the Proton Synchrotron. The Proton Synchrotron is a circular accelerator with the circumference of 628 metres, which accelerates the protons to 25 GeV and feed them to the Super Proton Synchrotron. The Super Proton Synchrotron is the second-largest accelerator at CERN, with about 7 km circumference. The protons are accelerated to 450 GeV in the Super Proton Synchrotron, which are finally injected to the LHC.

2.2 ATLAS detector

ATLAS is a multi-purpose detector placed at one of the collision points of the LHC, and are designed to explore a variety of high-energy physics. It aims to precisely measure the particles from the high-energy, high-intensity proton–proton collisions by the LHC, and reconstruct the initial interaction of the “partons” (quarks and gluons) in the proton.

Figure 2.3 shows the cut-away view of the ATLAS detector. It is a cylinder-shaped detector, with the height of 44 m, the diameter of 25 m, and the overall weight of approximately 7000 tonnes, covering nearly full solid-angle around the collision point. The detector is composed of several sub-detectors. The

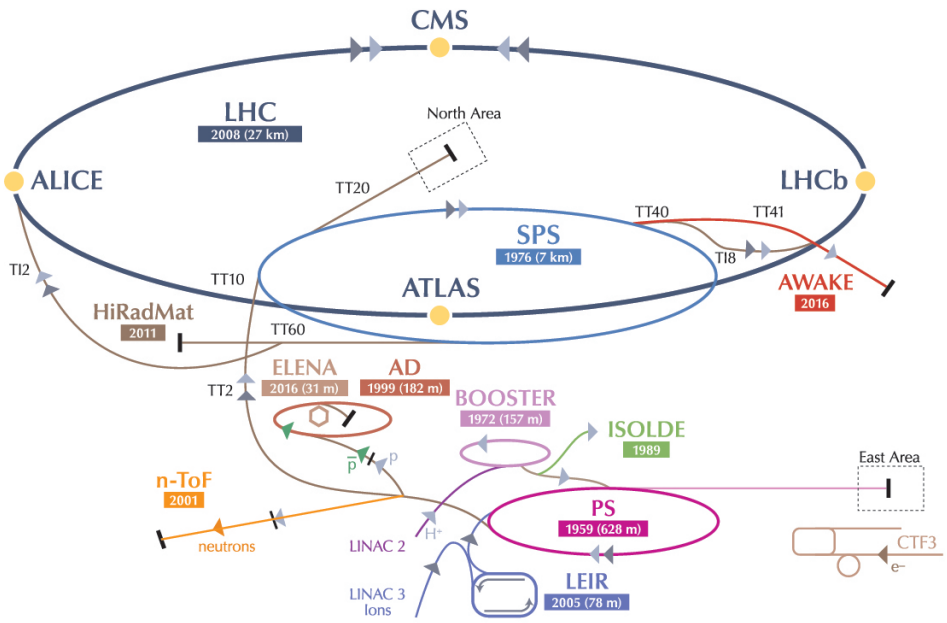

Figure 2.2: Accelerator system at CERN. [51]. The LINAC2, BOOSTER, PS, and the SPS are used as the injector to the LHC.

inner detectors, together with the the solenoid magnets, are placed at the innermost part of the detector. The inner detectors are designed to measure the momentum and the direction of the charged particles. The calorimeters lie outside the inner detectors, to measure the energy of the particles by absorbing their energy in the detector. The muons, however, have small energy deposit in the calorimeters, therefore their energies are not fully absorbed in the detector. Thus the muons reach the muon spectrometers, which are placed at the outermost part of the detector. The momentum of the muon is precisely measured at the muon spectrometers, with the aid of the magnetic field provided by the toroidal magnets. Each of the sub-detectors in the ATLAS has a cylinder-shaped structure, with the "barrel" component surrounding the central part of the cylinder, and two "end-cap" components covering either end of the barrel. The design of the sub-detectors are explained in the following sections.

The coordinate systems used extensively in this thesis are briefly summarized in the following paragraphs. Figure 2.4 shows the ATLAS coordinate system, overlayed to the ATLAS detector schematic diagram. The collision point is defined as the origin of the coordinate system. The z-axis is defined along the beam-pipe, the y-axis is defined to point upwards, and the x-axis is defined to point the center of the LHC ring. The $x-y$ plane is referred to as the "transverse" plane, while the z-direction is referred to as the "longitudinal" direction.

The polar coordinates are also commonly used, where (r, ϕ, θ) are defined in an ordinary way, related to the Cartesian coordinates by $x = r\sin\theta\cos\phi$, $y = r\sin\theta\sin\phi$, $z = r\cos\theta$. Pseudo-rapidity η, defined as $\eta = -\ln(\tan\theta/2)$ is also commonly used to express the θ direction of the particles. The pseudo-rapidity η is useful because $\Delta\eta$, defined as the difference in pseudo-rapidity of two particles, is invariant under Lorentz boost in z-direction, if we neglect the masses of the particles. Thus $\Delta\eta$ can be used as a Lorentz

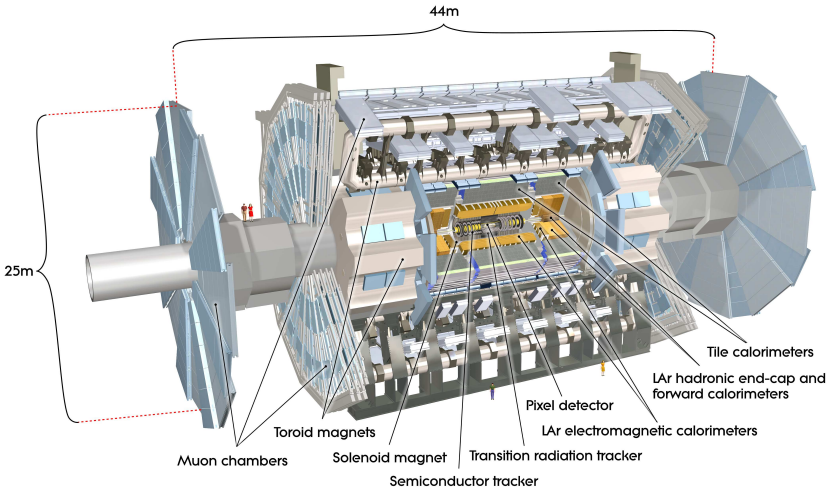

Figure 2.3: Cut-away view of the ATLAS detector. The dimensions of the detector are 25 m in height and 44 m in length. The overall weight of the detector is approximately 7000 tonnes.

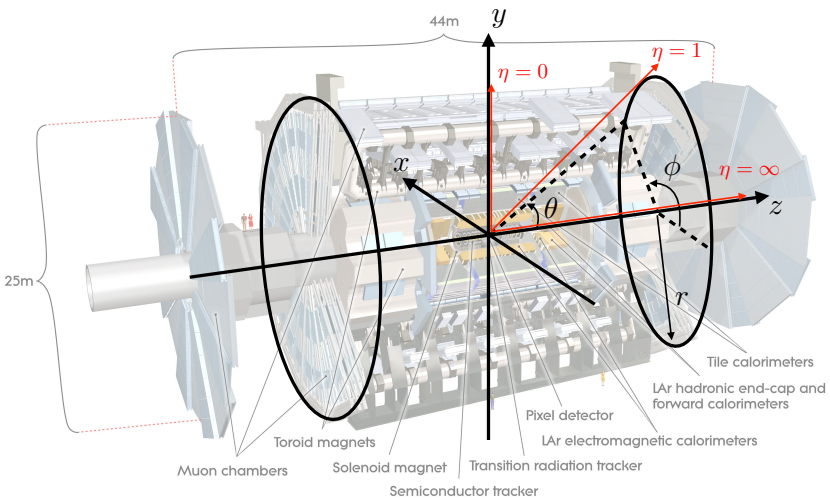

Figure 2.4: The ATLAS coordinate system. The origin of the coordinates are the center of the interaction point, x-axis is taken to point to the center of the LHC ring, y-axis to point upwards, and z-axis along the beam pipe. (r, ϕ, θ) coordinate is defined by $r = \sqrt{x^2 + y^2}$, $\phi = \arctan(y/x)$, $\theta = -\ln(r/z)$. Pseudo-rapidity $\eta = -\ln\tan(\theta/2)$ is often used instead of θ.

invariant measure of separation between two particles in θ direction. Angular separation ΔR, defined as $\Delta R = \sqrt{(\Delta\eta)^2 + \Delta\phi)^2}$ is commonly used as a measure of the angular separation of two particles.

In hadron collider experiments, the transverse direction plays an important role. When two protons collide at very high energy, the partons in each of the protons scatters inelastically to produce various final states. Because each parton only carries a fraction of the momentum of the proton, the parton scattering often takes place asymmetrically. This leads to a large boost of the parton–parton system in the longitudinal direction. On the other hand, the initial momentum of the partons in the transverse plane is small, and thus there would be little or no boost in the transverse direction. This feature is extremely useful, as the momenta of the particles from a parton–parton interaction always adds up to zero in the transverse plane. The transverse component of the variables commonly used in the analysis are the transverse momentum $p_{\mathrm{T}} = p \sin\theta$, and the transverse energy $E_{\mathrm{T}} = E \sin\theta$.

2.2.1 Magnet system

There are three superconducting magnets placed inside the ATLAS detector; the solenoid magnet, the barrel toroidal magnet, and the end-cap toroidal magnets. These magnets provide magnetic fields in the ATLAS detector, which bends the trajectory of the charged particles. The curvature of the trajectory is measured by the inner detectors or the muon spectrometers, to calculate the momentum of the particles.

Figure 2.5 shows the layout of the magnets in the ATLAS detector. The solenoid magnet is placed at the innermost part of the detector, and provides a 2 T axial magnetic field aligned to the beam axis. The trajectory of a charged particle is bent in the ϕ direction, which are measured by the inner detectors to determine the momentum. The barrel toroid and two end-cap toroid magnets each consist of eight coils arranged as shown in Figure 2.5, and are placed outside the calorimeter system. The toroid magnets produce "toroidal" magnetic fields inside the coils, where the magnetic field lines run along the ϕ direction. The trajectories of the muons are thus bent in the η directions, which are measured by the muon spectrometers. The magnetic flux density of the barrel and the end-cap toroids are approximately 0.5 T and 1 T, respectively.

2.2.2 Inner detectors

Inner detectors are placed at the innermost part of the ATLAS detector. Figure 2.6 shows the cut-away view of the inner detectors. The inner detectors consist of three different detectors: the Pixel detector, the Silicon Microstrip Tracker (SCT), and the Transition Radiation Tracker (TRT). The layout of the inner detectors are shown in Figure 2.7. Insertable B-Layer (IBL) [52] was introduced between Run1 and Run2, at the innermost layer of the Pixel detectors, which are not included in this figure.

Pixel detectors High-granularity silicon pixel detectors are placed in the innermost part of the inner detectors. The electron-hole pairs created in the silicon pixel are quickly drifted by the electric field, and collected by the on-detector readout chip. The size of each pixel, measured in $(R - \phi) \times z$ plane, is 50 μm × 200 μm for the IBL, and 50 μm × 400 μm for the other layers of the pixel detector. The hits in the pixel detectors are combined to reconstruct the trajectory of the particles, as explained in Section 4.2.1. A small pixel size is essential to separate close-by hits made by different tracks passing similar position on the

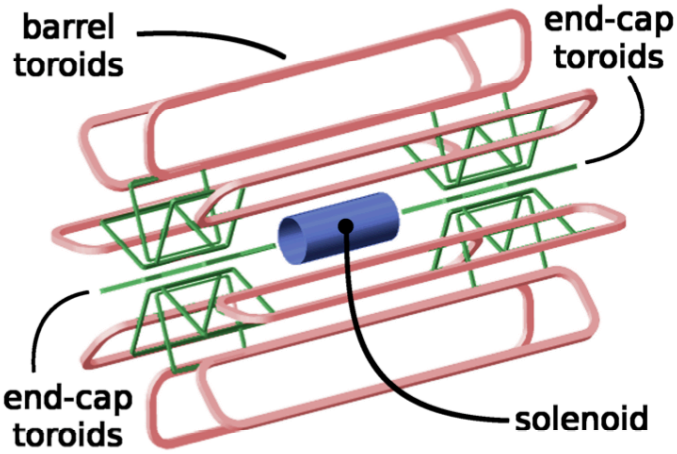

Figure 2.5: Layout of the superconducting magnet system in the ATLAS detector. The solenoid magnet is placed at the innermost part of the detector. The barrel and the end-cap toroidal magnets are placed at the outer part of the detector.

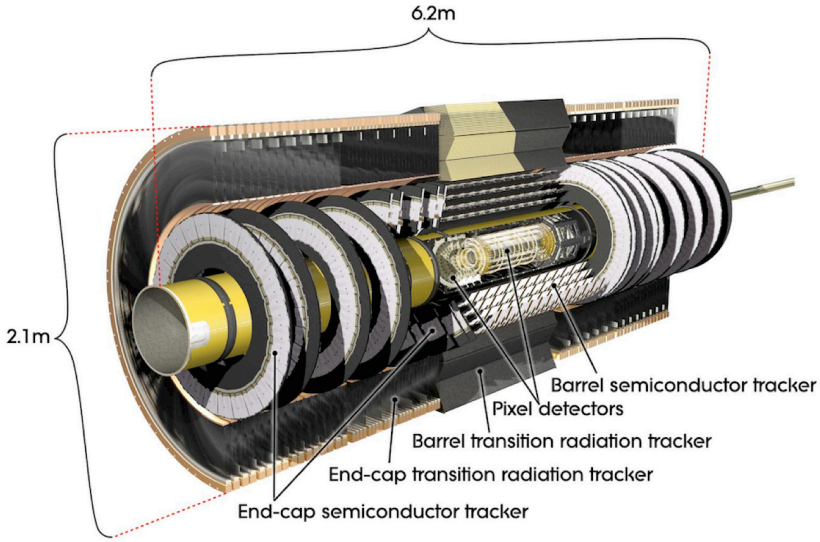

Figure 2.6: A cut-away view of the inner detectors. The inner detectors consists of the Pixel detectors,the semiconductor trackers, and the transition radiation trackers.

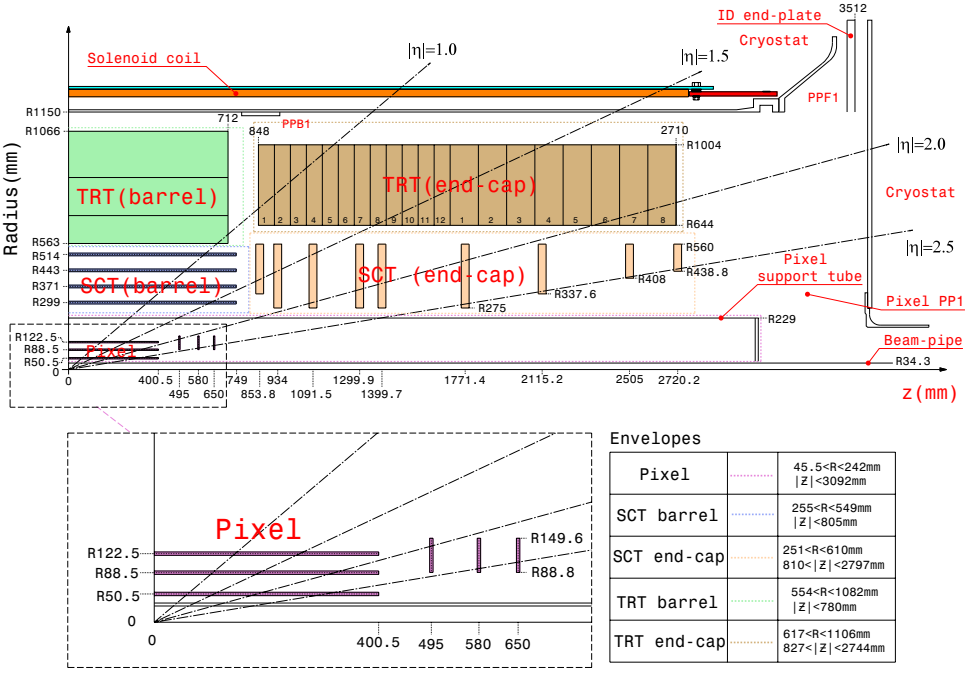

Figure 2.7: Inner detector layout.

detector, which is especially important in the situation with high-density of the tracks. In the barrel region, four layers of pixel detectors are installed; IBL at $R = 33.3$ mm, and three pixel layers at $R = 50.5, 88.5$ and 122.5 mm. In the endcap region, the detectors are constructed in a disk-shape, with three pixel disks installed at $z = 495, 580$ and 650 mm. The Pixel detectors cover up to $|\eta| < 2.5$. The IBL has about 6 million channels on its own, and the other layers of the Pixel detectors has 80 million channels in total.

Silicon Microstrip Tracker (SCT) The SCT is a silicon detector with fine read-out strips at 80 µm pitch. The strips are placed parallel to the magnetic field (z axis), to precisely measure the $R - \phi$ position of the hit. Two layers of sensors are combined to build an SCT module, where the layers are tilted against each other with stereo angle of 40 mrad, which allows 2D-position measurement of the hits. Four barrel cylinders at $R = 299, 371, 443$ and 514 mm, and nine endcap disks ranging from $z = 853.8$ to 2720.2 mm are installed, which covers $|\eta| < 2.5$. The SCT has about 6 million channels in total.

Transition Radiation Tracker The TRT is a straw-tube detector, which consists of polyimide straw tubes of 4 mm diameter, filled with Xe-based gas mixture. The ionized electrons are collected by a gold-plated tungsten anode wire inside each straw tube. The ionization of the Xe-gas is induced either directly by the particle transversing the volume, or by the transition radiation. The transition radiation is emitted when a charged particle passes through a boundary between two materials. The amount of the transition radiation is proportional to the particle velocity $\gamma = E/m$. Radiated photons are absorbed in the gas, which yield larger signal compared to the ionization by the particle itself. This feature is used for particle identification, especially to distinguish electrons from $\pi^{\pm}$. To enhance the emission of the transition radiation, a transition material is inserted between the straws. Polypropylene fibers with diameter

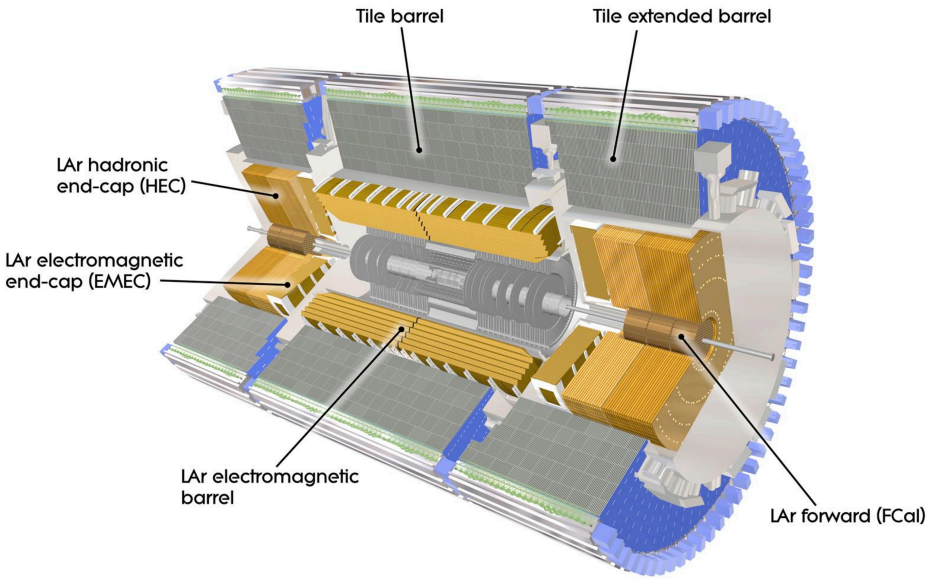

Figure 2.8: The layout of the ATLAS calorimeter system. The LAr electromagnetic calorimeters are installed inside the hadronic calorimeters. The electromagnetic calorimeters are subdivided into barrel and end-cap components. The hadronic calorimeters are subdivided into tile, end-cap, and forward.

of 19 μm are used in the barrel, and 15 μm-thick polypropylene radiator foils isolated by a polypropylene net are used for the end-caps. In the barrel (end-cap) regions, 73 (160) layers of aligned straw tubes are installed. The tube length is 144 cm (37 cm) in the barrel (end-cap) region. The barrel tubes are arranged in parallel with the beam pipe, with 7 mm of interval between the layers. In the end-cap, the tubes are arranged in the R direction. The intrinsic position resolution per straw is about 130 μm. A traverse of a charged particle fires 36 straws on average. The TRT covers the pseudo-rapidity range $|\eta| < 2.0$.

2.2.3 Calorimeters

The calorimeters are designed to measure the energy of the particles in a destructive way, by absorbing their energy. The calorimeters installed in the ATLAS detector are all "sampling calorimeters", where a dense absorber material is used to induce a large energy deposit to create a particle shower, and the active material converts the shower into detectable signal.

The ATLAS calorimeters are categorized in two components, the electromagnetic calorimeters and the hadronic calorimeters. Figure 2.8 shows the layout of the ATLAS calorimeter system. The electromagnetic calorimeters is segmented in fine granularity to precisely measure the energy of the electrons and photons. The hadronic calorimeters are designed to measure the energy of the hadrons, therefore they are more coarse but large to fully contain the hadron shower.

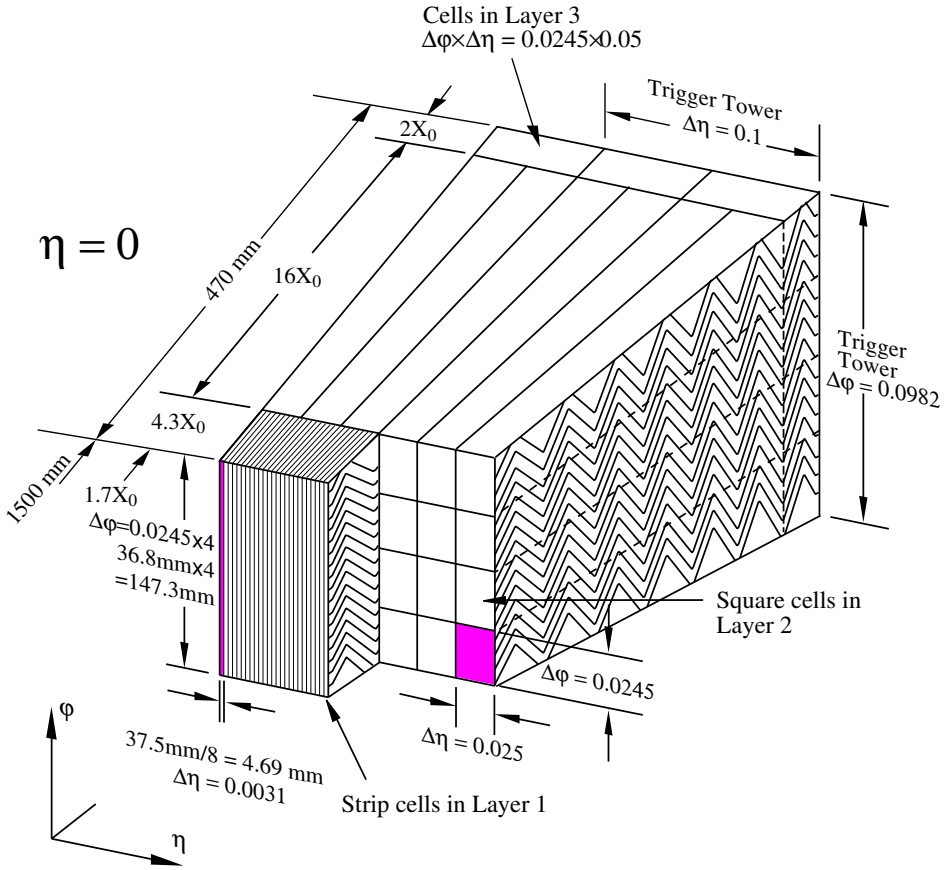

Figure 2.9: A sketch of an electromagnetic calorimeter module at $\eta = 0$. The segments in $\eta \times \phi$ are shown in the figure. The segments in the depth direction is referred to as Layer1, 2 and 3, from inside to outside.

Electromagnetic calorimeters The electromagnetic calorimeters are further divided into the barrel calorimeters, covering $|\eta| < 1.4$, and the endcap calorimeters, covering $1.375 < |\eta| < 3.2$. Both of the barrel and the endcap calorimeters use lead as the absorber, and LAr as the active material. A characteristic accordion-shaped lead absorber plates and kapton electrodes are used over its full coverage. Figure 2.9 shows an illustration of a barrel calorimeter module. The accordion-shaped electrodes and absorber plates are stack in ϕ direction, which gives a full coverage in the ϕ plane with an uniform detector geometry.

The electromagnetic calorimeters are segmented in η, ϕ, and also in the "depth" direction (along the direction of the particle). In the depth direction, the calorimeter is segmented into three parts, referred to as "layers". Layer 1 is the innermost part of the electromagnetic calorimeters, which is divided into smaller segments along the η direction compared to the other layers. This geometry is useful to separate between primary photon and two close-by photons from $\pi^0 \rightarrow \gamma\gamma$ decays. They have approximately 4.3 X_0 in the barrel region, where X_0 is the radiation length. The amount of material in layer 2 is about 16 X_0 in the barrel region, and most of the energy absorption occur in this layer. layer 3 is at the outermost part of the calorimeter, which is intended to measure the tail of the shower, useful to separate the electrons from $\pi^{\pm}$. The radiation length in layer 3 is about 2 X_0. The structure is similar in the end-cap region, up to $|\eta| < 2.5$. In the forward regions with $2.5 < |\eta| < 3.2$, however, there are only two layers, therefore have coarser resolution. Figure 2.10 shows the radiation length of the materials in the first, second and third layers. The

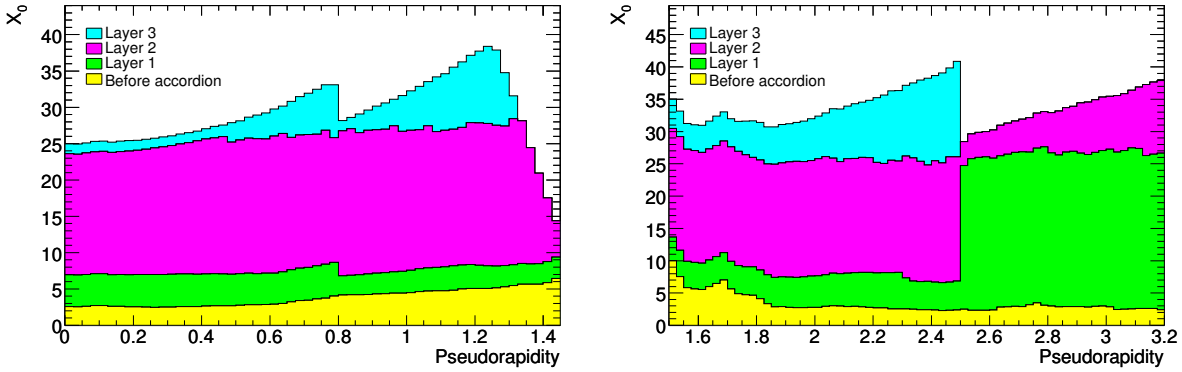

Figure 2.10: The amount of material in the electromagnetic calorimeters in units of radiation length X_0, as a function of η, for the barrel (left) and the end-cap (right) regions. The yellow histograms show the contributions from the material before the calorimeter. The histograms shown in green, magenta and cyan correspond to the radiation length by the absorber in layers 1, 2 and 3, respectively.

radiation length before the first layer is also shown in the plot. The intrinsic energy resolution is given as a function of the particle energy, by $\sigma_E/E = 10\%/\sqrt{E/\text{GeV}} \oplus 0.7\%$.

Hadronic calorimeters The hadronic calorimeters are subdivided into three components, tile, end-cap and forward calorimeters, each covering different $|\eta|$ range. The tile calorimeters have cylinder-shaped structures, which covers $|\eta| < 1.7$. Figure 2.11 shows the sketch of a tile calorimeter module. It is a sampling calorimeter with steel used as the absorber, and scintillating tiles used as the active material. The scintillation light is collected using the wavelength-shifting fiber, and converted into electrical signal using the photomultipliers. The tile calorimeter is segmented in three layers. In the first two layers, the cell granularity of the tile barrel, measured in in $\Delta\eta \times \Delta\phi$, is 0.1×0.1, whereas in the third layer, it is 0.1×0.2. The intrinsic energy resolution of the tile calorimeter is given by $\sigma_E/E = 50\%/\sqrt{E/\text{GeV}} \oplus 3\%$.

The end-cap hadronic calorimeter consists of the copper absorber and the LAr sensor. They are segmented in the depth (z) direction, to form two disk-shaped components, which covers $1.5 < |\eta| < 2.5$. The intrinsic energy resolution of the end-cap hadronic calorimeter is given by $\sigma_E/E = 100\%/\sqrt{E/\text{GeV}} \oplus 10\%$. The forward calorimeter covers $3.1 < |\eta| < 4.9$, and is designed to work as both electromagnetic and hadronic calorimeters. They are segmented in three layers, and in all the layers the active material is LAr. In the first layer copper is chosen as the absorber, where relatively high resolution can be obtained. In the second and third layers, tungsten is used as it has a large density useful to provide enough material to contain the full hadronic shower inside the detector in a limited space.

2.2.4 Muon spectrometers

The muon spectrometers are installed at the outermost part of the ATLAS detector. The toroidal magnets are also installed in this region, which provide magnetic field that bends the trajectories of the muons. The muon spectrometers are designed to detect the curvature of the muon trajectories to accurately measure the momentum of the muons.

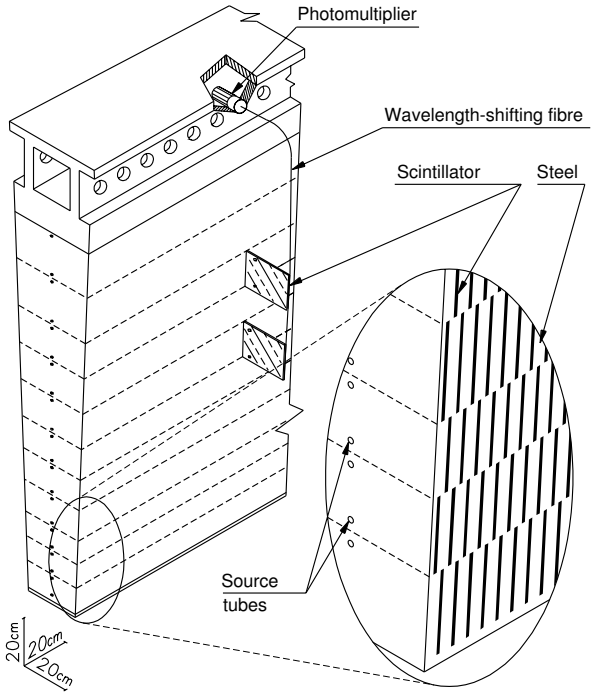

Figure 2.11: A sketch of the mechanical structure of a tile calorimeter module. The light from the scintillator tile is collected by the wavelength-shifting fibers, and are read out using the photomultipliers.

Another important role of the muon spectrometers is to provide "triggers" – a decision whether or not to record the detector information. The idea is that we only want to record the collision events when an "interesting" process takes place (details in to Section 2.3). Events with high-p_{T} muons are generally interesting in this context, as it is expected that a weak-interaction process have taken place. The muon spectrometers are used to quickly identify such events *before* recording the data.

Figure 2.12 shows a cut-away view of the muon spectrometers. The Monitored Drift Tubes (MDT) covers both of the barrel and end-cap regions, which are used for precision measurement of the muon trajectory. The Cathode Strip Chambers (CSC) cover the forward regions where MDTs do not cover, which are also used for the precision measurements. The Resistive Plate Chambers (RPC) and the Thin Gap Chambers (TGC) are mainly used for the triggers in the barrel and end-cap regions, respectively.

Figure 2.13 shows the layout the muon system at $\phi = \pi/2$. The muon spectrometers are organized in several layers in the barrel and the end-cap region, which is referred to as the "stations". In the barrel region, the inner station is at approximately $R = 5$ m, middle station at $R = 7$ m, and outer station at $R = 10$ m. In the end-cap, the inner station is at approximately $|z| = 7$ m, middle station at $|z| = 13$ m, and outer station at $|z| = 22$ m. There is also an "extra" station in the end-cap, at $|z| \sim 11$ m, $6 < R < 9$ m. The toroidal magnetic field is present between the inner and the outer stations in the barrel, and between the inner and the middle stations in the end-cap region.

Monitored Drift Tubes (MDT) The Monitored Drift Tube (MDT) is the main detector used for the precision measurement of the muon trajectory. Figure 2.14 shows the structure of the MDT. The MDT

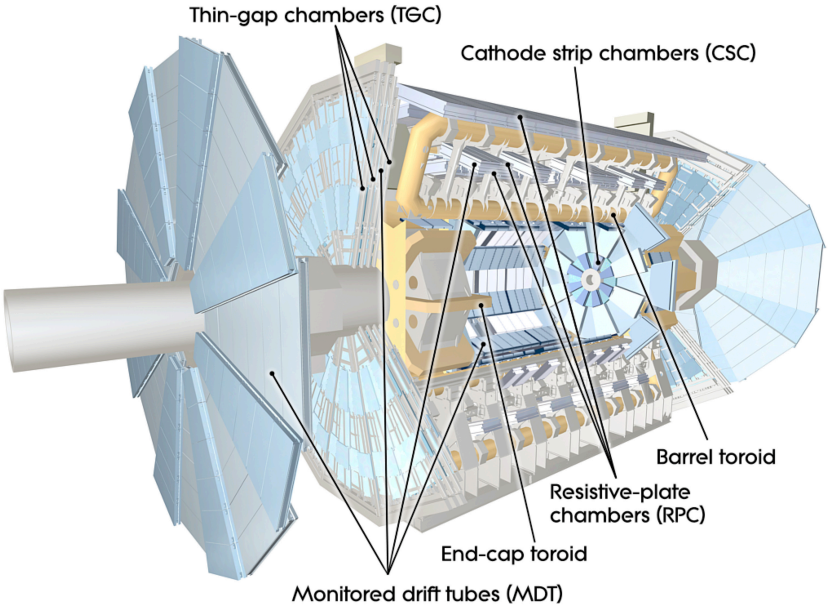

Figure 2.12: The cut-away view of the muon spectrometer system, composed of four types of detectors, the Monitored Drift Tubes (MDT), the Cathode Strip Chambers (CSC), the Resistive Plate Chambers (RPC), and the Thin Gap Chambers (TGC).

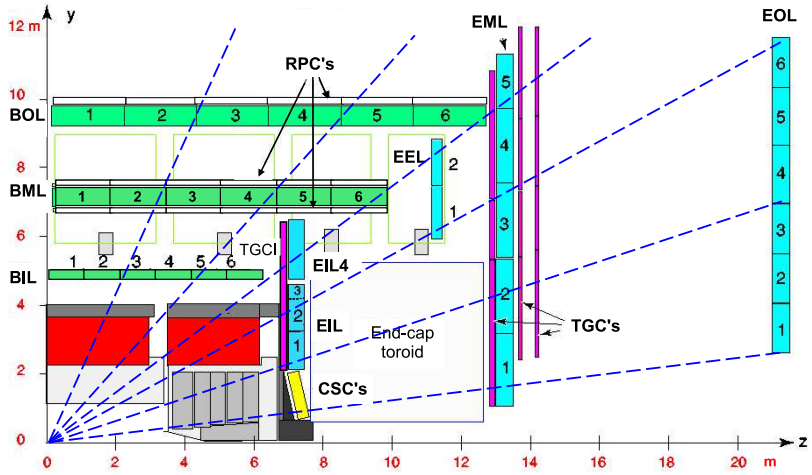

Figure 2.13: The layout of the muon system at $\phi = \pi/2$. Three barrel muon stations are labeled as BIL (inner), BML (middle), and BOL (outer). Four end-cap muon stations are labeled as EIL (inner), EEL (extra), EML (middle) and EOL (outer).

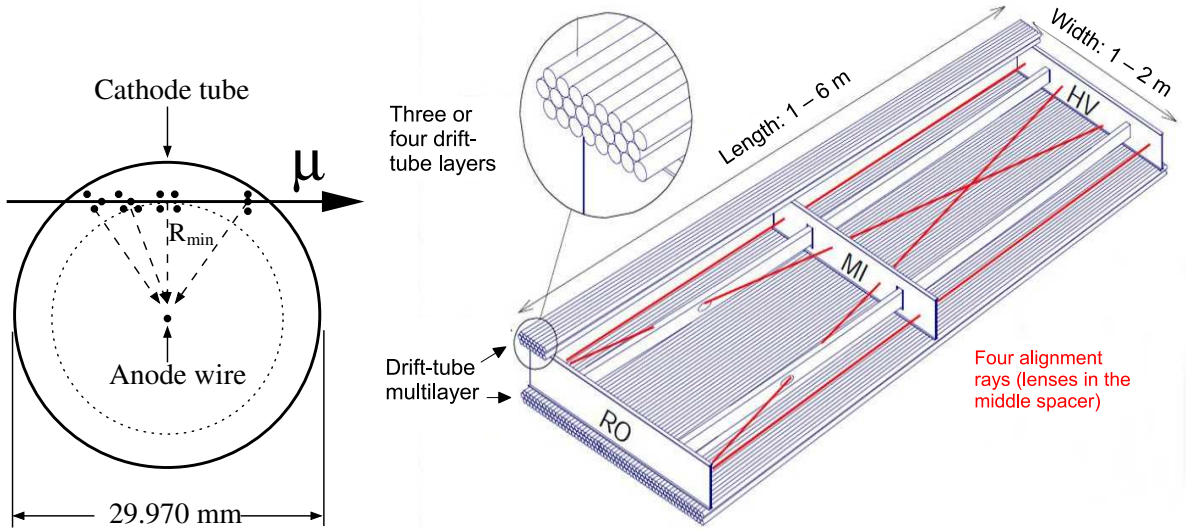

Figure 2.14: The cut-away view of a single tube of the MDT detector (left) and the structure of the MDT chamber (right).

detector is composed of pressurised drift tubes with the diameter of 29.970 mm, filled with Ar/CO_2 gas. A charged particle ionizes the gas and creates electrons, which is collected by the tungsten-rhenium anode wire at a potential of 3080 V set in the center of each tube. From the drift-time, the distance of the muon trajectory from the anode wire can be measured as shown in Figure 2.14 left, with the average resolution of 80 μm. Three or four layers of drift tubes are separated by the spacer with the height of 6.5 mm to 317 mm, to form a MDT chamber, as shown in Figure 2.14 right. In the barrel region, the MDT chambers are installed at inner, middle and outer stations. In the endcap, wheel-shaped layers are installed at inner, extra, middle and outer stations. The MDT covers $|\eta| < 2.7$ region, except for the end-cap inner region, where it only covers $|\eta| < 2.0$. In this region, the particle rate is extremely high and degrades the MDT performance. Thus the CSC is used for the precision measurement in this region.

Cathode Strip Chambers (CSC) The Cathode Strip Chamber (CSC) is a multi-wire proportional chamber, covering $2.0 < |\eta < 2.7$ in the inner station. The cathodes are segmented into strips of approximately 5 mm pitch, and are used to measure the R direction of the muon trajectory. The position resolution of the CSC is 65 μm in the R direction, and 5 mm in the ϕ direction.

Resistive Plate Chambers (RPC) The Resistive Plate Chamber (RPC) is a gas chamber with parallel electrode-plates, which are used for trigger in the barrel region. Two resistive electrodes are separated by a 2 mm gas-gap. The RPC is operated at 4.9 kV/mm applied between the plates. Ionized electrons created by a charged particle triggers the avalanche of the electrons, which is read out via strips mounted on the outer side of the plates. Fast rise-time of the signal is obtained by the small gas-gaps and the high voltage applied to the gas-gaps. Two layers of gas-gaps form an RPC chamber as shown in Figure 2.15. Two chamber planes are installed at the barrel middle layer, and one chamber plane is installed at the barrel outer layer.

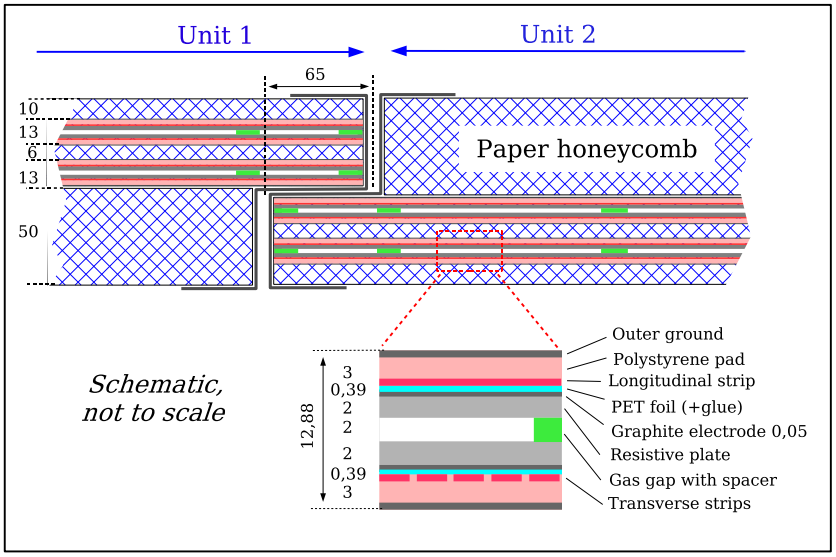

Figure 2.15: The cut-away view section of the RPC chamber. Two gas-gaps are joined to form a chamber.

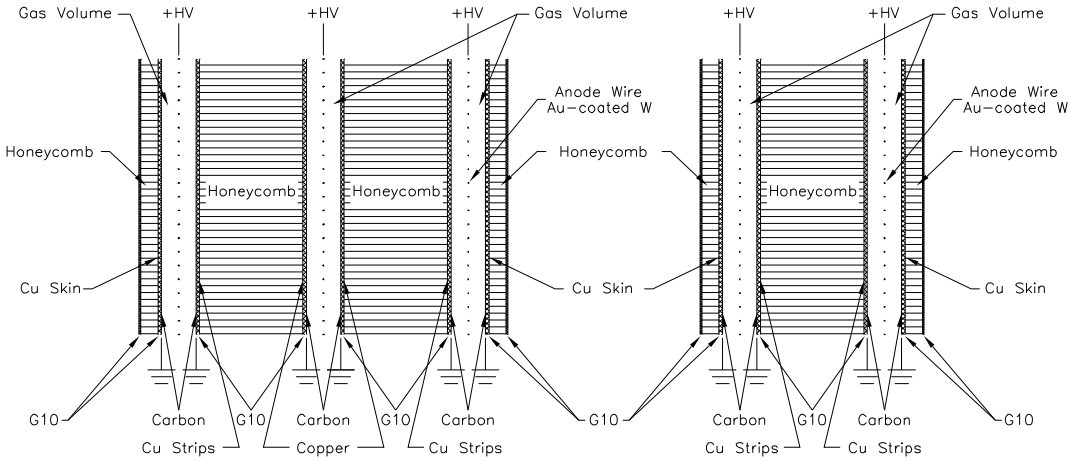

Figure 2.16: The schematic diagrams illustrating the structures of the triplet (left) and the doublet (right) TGC chambers.

Thin Gap Chambers (TGC) The Thin Gap Chamber is a multi-wire proportional chamber, filled with CO_2/n-C_5H_{12} mixture gas. The gas-gap is 2.8 mm, with anode wire plane in the middle, which makes the wire-to-cathode distance 1.4 mm. The small wire-to-cathode distance and the small pitch of the wire (1.8 mm) contribute to fast response of the chamber. About 99% of the signals arrive at the readout electronics inside a time window of 25 ns. Two or three gas-gaps are put together to form a doublet or triplet TGC, as shown in Figure 2.16. The doublet TGCs are used for the chambers at the endcap inner station and two outer chambers in the middle station. The triplet TGCs are used for the inner chamber in the end-cap middle station.

2.3 Data acquisition

As described in the previous sections, ATLAS is a large detector with millions of readout channels. The data size of the raw detector signals is about a few MBs per proton-bunch collision. The data rate, if we suppose recording all the events at 40 MHz, would be close to $O(1)$ TB per second, which is technically not possible to transfer or store in a reasonable amount of time/resource.

It is not only technically difficult, but also unnecessary in physics point of view, to record all the collision events. Figure 2.17 shows the cross section of some of the major SM processes at $\sqrt{s} = 5, 7, 8$ and 13 TeV, measured in the ATLAS detector. The cross section of the total inelastic proton–proton scattering is shown in the leftmost bin, which is $O(10^{10})$ pb. At the peak luminosity of $10^{34}\,\mathrm{cm}^{-2}\,\mathrm{s}^{-1}$, this corresponds to about 10^8 scattering per second, or $O(10)$ interactions per bunch crossing. Most of the scatters come from the QCD interactions with small momentum transfer. The cross sections of the processes we are interested in, such as those involving the electroweak gauge bosons, or processes with high momentum transfer, are at several orders smaller. For example, the cross sections of the SM processes including the production of W or Z boson is $O(10^3 - 10^4)$ pb, or $O(100)$ events per second. This is 6–7 orders of magnitude smaller than the total inelastic proton–proton scattering cross section.

In the ATLAS experiment, the collision event is quickly analyzed *before* recording the data, and only the events that are classified as "interesting" are recorded. This event selection procedure is called "trigger", and various selection criteria is defined to cover wide range of physics program. The basic concept of the trigger is to record events with high transverse momentum. Leptons with high-p_{T} are especially important, because it is expected that an electroweak process has taken place. In brief, the triggers are designed to collect events that have one or more

- leptons with high p_{T},
- photons with high p_{T},
- jets with significantly high p_{T}, or
- significant momentum imbalance in the transverse plane.

The last criteria tries to identify a production of high-p_{T} invisible particles. Candidate of such particle in the SM is the neutrino.

A schematic diagram of the trigger and data acquisition system of the ATLAS experiment is shown in Figure 2.18. The events are selected in two steps, the Level-1 trigger and the High-Level trigger. The Level-1 trigger is intended to quickly reduce the event rate to 100 kHz by rejecting relatively easy background events. Dedicated hardware modules are produced to implement calorimeter-based triggers (Level-1 Calo) and muon-spectrometer-based triggers (Level-1 Muon). The Central trigger system collects the output of Level-1 Calo and Level-1 Muon, and combine them to make a decision whether or not to pass the event to the High-Level trigger. The High-Level trigger is a software-based trigger, which analyzes the events using more detailed detector information, to reduce the data recording rate to 1 kHz.

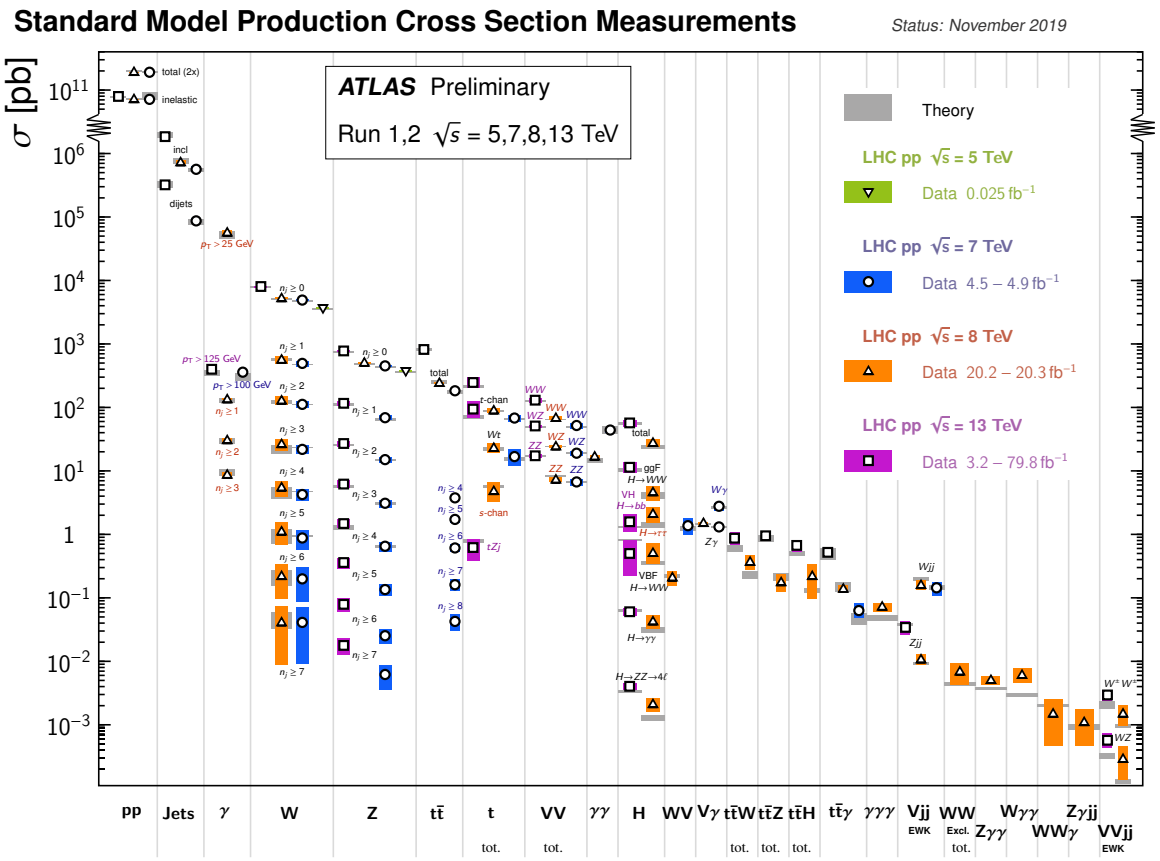

Figure 2.17: Cross sections for some of the major Standard Model processes measured at the ATLAS experiments, compared to the corresponding theoretical expectations.

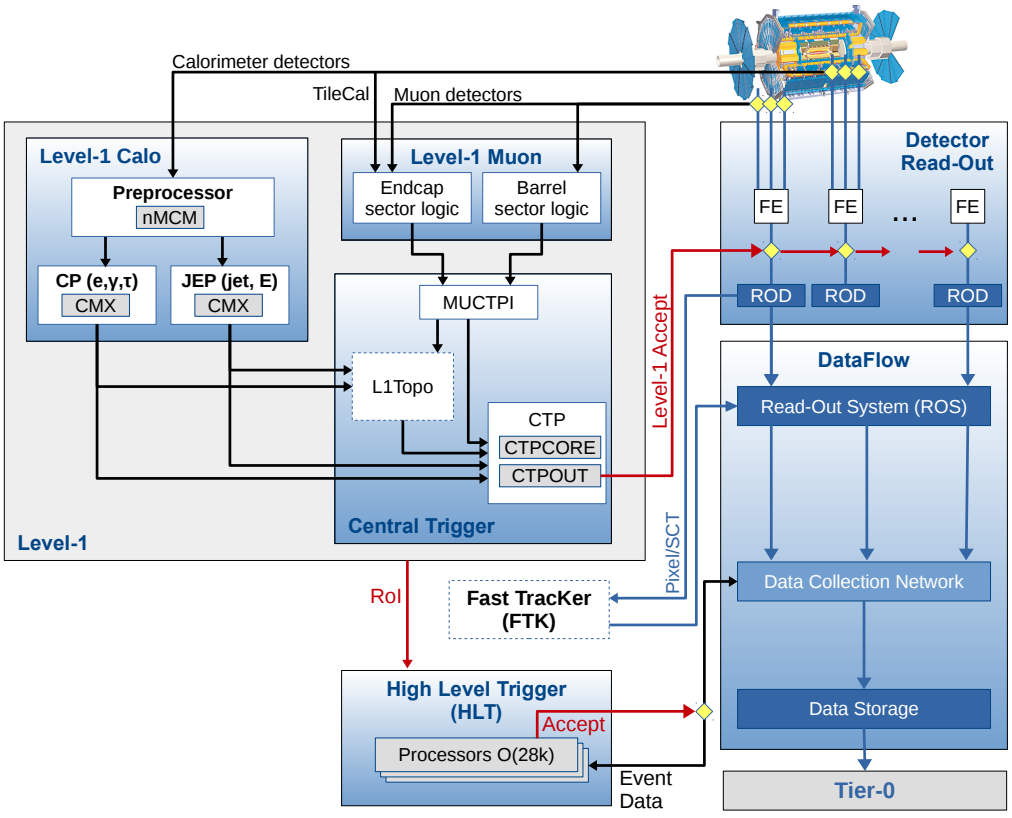

Figure 2.18: A schematic diagram of the ATLAS trigger and data acquisition system in Run2 [53].

Chapter 3

Data and Monte Carlo Simulation

The searches presented in this thesis are performed using the data from proton-proton collisions at the LHC, as well as simulated data samples produced using Monte-Carlo method. Monte-Carlo samples are used to understand the Standard Model processes in the collision data, and also to extract an estimate on a certain signal yield in the dataset. This chapter summarizes the setups of the collision data and the Monte Carlo simulated samples. The setups of the collision data samples used in this analysis, collected by the ATLAS detector in 2015–2018 are described in Section 3.1. The procedure to generate Monte-Carlo samples are explained in Section 3.2. The actual parameters used to generate the background SM samples and signal SUSY samples used in this thesis are shown in this section. The dedicated process required to generate the signal samples are explained in Section 3.3.

3.1 ATLAS Run2 data

The dataset used in the search presented in this thesis corresponds to 139 fb^{-1}of $\sqrt{s}$ = 13 TeV pp collision data, where the uncertainty on the integrated luminosity is 1.7%. Total integrated luminosity during stable beams in Run2 is shown in Figure 3.1. The amount of collision data collected in 2015, 2016, 2017 and 2018 are 3.2 fb^{-1}, 33.0 fb^{-1}, 44.3 fb^{-1} and 58.4 fb^{-1}, respectively. The luminosity is derived from the calibration of the luminosity scale using x-y beam-separation scans, following a methodology similar to that detailed in Ref. [54], and the LUCID-2 detector for the baseline luminosity measurements [55].

The average number of interactions per bunch-crossing varied between 13.4 in 2015 and 37.8 in 2017. Figure 3.2 shows the distribution of the number of interactions per bunch crossing in each data-taking year. These distributions are used to reweight the Monte-Carlo simulated samples, as described in Section 3.2.2.

3.2 Monte Carlo Simulation

Samples of Monte Carlo (MC) simulated events are used to estimate the distribution to background processes as well as to determine the systematic uncertainties. MC samples are also used to simulate the signal processes. MC samples are generated in three steps; the first step is the hard scatter event generation. The second step is pileup simulation, and the final step is detector simulation. Details of each step are described in the following sections.

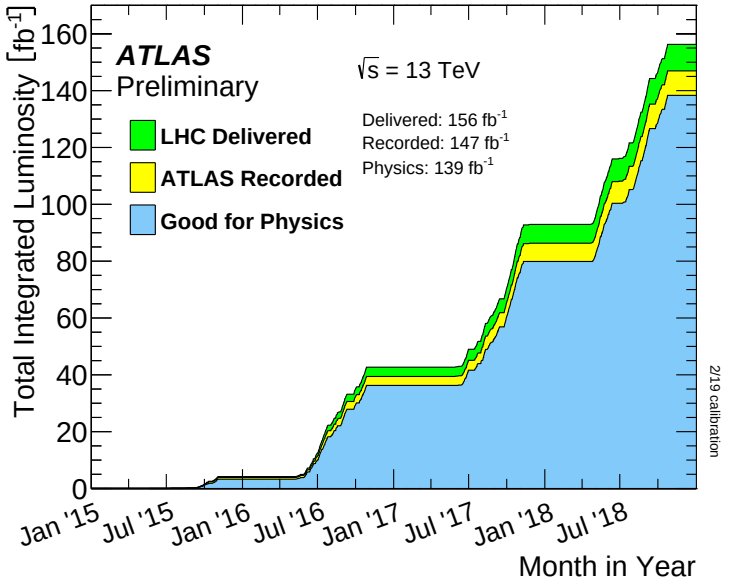

Figure 3.1: Integrated luminosity [56] delivered by the LHC (green) and recorded by the ATLAS detector (yellow). The data that matches certain criteria on the detector condition and data taking stability are considered as "good for physics", and are used in the analysis (blue).

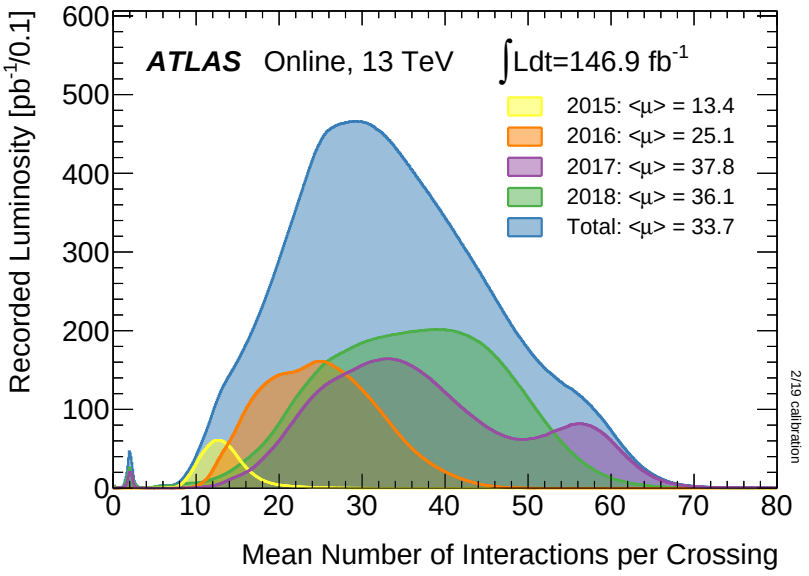

Figure 3.2: Number of interactions per proton bunch crossing [56]. The yellow, orange, purple and green graphs are the distributions for 2015, 2016, 2017 and 2018, respectively. The distribution for the entire period of 2015–2018 are shown with blue graph, with 33.7 average number of interaction per proton bunch.

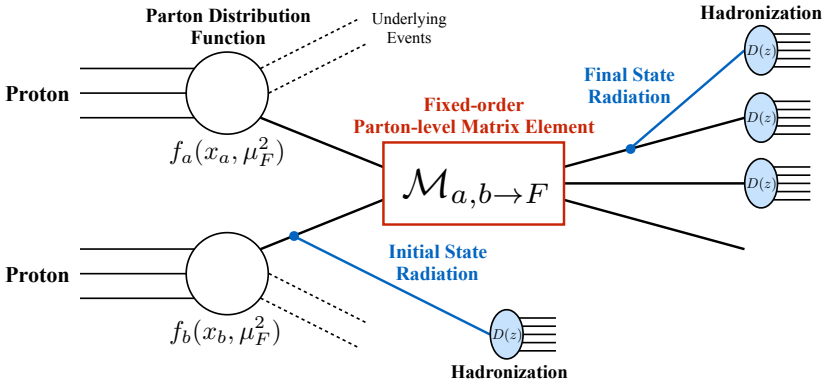

Figure 3.3: Schematic diagram for pp collision simulation procedure. Parton Distribution Function (PDF) $f_i(x, \mu_F)$, Matrix Element (ME) $\mathcal{M}$ and Fragmentation Functions $D(z)$ are used to fully simulate a pp collision.

3.2.1 Hard-scatter event generation

A proton-proton collision is modeled by factorizing the scattering process into several sub-processes. Figure 3.3 shows a schematic diagram of the factorization process. The differential cross-section of a hard-scattering process $pp \to F$ for an observable O can be written by this equation [57],

$$\frac{\mathrm{d}\sigma}{\mathrm{d}O} = \sum_{a,b} \int \mathrm{d}x_a \mathrm{d}x_b \sum_{qswswqswF} \int \mathrm{d}\Phi\, f_a(x_a, \mu_F^2)\, f_b(x_b, \mu_F^2)\, \frac{\mathrm{d}\hat{\sigma}_{ab\to F}}{\mathrm{d}\hat{O}} D_F(\hat{O} \to O; \mu_F), \tag{3.1}$$

which is a convolution of Parton Distribution Function part $f(x, \mu_F^2)$, parton-level differential cross section part $\frac{\mathrm{d}\hat{\sigma}_{ab\to F}}{\mathrm{d}\hat{O}}$ and hadronization part D_F. The main idea of factorization is to separate soft-QCD processes (PDF and hadronization) from the hard scattering part. This way, we can apply the perturbative quantum field theory to the QCD high-energy interaction calculation, while we can constrain the soft-QCD part from other macroscopic experiments. The energy scale where we switch from the soft-QCD to the perturbative QCD is denoted by μ_F in Eq. 3.1, which is a purely theoretical variable and often referred to as a factorization scale.

The Parton Distribution Function (PDF) of a proton, expressed as $f_i(x, \mu_F^2)$, represents the probability to find a parton i carrying a momentum fraction x, at a hard interaction of energy scale μ_F. The PDFs are calculated by simultaneously fitting some experimental inputs from deep-inelastic scattering experiments, fixed-target Drell-Yan data, and collider measurements. Several sets of the PDFs are provided from different groups, each with different fitting scheme and inputs. The uncertainties coming from the choice of the PDFs are taken into account, which is explained in Chapter 8.

The parton-level differential cross section $\sigma_{ab\to F}$ is related to the matrix element $\mathcal{M}_{ab\to F}$ by

$$\mathrm{d}\hat{\sigma}_{ab\to F} = \frac{1}{2\hat{s}} |\mathcal{M}_{ab\to F}|^2(\Phi; \mu_F, \mu_R), \tag{3.2}$$

where $\frac{1}{2\hat{s}}$ represents the parton flux factor. The matrix element (ME) is the sum of transition amplitude of all relevant processes with different intermediate states ($a, b \to X \to F$). The calculation of higher-order

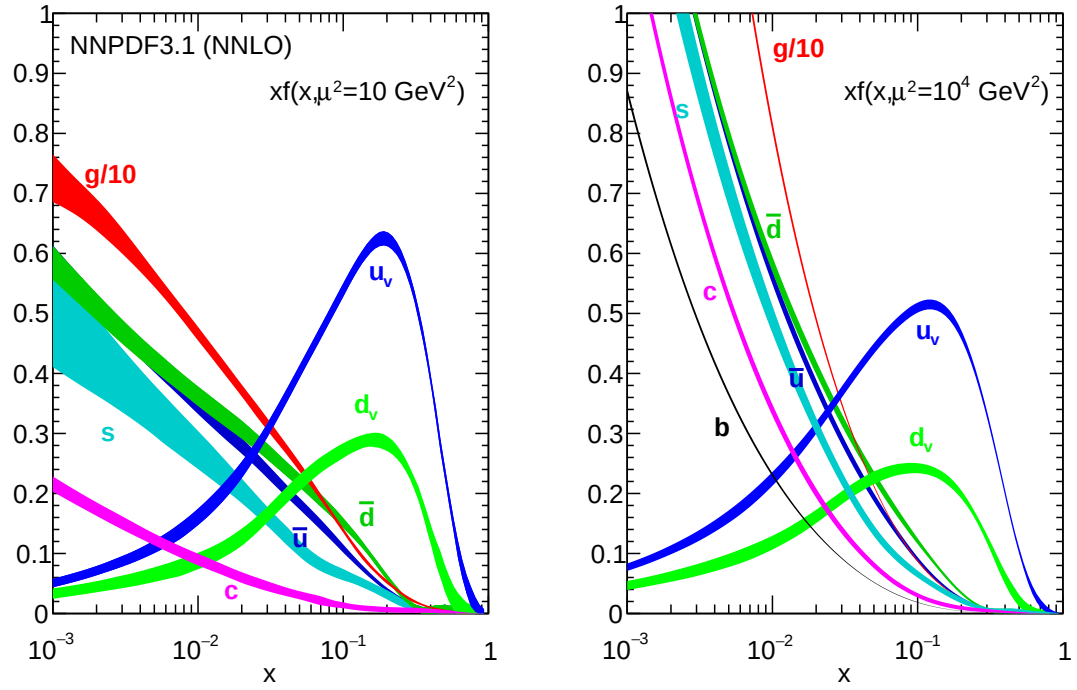

Figure 3.4: The NNPDF3.1 NNLO PDFs, evaluated at $\mu^2 = 10$ GeV^2 (left) and $\mu^2 = 10^4$ GeV^2 (right). [58]

terms is generally challenging, however, fixed order calculations are manageable up to the next-to-next-to-leading order (NNLO) for typical SM processes. Fixed-order matrix element is dependent on the choice of factorization scale μ_F and renormalization scale μ_R. On top of the fixed-order QCD matrix-element calculation, the parton shower approximation is further applied to complement the description of the additional parton emission.

Finally, all the colored particles in the final state are evolved into color-neutral hadrons. This process, hadronization, is calculated separately from the hard scattering part. The universal fragmentation function D_F characterizes this process.

A summary of the generator configurations for the samples used in this thesis is given in Table 3.1.

NNPDF 3.0 NNLO [59] is used for the V+jets ($V = W, Z/\gamma^*$) samples involving leptonically decaying vector bosons, as well as diboson (WW, ZZ and WZ, collectively referred to as VV), and fully leptonic triboson processes. NLO CTEQ6L1 [61] PDF is used for single-Higgs production via gluon–gluon fusion (ggF) and Vector Boson Fusion (VBF). NNPDF 2.3 LO [63] is used for all the other SM processes considered, as well as for signal Higgsino and Wino/Bino samples.

Sherpa 2.2.1 and 2.2.2 [74] are used to calculate the matrix elements and to model the PS and hadronization process of V+jets, VV and triboson processes. Higgs production in association with a vector boson is generated with Pythia 8.186. The matrix elements for ggF and VBF single-Higgs production, as well as Single top, $t\bar{t}$, and top quarks produced in association with W bosons are calculated with

Table 3.1: Summary of Monte-Carlo generator setups for SM background processes.

Process	Matrix element	Parton shower	PDF set	Cross section
V+jets	Sherpa 2.2.1		NNPDF 3.0 NNLO [59]	NNLO [60]
VV	Sherpa 2.2.1/2.2.2		NNPDF 3.0 NNLO	Generator NLO
Triboson	Sherpa 2.2.1		NNPDF 3.0 NNLO	Generator LO, NLO
$h[ggF]$	Powheg-Box	Pythia 8.212	NLO CTEQ6L1 [61]	N^{3}LO [62]
$h[VBF]$	Powheg-Box	Pythia 8.186	NLO CTEQ6L1 [61]	NNLO + NLO [62]
$h+W/Z$	Pythia 8.186		NNPDF 2.3 LO [63]	NNLO + NLO [62]
$h+t\bar{t}$	MG5_aMC@NLO 2.2.3	Pythia 8.210	NNPDF 2.3 LO	NLO [62]
$t\bar{t}$	Powheg-Box	Pythia 8.230	NNPDF 2.3 LO	NNLO+NNLL [64–68]
t (s-channel)	Powheg-Box	Pythia 8.230	NNPDF 2.3 LO	NNLO+NNLL [69]
t (t-channel)	Powheg-Box	Pythia 8.230	NNPDF 2.3 LO	NNLO+NNLL [70, 71]
$t+W$	Powheg-Box	Pythia 8.230	NNPDF 2.3 LO	NNLO+NNLL [72]
$t+Z$	MG5_aMC@NLO 2.3.3	Pythia 8.212	NNPDF 2.3 LO	NLO [73]
$t\bar{t}WW$	MG5_aMC@NLO 2.2.2	Pythia 8.186	NNPDF 2.3 LO	NLO [73]
$t\bar{t}+Z/W/\gamma^*$	MG5_aMC@NLO 2.3.3	Pythia 8.210/8.212	NNPDF 2.3 LO	NLO [62]
$t+WZ$	MG5_aMC@NLO 2.3.3	Pythia 8.212	NNPDF 2.3 LO	NLO [73]
$t+t\bar{t}$	MG5_aMC@NLO 2.2.2	Pythia 8.186	NNPDF 2.3 LO	LO [73]
$tt\bar{t}\bar{t}$	MG5_aMC@NLO 2.2.2	Pythia 8.186	NNPDF 2.3 LO	NLO [73]

Powheg-Box [75]. $t\bar{t}h$ production and rarer top processes is generated with MG5_aMC@NLO 2.2.2/2.2.3. Matrix elements, excluding those generated with Pythia or Sherpa, are then interfaced with Pythia 8 to model Parton Showering and hadronization. Further details on the configuration of the SM processes simulation can be found in Refs. [76–80].

3.2.2 Pileup Simulation

To simulate the effects of additional pp collisions, referred to as pileup, in the same and neighboring bunch crossings, additional interactions are generated using the soft QCD processes of Pythia 8.186 with the A3 tune [81] and the MSTW2008LO PDF set [82], and are overlaid onto each simulated hard-scatter event. The MC events are reweighted to match the pileup distribution observed in the data, as shown in Figure 3.2.

3.2.3 Detector Simulation

Background and signal samples make use of EvtGen 1.6.0 and 1.2.0 [83] to model the decay of bottom and charm hadrons, with the exception of the background samples modeled with Sherpa. All MC simulated samples are processed through the ATLAS simulation framework [84] in Geant4 [85]. The samples for the signals use the ATLAS fast simulation [86], which parametrizes the response of the calorimeters.

3.3 Signal MC samples

Generation of the MC samples for the Higgsino scenario

Signal samples are generated for the simplified Higgsino scenario, which include the production of $\tilde{\chi}_1^- \tilde{\chi}_1^+$, $\tilde{\chi}_2^0 \tilde{\chi}_1^\pm$ and $\tilde{\chi}_2^0 \tilde{\chi}_1^0$. The masses of the neutralinos are varied, while the chargino mass is set to $\tilde{\chi}_1^\pm = \frac{1}{2}\left[m(\tilde{\chi}_1^0) + m(\tilde{\chi}_2^0)\right]$, as discussed in Section 1.3. The mass splittings $\Delta m = m(\widetilde{\chi}_1^0) - m(\widetilde{\chi}_2^0)$ of the order of tens of GeV can be obtained by mixing with wino or Bino states. In this simplified model, mass differences ranging from 1 GeV to 60 GeV are considered, but the calculated cross-sections assume pure Higgsino $\widetilde{\chi}_2^0$, $\widetilde{\chi}_1^\pm$ and $\widetilde{\chi}_1^0$ states. All other SUSY particles are assumed to be decoupled, so that they do not affect the production/decay processes. Typical values of cross-sections for $m(\widetilde{\chi}_2^0) = 110$ GeV and $m(\widetilde{\chi}_1^0) = 100$ GeV are 4.3 ± 0.1 pb for $\widetilde{\chi}_2^0 \widetilde{\chi}_1^\pm$ production and 2.7 ± 0.1 pb for $\widetilde{\chi}_2^0 \widetilde{\chi}_1^0$ production.

The samples are generated at leading order with MG5_aMC@NLO 2.6.1 and included up to two extra partons in the matrix element. The neutralinos and charginos are decayed with MadSpin [87]. The events are then interfaced with Pythia 8.212 [88] to model the Parton Showering and hadronization. To enforce the ISR topology, at least one parton in the final state is required to have a p_{T} greater than 50 GeV.

Generation of the MC samples for the Wino/Bino scenario

In the Wino/Bino scenario, the $\tilde{\chi}_2^0 \tilde{\chi}_1^\pm$ final state is produced. The $\tilde{\chi}_1^0$ is a pure Bino state, with the $\tilde{\chi}_2^0$ and $\tilde{\chi}_1^\pm$ states forming degenerate pure Wino states. The generator configurations are consistent with those used for the Higgsino samples. A typical value of the $\widetilde{\chi}_2^0 \widetilde{\chi}_1^\pm$ production cross-section is 16.0 ± 0.5 pb for $m(\widetilde{\chi}_2^0) = m(\widetilde{\chi}_1^\pm) = 110$ GeV.

Simulation of the $m_{\ell\ell}$ distribution

The searches presented in this thesis exploit the kinematic limit in the dilepton invariant mass spectrum from the decay chain $\tilde{\chi}_2^0 \to Z^* \tilde{\chi}_1^0$, $Z^* \to \ell\ell$. Processes that involve the production of a $\tilde{\chi}_2^0$ neutralino dominate the sensitivity of the search. The branching ratios for the processes $\tilde{\chi}_2^0 \to Z^* \tilde{\chi}_1^0$ and $\tilde{\chi}_1^\pm \to W^* \tilde{\chi}_1^0$ are fixed to 100% for both the Higgsino and Wino/Bino scenarios. The branching ratios of $Z^* \to \ell\ell$ and $W^{\pm *} \to \ell\nu$ depend on the virtual mass of the off-shell vector boson. For both the Higgsino and Wino/Bino scenarios, the branching ratios are computed with SUSY-HIT 1.5a [89], which accounts for finite b-quark and τ masses. At $\Delta m = 40$ GeV, the $Z^* \to \ell\ell$ branching ratio to electrons or muons is 3.5%, and this increases to 5.3% and 5.0%, respectively, at $\Delta m = 1$ GeV as decays into heavier quarks or τ leptons become kinematically inaccessible. Similarly, for $W^* \to \ell\nu$, the branching ratios to electrons or muons are both 11% at $\Delta m = 40$ GeV, but increase to 20% and 17%, respectively, for $\Delta m = 1$ GeV.

The distribution of the dilepton invariant mass from the decay of the Z^* [90] depends on the relative sign of the $\widetilde{\chi}_1^0$ and $\widetilde{\chi}_2^0$ mass parameters. In the pure Higgsino scenario, the product of the signed mass eigenvalues $\left(m\left(\tilde{\chi}_2^0\right) \times m\left(\tilde{\chi}_1^0\right)\right)$ can only be negative while for the Wino/Bino case, either positive or

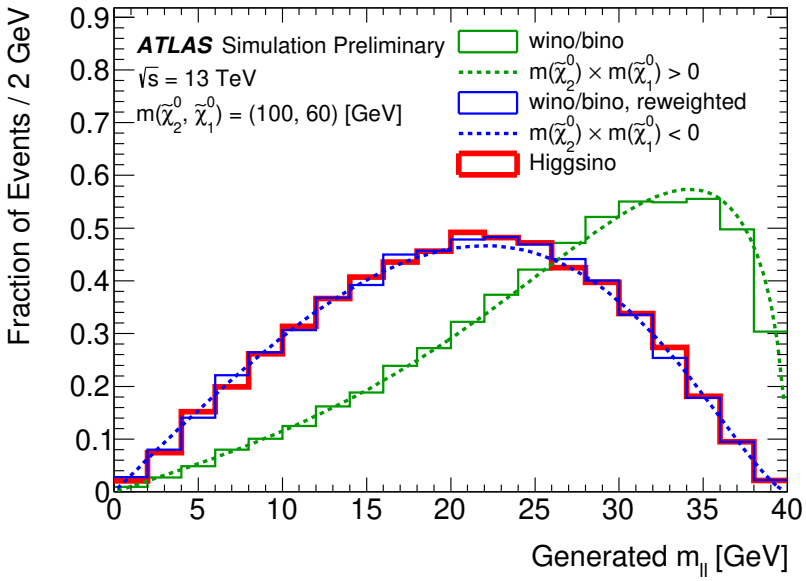

Figure 3.5: Invariant mass of the two leptons from $\widetilde{\chi}_2^0 \to Z^* \widetilde{\chi}_1^0$ followed by $Z^* \to \ell\ell$ decay, for the simplified Higgsino and Wino/Bino scenarios. The endpoint of the distribution is determined by the difference between the masses of the $\tilde{\chi}_2^0$ and $\tilde{\chi}_1^0$. The results from simulation (histograms) are compared against analytic calculations of the expected lineshape (dashed lines) presented in Ref. [90]. The product of the signed mass eigenvalues $\left(m\left(\tilde{\chi}_2^0\right) \times m\left(\tilde{\chi}_1^0\right)\right)$ is negative for Higgsino and can be either negative or positive for Wino/Bino scenarios.

negative products are allowed. [1] The simulated Wino/Bino process assumes the product of the signed mass eigenvalues is positive, and the analytic description of the expected lineshape is used to reweight the $m_{\ell\ell}$ distribution to the case of the product being negative. The difference between the Wino/Bino and Higgsino lineshapes, as well as the agreement of the reweighted distribution with the expected lineshape are shown in Figure 3.5. The two possible Wino/Bino $m_{\ell\ell}$ distributions are used to provide two separate model-dependent interpretations of the results.

Cross-sections for the signal samples are calculated with Resummino 2.0.1 at NLO+NLL [93–100] precision. The evaluation of the cross-sections and corresponding uncertainty are taken from an envelope of cross-section predictions using different PDF sets, and varied factorization and normalization scales. This procedure is described in Ref. [101], and the same procedure is used in the previous search result [43]. Figure 3.6 shows the Higgsino production cross section for various mass assumptions.

[1] The mixing matrix used to diagonalize the neutral electroweakino states is forced to be a real matrix in the SLHA2 format [91]. A consequence of this choice is a negative sign given to one or more mass eigenvalues, determined in part by the relative fractions of Wino, Bino, or Higgsino content of the physical states. For additional discussion, see Ref. [92].

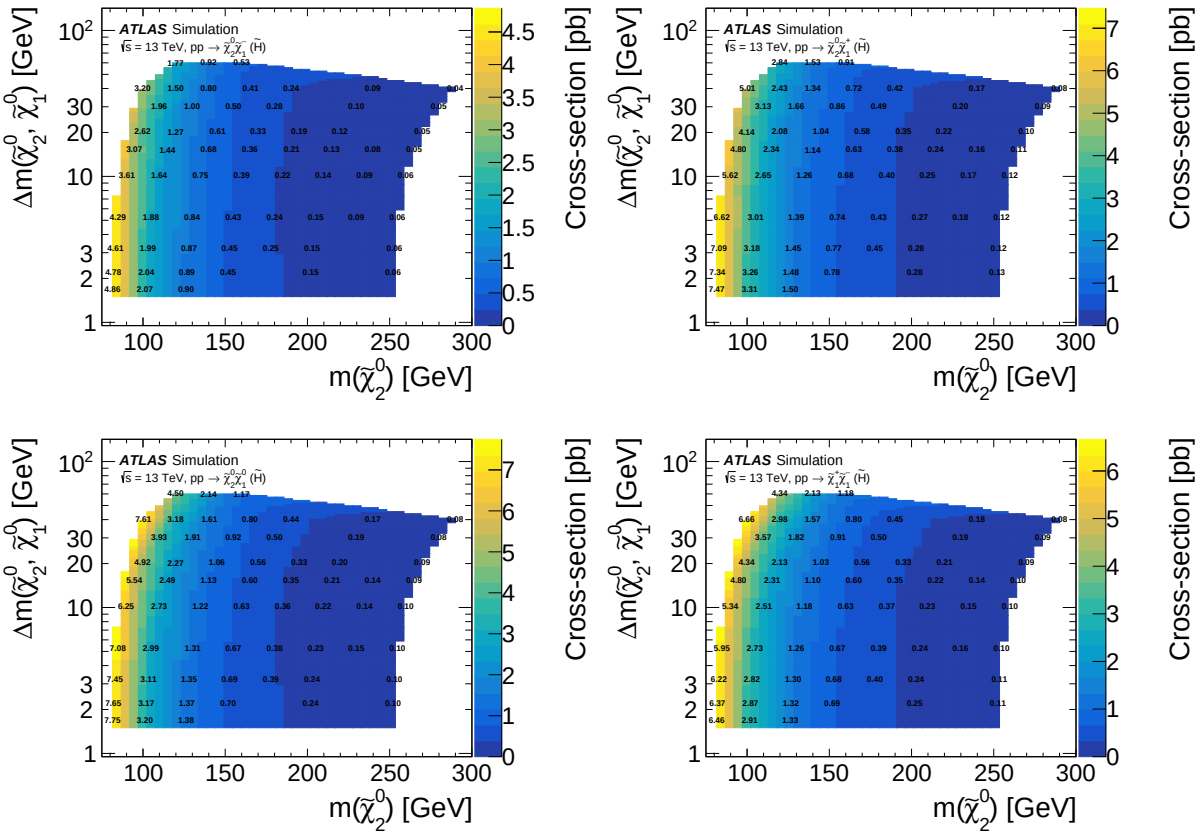

Figure 3.6: The cross sections for Higgsino scenarios, shown in $m(\widetilde{\chi}_2^0) \times \Delta m(m(\widetilde{\chi}_2^0), m(\widetilde{\chi}_1^0))$ plane. Four production modes are considered; $\widetilde{\chi}_2^0\widetilde{\chi}_1^-$ (top left), $\widetilde{\chi}_2^0\widetilde{\chi}_1^+$ (top right), $\widetilde{\chi}_2^0\widetilde{\chi}_1^0$ (bottom left), and $\widetilde{\chi}_1^+\widetilde{\chi}_1^-$ (bottom right). The $m(\widetilde{\chi}_2^0)$ and the Δm are varied in the indicated range, but assumes pure Higgsino $\widetilde{\chi}_2^0$, $\widetilde{\chi}_1^0$ and $\widetilde{\chi}_1^\pm$ for the calculation of the cross section.

Chapter 4

Object Reconstruction

Particles produced in the collision leave signals in various sub-detectors in ATLAS. These signals are combined to reconstruct low-level objects such as tracks and calorimeter clusters. The low-level objects are further combined and processed in dedicated algorithms to reconstruct physics objects, that are used in the analysis. The algorithms to reconstruct various physics objects in the ATLAS detector are summarized in this section.

4.1 Overview of the object reconstruction

Figure 4.1 shows a schematic diagram of the object reconstruction flow. Raw detector information from the inner detectors, calorimeters and muon spectrometers is combined to reconstruct low-level objects. The low-level objects considered in this analysis are inner detector tracks, vertices, topo-clusters, and muon spectrometer tracks. The procedures to reconstruct these low-level objects are described in Section 4.2. The low-level objects are further combined to reconstruct physics objects, such as jets, electrons, muons and photons. The algorithms of the jet reconstruction, as well as the energy corrections, are introduced in Section 4.3. The electrons and muons are reconstructed using the low-level objects, and are further required to pass the "identification", and the "isolation" steps. The details of each step are described in Sections 4.4 and 4.5, for electrons and muons, respectively. A dedicated calibration method using $Z \to \ell\ell$ events is also explained in these sections. Reconstructed jets, electrons and muons are required to pass the "baseline" selections, which are also summarized in each section. Reconstruction of the photons is explained in Section 4.6. Taus are not explicitly included in the object definition, but those decaying leptonically are reconstructed as electrons or muons, whereas those decaying hadronically are reconstructed as jets.

The jets, electrons and muons that pass the baseline requirements are handled by "overlap removal" algorithm to resolve ambiguity coming from duplicated objects. Details of the overlap removal algorithm are summarized in Section 4.7. Objects that pass all the above selections are referred to as "baseline objects", and are used in the analysis. The missing transverse energy, $E_{\mathrm{T}}^{\mathrm{miss}}$ is reconstructed using all the baseline objects and photons. Additional contribution from other low-p_{T} particles is considered in the calculation of $E_{\mathrm{T}}^{\mathrm{miss}}$, which is described in Section 4.8. In this thesis, a single track reconstructed in the inner detector is also treated as a physics object in some specific signal regions. The definition of a track as a physics object is presented in Section 4.9. The object definitions used in the analysis are summarized in Section 4.10. In the definitions of the objects, we often use "working points" for the cuts/selections. A working point in this context is a set of cuts or selections that is commonly used in many analyses in ATLAS. The performance of the working points is studied in detail and the modeling by the MC is carefully checked by the collaboration. Thus we select one of these working points to define the physics objects.

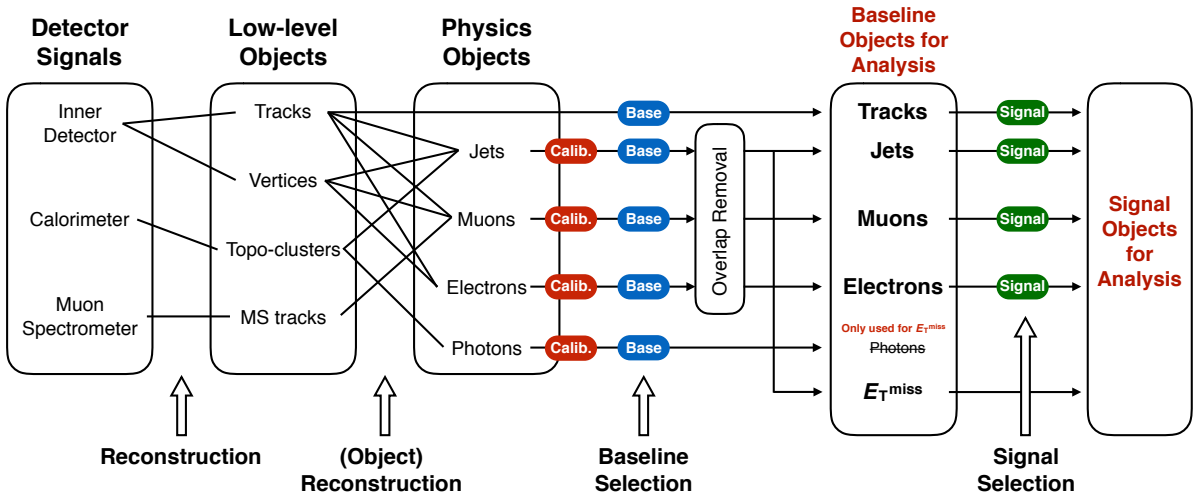

Figure 4.1: A schematic diagram of object reconstruction flow. Low-level objects are reconstructed directly from the detector information. Physics objects are reconstructed using the low-level objects. Calibrated physics objects that pass the baseline selections and overlap removal are treated as "baseline" objects. Physics objects that pass the signal selections are called "signal" objects. Photons are not explicitly used in the main analysis, but are used to calculate $E_{\mathrm{T}}^{\mathrm{miss}}$.

4.2 Low-level objects

4.2.1 Tracks

The inner detector tracks are reconstructed using only the information from the inner detector, and are simply referred to as "tracks" in this thesis. The algorithm of the track reconstruction is briefly introduced in this section. A detailed explanation can be found in Ref. [102].

Raw hits on the Pixel or SCT detectors are grouped by connected component analysis [103], to create clusters. One cluster from the Pixel detector, or two clusters from the SCT (each from the two layers in a same SCT module) give a three-dimensional coordinate, referred to as a "space point". A space point represents the path of the charged particle. Three space points are combined to form a track seed, extrapolated using combinatorial Kalman filter [104], and finally a track candidate is reconstructed. A "track score" is calculated for each track seed based on the number of clusters or holes in the track trajectory, and candidates with low scores are rejected at this point. If the track candidate is associated with clusters that are assigned to another track candidate, a neural network technique [105] is used to resolve the ambiguity.

The track candidates are accepted when they pass basic quality cuts on p_{T}, $|\eta|$, number of clusters/holes and "impact parameters". The impact parameters represent the distance of the track from the interaction point. Schematic diagrams showing the definitions of the impact parameters d_0 and z_0 are presented in Figure 4.2. The transverse impact parameter d_0 is defined as the distance between the extrapolated track and the interaction point in the transverse plane, whereas the longitudinal impact parameter z_0 is defined as the difference in z coordinate. The impact parameters of the track candidates are calculated assuming the interaction point is the center of the detector.

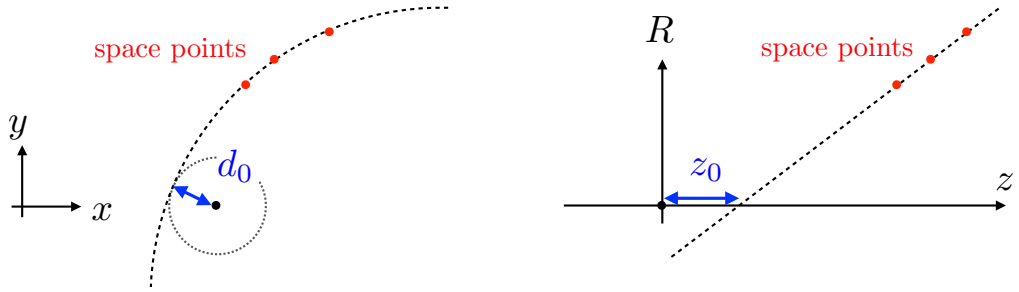

Figure 4.2: Schematic diagrams showing the definitions of the impact parameters. The diagram on the left shows the transverse view, and the diagram on the right shows the longitudinal view. The red points show the space points, and the dashed black lines show the trajectory of the extrapolated tracks. The blue arrow in each diagram represents the transverse and longitudinal impact parameters d_0 and z_0, respectively.

4.2.2 Vertices

The position of single pp collision is called a "vertex". The vertices are reconstructed by combining several tracks using the Iterative Vertex Finding algorithm [106], which takes all tracks that pass the quality cuts, explained in Ref. [107], as input.

The Iterative Vertex Finding algorithm first looks for a global maximum in the distribution of Z coordinates of the tracks, used as the vertex seed position. The seed position and the tracks around the seed are used as input to the Adaptive Vertex Fitting algorithm [108], to determine the position of the vertex. Finally, vertices with less than two associated tracks are discarded. Typically 10-30 vertices are reconstructed per event in ATLAS Run-2 as shown in Figure 4.3(a). The vertices are ordered in sum of squared transverse momentum of the associated tracks (Σp_{T}^2). The vertex with the largest Σp_{T}^2 is define as the "primary vertex" in this thesis, and all the physics objects are assumed to be produced in the interaction at this vertex. Figure 4.3(b) shows the vertex reconstruction efficiency as a function of the number of tracks associated to the vertex. In the analysis presented in this thesis, we require at least two leptons and a jet, therefore the number of tracks associated to the vertex is larger than three, where the vertex reconstruction efficiency is sufficiently high.

4.2.3 Topo-clusters

The energy deposit of a particle in the calorimeters is often divided into several cells. The energy deposit measured in the cells are merged into a cluster to calculate the total energy deposit by the particle(s). "Topo-cluster" is defined by merging topologically connected cells [111] into a cluster. The topo-clusters are used as the input for jet reconstruction, explained in Section 4.3, as well as for the isolation criteria of electrons and muons explained in Sections 4.4.3 and 4.5.3, respectively.

The clustering starts from finding a seed cell with energy deposit larger than 4σ significance over the expected noise level. The neighboring cells with 2σ significance over the noise level are added to the seed cell to form a cluster. This process is repeated until there are no more cells to be added to the cluster, then finally all the neighboring cells of the cluster are attached to the cluster. If there are multiple local maxima

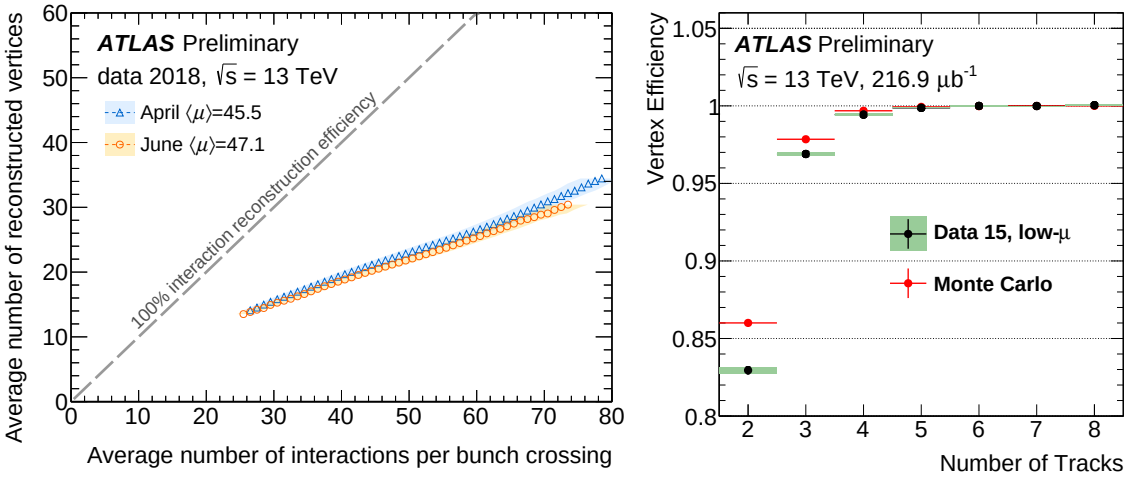

(a) (b)

Figure 4.3: (a) The number of reconstructed vertices as a function of the average number of interactions per bunch crossing (μ) [109]. The blue and orange points correspond to two fills with different average μ taken in 2018. (b) Vertex reconstruction efficiency as a function of number of tracks associated to the vertex [110]. The efficiency is measured using 2015 low pile-up data (black), and compared with MC (red).

in a cluster with total energy larger than 500 MeV, the cluster is split and the cell energy of the overlapping cells are divided based on the energy/distance from the split clusters.

4.2.4 Muon spectrometer tracks

Tracks that are reconstructed using the muon spectrometer information are called muon spectrometer tracks. Detailed reconstruction algorithm of the muon spectrometer tracks are described in Ref. [112]. A brief explanation of the reconstruction is given in the following paragraph.

The muon spectrometer track is reconstructed in two steps: segment finding and fitting. In the first step, a "segment" is defined in each muon station, which consists of three or four layers of the MDTs and CSCs. The segment is reconstructed by collecting several hits in a station that are aligned on a straight line. For the MDT segments, a Hough transform [113] is used to search for the straight hit patterns. RPC or TGC hits are used to measure the coordinate orthogonal to the bending plane. For the CSC segments, combinatorial search in the η and ϕ detector planes is performed. At least two segments are required to form a track candidate, except for in the transition region between barrel and endcap where muon detectors do not have full coverage. The track candidate is re-fitted using all the hits included in the segments, and a global χ^2 of the fit is calculated. The track candidate is accepted if the χ^2 of the fit satisfies the selection criteria, explained in Ref. [112].

4.3 Jets

4.3.1 Jet reconstruction

Jets in the most of ATLAS searches and measurements are reconstructed using the anti-k_t algorithm [114] with the radius parameter $R = 0.4$, implemented in the FastJet [115] package. The input to the algorithm can be tracks, topo-clusters or combination of those, depending on the analysis strategy. In the analysis presented in this thesis, topo-clusters are used as input to reconstruct "EM-topo-jets", denoted simply as "jets". Tracks are also used to reconstruct "track-jets", which are not directly used as physics objects, but are used for the "Prompt Lepton Tagging" method, described in Section 5.2.

4.3.2 Jet energy corrections

The energy of the topo-clusters are calculated assuming that the energy deposit is caused by the electromagnetic interaction. The jet energy needs to be scaled to account for the difference between the electromagnetic and the hadronic interaction, and correctly reconstruct the original energy of the parton. Multi-step correction is performed to the EM-topo jets mainly to account for this energy-scale correction, and also to subtract pile-up effects on the jet energy. An overview of the correction procedure is explained in the following paragraphs, while the details are discussed in Ref. [116].

First, the direction of a jet is re-calculated assuming the origin of the jet is the primary vertex. This correction is referred to as the origin correction, which improves the directional resolution of jets in the $|\eta|$ coordinate. Then, a two-stage correction is applied to subtract the pile-up contribution. Event-by-event correction based on the "area" of the jet is applied to subtract the overall pile-up contribution in the event. The correction is performed in a form of

$$p_{\mathrm{T}}{}^{\mathrm{corr}} = p_{\mathrm{T}}{}^{\mathrm{reco}} - \rho \cdot A, \tag{4.1}$$

where $p_{\mathrm{T}}{}^{\mathrm{reco}}$ and $p_{\mathrm{T}}{}^{\mathrm{corr}}$ are the energy of the jets before and after the correction, respectively. The ρ is median of the energy density of all the jets in $|\eta| < 2$ region, and A is the area of the jet. The area of the jet corresponds to the area in $\eta \times \phi$ plane where a virtual topo-cluster with infinitesimal energy would be merged to the jet (ghost association method [117]). The additional correction is applied to cover the dependence of the jet energy on the number of reconstructed vertex N_{PV} and the number of average interaction points $\langle\mu\rangle$.

After the origin and pile-up corrections, the jet energy scale is calibrated to the parton level energy. Energy response, defined as $E^{\mathrm{reco}}/E^{\mathrm{truth}}$ is measured by MC simulation and is used to scale the reconstructed energy E^{reco} to the truth particle energy E^{truth}.

Global sequential calibration [118] is applied to reduce flavor dependence and energy leakage effects. The idea is to take into account the differences coming from the particle origin, observed as the differences in shower shape or density of the tracks. Five additional variables that identify these characteristics are used for the correction, for example the fraction of the energy in certain layers of the calorimeter, and the number of tracks associated to the jet.

Finally, a residual *in-situ* calibration is applied to data. Differences between the data and MC simulation are quantified by balancing the p_{T} of a jet against other well-measured reference objects, such as photons

and Z bosons. The difference in the balance in the data and MC is used to calculate correction factors to be applied to the data.

4.3.3 Jet vertex tagger

In the pile-up correction explained in the previous section, the contributions from the pile-up are estimated using the average energy of the jets in the event. This approach does not account for the pile-up jets accidentally merged into the jets from the primary vertex. Jet vertex tagger [119] aims to reject such contributions, by discriminating whether a jet comes from the primary vertex or from a pile-up vertex.

The basic idea of the jet vertex tagger is to use the track information to associate a jet to the primary vertex. Tracks are associated to an EM-topo jet using the ghost association [117] method. Jet vertex fraction, denoted by JVF in the following equation, is defined as the ratio of sum of track p_{T} associated to the primary vertex over the sum of track p_{T} associated to any of the vertices, which can be written as

$$\mathrm{JVF}(\mathrm{jet}_i, PV_0) = \frac{\Sigma_j {p_{\mathrm{T}}}^j(PV_0)}{\Sigma_k \Sigma_l {p_{\mathrm{T}}}^l(PV_k)}, \tag{4.2}$$

where $p_{\mathrm{T}}^i(PV_j)$ is the p_{T} of the i-th track associated to the j-th vertex, and PV_0 is the primary vertex which the most contribution of the jet is from. A correction is applied to the jet vertex fraction as explained in Ref. [119] to account for the dependence on the number of vertex in the event. The corrected JVF discriminant is combined with $R_{p_{\mathrm{T}}} = \Sigma_j {p_{\mathrm{T}}}^j(PV_0)/{p_{\mathrm{T}}}^{\mathrm{jet}}$ based on a 2-D likelihood method, to build a new discriminant. Cuts on this discriminant are used to define several working points to reject the pile-up jets. A dedicated jet vertex tagger for the forward region is constructed with a similar concept [120].

4.3.4 Jet flavor tagging

Jets originating from b-quarks are identified by exploiting the long life-time, high mass and decay multiplicity of b-hadrons. Outputs of three different algorithms are combined with kinematic variables to obtain a final discriminant for the jet flavor tagging. Two algorithms called $IP2D$ and $IP3D$ [121] use the impact parameter information of all the tracks associated to the jet. Probability density functions (PDFs) for the impact parameters are constructed using MC, and are used to calculate the likelihood of the jet originating from b/c- or light-flavor quarks. The vertex-based algorithm [121] uses tracks in the jet to reconstruct a secondary vertex. The JetFitter algorithm [122] aims to reconstruct full decay chain of "primary vertex$\longrightarrow b \longrightarrow c$-hadron" within a jet. These variables are combined using the Boosted Decision Tree [123] to construct a final discriminant, *MV2c10* [124, 125].

4.4 Electrons

Electrons used in this thesis are required to pass three-step selections, the "reconstruction", "identification", and "isolation". The reconstruction step is designed to collect electron candidates at high efficiency, allowing certain amount of background coming from jets and photons. In the identification step, these backgrounds are suppressed using algorithms based on a likelihood method. In the isolation step, the

electrons are required to be isolated from other objects to further reject backgrounds, which mainly come from semi-leptonic decays of heavy hadrons.

4.4.1 Electron reconstruction

Electrons are reconstructed by matching topo-clusters to tracks, based on the distance between the clusters and the tracks. Direction and p_{T} of the matched tracks are corrected using the Gaussian-sum filter [126], where bremsstrahlung of the charged particles are taken into account.

4.4.2 Electron identification

The reconstruction step explained in the previous section is not intended to reject backgrounds such as hadrons in light-flavor jets, photons or non-prompt electrons from the semi-leptonic decay of heavy hadrons. In the identification step, an algorithm based on likelihood is designed to collect prompt electrons from decays of W/Z while rejecting these backgrounds. Fourteen variables in total are used as input to the likelihood identification, for example the shower shape (depth) in the calorimeters, the quality and impact parameters of the tracks, and the information of the TRT. The probability density functions (PDFs) for the electron identification are derived from the $J/\psi \rightarrow ee$ and $Z \rightarrow ee$ MC samples, and are corrected using the $Z \rightarrow ee$ events in data to account for the mis-modeling in the MC. The PDFs are defined in nine η bins to model the different detector regions separately, and seven E_{T} bins to evaluate the E_{T} dependence of the input variables.

The working points are defined by applying cuts on the likelihood discriminant. The cut values for the likelihood discriminants are determined in η and E_{T} bins. Four working points, *VeryLoose*, *Loose*, *Medium* and *Tight* are defined [127] to cover various physics analyses in ATLAS. Figure 4.4 shows the efficiencies of the *Loose*, *Medium* and *Tight* working points measured using the $Z \rightarrow ee$ events.

4.4.3 Electron isolation

In the isolation step, the electrons are required to be isolated from other tracks/clusters, to further reject backgrounds. The activities close by the lepton are used in the isolation step to distinguish the prompt lepton from the background. Isolation variables are defined as scalar sum of the E_{T} of the topo-clusters or p_{T} of the tracks around the lepton, and are used to define several isolation working points. The definitions of the isolation variables and the isolation working points are explained in Section 5.2. The efficiencies of the isolation working points for the electrons are shown in Figure 4.5.

4.4.4 Electron calibration

The electron reconstruction, identification and isolation efficiencies are measured using the $Z \rightarrow ee$ process. The tag-and-probe method [127] is used to measure the efficiencies both in the data and MC. The measured efficiencies are compared between the data and MC to check the modeling. Data/MC ratio is shown in the bottom panel of each plot in Figure 4.4 and Figure 4.5. A mis-modeling of a few % level is observed in

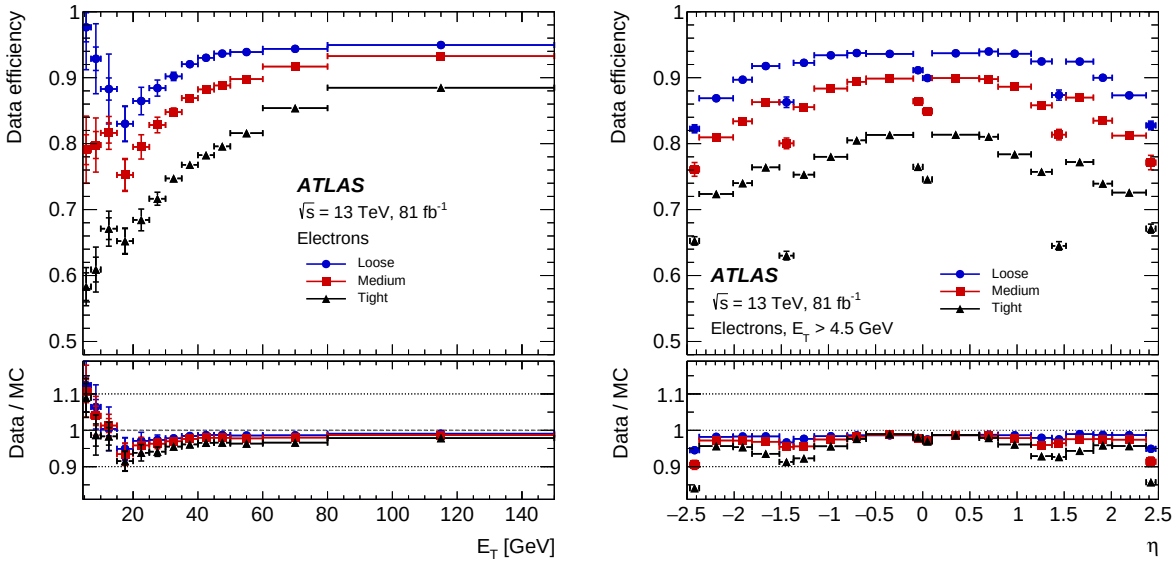

Figure 4.4: Electron identification efficiency as a function of E_{T} (left) and η (right) for *Loose*, *Medium* and *Tight* working points [127].

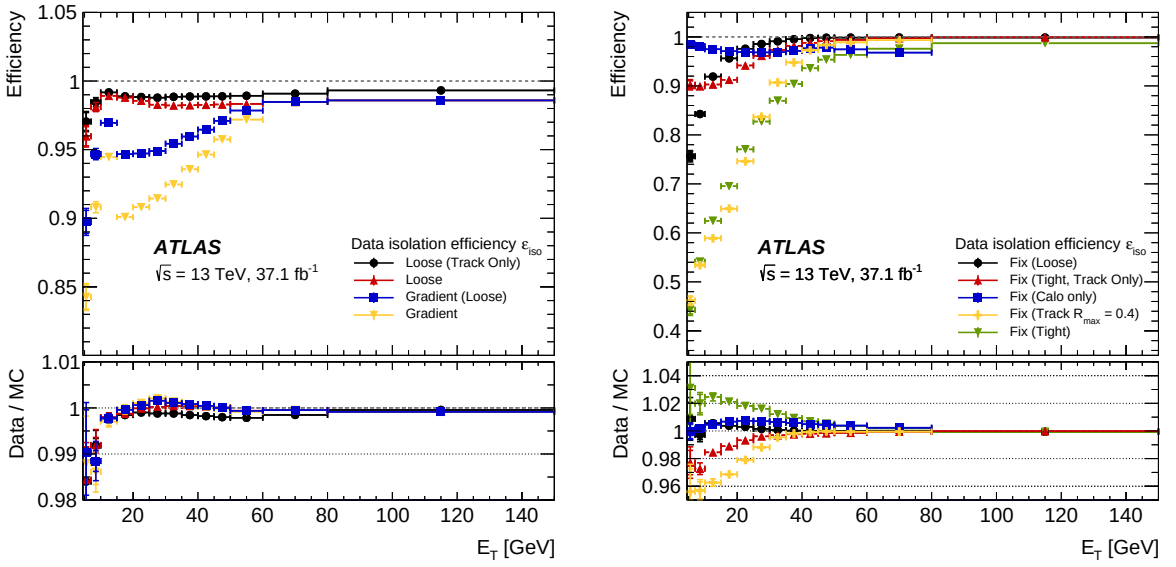

Figure 4.5: Electron isolation efficiency as a function of E_{T} for various working points. The jump in efficiency at 15 GeV in the left plot comes from the discontinuity of the samples used to define these working points; $J/\psi \rightarrow ee$ is used for $p_{\mathrm{T}} < 15$ GeV, while $Z \rightarrow ee$ is used for $p_{\mathrm{T}} > 15$ GeV.

low-E_{T} electrons. The mis-modeling is corrected by applying an E_{T}-dependent scale factor on the MC events.

4.5 Muons

Muons are required to pass three-step selections, the "reconstruction", "identification", and "isolation". The reconstruction step is designed to collect muon candidates at high efficiency, and the identification step aims to suppress backgrounds from hadron decays. In the isolation step, the muons are required to be isolated to reject backgrounds from semi-leptonic decays of heavy hadrons.

4.5.1 Muon reconstruction

The inner detector tracks and the muon spectrometer tracks are combined to reconstruct muons. Information of the calorimeters are also used to complement the measurement at $|\eta| < 0.1$, where the muons spectrometers are only partially installed. Primary vertex information is used in the forward region at $|\eta| > 2.5$, where the inner detectors do not cover. Four types of muons pass the reconstruction step, depending on which sub-detectors are used:

Combined muons: Inner detector track + Muon spectrometer track When a muon spectrometer track is matched to an inner detector track, a global re-fit is performed to reconstruct a combined muon.

Segment-tagged muons: Inner detector track + Muon spectrometer segment A segment-tagged muon is reconstructed when an inner detector track matches with an MDT or CSC segment. The muon segment, described in Section 4.2.4, only requires several hits in the same muon station. The segment-tagged muons can be used to efficiently reconstruct muons in the regions where the muon detectors does not fully cover. The momentum of the segment-tagged muons is taken from the inner detector track.

Calorimeter-tagged muons: Inner detector track + Topo cluster An inner detector track assisted by calorimeter energy deposit compatible with minimum-ionizing particle is identified as calorimeter-tagged muons. This type of muon is used to recover efficiencies at the $|\eta| < 0.1$ region, where the coverage by the muon spectrometers is limited.

Standalone muons: Muon spectrometer track + Primary Vertex The muon spectrometer tracks which are extrapolated to the interaction point are reconstructed as standalone muons. The standalone muons are used to recover acceptance in the $2.5 < |\eta| < 2.7$ region, where the inner detectors do not cover.

4.5.2 Muon identification

The reconstructed muons are further required to pass a set of quality cuts to reduce contribution from the backgrounds. Here, the backgrounds are defined as K or π meson decaying in-flight into muons, whereas muons from heavy-flavor decays are not regarded as backgrounds. The background muons are characterized by significant difference in the momentum measured in the inner detectors and the muon spectrometer. Five muon identification working points are defined [112]: *Loose*, *Medium*, *Tight*, *LowPt* and *HighPt*.

All the muons except for the standalone muons at high-η are required to pass quality cuts on the inner detector track, which are:

- at least 1 Pixel hit,
- at least 5 SCT hits, and
- less than 3 Pixel or SCT holes,

to ensure the track quality.

The *Loose*, *Medium* and *Tight* working points [112] are defined by applying cuts on three variables; q/p significance, ρ', and normalized χ^2. The q/p significance is defined as

$$\frac{|(q/p)_{\mathrm{ID}} - (q/p)_{\mathrm{MS}}|}{\sqrt{\sigma^2_{\mathrm{ID}} + \sigma^2_{\mathrm{MS}}}}, \tag{4.3}$$

where q/p is the charge of the muon candidate divided by the momentum of the muon candidate, and σ corresponds to its error. The subscripts show the detector where the variables are measured; ID and MS denotes the inner detectors and the muon spectrometers, respectively. The q/p significance represents the incompatibility of the momentum measurement by the inner detectors and the muon spectrometers, which provides a good separation between the background and signal muons. An upper cut on the q/p significance, $q/p < 7$, is applied to the *Loose* and the *Medium* working working points, while tighter η/p_{T} dependent cuts are applied to the *Tight* working point. The difference between *Loose* and *Medium* is that, while *Medium* only allows combined and standalone muons at high $|\eta|$, *Loose* additionally allows calorimeter-tagged and segment-tagged muons in the $|\eta| < 0.1$ region. For the *Tight* working point, additional cuts are applied on the absolute difference in the p_{T} measured at the inner detectors and the muon spectrometers. The cuts on χ^2 are also applied to the *Tight* muons to reject muons with low fit quality. Figure 4.6 shows the efficiency for the *Medium* muon selection as a function of the p_{T} of the muon.

The *LowPt* and *HighPt* [112] working points are dedicated to specific p_{T} regions. The *LowPt* working point is a multi-variate identification that makes use of additional variables with separation power at low-p_{T}, discussed in Chapter 5. The *HighPt* working point aims to reject high-p_{T} muons with poor momentum resolution due to detector ununiformity or bad alignment resolution of the muon spectrometers.

4.5.3 Muon isolation

The muon isolation criteria are defined in a similar way as for the electrons. Scalar sum of the E_{T} of the topo-clusters or the p_{T} of the tracks around the muon are used to define the isolation working points. The

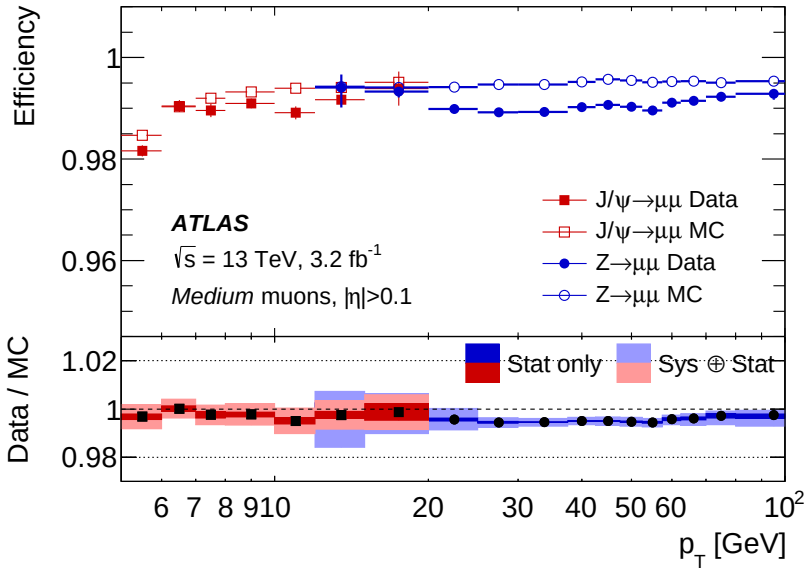

Figure 4.6: Identification efficiency for the *Medium* muon selection as a function of the p_{T} of the muon, in the region $0.1 < |\eta| < 2.5$ as obtained with the $Z \to \mu\mu$ and $J/\psi \to \mu\mu$ events [112]. The error bars on the efficiencies indicate the statistical uncertainty. The panel at the bottom shows the ratio of the measured to predicted efficiencies, with statistical and systematic uncertainties.

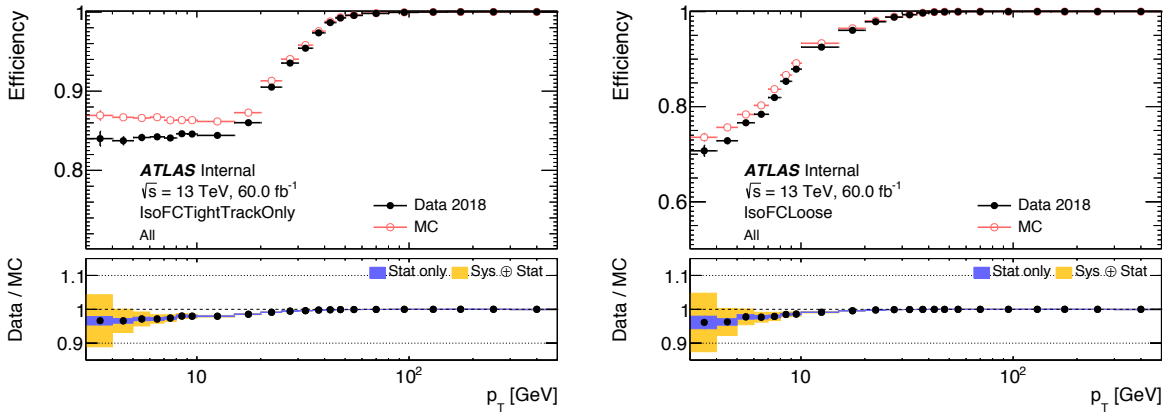

Figure 4.7: Muon isolation efficiency as a function of p_{T} for the *FCTightTrackOnly* (left) and *FCLoose* (right) working points, measured using the $Z \to \mu\mu$ events in 2018 data. Data/MC ratio is shown in the bottom panels.

definition of the isolation variables and the working points are explained in Section 5.2. The efficiencies for the *FCTightTrackOnly* and *FCLoose* working points are shown in Figure 4.7.

4.5.4 Muon calibration

The muon reconstruction and identification efficiencies are measured using the $J/\psi \to \mu\mu$ events for low-p_{T}, and the $Z \to \mu\mu$ events for high-p_{T}. The isolation efficiencies are measured using the $Z \to \mu\mu$ process over the whole p_{T} range. The efficiencies are measured using the tag-and-probe method both in

the data and MC, and are compared to check the MC modeling. Data/MC ratio is shown in the bottom panel of each plot in Figure 4.6 and Figure 4.7. A mis-modeling of a few % is observed in low-p_{T} muons, which are corrected by applying a p_{T}-dependent scale factor on the MC events.

4.6 Photons

Topo-clusters that do not match to any track are reconstructed as photons. The reconstructed photons that pass cuts on the shower-shape are identified as baseline photons and are used in the analyses. In this thesis, baseline photons are required to have p_{T} >25 GeV and pass the *Tight* identification criteria defined in Ref. [128]. Photons are not explicitly used to define signal regions, but are included in the calculation of the $E_{\mathrm{T}}^{\mathrm{miss}}$, as explained in Section 4.8.

4.7 Overlap removal

Reconstruction steps for jets, electrons and muons proceed independently, thus a single particle may be reconstructed as two or more objects at the same time. For example, an electron can create a topo-cluster with sufficient energy and can be reconstructed as a jet. Ambiguities between the objects are resolved by a dedicated procedure called "overlap removal".

The overlap removal resolves the ambiguity of two objects when both objects share a common low-level object or are within a certain distance. In the latter case, ΔR between the objects is used. The first step is to resolve overlaps between two leptons. Electrons that share an inner detector track with a muon candidate are discarded to remove bremsstrahlung from muons followed by a photon conversion, reconstructed as electrons. The next step is to resolve overlaps between a lepton and a jet. We need to efficiently collect leptons by removing jets that overlap with leptons, but at the same time, need to suppress non-prompt leptons from heavy-flavor hadron decays. For this purpose, reconstructed jets that less likely originate from heavy-flavor decays are given lower priority than the lepton candidates. Non-b-tagged jets that are within $\Delta R < 0.2$ from the electrons are removed. Jets with fewer than three tracks with $p_{\mathrm{T}} > 500$ MeV and are with $\Delta R < 0.4$ from a muon candidate are also removed to suppress the muon bremsstrahlung. Finally, electrons or muons within $\Delta R < 0.4$ from the remaining jet candidates are removed to suppress leptons from b- and c- hadron decays to be reconstructed as leptons.

4.8 Missing Transverse Energy

The missing transverse momentum $\mathbf{p}_{\mathrm{T}}^{\mathrm{miss}}$, with the magnitude $E_{\mathrm{T}}^{\mathrm{miss}}$, is defined as the negative vector sum of the transverse momenta of all the baseline objects (electrons, muons, jets, and photons) and an additional "soft term" [129]. Corrected and calibrated four-momentum of the objects after the overlap removal are used to calculate the $E_{\mathrm{T}}^{\mathrm{miss}}$. The soft term is constructed from all the tracks that are not associated with any lepton or jet, but that are associated with the primary vertex. The tracks are required to pass $p_{\mathrm{T}} > 400$ MeV, $|\eta| < 2.5$, $d_0/\sigma(d_0) < 2$, $|z_0 \sin\theta| < 3.0$ mm and some cuts on the track quality to remove high-p_{T} tracks with worse p_{T} resolution.

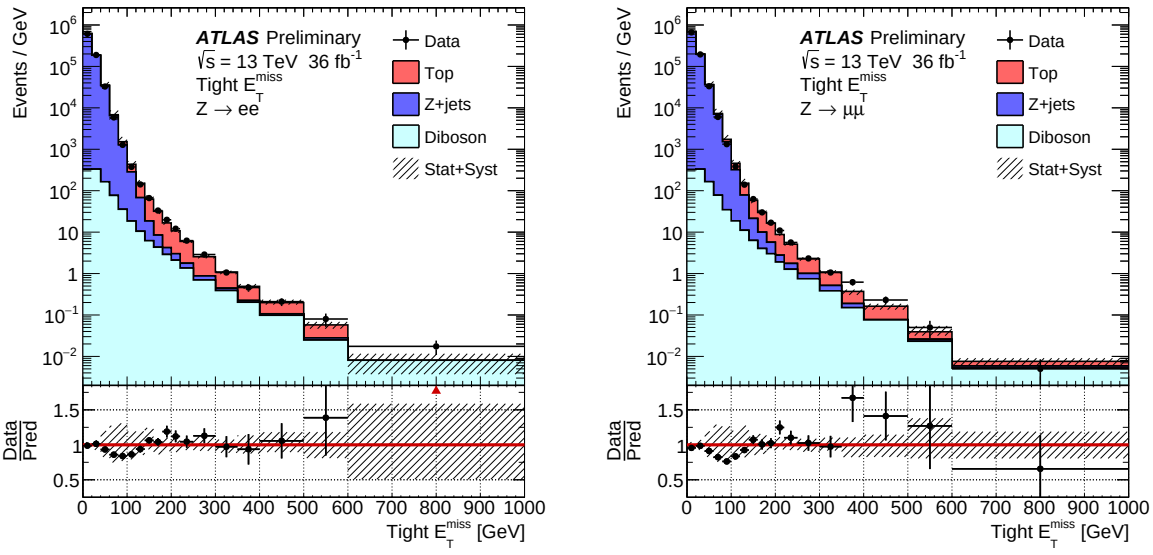

Figure 4.8: Distributions of the Tight working point of the EM-topo $E_{\mathrm{T}}^{\mathrm{miss}}$ in data and MC for events satisfying $Z \to ee$ (left) or $Z \to \mu\mu$ (right) selections. The lower panels of the figures show the ratio of data to MC simulation, and the bands correspond to the sum of the systematic and MC statistical uncertainties. The far right bin includes the integral of all events with $E_{\mathrm{T}}^{\mathrm{miss}}$ above 600 GeV. [129]

There are *Loose* and *Tight* working points [129] defined for the $E_{\mathrm{T}}^{\mathrm{miss}}$, based on the selections applied to the jets included in the calculation. The *Loose* working point uses all the jets with $p_{\mathrm{T}} > 20$ GeV that pass the jet vertex tagger criteria when the jet has $|\eta| < 2.4$ and $p_{\mathrm{T}} < 60$ GeV. The *Tight* working point removes the forward jets with $|\eta| > 2.4$ and $20 < p_{\mathrm{T}} < 30$ GeV, to reduce pileup dependence of the $E_{\mathrm{T}}^{\mathrm{miss}}$. Figure 4.8 shows the reconstructed *Tight* $E_{\mathrm{T}}^{\mathrm{miss}}$ distribution in the $Z \to \ell\ell$ selections, compared between the data and MC.

4.9 Tracks as physics object

Signal regions based on one lepton and an isolated low-p_{T} track (details in Section 6.5) are used to increase the efficiency for the signals with small mass splittings where the p_{T} of the leptons becomes low. For these regions the track is regarded as a physics object. There are no official working points defined for tracks as physics object, thus we defined a set of criteria to select tracks that are likely from a prompt lepton with very low-p_{T}.

The tracks are required to be matched to a reconstructed electron or muon candidate with no identification requirements, including the calorimeter-tagged and segment-tagged muons described in Section 4.5. Additional cuts on the p_{T}/η of the tracks and the quality of the matched leptons are applied, to define baseline and signal tracks. The definitions of the baseline and signal tracks used in this thesis are explained in Section 4.10.

4.10 Object definition in the analysis

Jets are required to have $p_{\mathrm{T}} > 20$ GeV, after all the calibration steps explained in the previous sections are applied. To suppress the pile-up jets, they are required to pass the *Medium* [130] working point of the jet vertex tagger for jets with $p_{\mathrm{T}} < 120$ GeV and $|\eta| < 2.5$, and the *Loose* [120] working point of the forward jet vertex tagger for jets with $p_{\mathrm{T}} < 50$ GeV and $|\eta| > 2.5$. Jets passing all the requirements above are accepted as the baseline jets. The signal jets are required to satisfy $p_{\mathrm{T}} > 30$ GeV and $|\eta| < 2.8$.

b-tagged jets are required to pass baseline jet selections, and additionally to pass $|\eta| < 2.5$ and b-tagging cuts. The *MV2c10* algorithm is used for the b-tagging. A working point with an 85% efficiency for b-hadron jets is selected, with rejection factors of 3 for charm-quark jets and 34 for light-quark and gluon jets.

Electrons are required to have $p_{\mathrm{T}} > 4.5$ GeV and $|\eta| < 2.47$. The baseline electrons are required to pass the *VeryLoose* likelihood identification, and the $|z_0 \sin\theta| < 0.5$ mm cut. The signal electrons are required to pass the *Medium* identification and the $|d_0|/\sigma(d_0) < 5$ cut, where $\sigma(d_0)$ is the error of the transverse impact parameter. The signal electrons are further required to pass the *Gradient* isolation working point to reject contributions from the background electrons.

Muons are required to satisfy $p_{\mathrm{T}} > 3$ GeV and $|\eta| < 2.5$. The preselected muons are identified using the *LowPt* identification [112], which is explained in Section 5.2. The preselected muons must also satisfy $|z_0 \sin\theta| < 0.5$ mm to suppress contribution from pile-up. The signal muons are required to pass the $|d_0|/\sigma(d_0) < 3$ cut, to suppress non-prompt muons from heavy-flavor hadron decays. Finally, the signal muons are required to pass the *FCTightTrackOnly* isolation working point [112], which uses only the tracking information.

The baseline tracks are required to pass $p_{\mathrm{T}} > 500$ MeV, $|\eta| < 2.5$ and to pass the *Tight-Primary* working point defined in Ref. [131]. Signal tracks are required to be within $\Delta R < 0.01$ from a reconstructed electron or muon candidate. The matched electron (muon) candidates can be reconstructed with p_{T} as low as 1 (2) GeV, and are required to "fail" the signal lepton requirements defined above to avoid any overlap. The p_{T} of the signal tracks are required to match with the p_{T} of the matched lepton within 20%. The signal tracks must also satisfy dedicated isolation criteria: they are required to be separated from the preselected jets by $\Delta R > 0.5$, and the $\sum p_{\mathrm{T}}$ of the preselected tracks within $\Delta R < 0.3$ from signal tracks is required to be smaller than 0.5 GeV. Finally, the signal tracks must satisfy $p_{\mathrm{T}} > 1$ GeV, $|z_0 \sin\theta| < 0.5$ mm and $|d_0|/\sigma(d_0) < 3$.

After the overlap removal is applied, the $E_{\mathrm{T}}^{\mathrm{miss}}$ is reconstructed using all the baseline objects and reconstructed photons. The *Tight* $E_{\mathrm{T}}^{\mathrm{miss}}$ working point is selected in this analysis, to suppress the pile-up dependence.

The efficiency for the signal electrons and muons in the signal samples is shown in Figure 4.9 as a function of lepton p_{T}. The efficiency for reconstructing and identifying the signal electrons in the signal samples ranges from 20% for $p_{\mathrm{T}} = 4.5$ GeV to over 75% for $p_{\mathrm{T}} > 30$ GeV. The corresponding efficiency for the signal muons ranges from approximately 50% at $p_{\mathrm{T}} = 3$ GeV to 90% for $p_{\mathrm{T}} > 30$ GeV.

Table 4.1 summarizes the object definitions used in the analysis presented in this thesis.

Table 4.1: Summary of object definitions in this analysis. Requirements for baseline objects are also applied to signal objects. The $E_{\mathrm{T}}^{\mathrm{miss}}$ is calculated as a negative vector sum of the baseline objects after overlap removal.

Object	**Baseline**	**Signal**
Jets	$p_{\mathrm{T}} > 20$ GeV $\lvert\eta\rvert < 4.0$ pass jet vertex tagger cut [119]	$p_{\mathrm{T}} > 30$ GeV $\lvert\eta\rvert < 2.8$ –
b-tagged Jets	pass Baseline jet requirements $\lvert\eta\rvert < 2.5$ pass *MV2c10* 85% WP [124, 125]	– – –
Electrons	$p_{\mathrm{T}} > 4.5$ GeV $\lvert\eta\rvert < 2.47$ *VeryLoose* ID [127] $\lvert z_0 \sin\theta\rvert < 0.5$ mm – –	– – *Medium* ID [127] – $d_0/\sigma_{d_0} < 5$ *Gradient* isolation [127]
Muons	$p_{\mathrm{T}} > 3.0$ GeV $\lvert\eta\rvert < 2.5$ *LowPt* ID $\lvert z_0 \sin\theta\rvert < 0.5$ mm – –	– – – – $d_0/\sigma_{d_0} < 3$ *FCTightTrackOnly* isolation [112]
Photons	$p_{\mathrm{T}} > 25$ GeV *Tight* ID [128]	– –
Tracks	matched to a lepton $p_{\mathrm{T}} > 500$ MeV $\eta < 2.5$ *Tight-Primary* [131] – – –	– $p_{\mathrm{T}} > 1$ GeV – – pass custom isolation $\lvert z_0 \sin\theta\rvert < 0.5$ mm $d_0/\sigma_{d_0} < 3$
$E_{\mathrm{T}}^{\mathrm{miss}}$	Negative vector sum of baseline Jets, Electrons, Muons, Photons and soft term	

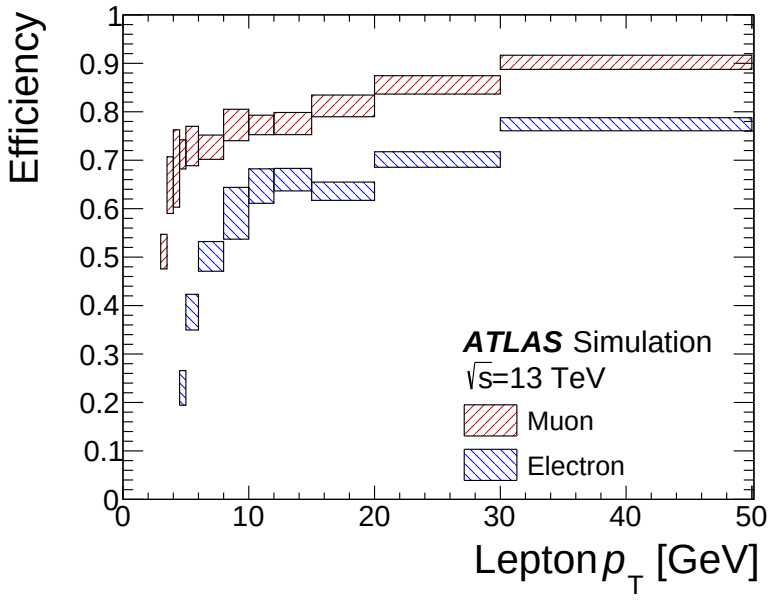

Figure 4.9: Efficiencies for electrons and muons in signal samples. Combined reconstruction, identification, isolation and vertex association efficiencies are included here. Uncertainty bands represent the range of efficiencies observed across all signal samples used for the given p_{T} bin.

Chapter 5

Low-p_{T} lepton reconstruction

The most challenging part of this analysis is to efficiently collect low-p_{T} leptons. It is also important to control the contribution from the fake or non-prompt leptons passing the signal criteria. In this chapter, several new methods used in this analysis to obtain higher efficiency for the low-p_{T} leptons are discussed. A dedicated identification technique for low-p_{T} muons is introduced in Section 5.1. In Section 5.2, a new multi-variate isolation technique called "Prompt Lepton Tagging" is explained. Optimization studies of the Prompt Lepton Tagging for the low-p_{T} leptons are also discussed. In Section 5.3, a special correction method is presented for two leptons reconstructed close to each other.

5.1 Muon identification at low-p_{T}

As described in Section 4.5.2, the goal of the muon identification is to efficiently collect the muon candidates with high rejecting power against the "fake" backgrounds. The fake backgrounds considered at the muon identification stage are K/π hadrons that decay in-flight. Non-prompt muons from b/c hadrons are produced before the first layer of the inner detector, and are considered as signal muons at this stage. The muon identification is performed by applying cuts on several low-level objects. The most important cut for the muon identification is the q/p significance cut, which imposes an upper limit on the q/p significance defined in Eq. 4.3. The upper cut value used for the *Medium* working point is selected to have a high efficiency for muons with p_{T} larger than 10 GeV, and to reject the fake background considerably.

For muons with p_{T} smaller than 5 GeV, the cut on the q/p significance is not as efficient as for muons with high-p_{T}. This is because the low-p_{T} muons deposit relatively more energy in the calorimeter compared to the high-p_{T} muons. This makes a significant difference between the momentum measured at the inner detectors and the muon spectrometers, and leads the low-p_{T} muon to failing the q/p significance cut. In the end-cap region ($1.55 > |\eta|$), however, the efficiency loss is not very large because muons are boosted in the longitudinal direction, and this gives sufficiently high momentum to the muons. The efficiency loss is only apparent in the barrel ($|\eta| < 1.3$) and transition ($1.3 < |\eta| < 1.55$) regions, where the absolute momentum of the muon is close to the transverse momentum. The idea of the *LowPt* identification is to replace the q/p significance cut with other cuts, to obtain a reasonably high efficiency for the muon identification down to a p_{T} of 3 GeV. An additional variable that takes into account the energy deposit in the calorimeter, as well as variables to identify the kink in the trajectory made by a hadron decay in-flight to a muon, are used to in the *LowPt* identification definition.

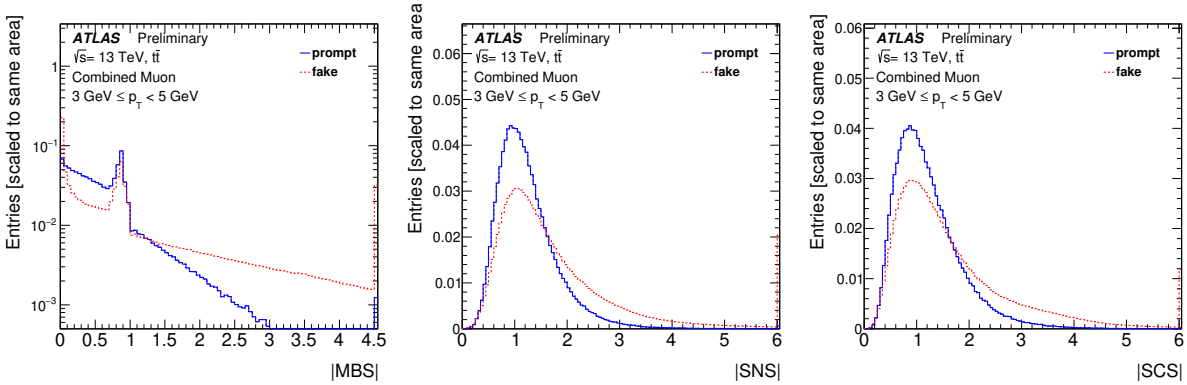

Figure 5.1: Distributions of the MBS (left), SNS (center) and SCS (right) in $t\bar{t}$ events, for tracks associated to the prompt muons (blue) and to the fake leptons (red) with 3 GeV $< p_{\mathrm{T}} <$ 5 GeV [132]. The definition of each variable is given in the text.

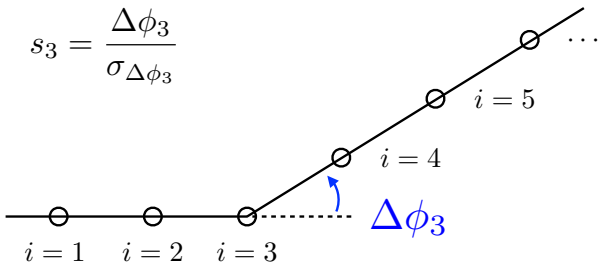

Figure 5.2: Schematic diagram showing the definition of the scattering significance. The scattering significance at 3rd hit point is defined by $\frac{\Delta\phi_3}{\sigma_{\Delta\phi_3}}$, where $\Delta\phi_3$ is the scattering angle obtained by splitting the track into two tracks at the 3rd hit point.

5.1.1 Variables used for the *LowPt* working point

Three variables are selected to define the identification criteria to discriminate the signal muons from the hadron decays. Figure 5.1 shows the distributions of the three variables for the prompt muons and for the muons from hadron decays (fakes) in simulated $t\bar{t}$ events.

The momentum balance significance (MBS) is defined as the difference between the momentum measured in the inner detectors and the muon spectrometers, divided by the uncertainty on expected energy loss in the calorimeter system. For the prompt muons, the difference of the momentum in the inner detector and the muon spectrometers mainly comes from the energy loss in the calorimeters and thus are within the uncertainty on the expected energy loss in the calorimeter. For the fake muons, however, the difference in the momentum measurements is enhanced by the decay of the hadrons, which lead to longer tail in the distribution.

The scattering neighbor significance (SNS) and the scattering curvature significance (SCS) are designed to identify significant changes in the trajectory (kinks) along the track, which are expected for the fake leptons. The kink is identified by re-fitting the track assuming that it can be divided into two track

components. Figure 5.2 shows a schematic diagram illustrating this procedure. A track, with N hits in the inner detectors or muon spectrometers, is first split into two half-tracks at i-th hit point. In Figure 5.2, $i = 3$ is chosen for demonstration. The two tracks are re-fitted using only the $[1, \cdots i]$-th hits and $[i, \cdots N]$-th hits. In the figure, the two half-tracks are fit with two straight trajectories. The scattering angle at i-th hit point $\Delta\phi_i$ is computed by the angle difference of the two half-tracks. The significance of the scattering angle, s_i, is defined as

$$s_i = \frac{\Delta\phi_i}{\sigma_{\Delta\phi_i}}, \tag{5.1}$$

where $\sigma_{\Delta\phi_i}$ is the uncertainty of the scattering angle.

The scattering neighbor significance (SNS) is defined by

$$SNS = \arg\max_k \frac{1}{\sqrt{k}} \left| \sum_{i=1}^{k} s_i \right|, \tag{5.2}$$

which corresponds to the largest significance of the scattering angle obtained over the whole track. When the track is consistent with no kink, then a small SNS value is obtained. When the track has a kink at i-th hit, then a large significance s_i will be obtained, which results in large SNS value.

The scattering curvature significance (SCS) is define by

$$SCS = \arg\max_k \frac{1}{\sqrt{N}} \left| \sum_{i=1}^{k} s_i - \sum_{i=k+1}^{N} s_i \right|, \tag{5.3}$$

computed as the normalized sum of the significance of the scattering angle. The minus sign in the second term allows to identify multiple kinks in different direction.

5.1.2 *LowPt* working point definition

Low-p_{T} muons deposit about a few GeV of energy in the calorimeter, before reaching the muon spectrometer. When we consider muons with $p_{\mathrm{T}} \lesssim 5$ GeV, the energy loss is comparable to the energy of the muons in the barrel region, thus the muons are expected to have very low momentum at the muon spectrometer. In the endcap region, the muons receive Lorentz boost in the z direction and can have considerably high momentum. The *LowPt* working points require different selections depending on the η region of the detector, to account for this difference.

The *LowPt* working point only considers the combined muons, which is reconstructed using both the inner detector tracks and the muon spectrometer tracks. For $|\eta| < 1.3$, only one hit in the muon spectrometer station is required in the combined muon track, whereas for $1.3 < |\eta| < 1.55$, at least two muon spectrometer stations are required. This is because in the transition region $1.3 < |\eta| < 1.55$, the muons receive sufficient Lorentz boost to reach the second layer of the muon spectrometer, thus the additional requirement is efficient for signal muons. For $|\eta| > 1.55$, the *Medium* working point requirements are applied because the q/p significance cut is valid in this region. Loose cuts on the variables defined in the previous section are applied in all the detector regions to suppress the fakes: |MBS| < 3.0, |SNS| < 3.0 and |SCS| < 3.0.

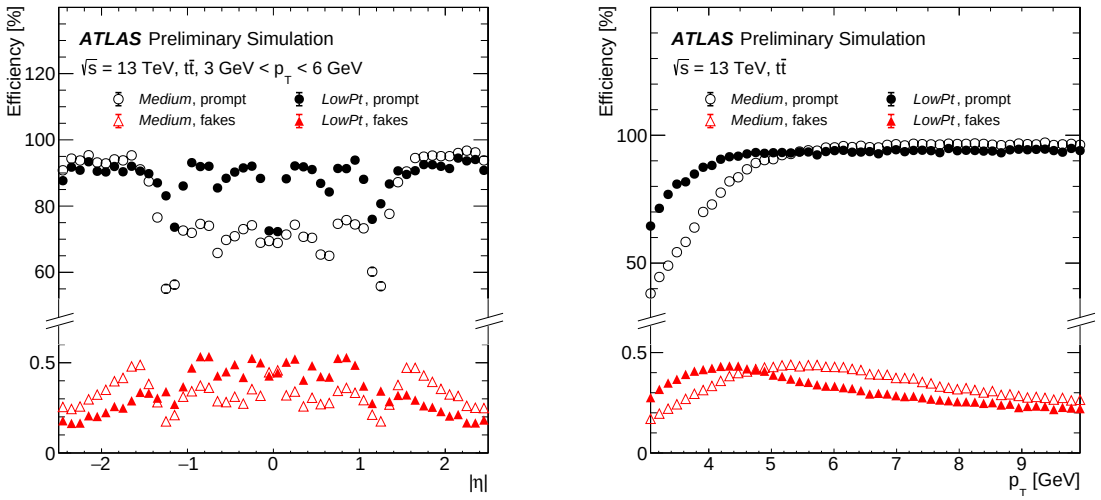

Figure 5.3: Expected efficiency as a function of (a) η and (b) p_{T} fulfilling the *Low-*p_T (filled markers) and *Medium* (empty markers) requirements in simulated $t\bar{t}$ events. The black markers show the efficiencies for the prompt leptons, and the red markers show the efficiencies for the fake muons.

5.1.3 *LowPt* working point performance

The expected efficiencies for the prompt and fake muons to pass the *LowPt* working point are shown as a function of the track η and p_{T} in Figure 5.3. The efficiencies are measured using $t\bar{t}$ MC events. The *LowPt* working point recovers the efficiencies for muons in the barrel and transition regions by about 20%, at a cost of increased mis-identification rate by about 40% compared to the *Medium* working point. In the endcap region, the fake rate is suppressed by the about 30%, with a few percent loss of efficiency. As a whole, the prompt lepton efficiency at low-p_{T} increase from 40% to 65%, with about 50% increase in the fake rate. Note that the fake rate can be further suppressed by the isolation requirements, and thus the increase in the fake rate does not proportionally increase the number of the background in the analysis.

5.2 Prompt Lepton Tagging

5.2.1 Overview

The background leptons that pass the lepton identification are categorized into two groups, "fake" and "non-prompt". The fake lepton background is from other particles identified as leptons. For electrons, the fake leptons mainly come from π-mesons mis-identified as electrons, or photons converted into two electrons in the detector material, which are reconstructed as one electron ("photon conversion"). For muons, the fake leptons are mainly caused by π/K decaying in-flight into muons. The non-prompt leptons are those made in semi-leptonic decays of heavy hadrons that are mis-identified as prompt leptons. To correctly identify electrons and muons from the prompt decays, i.e. from W or Z boson decays, we require the leptons to be isolated. The basic idea of the isolation is to require that there are few or no other particles observed close to the lepton.

Table 5.1: Definitions of the conventional isolation variables. All the variables are calculated by the scalar sum of the tracks or clusters that passes the selection in the second column.

Variable name	Track/Cluster selection	Description
$p_{\mathrm{T}}^{\mathrm{varcone20}}$	Track $p_{\mathrm{T}} > 1$ GeV, $\Delta R_{\ell\mathrm{track}} < \min(0.2, 10/p_{\mathrm{T}}\ [\mathrm{GeV}])$	Scalar sum of track p_{T}
$p_{\mathrm{T}}^{\mathrm{varcone30}}$	Track $p_{\mathrm{T}} > 1$ GeV, $\Delta R_{\ell\mathrm{track}} < \min(0.3, 10/p_{\mathrm{T}}\ [\mathrm{GeV}])$	Scalar sum of track p_{T}
$p_{\mathrm{T}}^{\mathrm{varcone20,TightTTVA}}$	$p_{\mathrm{T}}^{\mathrm{varcone20}}$ + tighter track-to-vertex association	Scalar sum of track p_{T}
$p_{\mathrm{T}}^{\mathrm{varcone30,TightTTVA}}$	$p_{\mathrm{T}}^{\mathrm{varcone30}}$ + tighter track-to-vertex association	Scalar sum of track p_{T}
$E_{\mathrm{T}}^{\mathrm{topocone20}}$	Topo-clusters, $\Delta R_{\ell\mathrm{cluster}} < 0.2$	Scalar sum of cluster E_{T}

Table 5.2: Definitions of some of the conventional isolation working points. For the *FCTightTrackOnly* working point, only the track isolation selection is applied, and for all the other working points, both the track and calorimeter isolation selections are applied.

Working point name	flavor	Track isolation	Calorimeter isolation
FCTightTrackOnly	muon	$p_{\mathrm{T}}^{\mathrm{varcone30,TightTTVA}}/p_{\mathrm{T}} < 0.06$	–
FCLoose	electron	$p_{\mathrm{T}}^{\mathrm{varcone20,TightTTVA}}/p_{\mathrm{T}} < 0.15$	$E_{\mathrm{T}}^{\mathrm{topocone20}}/p_{\mathrm{T}} < 0.2$
	muon	$p_{\mathrm{T}}^{\mathrm{varcone30,TightTTVA}}/p_{\mathrm{T}} < 0.15$	$E_{\mathrm{T}}^{\mathrm{topocone20}}/p_{\mathrm{T}} < 0.3$
FCTight	electron	$p_{\mathrm{T}}^{\mathrm{varcone20,TightTTVA}}/p_{\mathrm{T}} < 0.06$	$E_{\mathrm{T}}^{\mathrm{topocone20}}/p_{\mathrm{T}} < 0.06$
	muon	$p_{\mathrm{T}}^{\mathrm{varcone30,TightTTVA}}/p_{\mathrm{T}} < 0.04$	$E_{\mathrm{T}}^{\mathrm{topocone20}}/p_{\mathrm{T}} < 0.15$
Gradient	electron	p_{T}-dependent $p_{\mathrm{T}}^{\mathrm{varcone20}}$ cut, $\epsilon = (0.1143 \times p_{\mathrm{T}}[\mathrm{GeV}] + 92.14)\%$	p_{T}-dependent $E_{\mathrm{T}}^{\mathrm{topocone20}}$ cut, $\epsilon = (0.1143 \times p_{\mathrm{T}}[\mathrm{GeV}] + 92.14)\%$

The isolation requirement reduces the fake/non-prompt backgrounds dramatically, but at the same time lose some fraction of the prompt leptons especially when their p_{T} is small. In the conventional isolation, $p_{\mathrm{T}}^{\mathrm{cone}}/E_{\mathrm{T}}^{\mathrm{topocone}}$ variables are calculated by adding up $p_{\mathrm{T}}/E_{\mathrm{T}}$ of the tracks/clusters within a certain distance from the lepton. These variables are collectively called "isolation variables" or "cone variables", and are used to estimate the activity around the lepton. Some of the mostly used isolation variables are summarized in Table 5.1. In addition to the cuts on the distance from the lepton, tracks are required to be associated to the same vertex as the lepton. Several cuts on the isolation variables are combined to define an "isolation working point". A list of typical isolation working points considered in this analysis is shown in Table 5.2.

A major challenging point in the low-p_{T} lepton isolation is that the p_{T} of the lepton candidate itself becomes comparable with the isolation variables, due to the $p_{\mathrm{T}}/E_{\mathrm{T}}$ thresholds applied to the tracks or topo-clusters. This is problematic because it is more difficult for low-p_{T} prompt leptons to pass the isolation requirements. For example, the cone variables for the track isolation are calculated by adding up tracks with p_{T} larger than 1 GeV, thus they always have values larger than 1 GeV if there are any single track found within the cone. If we consider the *FCTightTrackOnly* isolation for muons, $p_{\mathrm{T}}^{\mathrm{varcone30}}/p_{\mathrm{T}}$ must be smaller than 0.06 in order for the lepton to pass this isolation requirement. Muons with p_{T} smaller than 16.7 GeV automatically fail the isolation selection if there are any single track found within the $dR < 0.3$ cone, because the $p_{\mathrm{T}}^{\mathrm{varcone30}}/p_{\mathrm{T}}$ value become larger than 0.06 regardless of the p_{T} of the track. This makes the *FCTightTrackOnly* isolation selection essentially a binary selection, and as a result the prompt lepton efficiency tends to degrade ending up in $70 - 80\%$. The inefficiency can be partially recovered by lowering the threshold for the tracks or topo-clusters, but currently that is difficult because it would cost a huge

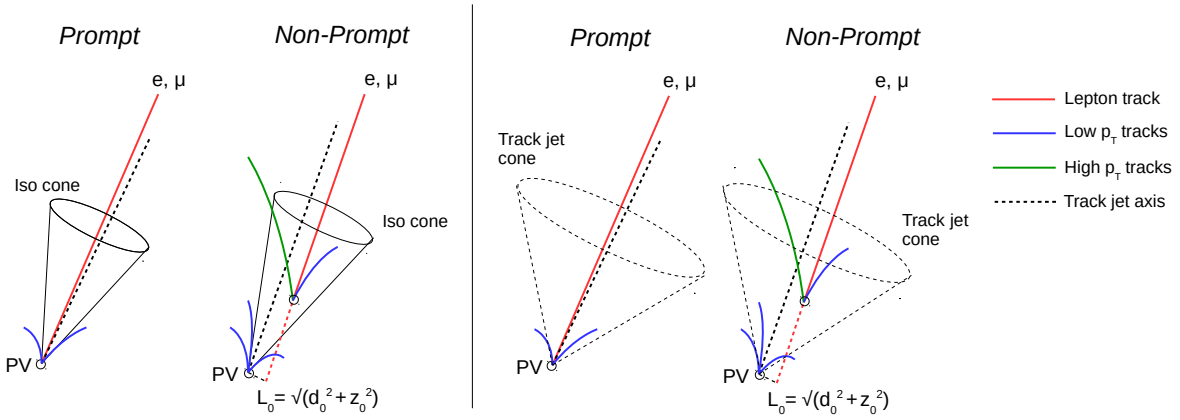

Figure 5.4: A schematic diagram of prompt and non-prompt leptons, for isolation based on cone variables (left) and Prompt Lepton Tagging (right). The red line in each diagram shows the track of the lepton. The blue lines show the low-p_{T} tracks that are below the threshold of the track reconstruction. The green lines show high-p_{T} tracks from the parent jet of the non-prompt leptons. The d_0 and z_0 correspond to the transverse and longitudinal impact parameters respectively, with L_0 corresponding to the secondary vertex decay length from the primary vertex (PV). In the left diagram, only the scalar sum of the tracks around the lepton is used. In the right diagram, the angular distance between the background tracks and the lepton, as well as the information of the impact parameters are available.

amount of computing power due the number of low-p_{T} tracks/clusters, and also because the modeling of contribution by the low-p_{T} particles in MC is generally difficult.

To recover the prompt lepton efficiency while keeping the fake and non-prompt rejection at a decent level, a new isolation criteria has been developed using the "Prompt Lepton Tagging" (PLT) method. The Prompt Lepton Tagging is a multi-variate tagger optimized to reject fake or non-prompt leptons. The goal is to get more detailed information of the particles around the leptons, rather than only using the isolation variables, which are simply the scalar sums of $p_{\mathrm{T}}/E_{\mathrm{T}}$ of the particles.

We use track-jets to exploit these additional information, as shown in Figure 5.4. Track-jets are reconstructed by clustering the tracks matched to the primary vertex, using the anti-k_t algorithm with a radius parameter $R = 0.4$. The reconstructed track-jets contains tracks within $dR < 0.4$ from the jet "axis", which is defined by the vector sum of all the tracks in the track-jet. An important feature is that the track-jets can be formed from a single track. This allows the track-jet closest to a lepton to be the track of the lepton itself, which is expected to happen for the prompt leptons with no extra tracks around. For the fake/non-prompt leptons, however, there is always a parent jet in the event which is usually reconstructed close to the lepton, thus the nearest track-jet is likely to be coming from the parent jet. This makes a large difference in the characteristics and the positional relation between the track-jet and the lepton. An obvious example is that only one track is expected to be included in the track-jet for the prompt leptons, whereas for the non-prompt leptons, the fraction of events with multiple tracks is larger. Another benefit of using the track-jets is that we can apply the b-tagging algorithms on them, which is useful to tag heavy hadron decays.

The Prompt Lepton Tagging is originally developed for high-p_{T} leptons, and is applied in the the $t\bar{t}H$ multi-lepton analysis [133] to reject the non-prompt leptons. In Section 5.2.2, a brief summary of the original Prompt Lepton Tagging is presented. To avoid confusion, we refer to the original Prompt Lepton

Tagging as `HighPtPLT`. A new version of the Prompt Lepton Tagging tuned for low-p_{T} is referred to as `LowPtPLT`, and is discussed in Section 5.2.3.

5.2.2 High-p_{T} Prompt Lepton Tagging

A multi-variate-analysis technique is applied to combine and take advantage of the correlations between the input variables for `HighPtPLT`. The Boosted Decision Tree (BDT) algorithm is selected to analyze these variables. Eight variables are selected as input to the BDT, which are summarized in Table 5.3. Definitions of the variables are explained in the following paragraphs. The distributions of the variables are compared between the prompt and non-prompt leptons in Figures 5.5 and 5.6.

N_{track} The number of tracks included in the track-jet nearest from the lepton, N_{track}, is used as an input variable to the Prompt Lepton Tagging. It has a strong discrimination power because the prompt leptons tend to have only single track in the track-jet, whereas the non-prompt leptons are likely to have more tracks coming from the parent jets.

$p_{\mathrm{T}}(\ell)/p_{\mathrm{T}}(j)$ The ratio of the lepton p_{T} and the p_{T} of the track-jet, $p_{\mathrm{T}}(\ell)/p_{\mathrm{T}}(j)$, is also used as an input variable. The track consisting the lepton is always included in the track-jet. Thus in the case the track-jet only contains single track, this ratio becomes close to 1. For track-jets with multiple tracks, which is expected for the non-prompt leptons, the $p_{\mathrm{T}}(\ell)/p_{\mathrm{T}}(j)$ becomes smaller.

$p_{\mathrm{T}}^{\mathrm{rel}}$, $\Delta R(\ell, j)$ The $p_{\mathrm{T}}^{\mathrm{rel}}$ is the p_{T} of the lepton with respect to the track-jet axis, defined as $p_{\mathrm{T}}(\ell) \times \sin\theta$, where θ is the opening angle between the track-jet axis and the lepton. The $\Delta R(\ell, j)$ is a distance in the $\eta - \phi$ plane between the track-jet axis and the lepton. Both $p_{\mathrm{T}}^{\mathrm{rel}}$ and $\Delta R(\ell, j)$ extract information of the positional relation between the lepton and the track-jet. The non-prompt leptons have longer tail in the distribution, because the extra tracks changes the track-jet axis away from the lepton track.

Cone variables The original cone variables divided by the lepton p_{T}, are also used as input to the BDT. A longer tail in the distribution for the non-prompt leptons comes from extra tracks/clusters from the parent jet.

***b*-tagging variables** Scores of two b-tagging algorithms, RNNIP [134] and DL1mu [134] are used to enhance the performance to reject the non-prompt leptons from heavy-flavor decays. For the RNNIP, the recurrent neural networks (RNN) [135] are used to learn the dependencies in an arbitrary-length "list" of tracks. The tracks in the jet are ordered in the significance of the transverse impact parameter $d_0/\sigma(d_0)$, to form an ordered list of tracks. This list is handed to the RNN, which returns an output score, RNNIP. The RNNIP score corresponds to compatibility of the jet to a b-hadron jet. The DL1mu is based on the Deep Neural Network technique, trained with Keras [136]. Several outputs from "low-level" taggers are used as inputs for the DL1mu algorithm. The output of the DL1mu also provides compatibility of a jet with b-hadron decay hypothesis. The low-level taggers are designed to tag a specific feature of b-jets, such as the impact parameters of the tracks, the secondary vertex, and the existence of the soft muons from hadron

Table 5.3: List of input variables used in the HighPtPLT (nominal Prompt Lepton Tagging).

Variable name	Description
N_{track}	Number of tracks consisting the track-jet.
$p_{\text{T}}(\ell)/p_{\text{T}}(j)$	Ratio of the lepton p_{T} over the track-jet p_{T}.
$p_{\text{T}}^{\text{rel}}$	Lepton p_{T} with respect to the track-jet axis.
$\Delta R(\ell, j)$	ΔR between the lepton and the track-jet axis.
$p_{\text{T}}^{\text{varcone30}}/p_{\text{T}}$	Sum of p_{T} of the tracks within $\Delta R < 0.3$ of the lepton candidate, divided by the lepton p_{T}.
$E_{\text{T}}^{\text{topocone30}}/p_{\text{T}}$	Sum of E_{T} of the topological clusters within $\Delta R < 0.3$ of the lepton candidate, divided by the lepton p_{T}.
RNNIP	Output of the Recurrent Neural Network based IP flavor-tagger [134].
DL1mu	Output of the DL1mu algorithm [137].

Table 5.4: Lepton training selections for the high-p_{T} Prompt Lepton Tagging.

Object	p_T [GeV]	$\lvert\eta\rvert$	identification	$\lvert d_0/\sigma(d_0)\rvert$	$\lvert z_0 \sin\theta\rvert$ [mm]	Isolation
Electron	> 10	< 2.47, < 1.37 *or* > 1.52	*Loose*	< 5	< 0.5	*Loose*
Muon	> 10	< 2.5	*Loose*	< 3	< 0.5	*Loose*

decays. The distributions of the RNNIP and the DL1mu distributions have longer tail for the track-jets matched to the non-prompt leptons.

HighPtPLT is trained using the ROOT Toolkit for Multivariate Data Analysis (TMVA) [138]. Leptons from the $t\bar{t}$ MC are used in the training, and the leptons are required to have $p_{\text{T}} > 10$ GeV. Other selection criteria are summarized in Table 5.4. The track-jet candidates are reconstructed using the anti-kt algorithm with a ΔR of 0.4. The selected jets are required to have $p_{\text{T}} > 10$ GeV and $|\eta| < 2.5$.

The HighPtPLT score distributions at high and low p_{T} are shown in Figure 5.7. The original HighPtPLT score becomes close to -1 for the prompt leptons but in the plots the score is inverted. This is for a comparison between the LowPtPLT score, which are close to 1 for the prompt leptons. The plots on the top show the score distribution for the electrons in $p_{\text{T}} \in [4, 5]$ GeV (left) and $p_{\text{T}} \in [19, 20]$ GeV (right). The plots on the bottom show the score distribution for the muons in $p_{\text{T}} \in [3, 4]$ GeV (left) and $p_{\text{T}} \in [19, 20]$ GeV (right). For both electrons and muons, the separation become worse at low-p_{T} compared to at $p_{\text{T}} \in [19.20]$ GeV. This is because HighPtPLT is trained using leptons with $p_{\text{T}} > 10$ GeV, and the performance is optimized for leptons at this p_{T} range.

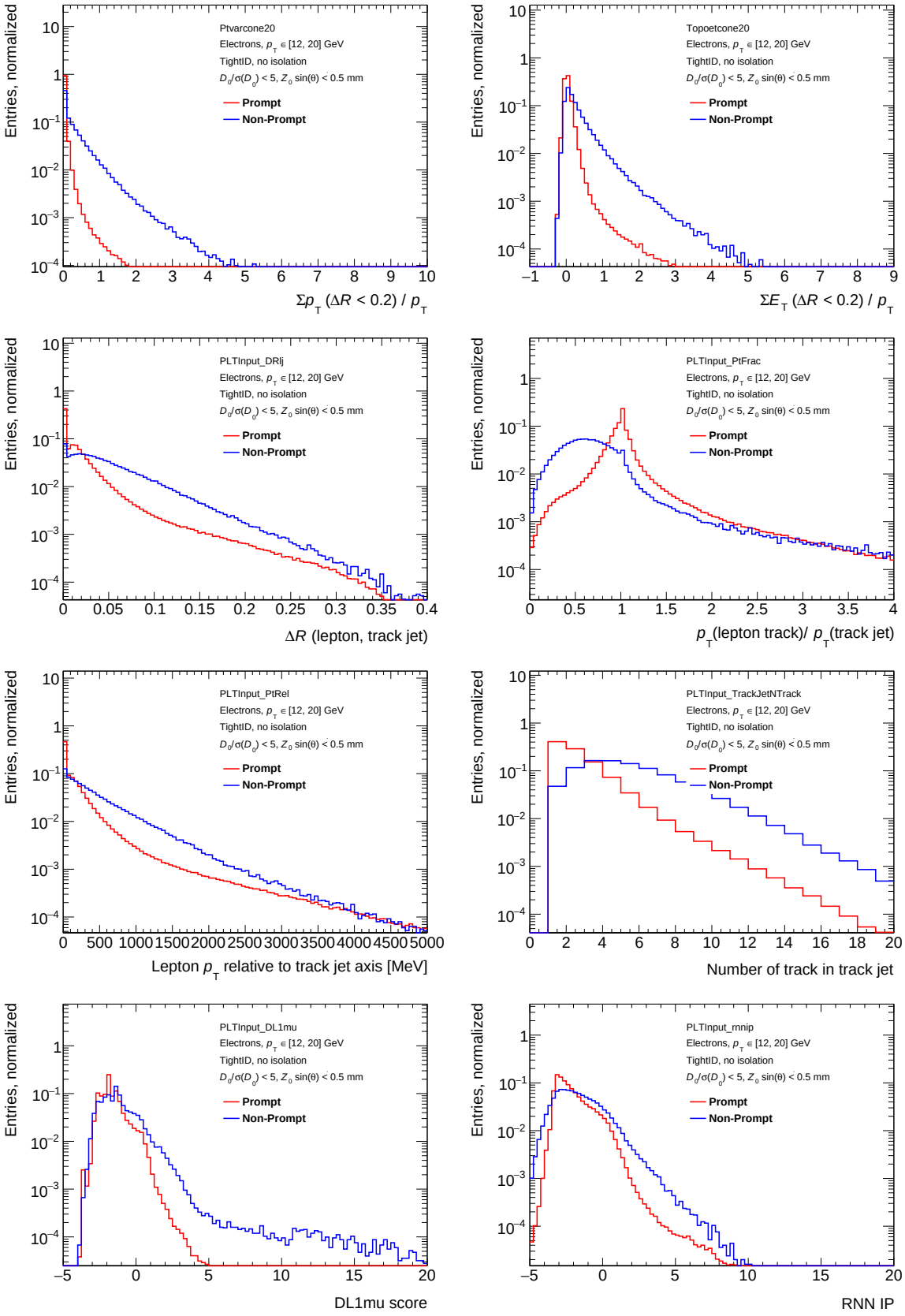

Figure 5.5: Distributions of the input variables to the PLT, for electrons with $p_T \in [12, 20]$ GeV. The red (blue) histograms show the distributions for the prompt (non-prompt) leptons. The distributions are obtained using the $t\bar{t}$ MC. The definition of each variables are explained in the text.

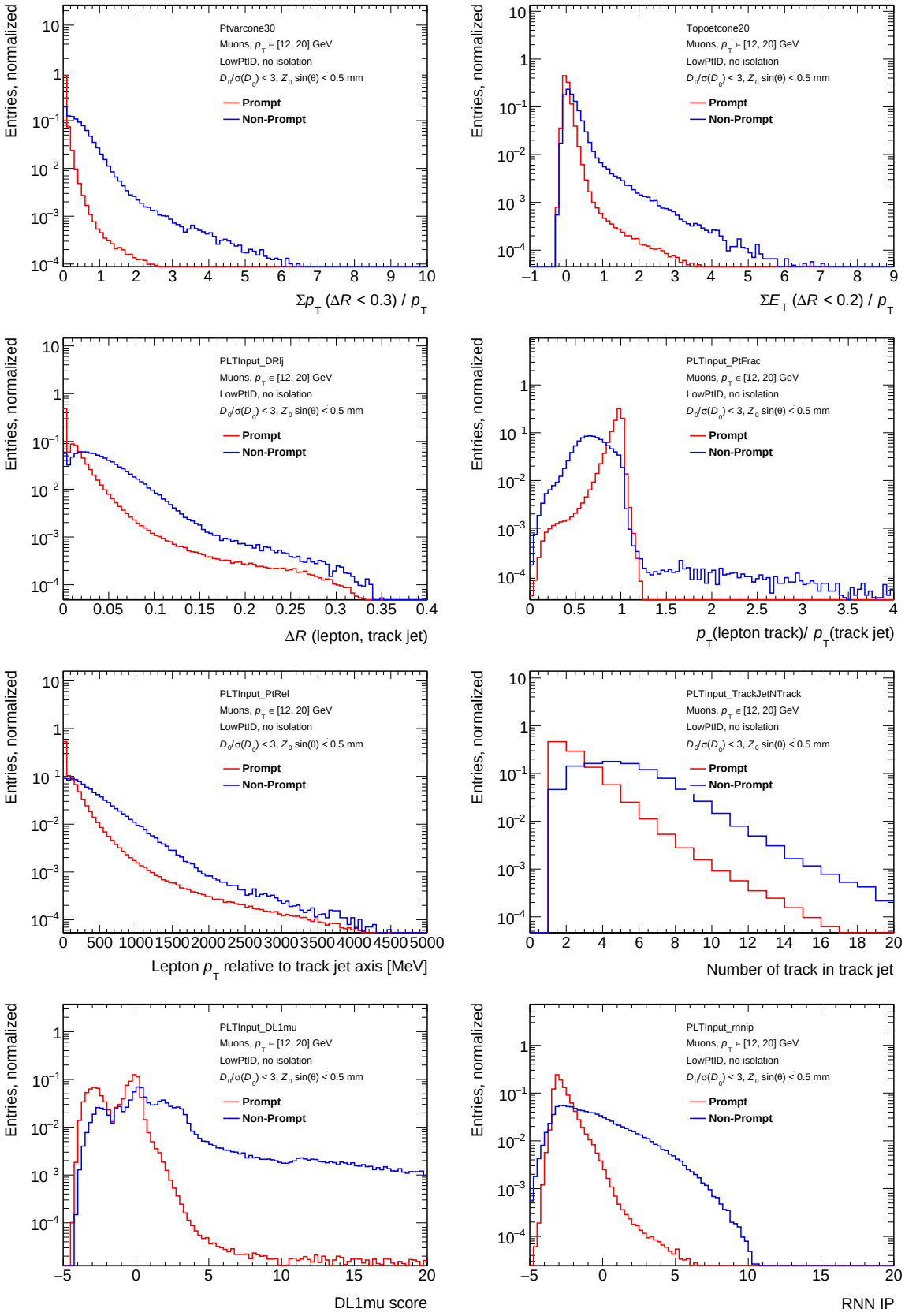

Figure 5.6: Distributions of the input variables to the PLT, for muons with $p_T \in [12, 20]$ GeV. The red (blue) histograms show the distributions for the prompt (non-prompt) leptons. The distributions are obtained using the $t\bar{t}$ MC. The definition of each variables are explained in the text.

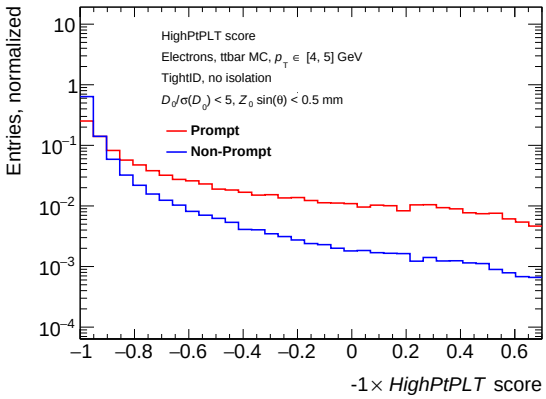

(a) Electrons, $p_{\mathrm{T}} \in [4, 5]$ GeV

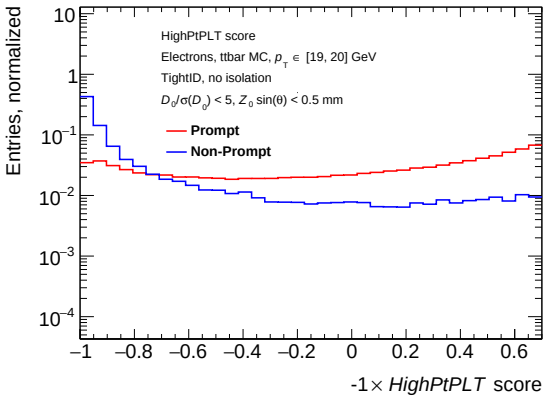

(b) Electrons, $p_{\mathrm{T}} \in [19, 20]$ GeV

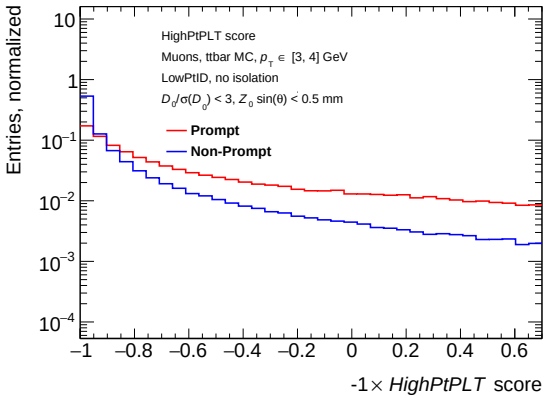

(c) Muons, $p_{\mathrm{T}} \in [3, 4]$ GeV

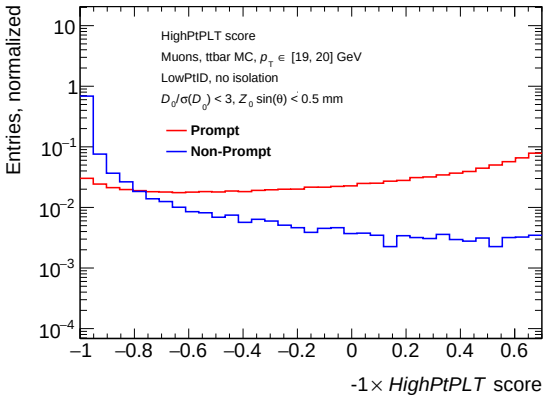

(d) Muons, $p_{\mathrm{T}} \in [19, 20]$ GeV

Figure 5.7: Distribution of the `HighPtPLT` score at low-p_{T} (left) and high-p_{T} (right) for electrons (top) and muons (top). Red histograms show the distributions of prompt leptons, and the blue histograms show the distribution of the fake/non-prompt leptons.

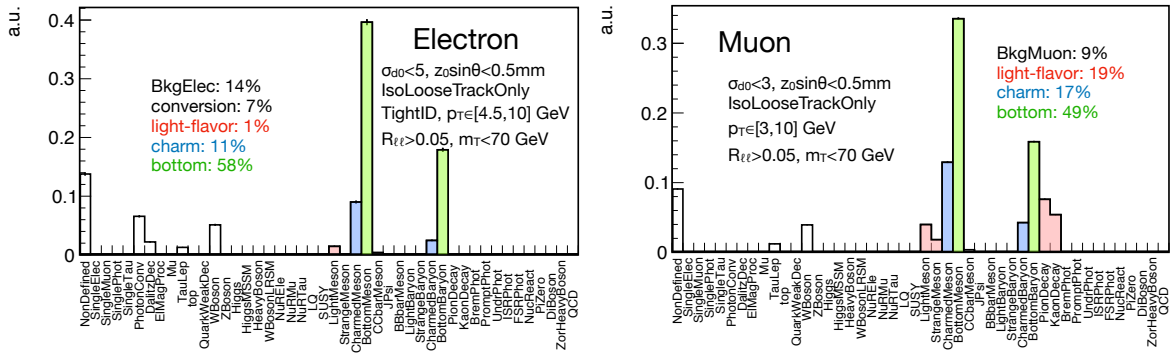

(a) Electrons

(b) Muons

Figure 5.8: Origin of the sub-leading leptons at the MC truth level, with the preselection for W+jets events. The selection cuts in each plot are described on the labels is applied to the events. The green, blue, red and white histograms show the fraction of leptons that originate from b-hadrons, c-hadrons, light-flavor hadrons, and other processes, respectively.

5.2.3 Low-p_{T} Prompt Lepton Tagging

The Prompt Lepton Tagging tuned for low-p_{T} (`LowPtPLT`) is developed to recover the lepton isolation efficiency. The idea of `LowPtPLT` is basically the same as `HighPtPLT`; we use the track-jet information to separate the prompt and non-prompt leptons. The training setups, discussed later in this section, are re-optimized for low-p_{T}. Difference in the setups comes from the difference in the origin of the background leptons. At low-p_{T}, the background leptons are less dominated by heavy-flavor decays than at high p_{T}, and the contributions from light-flavor hadrons, photon conversion, or pile-up particles become more important. Hence, various kind of background sources are taken into account in the training, and the input variables are also reconsidered. The major differences between `LowPtPLT` and `HighPtPLT` are listed below.

- Only leptons with $p_{\mathrm{T}} < 6$ GeV are used for the training.
- Leptons from various background sources are considered in the training.
- The input variables are re-arranged as described below.
- The difference in the p_{T} distribution of the prompt and non-prompt leptons is taken into account.

Figure 5.8 shows the breakdown of the origin of the background lepton with $p_{\mathrm{T}} < 10$ GeV, measured in the W+jets MC. Although the leptons from heavy-flavor hadron decays (b or c hadrons) dominate the background, there are considerable amount of fakes coming from the light-flavor or the photon conversion, as well as the pile-up (shown as "BkgElec" or "BkgMuon" in the plots). While the `HighPtPLT` is dedicated to reject heavy flavor backgrounds, `LowPtPLT` need to take all the background components into account. The flavor-tagging variables (RNNIP, DL1mu) are removed from the training in the low-p_{T} tuning, to prevent the performance to become highly flavor dependent.

The cone size for the lepton isolation variables, $p_{\mathrm{T}}^{\mathrm{varcone}}$ and $E_{\mathrm{T}}^{\mathrm{topocone}}$ is also revisited for the low-p_{T} tuning. In the training sample, it is found that variables with larger cone sizes have better separation power. The largest cone size variables available in the analysis are $p_{\mathrm{T}}^{\mathrm{varcone30(20)}}$ for muons (electrons) and

Table 5.5: List of input variables used for the Prompt Lepton Tagging tuned for low-p_{T}.

Variable name	Description
N_{track}	Number of tracks consisting the track-jet.
$p_{\mathrm{T}}(\ell)/p_{\mathrm{T}}(j)$	Ratio of the lepton p_{T} over the track-jet p_{T}.
$p_{\mathrm{T}}^{\mathrm{rel}}$	Lepton p_{T} with respect to the track-jet axis.
$\Delta R(\ell, j)$	ΔR between the lepton and the track-jet axis.
$p_{\mathrm{T}}^{\mathrm{varcone30}}/p_{\mathrm{T}}$ (muons)	Sum of p_{T} of the tracks within $\Delta R < 0.3$ of the lepton candidate divided by the lepton p_{T}.
$p_{\mathrm{T}}^{\mathrm{varcone20}}/p_{\mathrm{T}}$ (electrons)	Sum of p_{T} of the tracks within $\Delta R < 0.2$ of the lepton candidate divided by the lepton p_{T}.
$E_{\mathrm{T}}^{\mathrm{topocone20}}/p_{\mathrm{T}}$	Sum of E_{T} of the topological clusters within $\Delta R < 0.3$ of the lepton candidate.

Table 5.6: Summary of the preselection applied to the leptons used in the training of `LowPtPLT`.

Electrons	Prompt	Non-Prompt
Truth Matching	Originate from W-boson decay	Originate from b/c or light jets, photon conversion
Kinematic	$p_{\mathrm{T}} > 4.5$ GeV, $p_{\mathrm{T}} < 6.0$ GeV, $\lvert\eta\rvert < 2.47$	
Identification	*Tight* working point	
Isolation	None	
Impact parameter	$\lvert d_0/\sigma(d_0)\rvert < 5$, $\lvert z_0 \sin\theta\rvert < 0.5$ mm	
Muons	**Prompt**	**Non-Prompt**
Truth Matching	Originate from W-boson decay	Originate from b/c or light jets, photon conversion
Kinematic	$p_{\mathrm{T}} > 3$ GeV, $p_{\mathrm{T}} < 6$ GeV, $\lvert\eta\rvert < 2.5$	
Identification	*Low-p_T* working point	
Isolation	None	
Impact parameter	$\lvert d_0/\sigma(d_0)\rvert < 3$ & $\lvert z_0 \sin\theta\rvert < 0.5$ mm	

$E_{\mathrm{T}}^{\mathrm{topocone20}}$ for both muons and electrons. The final selection of the variables are listed in Table 5.5. The distributions of all the input variables are shown in Fig. 5.9 and Fig. 5.10.

Preselections applied to the leptons used for the training of `LowPtPLT` are summarized in Table 5.6. The selections follow the signal lepton definitions used in the analysis, except for the isolation and electron identification requirements. Additional upper cut of $p_{\mathrm{T}} < 6$ GeV is applied to tune the BDT particularly for low-p_{T}. Signal and background samples are then extracted using the truth-level MC information. After all the selections, the number of events available for the training is (prompt, non-prompt) = (78887, 50056) for electrons, and (315896, 536329) for muons. Since the fake/non-prompt leptons tend to have lower p_{T} compared to the prompt leptons, a weight is applied to each event to make the distribution become flat in the p_{T} distribution at the training to avoid the BDT to indirectly learn the p_{T} distribution. The distributions of the p_{T} of the leptons for the prompt and non-prompt leptons before and after the weight are shown in Figure 5.11.

The training sample is split into two independent sets. One of those datasets, referred to as "training sample" is used for the training. The other sample, "test sample", is used to evaluate the output score, so that one can compare the output score distribution of the training sample and the testing sample to check that there is no significant overtraining. The distributions of the `LowPtPLT` score for the training sample

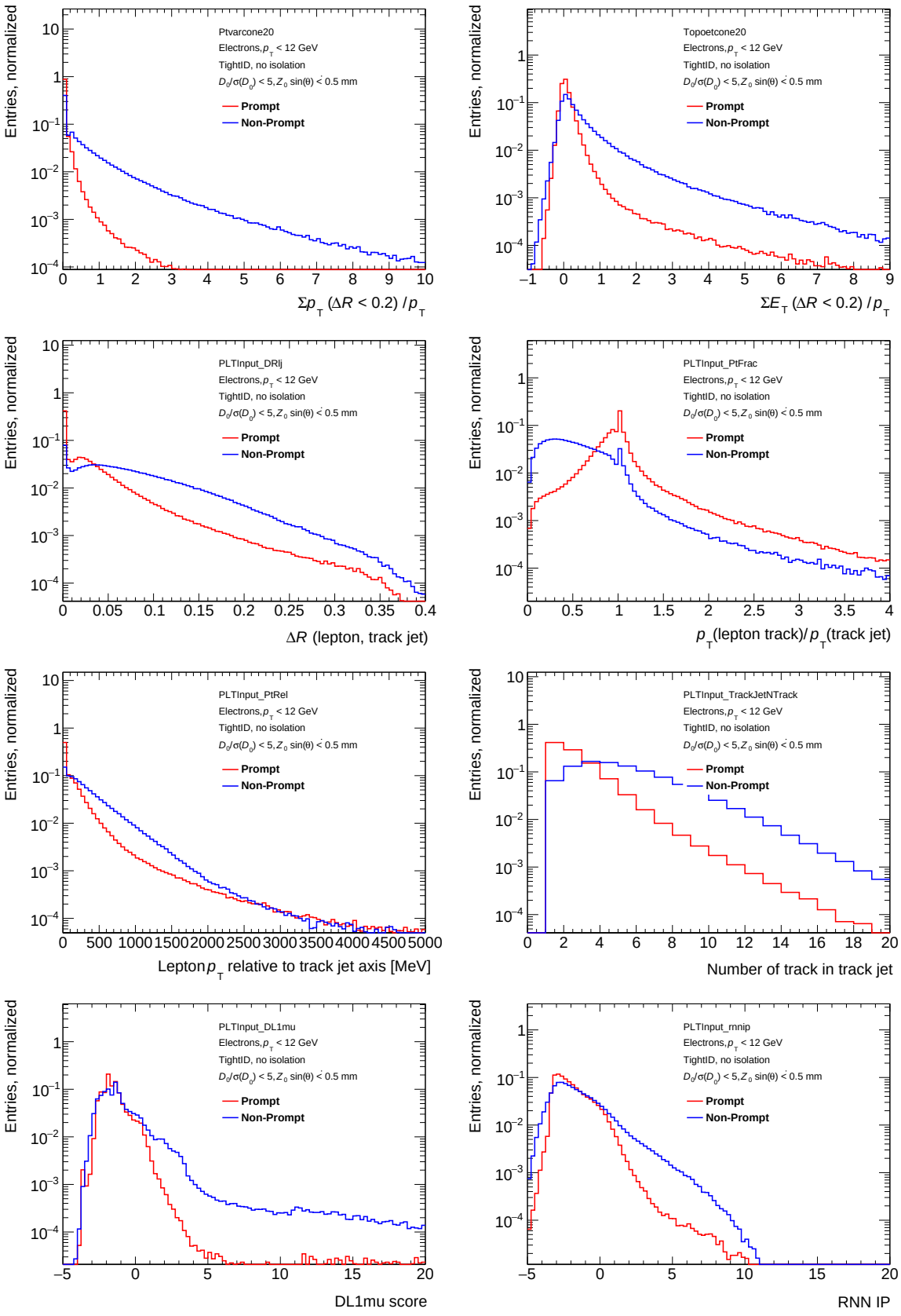

Figure 5.9: Distributions of the input variables to the `LowPtPLT`, for electrons with p_T < 12 GeV. The red (blue) histograms show the distributions for the prompt (non-prompt) leptons. The distributions are obtained using the $t\bar{t}$ MC. The definition of each variables are explained in the text.

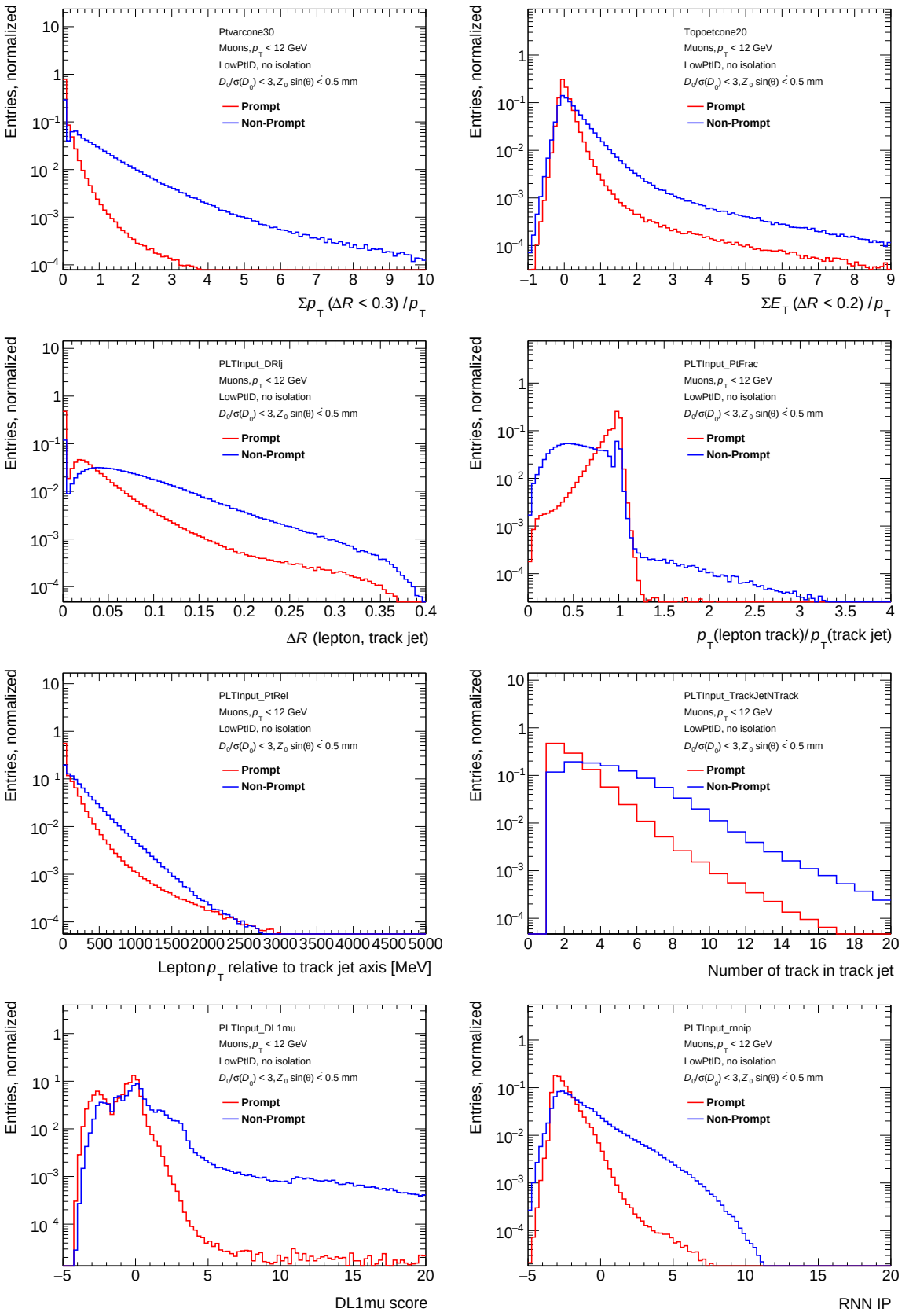

Figure 5.10: Distributions of the input variables to the `LowPtPLT`, for muons with p_T < 12 GeV. The red (blue) histograms show the distributions for the prompt (non-prompt) leptons. The distributions are obtained using the $t\bar{t}$ MC. The definition of each variables are explained in the text.

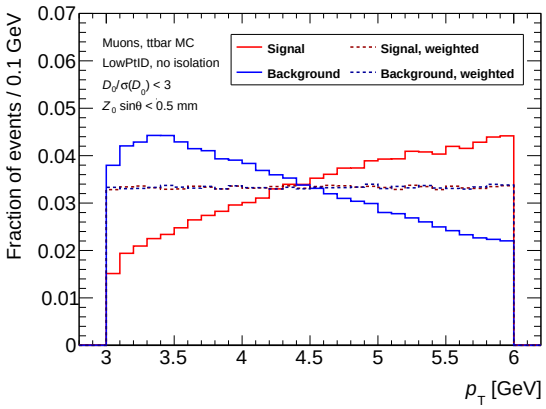

Figure 5.11: The distributions of the p_T for the prompt (red) and non-prompt (blue) leptons in training samples. The p_T-dependent weights are applied to each event to make the distribution flat. The distributions after the weights applying the weights are shown with red and blue dashed lines, for the prompt and non-prompt leptons, respectively.

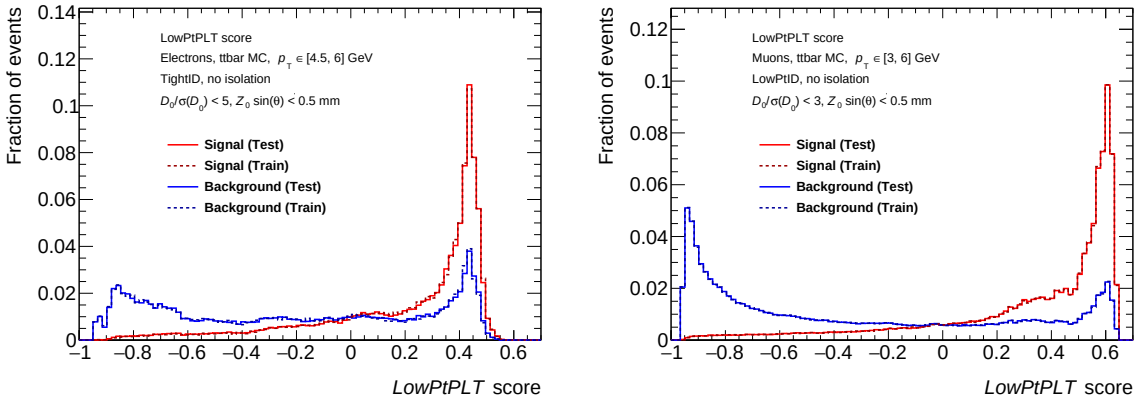

(a) LowPtPLT score, electrons

(b) LowPtPLT score, muons

Figure 5.12: LowPtPLT score distributions for electrons (left) and muons (right). The solid and dashed lines show the distributions of the scores obtained in the test and training samples, respectively. The red lines show the distributions of the prompt leptons, and the blue lines show the distributions of the non-prompt leptons.

and the testing sample are compared in Figure 5.12. Since the two distributions are consistent, we conclude that there are no significant overtraining in our setup.

The performance of LowPtPLT is compared with HighPtPLT and other isolation working points for leptons with $p_T < 12$ GeV, and the results are shown in Figure 5.13. The horizontal axis represent the efficiency for the prompt leptons, and the vertical axis represent the "rejection" of the fake/non-prompt leptons, defined as "1− (non-prompt efficiency)". The lower cut values on the BDT scores are varied, and the efficiency and the rejection are plotted for electrons (Figure 5.13(a)) and muons (Figure 5.13(b)). The BDT with the curve closer to the top-right corner indicate a better performance. These curves are called Receiver Operating Characteristic (ROC) curves, and are used to evaluate the performance of the BDT. The efficiencies for the conventional isolation working points are also shown in the plots. For both electrons and muons, LowPtPLT performs better than HighPtPLT and other working points.

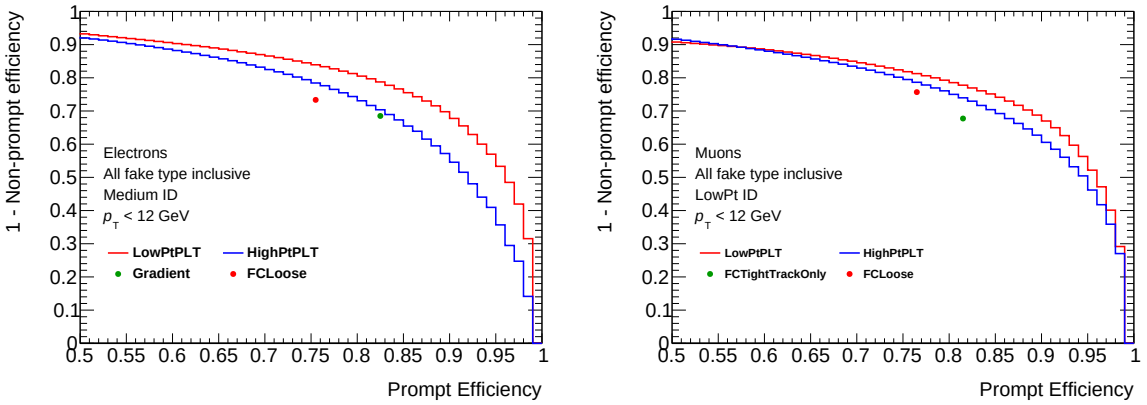

(a) Electrons, $p_{\mathrm{T}} < 12$ GeV

(b) Muons, $p_{\mathrm{T}} < 12$ GeV

Figure 5.13: ROC curves of the `LowPtPLT` and `HighPtPLT` for electrons (left) and muons (right) in the $p_{\mathrm{T}} < 12$ GeV region. The horizontal axis indicate the prompt lepton efficiency, and the vertical axis indicate the rejection of the non-prompt leptons, defined by "1− (non-prompt efficiency)". The red (blue) lines show the ROC curves for `LowPtPLT` (`HighPtPLT`). The points indicate the efficiency and the rejection for some of the conventional isolation working points. All the efficiencies are evaluated using the $t\bar{t}$ MC.

The rejection power of `LowPtPLT` against different background composition are shown in Figures 5.14 and 5.15, for electrons in the $p_{\mathrm{T}} \in [4, 5]$ GeV region and muons in the $p_{\mathrm{T}} \in [3, 4]$ GeV regions, respectively. These plots indicate that tuning for the low-p_{T} improves the rejection of the light-flavor jets and other backgrounds (mainly photon conversion and pile-up contribution) dramatically, while the improvement on the heavy-flavor jets are limited.

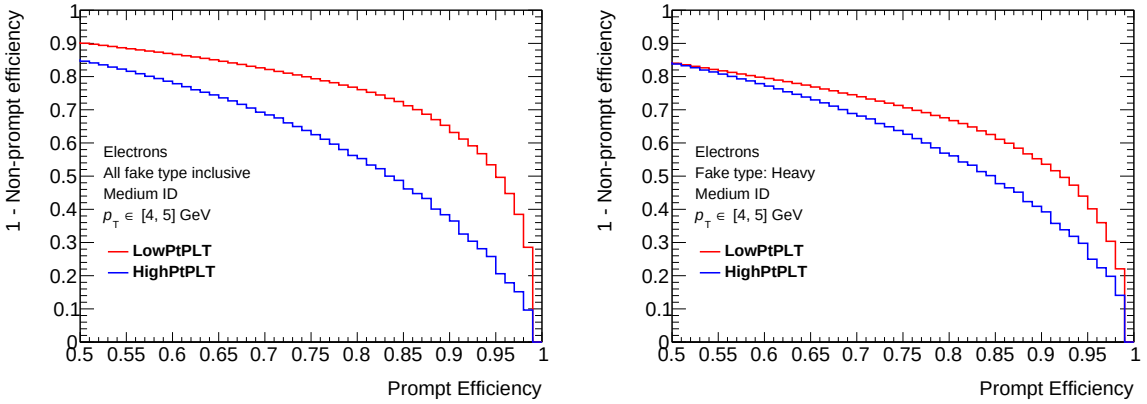

(a) All background component inclusive

(b) Backgrounds from heavy-flavor decays

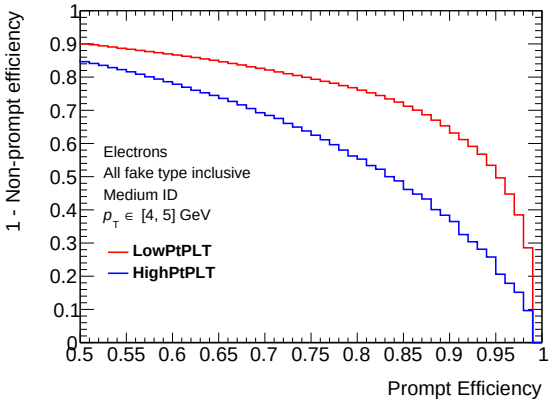

(c) Backgrounds from light-flavor decays

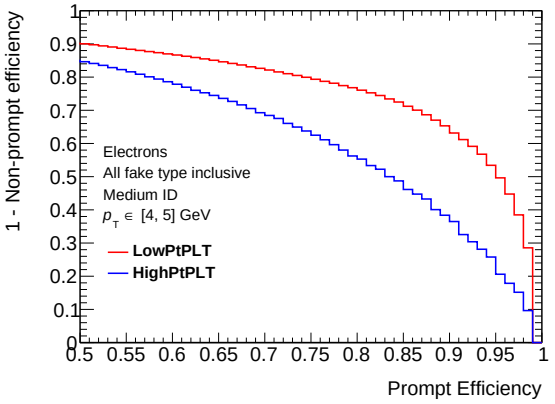

(d) Other backgrounds

Figure 5.14: ROC curves for `LowPtPLT` (red lines) and `HighPtPLT` (blue lines) for electrons in $p_{\mathrm{T}} \in [4, 5]$ GeV. The horizontal axis indicate the prompt lepton efficiency, and the vertical axis indicate the rejection of the backgroun leptons, defined by "1− (background efficiency)". Different source of the background leptons is considered in each plot; all background source inclusive (top left), heavy-flavor decays (top right), light-flavor decays (bottom left), and other background sources (bottom right). The efficiencies are evaluated using the $t\bar{t}$ MC.

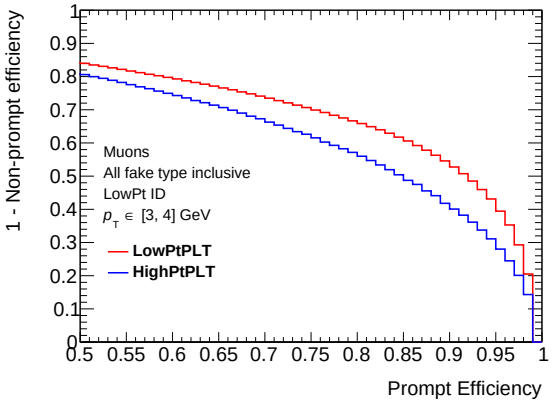

(a) All background component inclusive

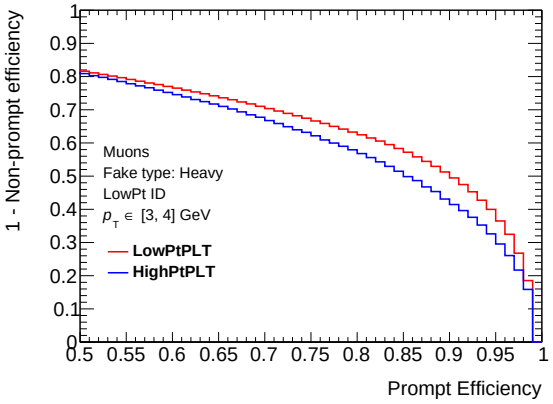

(b) Backgrounds from heavy-flavor decays

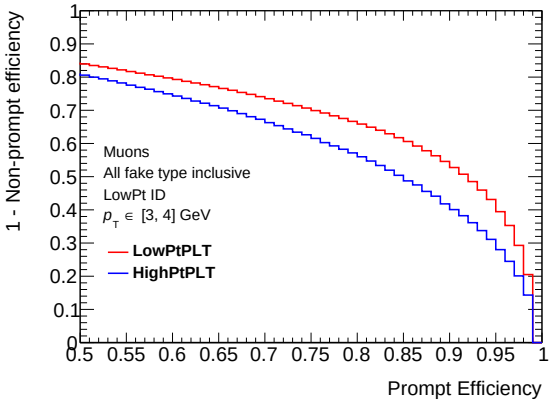

(c) Backgrounds from light-flavor decays

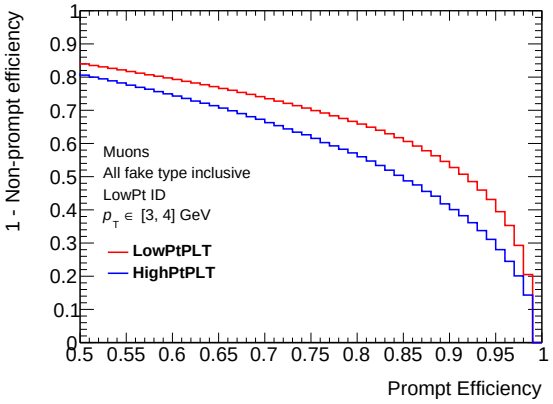

(d) Other backgrounds

Figure 5.15: ROC curves for `LowPtPLT` (red lines) and `HighPtPLT` (blue lines) for muons in $p_{\mathrm{T}} \in [3, 4]$ GeV. The horizontal axis indicate the prompt lepton efficiency, and the vertical axis indicate the rejection of the backgroun leptons, defined by "1− (background efficiency)". Different source of the background leptons is considered in each plot; all background source inclusive (top left), heavy-flavor decays (top right), light-flavor decays (bottom left), and other background sources (bottom right). The efficiencies are evaluated using the $t\bar{t}$ MC.

Table 5.7: The design of the efficiencies for the *PLTLoose* and *PLTTight*. The *PLTLoose*, *PLTTight* working points are defined to have comparable efficiencies with the *FCLoose*, *FCTight*, respectively. The exception is the *PLTLoose* working point for leptons with p_{T} smaller than 12 GeV. For electrons, the efficiency is defined to be 80%, and for muons the efficiency is defined to be comparable with the *FCTightTrackOnly* working point.

Working Point	flavor	$p_{\mathrm{T}} < 12$ GeV	$p_{\mathrm{T}} > 12$ GeV
PLTLoose	electron	flat efficiency 80%	*FCLoose*
	muon	*FCTightTrackOnly*	*FCLoose*
PLTTight	all	*FCTight*	

5.2.4 Definitions of the working points

Working points based on the `HighPtPLT` and the `LowPtPLT` scores are defined to obtain comparable prompt lepton efficiencies with the existing isolation working points. Two working points based on the Prompt Lepton Tagging scores, *PLTLoose* and *PLTTight*, are defined. Cuts are applied on either of the `LowPtPLT` or the `HighPtPLT` scores, depending on the p_{T} of the lepton. For leptons with $p_{\mathrm{T}} < 12$ GeV, a p_{T}-dependent cut shown in Equation 5.4 is applied to the `LowPtPLT` score. For leptons with $p_{\mathrm{T}} > 12$ GeV, a similar cut shown in Equation 5.5 is applied to the `HighPtPLT` score,

$$\texttt{LowPtPLT score} > \quad a' p_{\mathrm{T}}^3 + b' p_{\mathrm{T}}^2 + c' p_{\mathrm{T}} + d' \quad (p_{\mathrm{T}} < 12 \text{ GeV}), \tag{5.4}$$

$$\texttt{HighPtPLT score} < \begin{cases} a p_{\mathrm{T}}^3 + b p_{\mathrm{T}}^2 + c p_{\mathrm{T}} + d & (12 \text{ GeV} < p_{\mathrm{T}} < p_{\mathrm{T0}}) \\ \max(-0.88, A + B e^{-p_{\mathrm{T}}/C}) & (p_{\mathrm{T0}} < p_{\mathrm{T}}) \end{cases} . \tag{5.5}$$

The parameters a', b' etc. are tuned to obtain comparable efficiencies with some of the conventional isolation working points, listed in Table 5.7. The *PLTLoose*, *PLTTight* are designed to have comparable efficiencies with the *FCLoose*, *FCTight* working points, respectively. The exception is the *PLTLoose* working point in the low-p_{T} region. In the low-p_{T} region, we give priority to better efficiency for the prompt leptons rather than reducing the backgrounds. For muons with p_{T} smaller than 12 GeV, the *PLTLoose* working point is switched to have comparable efficiency with the *FCTightTrackOnly*. This working point is, despite its name, the loosest working point for the muons at this p_{T} range. For electrons, the loosest working point is the *Gradient* working point which is found to be too tight, thus we keep the efficiency for the prompt electrons with the *PLTLoose* at 12 GeV (which is approximately 80%) down to 4.5 GeV. All the parameters used to define the cut values are summarized in Table 5.8.

The efficiencies of the *PLTLoose* and *PLTTight* working points for the prompt leptons and the backgrounds are compared with the nominal working points. In Figure 5.16, the efficiencies are shown for electrons (top) and muons (bottom). The red distributions show the efficiencies for the *PLTLoose* or *PLTTight*, and the blue distributions show the efficiencies for *FCLoose* or *FCTight*. The points shown with circles (triangles) indicate the efficiencies for prompt (non-prompt) leptons. For the low-p_{T} electrons, the *PLTLoose* working point has higher efficiency for the prompt lepton compared to *FCLoose*, while further reducing the background by more than 50%. For the low-p_{T} muons, the *PLTLoose* working point has efficiency for the prompt leptons comparable with *FCTightTrackOnly*, while reducing the backgrounds by

Table 5.8: Parameters for the PLT-score based isolation working points, used in Eqs. 5.4 and 5.5.

Working Point	flavor	a'	b'	c'	d'
PLTLoose	electron	0.000345	-0.016259	0.243588	-1.133747
	muon	0.000335	-0.014904	0.215737	-0.730525
PLTTight	electron	0.000041	-0.002542	0.041502	0.152846
	muon	0.000099	-0.004141	0.056019	0.207732

Working Point	flavor	a	b	c	d	A	B	C	p_{T0} [GeV]
PLTLoose	electron	0	-0.000106967	-0.0160896	0.960105	-0.94386	3.03257	28.0508	18.457
	muon	-0.000186	0.0058481	-0.0788936	1.05942	-0.958651	3.54785	19.6155	18.452
PLTTight	electron	0	-0.000722487	-0.0750674	1.13016	-0.881497	2.29469	11.5776	16.967
	muon	0	-0.000992265	-0.0597252	0.998203	-0.929774	2.9159	10.2339	18.603

about 10%. The rejection power for the fake leptons is evaluated for different background processes in Appendix A.2.

5.2.5 Calibration

Agreement between the data and MC in the efficiency for the prompt leptons is checked using the $Z \to ee$ and $Z \to \mu\mu$ samples. Figures 5.17 and 5.18 show the efficiencies of the prompt electrons and muons as a function of p_{T}, compared between the data and MC. The efficiencies agree within 5% at lowest p_{T} bin. A p_{T}-dependent scale factor is applied as event weights to the MC events with electrons or muons to adjust the difference. The systematic uncertainties are assigned to cover the uncertainties on the measurement of this scale factor. The uncertainty mainly comes from the choice of the phase-space and the background estimation at the low-p_{T} region.

5.3 Correction of the isolation variables for close-by leptons

The Higgsino and Wino/Bino signals with small mass splitting often lead to two leptons reconstructed very close to each other. In this case, the other lepton enters the calculation of the isolation variables, and that makes the lepton to be regarded as non-isolated. Thus it is important to subtract the contribution of the other lepton when we require the lepton to be isolated.

The basic idea of the correction is to remove tracks/clusters that directly match to the other lepton when calculating the isolation variables, $p_{\mathrm{T}}^{\mathrm{cone}}/E_{\mathrm{T}}^{\mathrm{topocone}}$. Figure 5.19 briefly highlights the idea of the correction, for $p_{\mathrm{T}}^{\mathrm{cone}}$ variables (same method can be applied to $E_{\mathrm{T}}^{\mathrm{topocone}}$). The track matched to the other lepton can simply be ignored when calculating the cone variables, which makes both of the lepton to be treated as isolated. This method works when both of the two leptons have no other tracks close-by.

The difficulty occurs when one or both of the two leptons are non-prompt. In our analysis, it is important to tag the non-prompt leptons correctly, especially for the data-driven background estimation (detailed in Chapter 7). A dedicated correction method is developed for this purpose. Figure 5.20 shows a schematic diagram when one of the leptons (labeled as "lep2" in the figure) is non-prompt. Shared tracks,

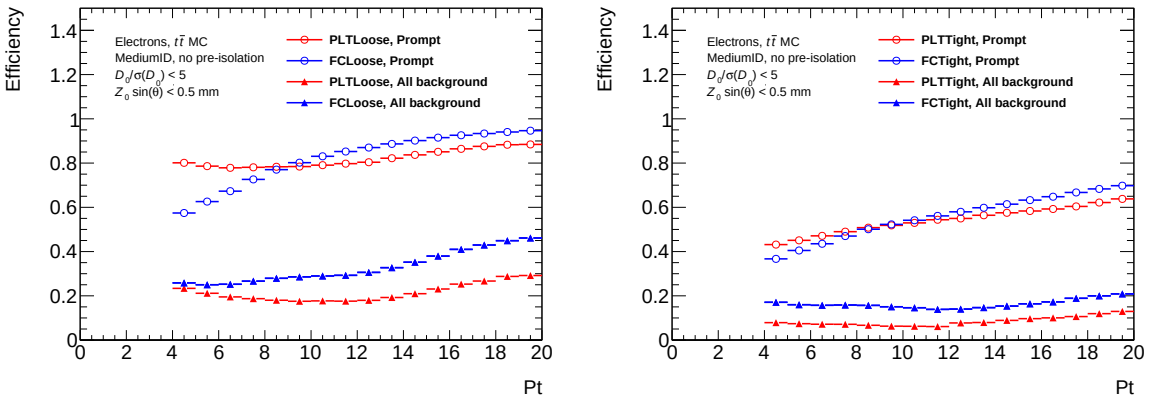

(a) Electrons, *PLTLoose*

(b) Electrons, *PLTTight*

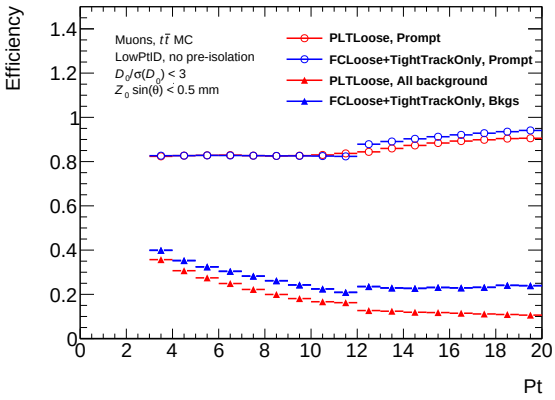

(c) Muons, *PLTLoose*

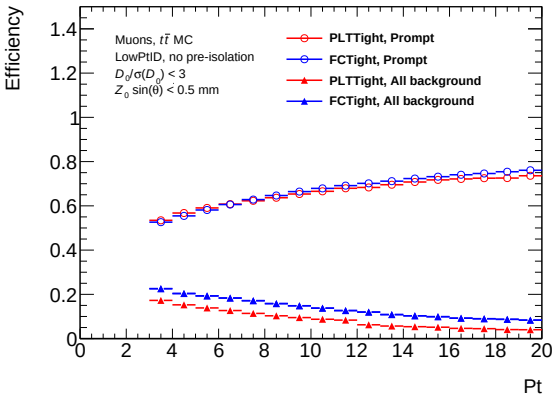

(d) Muons, *PLTTight*

Figure 5.16: Efficiencies for the prompt and background electrons with the (a) *PLTLoose* and (b) *PLTTight*, and for the muons with the (c) *PLTLoose* and (d) *PLTTight*, as a function of lepton p_{T}. The red and blue circles show the efficiencies for the prompt leptons, with the Prompt Lepton Tagging and the nominal working points, respectively. The red and blue triangles show the efficiencies for the backgrounds, with the Prompt Lepton Tagging and the nominal working points, respectively.

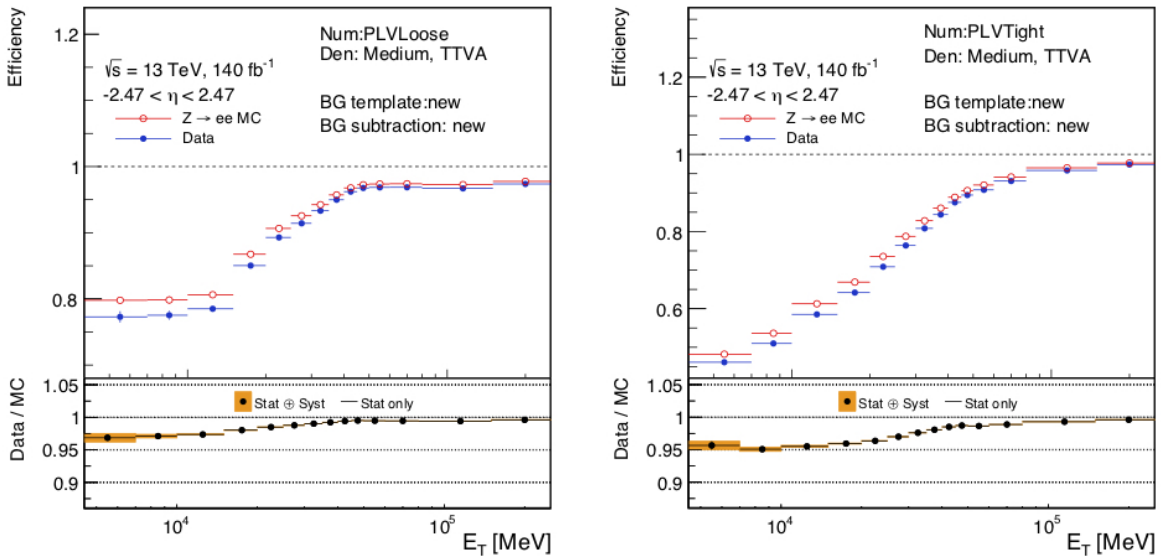

Figure 5.17: Data/MC comparison of the efficiencies for the prompt electrons as a function of p_{T}, with the *PLTLoose* and *PLTTight*, measured using 2015-2018 data (140 fb^{-1}) [139]. The efficiencies are measured in $Z \rightarrow ee$ events in data and MC.

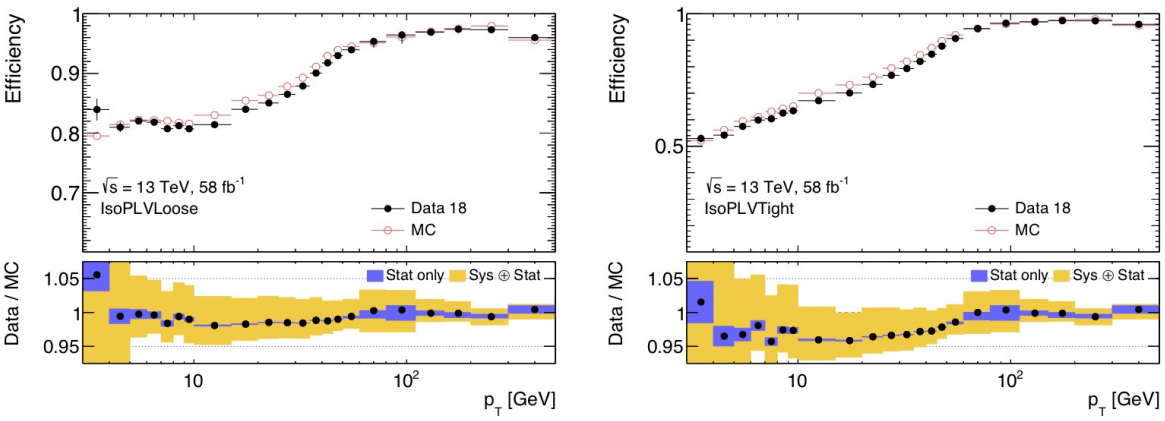

Figure 5.18: Data/MC comparison of the efficiencies for the prompt electrons as a function of p_{T}, with the *PLTLoose* and *PLTTight*, measured using 2018 data (58 fb^{-1}) [140]. The efficiencies are measured in $Z \rightarrow \mu\mu$ events in data and MC.

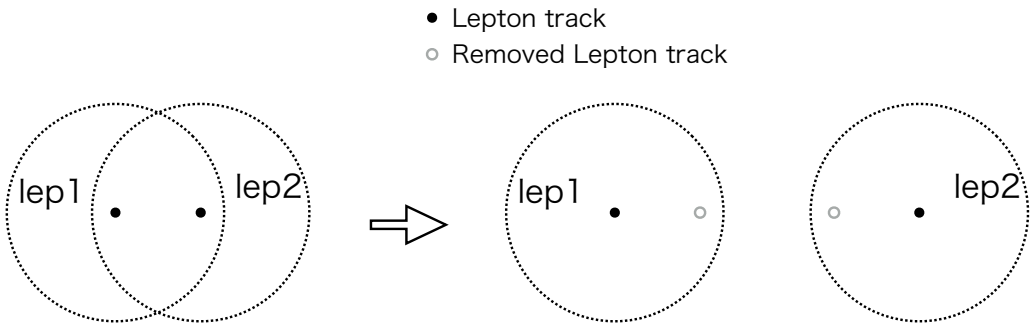

Figure 5.19: Schematic diagram of correction for isolation variables, in events with of two prompt leptons. The track assigned directly to the other lepton is ignored in $p_{\mathrm{T}}^{\mathrm{cone}}$ calculation, and both leptons are treated as isolated after correction.

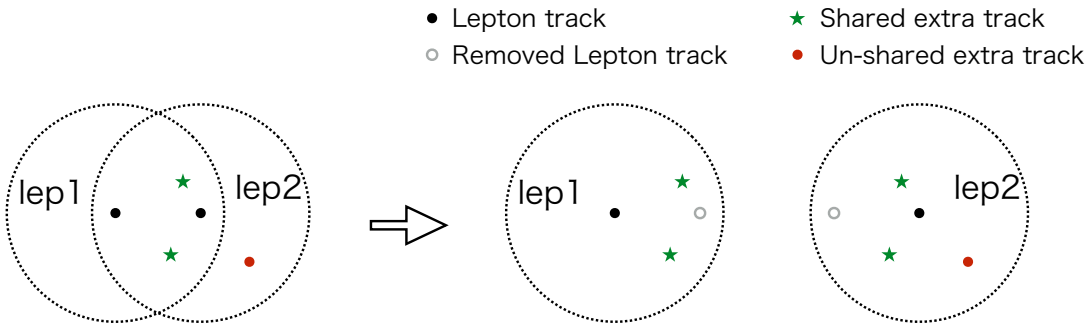

Figure 5.20: Schematic diagram of correction for isolation variables, in a case one of the lepton is non-prompt. The lepton labeled "lep2" label in the diagram is assumed to be non-prompt. The tracks from the parent jet of "lep2" are reconstructed close to both leptons, and the shared tracks are double-counted even after the correction.

shown in the figures with the green star-shaped dots, are the tracks that are within the cone-size from both of the leptons, but are not directly matched to either of the leptons. These shared tracks are duplicated during the calculation of the cone variables, therefore both of the leptons can be non-isolated. To avoid this, we need to assign the shared tracks to either of the leptons so that they are not duplicated during the calculation. The choice of the lepton to assign the tracks is not trivial. We take a lepton that is "closer" to the shared tracks because the parent track is more likely to be reconstructed closer to its daughter lepton. The vector sum of the shared tracks are used to define the distance between the leptons, and all the shared tracks are assigned to the closer lepton.

Similar corrections are applied to the input variables for the Prompt Lepton Tagging. The corrections are needed when two leptons are close to each other within a $\Delta R < 0.4$ cone and are included in a same track-jet. In this case, the same track-jet is used to calculate the input variables for both of the leptons, thus the tracks in the track-jet are effectively double-counted. Figure 5.21 shows a schematic diagram for the correction of the input variables for the Prompt Lepton Tagging. We need to assign the tracks in the

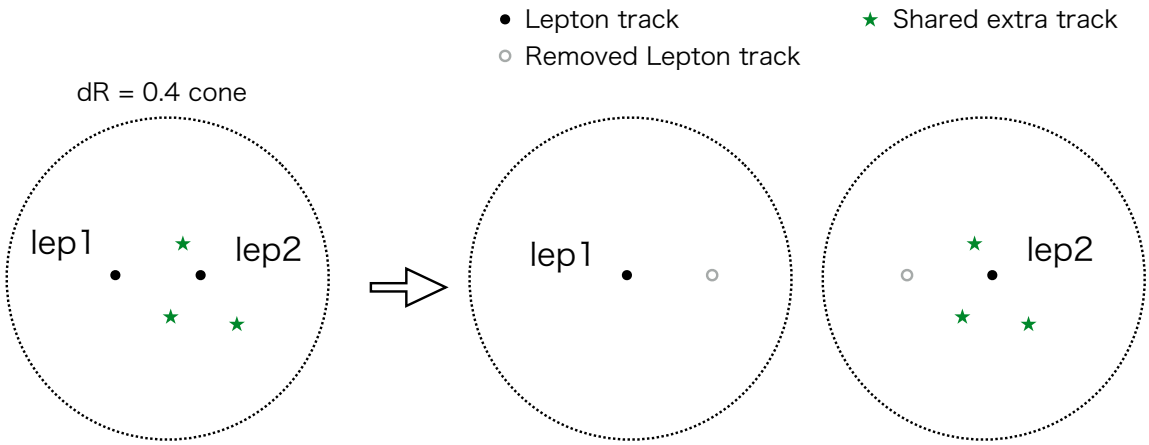

Figure 5.21: Schematic diagram of correction for input variables to the Prompt Lepton Tagging. When two leptons are included in a common track-jet, all the tracks other than the tracks of the leptons are summed up and assigned to a closer lepton. In this diagram, vector sum of all the tracks indicated by green stars ("shared tracks") are assigned to the closer lepton, "lep2".

track-jet to either of the leptons to correctly tag non-prompt leptons. We assign all the tracks to the "closer" lepton, defined by ΔR between the lepton and the vector sum of all the shared tracks.

Figures 5.22 and 5.23 show the performance of the correction for the Prompt Lepton Tagging input variables, for electrons and muons, respectively. Figure 5.24 shows the `LowPtPLT` score distributions before and after the correction is applied, for electrons (left) and muons (right). The performance is checked using signal samples of the Wino/Bino model, with the mass parameters of $m(\widetilde{\chi}_1^{\pm}) = 100$ GeV and $m(\widetilde{\chi}_1^0) = 97$ GeV. The histograms shown with orange (red) solid lines are the distributions of the variables before (after) the corrections. The histograms with dashed lines are the distributions for W+jets events with two leptons, shown for comparison. The red dashed lines are distributions for leptons with higher p_{T} (leading lepton) in the W+jets events, which are dominated by prompt leptons. The blue dashed lines are the same distribution for leptons with lower p_{T} (sub-leading lepton) in the W+jets events, dominated by the fake/non-prompt leptons. Note that for the W+jets events, two leptons are rarely produced close to each other, thus no correction is applied to most of the events. Before the correction, the signal distributions (solid orange) are more similar to the fake/non-prompt distribution (dashed blue). After the correction, the signals (solid red) behave very similar to the prompt events (dashed red). That indicates that the correction is working as expected.

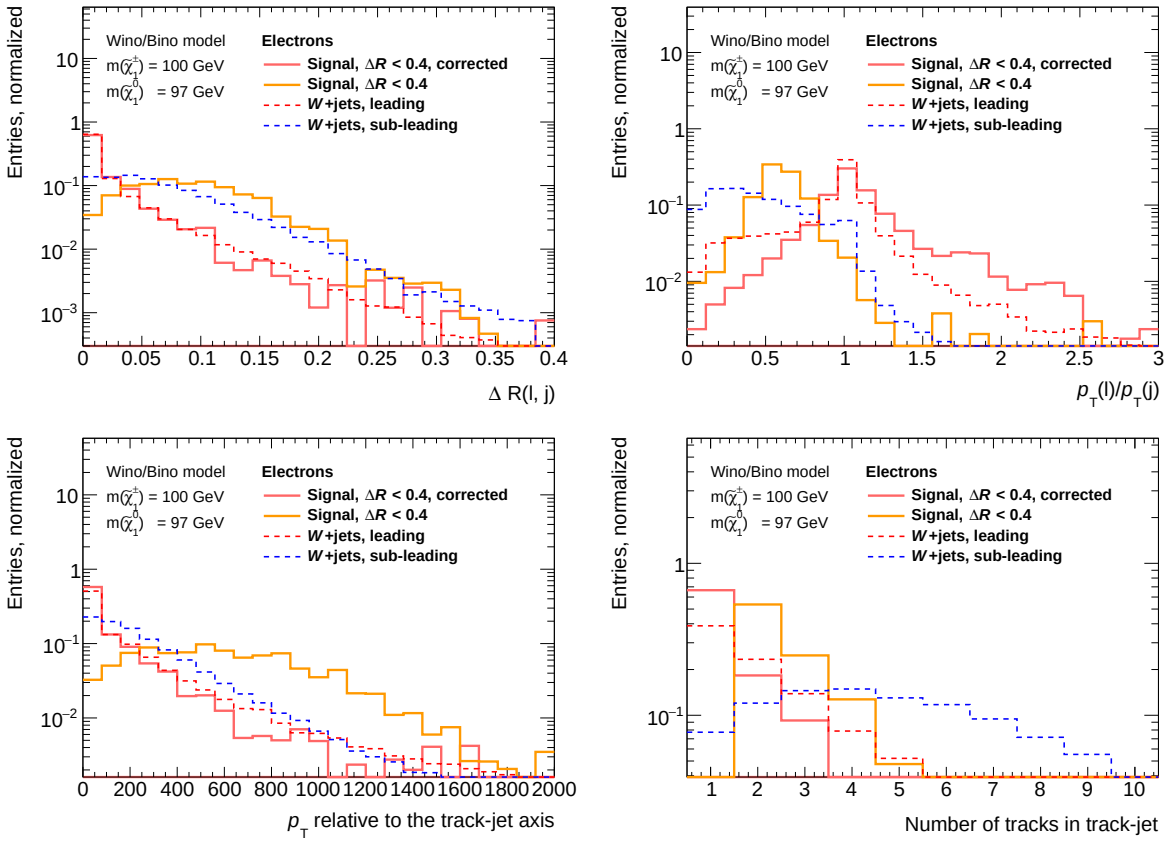

Figure 5.22: Distributions of the input variables to the Prompt Lepton Tagging: $\Delta R(\ell, j)$ (top left, distance between the lepton and the track-jet), $p_{\mathrm{T}}(\ell)/p_{\mathrm{T}}(j)$ (top right, p_{T} of the lepton divided by the p_{T} of the track-jet), $p_{\mathrm{T}}^{\mathrm{rel}}$ (bottom left, p_{T} of the lepton relative to the axis of the track-jet), and N_{track} (bottom right, number of tracks in the track-jet). The orange solid and red solid histograms show the distribution before and after the close-by track correction, for the sub-leading electron in the Wino/Bino model with $m(\widetilde{\chi}_1^{\pm}) = 100$ GeV and $m(\widetilde{\chi}_1^0) = 97$ GeV. Events with $\Delta R_{\ell\ell} < 0.4$ are selected, where the correction is essential. Same distributions for leading leptons (dashed red) and sub-leading leptons (dashed blue) in the W+jets MC are shown for comparison.

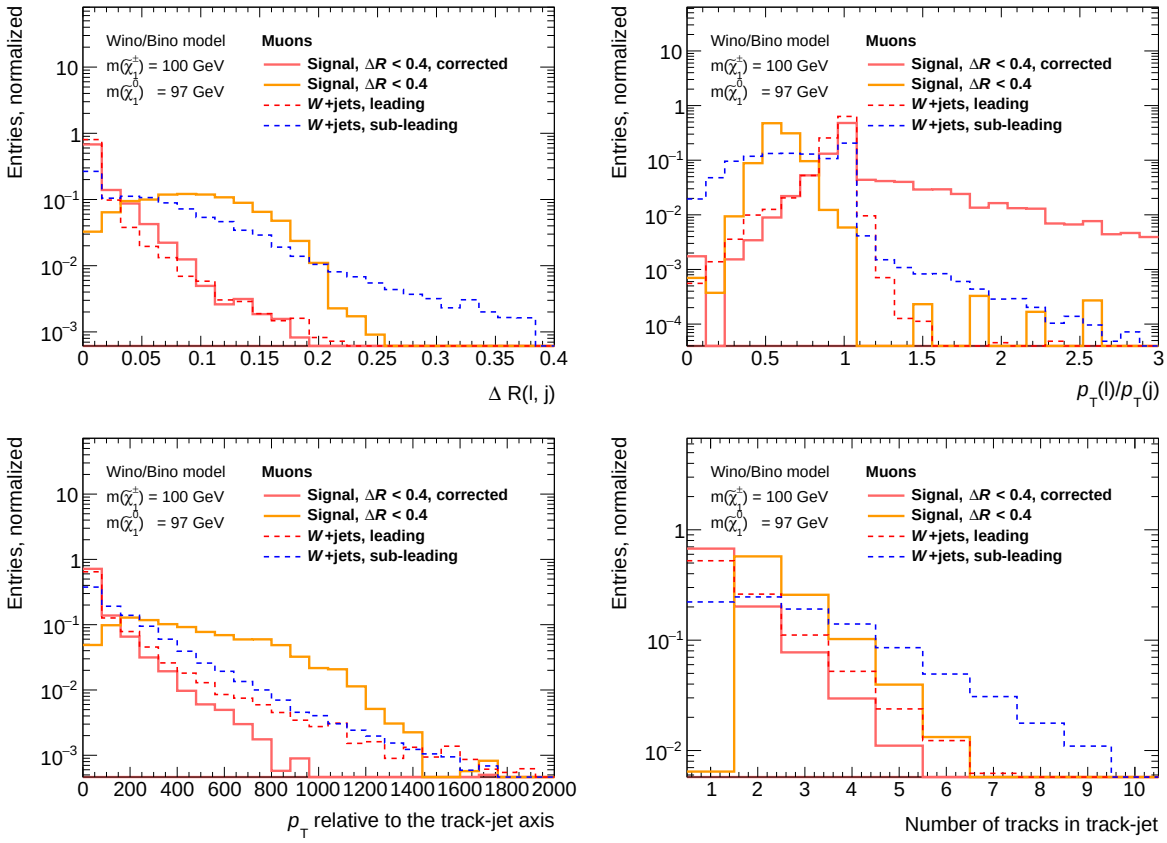

Figure 5.23: Distributions of the input variables to the Prompt Lepton Tagging: $\Delta R(\ell, j)$ (top left, distance between the lepton and the track-jet), $p_{\mathrm{T}}(\ell)/p_{\mathrm{T}}(j)$ (top right, p_{T} of the lepton divided by the p_{T} of the track-jet), $p_{\mathrm{T}}^{\mathrm{rel}}$ (bottom left, p_{T} of the lepton relative to the axis of the track-jet), and N_{track} (bottom right, number of tracks in the track-jet). The orange solid and red solid histograms show the distribution before and after the close-by track correction, for the sub-leading muon in the Wino/Bino model with $m(\widetilde{\chi}_1^{\pm}) = 100$ GeV and $m(\widetilde{\chi}_1^0) = 97$ GeV. Events with $\Delta R_{\ell\ell} < 0.4$ are selected, where the correction is essential. Same distributions for leading leptons (dashed red) and sub-leading leptons (dashed blue) in the W+jets MC are shown for comparison.

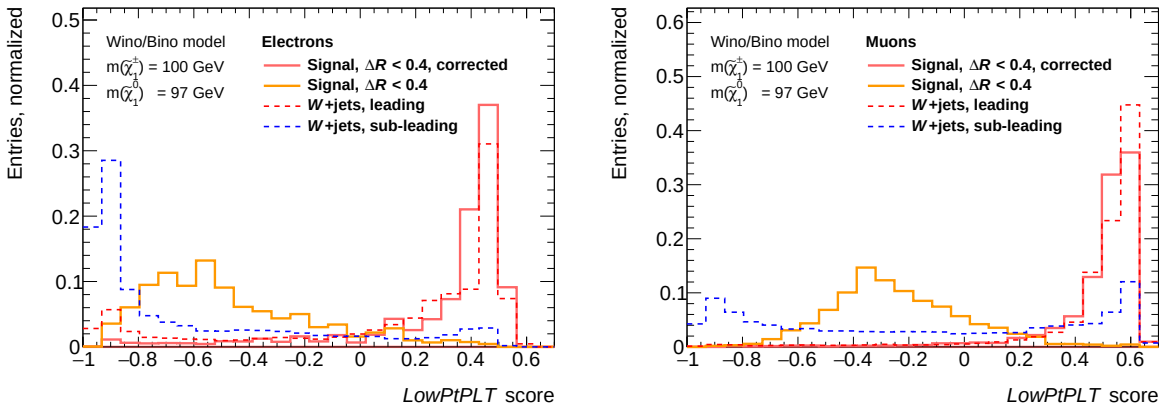

Figure 5.24: Distributions of the `LowPtPLT` scores for electrons (left) and muons (right) before (orange solid) and after (red solid) the correction, for the sub-leading lepton in the Wino/Bino model with $m(\widetilde{\chi}_1^{\pm}) = 100$ GeV and $m(\widetilde{\chi}_1^0) = 97$ GeV. Events with $\Delta R_{\ell\ell} < 0.4$ are selected, where the correction is essential. Same distributions for W+jets MC leading lepton (dashed red) and sub-leading lepton (dashed blue) are shown for comparison.

Chapter 6

Event Selections

A set of cuts is applied to the events to define "signal regions", where the data are compared with the SM prediction to search for the signal events. The signal regions are thus required to have good signal to background ratio. In this chapter, the definitions of the signal regions are presented. In Section 6.1, an overview of the strategy of the event selection is highlighted. In Section 6.2, the triggers used to collect the collision data in this analysis are explained. In Section 6.3, the definitions of the variables used to define the signal regions are described. These variables are also used to define "control regions" and "validation regions", which are used for background yield estimation and validation, described in Chapter 7. The common preselections applied to all the signal regions are summarized in Section 6.4. Finally, in Section 6.5, the definitions of the four exclusive signal regions used in this analysis are explained.

6.1 Analysis Strategy

As discussed in Section 1.3, we search for SUSY signals with small mass difference $\Delta m = m(\widetilde{\chi}_2^0) - m(\widetilde{\chi}_1^0)$. We use final states with two opposite-sign same-flavor leptons from $\widetilde{\chi}_2^0 \to \widetilde{\chi}_1^0 Z^*$ followed by the $Z^* \to \ell\ell$ decay, so that the invariant mass of the two leptons are sensitive to the Δm. We additionally require a large initial-state radiation (ISR). As explained in Section 1.3, this topology boosts the SUSY particles in the opposite direction to the ISR, and enhances the transverse momentum of the two $\widetilde{\chi}_1^0$ s which are observed as large $E_{\mathrm{T}}^{\mathrm{miss}}$. To conclude, the strategy of the analysis is to find events with a high-p_{T} jet and a significant $E_{\mathrm{T}}^{\mathrm{miss}}$ in the opposite direction, associated with two leptons that form a small invariant mass.

Two types of analysis channels are considered in this analysis: two-lepton (2ℓ) channel and one-lepton plus one-track ($1\ell 1T$) channel. The 2ℓ channel requires two signal leptons in the event, and is further divided into three types of signal regions. The $1\ell 1T$ channel requires one signal lepton and one isolated track with opposite charge. Total of four signal region categories, the $1\ell 1T$ and three 2ℓ signal regions, are defined. All the signal regions are binned in $m_{\ell\ell}$ to exploit the characteristic shape of the $m_{\ell\ell}$ expected for the signal events.

6.2 Trigger

The search presented in this thesis uses the pp collision data at $\sqrt{s} = 13$ TeV collected with the ATLAS detector during 2015–2018, as described in Section 3.1. Events are collected using the $E_{\mathrm{T}}^{\mathrm{miss}}$ triggers. The setups of the $E_{\mathrm{T}}^{\mathrm{miss}}$ triggers with the lowest threshold depend on the period of the data taking, and are summarized in Table 6.1. The $E_{\mathrm{T}}^{\mathrm{miss}}$ trigger is characterized by the thresholds applied at the level-1 (L1)

Table 6.1: The setups of the $E_{\mathrm{T}}^{\mathrm{miss}}$ trigger in different data taking period. The first column indicates the data taking period, which corresponds to the integrated luminosity shown in the second column. The third and fourth columns indicate the thresholds applied at the level-1 trigger (L1) and high-level trigger (HLT), respectively. The last column shows the reconstruction algorithm of the $E_{\mathrm{T}}^{\mathrm{miss}}$ at the HLT, described in [141]. The jet-based algorithm simply takes the negative vector sum of the p_{T} of the jets, while the pile-up fit algorithm uses the energy of the topo-clusters directly, with the effect of the jets from the pile-up taken into account. For the $E_{\mathrm{T}}^{\mathrm{miss}}$ triggers in 2018, pre-thresholds are applied to the $E_{\mathrm{T}}^{\mathrm{miss}}$ before the pile-up fit algorithm, which are also shown in the last column.

Period	int. lumi [fb^{-1}]	L1 threshold	HLT threshold	$E_{\mathrm{T}}^{\mathrm{miss}}$ algorithm
2015	3.2	50 GeV	70 GeV	Jet-based
2016 A–D3	6.0	50 GeV	90 GeV	Jet-based
2016 D4–F1	6.5	50 GeV	100 GeV	Jet-based
2016 F2–	20.5	50 GeV	110 GeV	Jet-based
2017 B1–D5	12.1	55 GeV	110 GeV	Pile-up fit
2017 D6–	32.2	50 GeV	110 GeV	Pile-up fit
2018 B–C5	8.8	50 GeV	110 GeV	Pile-up fit, pre-threshold 70 GeV
2018 C5–	49.6	50 GeV	110 GeV	Pile-up fit, pre-threshold 65 GeV

hardware trigger and at the high-level trigger (HLT). The algorithms used to reconstruct the $E_{\mathrm{T}}^{\mathrm{miss}}$ at the HLT are also shown in the table. The reconstruction algorithm at the HLT is different from the algorithm used in the analysis, because the information available at the HLT is limited.

The efficiency of the $E_{\mathrm{T}}^{\mathrm{miss}}$ trigger in each year is measured using the $Z \to \mu\mu$ events, as shown in Fig. 6.1. At the L1 and the HLT, muons are observed as $E_{\mathrm{T}}^{\mathrm{miss}}$ because they are not included in the calculation of the $E_{\mathrm{T}}^{\mathrm{miss}}$. Thus the p_{T} of the Z boson (p_{T} (Z)) calculated offline can be used as a proxy for the $E_{\mathrm{T}}^{\mathrm{miss}}$. The efficiency of the $E_{\mathrm{T}}^{\mathrm{miss}}$ trigger has a slow rising curve as a function of p_{T} (Z), due to the limited resolution of the $E_{\mathrm{T}}^{\mathrm{miss}}$ at the trigger level. With the different trigger requirements, the efficiencies in $E_{\mathrm{T}}^{\mathrm{miss}} < 200$ GeV vary from period to period. For the region with $E_{\mathrm{T}}^{\mathrm{miss}} > 200$ GeV, the trigger efficiency is $> 95\%$ for all the data taking periods.

6.3 Discriminating Variables

In this section, the variables used to define the signal regions are defined. A brief explanation of how each of these variable are used is given in each paragraph. The cut values used in the analysis are summarized in Section 6.5.

$p_{\mathrm{T}}(j_1)$: The transverse momentum of the leading jet (j_1, jet with the highest p_{T}), required to be above 100 GeV to collect signal events with a large ISR.

$E_{\mathrm{T}}^{\mathrm{miss}}$: The missing transverse momentum, calculated as described in Section 4.8. The SUSY particles are boosted in the opposite direction to the ISR, and this enhances the transverse momentum of the SUSY particles. For signal events with small mass difference between the $\widetilde{\chi}_1^{\pm}/\widetilde{\chi}_2^0$ and $\widetilde{\chi}_1^0$, most of the transverse

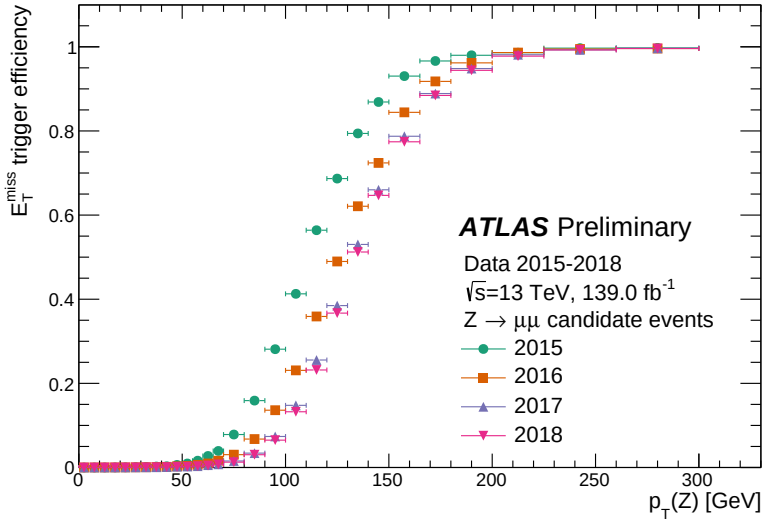

Figure 6.1: Efficiencies of $E_{\mathrm{T}}^{\mathrm{miss}}$ trigger as functions of p_{T} of Z bosons [142]. The events are taken from data with a $Z \to \mu\mu$ selection, and p_{T} of the Z boson is used as a proxy for the $E_{\mathrm{T}}^{\mathrm{miss}}$ in the event, as muons are treated as invisible objects by the $E_{\mathrm{T}}^{\mathrm{miss}}$ triggers.

momentum is carried by the two $\widetilde{\chi}_1^0$ s in the final state. The $\widetilde{\chi}_1^0$ s are invisible in the ATLAS detector and are thus observed as large $E_{\mathrm{T}}^{\mathrm{miss}}$.

$\Delta\phi(j_1, \mathbf{p}_{\mathrm{T}}^{\mathrm{miss}})$: Difference in the azimuthal angle between the leading jet (j_1) and the $E_{\mathrm{T}}^{\mathrm{miss}}$. Signals considered in this analysis produce a significant $E_{\mathrm{T}}^{\mathrm{miss}}$ by recoiling against the ISR jet. Thus the ISR jet and the $E_{\mathrm{T}}^{\mathrm{miss}}$ are likely to be produced back-to-back. ISR-like events are efficiently collected with requiring a large angular separation between the leading jet and $E_{\mathrm{T}}^{\mathrm{miss}}$.

$\min(\Delta\phi(\text{any jet}, \mathbf{p}_{\mathrm{T}}^{\mathrm{miss}}))$: The minimum angular separation between any of the jets and the $E_{\mathrm{T}}^{\mathrm{miss}}$. A lower cut on the $\min(\Delta\phi(\text{any jet}, \mathbf{p}_{\mathrm{T}}^{\mathrm{miss}}))$ is required in the signal regions. This cut is intended to suppress the contribution from the $E_{\mathrm{T}}^{\mathrm{miss}}$ incorrectly reconstructed due to mis-measurement of the jet energy, which is often reconstructed close to the jet.

$m_{\ell\ell}$: The dilepton invariant mass $m_{\ell\ell}$, used as the final discriminant to define the signal regions. As discussed in Section 1.3, the $m_{\ell\ell}$ of the signal events are sensitive to the mass difference Δm, thus the signal regions are binned in $m_{\ell\ell}$ to exploit this feature. An upper bound on $m_{\ell\ell}$ is placed at 60 GeV, to suppress events with two leptons coming from the decay of an on-shell Z boson. The upper bound also helps in suppressing harder leptons from SM processes such as WW and $t\bar{t}$.

$\Delta R_{\ell\ell}$: The distance between two leptons, defined as

$$\Delta R_{\ell\ell} = \sqrt{\left(\eta_{\ell_1} - \eta_{\ell_2}\right)^2 + \left(\phi_{\ell_1} - \phi_{\ell_2}\right)^2}, \tag{6.1}$$

where the subscripts ℓ_1 and ℓ_2 indicate leading and sub-leading lepton, respectively. The kinematic phase space of the leptons is restricted by the small Δm, which lead to small angular separation of the leptons. Events with small $\Delta R_{\ell\ell}$ are difficult to handle because of technical reasons as described in Section 5.3. A dedicated correction, also described in Section 5.3, is applied to resolve the overlapping contributions, however, a minimum angular separation is required for the two leptons to avoid the contributions that cannot be resolved by this correction.

$E_{\mathrm{T}}^{\mathrm{miss}}/H_{\mathrm{T}}^{\mathrm{leptons}}$: The $E_{\mathrm{T}}^{\mathrm{miss}}$ divided by the scalar sum of the lepton momenta ($H_{\mathrm{T}}^{\mathrm{lep}}$),

$$H_{\mathrm{T}}^{\mathrm{leptons}} = \sum_{i}^{\mathrm{leptons}} p_{\mathrm{T}}^{\ell_i}. \tag{6.2}$$

In the signal events with small mass difference, the $\widetilde{\chi}_1^0$ carries most of the transverse momentum and little momentum is transferred to the leptons. This favors larger values of $E_{\mathrm{T}}^{\mathrm{miss}}/H_{\mathrm{T}}^{\mathrm{lep}}$ compared to the background. The background processes from diboson and $t\bar{t}$ tend to have harder leptons, thus the values of $E_{\mathrm{T}}^{\mathrm{miss}}/H_{\mathrm{T}}^{\mathrm{lep}}$ become smaller.

$m_{\mathrm{T}}^{\ell_1}$: The transverse mass of the leading lepton and the $E_{\mathrm{T}}^{\mathrm{miss}}$, defined by

$$(m_{\mathrm{T}}^{\ell_1})^2 = (E_{\mathrm{T}}^{\ell_1} + E_{\mathrm{T}}^{\mathrm{miss}})^2 - (\mathbf{p}_{\mathrm{T}}^{\ell_1} + \mathbf{p}_{\mathrm{T}}^{\mathrm{miss}})^2. \tag{6.3}$$

With approximations of $m_{\ell_1} = 0$ and $m_\nu = 0$, it becomes

$$\begin{aligned} m_{\mathrm{T}}^{\ell_1} &= \sqrt{2(E_{\mathrm{T}}^{\ell_1} E_{\mathrm{T}}^{\mathrm{miss}} - \mathbf{p}_{\mathrm{T}}^{\ell_1} \cdot \mathbf{p}_{\mathrm{T}}^{\mathrm{miss}})} \\ &= \sqrt{2(E_{\mathrm{T}}^{\ell_1} E_{\mathrm{T}}^{\mathrm{miss}}(1 - \cos\theta))}, \end{aligned} \tag{6.4}$$

where θ is the angle between the leading lepton (ℓ_1) and the $E_{\mathrm{T}}^{\mathrm{miss}}$ in the transverse plane. This variable is used to suppress events with on-shell W bosons decaying leptonically, by setting an upper cut. In the decay of an on-shell W-boson, the $m_{\mathrm{T}}^{\ell_1}$ corresponds to the transverse mass of the W boson, and thus peaks at the $m_W \sim 80$ GeV. For the signals, $m_{\mathrm{T}}^{\ell_1}$ tends to take smaller values because ${p_{\mathrm{T}}}^{\ell_1}$ is generally small, and also because ℓ_1 is likely to be reconstructed close to the $E_{\mathrm{T}}^{\mathrm{miss}}$, leading to small θ.

$m_{\tau\tau}$: The di-tau invariant mass, defined by the following equations,

$$m_{\tau\tau}\left(p_{\ell_1}, p_{\ell_2}, \mathbf{p}_{\mathrm{T}}^{\mathrm{miss}}\right) = \begin{cases} \sqrt{m_{\tau\tau}^2} & m_{\tau\tau}^2 \geq 0, \\ -\sqrt{|m_{\tau\tau}^2|} & m_{\tau\tau}^2 < 0, \end{cases} \tag{6.5}$$

$$m_{\tau\tau}^2 = \left(p_{\tau_1} + p_{\tau_2}\right)^2. \tag{6.6}$$

The $m_{\tau\tau}$ is calculated as described in the following paragraphs, assuming that the two leptons and the $E_{\mathrm{T}}^{\mathrm{miss}}$ are produced by fully leptonic $Z \to \tau\tau$ processes. For the fully leptonic $Z \to \tau\tau$ events, the $m_{\tau\tau}$ peaks at $m_Z \sim 90$ GeV. In Eq. 6.6, p_{τ_1} and p_{τ_2} are four-momenta of the two taus which cannot be extracted

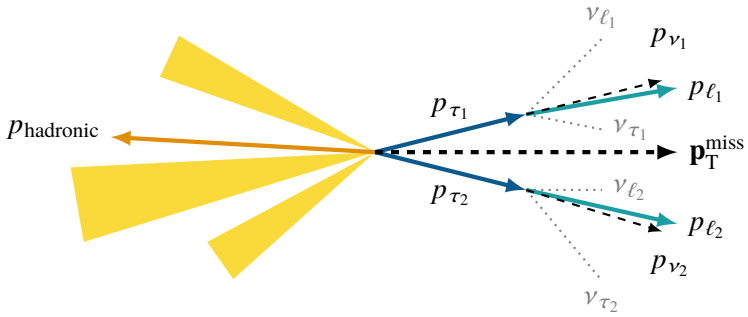

Figure 6.2: Schematic illustration of the fully leptonic ($Z \rightarrow \tau\tau$) + jets system, assuming that the lepton and the neutrinos from each tau decay are nearly collinear. The four-momenta of the two light leptons in the final state are denoted by p_{ℓ_1} and p_{ℓ_2}. The four-momenta of the two taus and the sum of the neutrinos from each tau decay are denoted by p_{τ_1}, p_{τ_2} and p_{ν_1}, p_{ν_2}, respectively. The p_{ν_1} and p_{ν_2} are not detectable, but are calculated under the collinear assumption, using the observed $\mathbf{p}_{\text{T}}^{\text{miss}}$.

directly from the measurements, because of the kinematic ambiguities from immeasurable neutrinos in the final state.

To resolve the ambiguity, we set an approximation that the taus are highly boosted, and thus the lepton and the neutrinos from each tau decay are nearly collinear [143–145]. Figure 6.2 illustrates a schematic diagram of this assumption. The four neutrinos in the final state, $\nu_{\ell_1}, \nu_{\ell_2}, \nu_{\tau_1}$ and ν_{τ_2} cannot be measured in the detector. Under the "collinear" assumption, the sum of the four-momenta the two neutrinos in each tau decay (p_{ν_1}, p_{ν_2}) can be calculated. We set

$$p_{\nu_i} = \xi_i \cdot p_{\ell_i}, \tag{6.7}$$

and thus

$$p_{\tau_i} = p_{\ell_i} + p_{\nu_i} = (1 + \xi_i) \cdot p_{\ell_i}, \tag{6.8}$$

where $i = \{1, 2\}$. The parameters ξ_i are determined from the $\mathbf{p}_{\text{T}}^{\text{miss}}$ measurement,

$$\mathbf{p}_{\text{T}}^{\text{miss}} = \xi_1 \mathbf{p}_{\text{T}}^{\ell_1} + \xi_2 \mathbf{p}_{\text{T}}^{\ell_2}. \tag{6.9}$$

This collinear approximation is justified because the two taus from the decay of the Z-boson are generally boosted, and moreover, in our analysis the mother Z boson itself is boosted by the ISR topology.

Assuming highly boosted taus such that $m_\tau^2 \sim 0$, the $m_{\tau\tau}^2$ in Equation (6.6) can be written by

$$m_{\tau\tau}^2 \simeq 2 p_{\ell_1} \cdot p_{\ell_2} (1 + \xi_1)(1 + \xi_2). \tag{6.10}$$

The $m_{\tau\tau}^2$ in Equation (6.10) can go negative, depending on the position of $\mathbf{p}_{\text{T}}^{\text{miss}}$ relative to p_{ℓ_1} and p_{ℓ_2}. Negative value of $m_{\tau\tau}^2$ implies that the collinear approximation has failed for that particular event, and thus this information need to be kept in the definition of the $m_{\tau\tau}$. To construct a variable that properly captures this information across the full range of $m_{\tau\tau}^2 \in [-\infty, \infty]$, the signed square root as shown in Equation (6.5) is used in this analysis. This prescription maintains a one-to-one map from the two lepton system to $m_{\tau\tau}^2$ and its distinct behaviour at negative values.

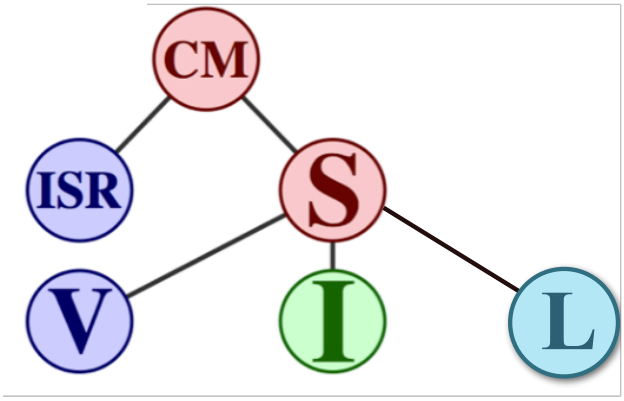

Figure 6.3: Decay tree corresponding to the signal processes [146]. In the center-of-mass frame indicated by CM in the figure, the ISR (initial-state radiation) the S (SUSY) systems are produced back-to-back. The S system further decays into I (invisible particles), V (visible particles), and L (leptons). The particles in the final state are categorized into either of the ISR, I, V or L system, according to the *Jigsaw Rules*.

R_{ISR}**:** The fraction of the ISR energy carried out by $\widetilde{\chi}_1^0$ s, defined as

$$R_{\mathrm{ISR}} = \frac{\mathbf{p}_{\mathrm{T}}^{\mathrm{miss}} \cdot \mathbf{p}_{\mathrm{SUSY}}^{\mathrm{CM}}}{|\mathbf{p}_{\mathrm{SUSY}}^{\mathrm{CM}}|^2}, \tag{6.11}$$

where $\mathbf{p}_{\mathrm{SUSY}}^{\mathrm{CM}}$ is the momentum of the "SUSY system", calculated as explained in the following paragraphs. The R_{ISR} is used to discriminate signals with small mass difference from the background events, as it has a value close to 1 for the signal event with small mass difference.

The R_{ISR} variable is calculated using the Recursive Jigsaw Reconstruction technique [146], to determine the rest frames of the intermediate states. The Recursive Jigsaw Reconstruction resolves kinematic ambiguities coming from invisible or indistinguishable particles, by estimating the missing information using some *Jigsaw Rules*. The brief idea of how the Recursive Jigsaw framework has been applied to a decay chain with ISR is demonstrated in the following paragraphs. More detailed discussion is summarized in Appendix B.2.

Figure 6.3 shows a decay tree diagram for this analysis. All the particles in the final state are categorized into four groups, or "frames"; I (invisible particles), V (visible particles), L (leptons) and ISR (initial-state-radiation jets). Each frame is defined by a four-vector, calculated by the sum of all the particles categorized into that group. The intermediate frames, CM and S correspond to center-of-mass system and the SUSY system, respectively, and can be calculated once all the particles are assigned to one of the frames. In this analysis, we only use the transverse kinematic variables to reconstruct transverse view of the full decay chain. Thus, each frame is characterized by transverse momentum vector $\mathbf{p}_{\mathrm{T}}$, and transverse mass m_{T}.

At the beginning, all the observed leptons are categorized in the L frame. Then for the I frame, information of $E_{\mathrm{T}}^{\mathrm{miss}}$ is assigned. The $E_{\mathrm{T}}^{\mathrm{miss}}$ only has two components: the energy and the direction of the transverse momentum. Here, we assume $|p_{\mathrm{T}}| = E_{\mathrm{T}}^{\mathrm{miss}}$, i.e. the masses of invisible particles are zero. This is not a correct assignment especially when we assume massive $\widetilde{\chi}_1^0$, but the choice of the mass parameters does not affect the relations of the kinematic variables we are interested in (see Appendix B.2 for details).

Table 6.2: Preselection requirements applied to all events entering into signal regions.

	Preselection requirements	
Variable	2ℓ	$1\ell 1T$
Number of leptons (tracks)	= 2 leptons	= 1 lepton and ≥ 1 track
Lepton p_{T} [GeV]	$p_{\mathrm{T}}^{\ell_1} > 5$	$p_{\mathrm{T}}^{\ell} < 10$
$\Delta R_{\ell\ell}$	$\Delta R_{ee} > 0.30$, $\Delta R_{\mu\mu} > 0.05$, $\Delta R_{e\mu} > 0.2$	$0.05 < \Delta R_{\ell\mathrm{track}} < 1.5$
Lepton (track) charge and flavor	$e^{\pm}e^{\mp}$ or $\mu^{\pm}\mu^{\mp}$	$e^{\pm}e^{\mp}$ or $\mu^{\pm}\mu^{\mp}$
Lepton (track) invariant mass [GeV]	$3 < m_{ee} < 60$, $1 < m_{\mu\mu} < 60$	$0.5 < m_{\ell\mathrm{track}} < 5$
J/ψ invariant mass [GeV]	veto $3 < m_{\ell\ell} < 3.2$	veto $3 < m_{\ell\mathrm{track}} < 3.2$
$m_{\tau\tau}$ [GeV]	< 0 or > 160	no requirement
$E_{\mathrm{T}}^{\mathrm{miss}}$ [GeV]	> 120	> 120
Number of jets	≥ 1	≥ 1
Number of b-tagged jets	= 0	no requirement
Leading jet p_{T} [GeV]	≥ 100	≥ 100
$\min(\Delta\phi(\text{any jet}, \mathbf{p}_{\mathrm{T}}^{\mathrm{miss}}))$	> 0.4	> 0.4
$\Delta\phi(j_1, \mathbf{p}_{\mathrm{T}}^{\mathrm{miss}})$	≥ 2.0	≥ 2.0

Then at last, jets are assigned to either the V or ISR frame. The ambiguity is resolved by Recursive Jigsaw Reconstruction technique, by applying *Jigsaw Rule VIII.2* in [146]. We assign the jets to V or ISR so that the transverse masses of the ISR and S (SUSY) frame, $M_{\mathrm{T}}^{\mathrm{ISR}}$ and $M_{\mathrm{T}}^{\mathrm{S}}$, are minimized simultaneously. From energy conservation, the total invariant mass in centre-of-mass frame, $M_{\mathrm{T}}^{\mathrm{CM}}$ can be calculated as

$$M_{\mathrm{CM}} = \sqrt{(M_{\mathrm{T}}^{\mathrm{ISR}})^2 + (\mathbf{p}_{\mathrm{ISR}}^{\mathrm{CM}})^2} + \sqrt{(M_{\mathrm{T}}^{\mathrm{S}})^2 + (\mathbf{p}_{\mathrm{SUSY}}^{\mathrm{CM}})^2}, \tag{6.12}$$

where $\mathbf{p}_{\mathrm{ISR}}^{\mathrm{CM}} = -\mathbf{p}_{\mathrm{SUSY}}^{\mathrm{CM}}$ are the transverse momenta of the two systems. Given that M_{CM} is constant in each event, Eq. 6.12 shows that maximizing the $\mathbf{p}_{\mathrm{ISR}}^{\mathrm{CM}^2}$ would minimize $M_{\mathrm{T}}^{\mathrm{ISR}}$ and $M_{\mathrm{T}}^{\mathrm{S}}$ simultaneously.

M_T^S : The transverse mass of the SUSY system, also calculated using the Recursive Jigsaw Reconstruction.

6.4 Preselection

Events are required to have at least one reconstructed pp interaction vertex. The vertex with the highest $\sum p_{\mathrm{T}}^2$ of associated tracks is selected as the primary vertex. Using the objects defined in Chapter 4, a set of common cuts listed in Table 6.2 are applied to all the signal regions in the 2ℓ and $1\ell 1T$ channels.

The reconstructed $E_{\mathrm{T}}^{\mathrm{miss}}$ is required to be greater than 120 GeV in the preselection. All events are required to have at least one jet with $p_{\mathrm{T}} > 100$ GeV. The leading jet is required to be separated from the $\mathbf{p}_{\mathrm{T}}^{\mathrm{miss}}$ by at least 2.0 radians in ϕ. Additional jets in the event are also required to be separated from the $\mathbf{p}_{\mathrm{T}}^{\mathrm{miss}}$ by $\min(\Delta\phi(\text{any jet}, \mathbf{p}_{\mathrm{T}}^{\mathrm{miss}}))$ >0.4.

The 2ℓ channels require exactly two opposite-sign leptons of the same flavor. The leading lepton is required to have $p_{\mathrm{T}} > 5$ GeV, which reduces backgrounds from the fake or the non-prompt leptons. Muons

Table 6.3: Requirements applied to events entering into the four signal regions used for the search. The $1\ell 1T$ preselection requirements from Table 6.2 are applied to the SR–E–$1\ell 1T$ region, while the 2ℓ ones are applied to the remaining signal regions.

	Electroweakino SR Requirements			
Variable	SR–E–low	SR–E–med	SR–E–high	SR–E–$1\ell 1T$
$E_{\mathrm{T}}^{\mathrm{miss}}$ [GeV]	$[120, 200]$	$[120, 200]$	> 200	> 200
$E_{\mathrm{T}}^{\mathrm{miss}}/H_{\mathrm{T}}^{\mathrm{lep}}$	< 10	> 10	–	> 30
$\Delta\phi(\mathrm{lep}, \mathbf{p}_{\mathrm{T}}^{\mathrm{miss}})$	–	–	–	< 1.0
Lepton or track p_{T} [GeV]	$p_{\mathrm{T}}^{\ell_2} > 5 + m_{\ell\ell}/4$	–	$p_{\mathrm{T}}^{\ell_2} > \min(10, 2 + m_{\ell\ell}/3)$	$p_{\mathrm{T}}^{\mathrm{track}} < 5$
$M_{\mathrm{T}}^{\mathrm{S}}$ [GeV]	–	< 50	–	–
$m_{\mathrm{T}}^{\ell_1}$ [GeV]	$[10, 60]$	–	< 60	–
R_{ISR}	$[0.8, 1.0]$	–	$[\max(0.85, 0.98 - 0.02 \times m_{\ell\ell}),\ 1.0]$	–

are required to be separated by $\Delta R_{\mu\mu} > 0.05$, while electrons are required to be separated by $\Delta R_{ee} > 0.3$ to avoid reconstruction inefficiencies due to overlapping showers in the EM calorimeter. An additional requirement that $m_{\ell\ell}$ be outside of $[3.0, 3.2]$ GeV is applied to remove contributions from J/ψ decays. Requirement of $m_{\ell\ell} < 60$ GeV are applied to reduce contributions from the on-shell Z-boson decays. Requirements on the $\Delta R_{\ell\ell}$ and $m_{\ell\ell}$ removes events in which an energetic photon produces collinear lepton pairs (photon conversion). Events with $0 < m_{\tau\tau} < 160$ GeV are rejected to reduce backgrounds from $Z \to \tau\tau$. Events with one or more b-tagged jets with $p_{\mathrm{T}} > 20$ GeV are vetoed to reduce backgrounds from $t\bar{t}$ production.

The $1\ell 1T$ channel require exactly one lepton and one opposite-sign signal track. The track is required to be associated with the lepton that has the same flavor with the leading lepton. In case more than one signal track is present, the candidate with the highest p_{T} is used. In contrast to the 2ℓ channels, an upperlimit of $p_{\mathrm{T}} < 10$ GeV is applied to the leptons in the $1\ell 1T$ channels. This requirement reduces the background from W+jets where the p_{T} of the leading lepton is generally larger than 10 GeV, with keeping the efficiencies for signals with small mass difference. The invariant mass of the lepton and the track $m_{\ell\mathrm{track}}$ is required to be $0.5 < m_{\ell\mathrm{track}} < 5$ GeV. The lower bound of $m_{\ell\mathrm{track}}$ and $\Delta R_{\ell\mathrm{track}}$ was set for the same reason as the 2ℓ channels, to avoid reconstruction inefficiencies in the overlaps. No requirement on $m_{\tau\tau}$ or number of b-tagged jets are present, as there are negligible contamination from $Z \to \tau\tau$ or $t\bar{t}$ processes in the phase-space we are interested in.

6.5 Signal Regions

The definitions of the signal regions are shown in Table 6.3. The 2ℓ channel is divided into three types of signal regions. The high-$E_{\mathrm{T}}^{\mathrm{miss}}$ signal region, denoted by "SR–E–high", requires $E_{\mathrm{T}}^{\mathrm{miss}} > 200$ GeV where the efficiency of the $E_{\mathrm{T}}^{\mathrm{miss}}$ trigger is $> 95\%$. The other two signal regions require 120 GeV $< E_{\mathrm{T}}^{\mathrm{miss}} < 200$ GeV, and are denoted by "SR–E–low" and "SR–E–med". These two signal regions are also collectively referred to as the low-$E_{\mathrm{T}}^{\mathrm{miss}}$ signal regions. The SR–E–med signal region is especially optimized for signals with small mass splittings, while the SR–E–low signal region targets mass splittings larger than 10 GeV. The $1\ell 1T$ signal region, denoted by "SR–E–$1\ell 1T$", requires $E_{\mathrm{T}}^{\mathrm{miss}} > 200$ GeV and targets signals with small mass splittings.

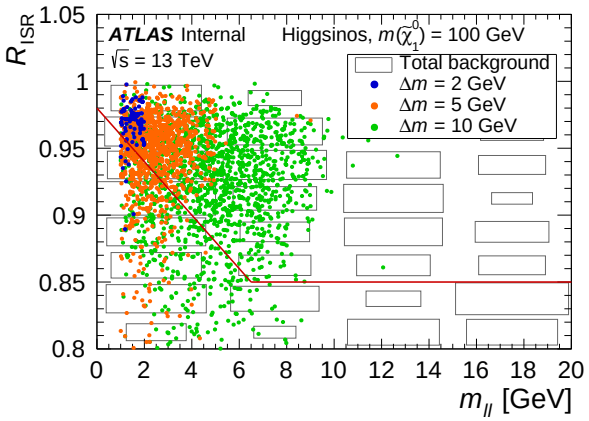

Figure 6.4: Correlation between the R_{ISR} and the $m_{\ell\ell}$ in the high-$E_{\mathrm{T}}^{\mathrm{miss}}$ signal regions, after applying all signal selection criteria except those on R_{ISR}. Signals for the higgsino simplified scenarios with different mass splittings are shown with circles. The blue, orange and green circles shows the distribution for the signals with $\Delta m = 2, 5$ and 10 GeV, respectively. The rectangle shows the amount of total background in the region. The solid red line indicates the requirement applied in the signal region; events in the region below the red line are rejected.

High-$E_{\mathrm{T}}^{\mathrm{miss}}$ signal region : SR–E–high

The high-$E_{\mathrm{T}}^{\mathrm{miss}}$ signal region requires $E_{\mathrm{T}}^{\mathrm{miss}} > 200$ GeV, and is sensitive to signals with wide range of Δm. A lower threshold for the p_{T} of the subleading lepton is applied to suppress backgrounds from fake/non-prompt leptons (described in Chapter 7), which tend to have small p_{T}. For small $m_{\ell\ell}$ region, however, the signal evens also have sub-leading lepton with small p_{T}, and thus a looser cut is applied. The final function of the cut value is $p_{\mathrm{T}}^{\ell_2} > \min(10, 2 + m_{\ell\ell}/3)$, where higher threshold is applied to events with large $m_{\ell\ell}$, and lower threshold is applied to events with small $m_{\ell\ell}$. The cut values are optimized using a Z_N significance metric [147] considering signals with different mass splittings. The R_{ISR} variable is sensitive to the mass splitting of the signal, with values near 1.0 for the signals with small mass splittings. Figure 6.4 shows the relationship between R_{ISR} and $m_{\ell\ell}$. For signals with smaller mass splittings, the $m_{\ell\ell}$ tends to become small and the R_{ISR} becomes close to 1.0. For signals with larger mass splittings, the $m_{\ell\ell}$ becomes larger and the R_{ISR} becomes smaller. A lower cut value for the R_{ISR} is determined as a function of $m_{\ell\ell}$, to exploited in this distribution. An upper cut on $m_{\mathrm{T}}^{\ell_1}$ is applied to suppress events with on-shell W boson.

Low-$E_{\mathrm{T}}^{\mathrm{miss}}$ signal regions : SR–E–low, SR–E–med

The two low-$E_{\mathrm{T}}^{\mathrm{miss}}$ signal regions are made orthogonal by requiring $E_{\mathrm{T}}^{\mathrm{miss}}/H_{\mathrm{T}}^{\mathrm{lep}} > 10$ for SR–E–med, and $E_{\mathrm{T}}^{\mathrm{miss}}/H_{\mathrm{T}}^{\mathrm{lep}} < 10$ for SR–E–low. The SR–E–low signal region targets scenarios with larger mass splittings, where the $H_{\mathrm{T}}^{\mathrm{lep}}$ becomes larger. For the SR–E–low signal region, lower cuts on the p_{T} of the sub-leading lepton and the R_{ISR}, as well as the upper cut on $m_{\mathrm{T}}^{\ell_1}$ is applied, with similar concept to the high-$E_{\mathrm{T}}^{\mathrm{miss}}$ signal region. The SR–E–med signal region is optimized for signal events with small mass splittings, where the $H_{\mathrm{T}}^{\mathrm{lep}}$ is expected to be small. For the SR–E–med signal region, an upper cut on M_T^S is applied, which is found to suppress fake/non-prompt background effectively.

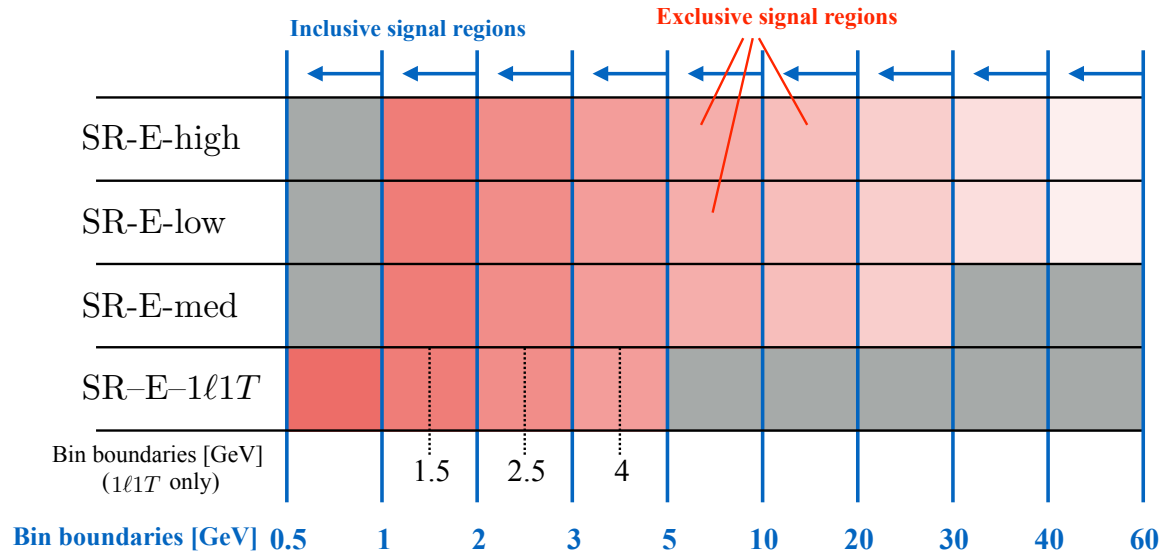

Figure 6.5: Schematic diagram illustrating the $m_{\ell\ell}$ bins in the signal regions. Four types of signal regions, SR–E–high, SR–E–low, SR–E–med and SR–E–$1\ell1T$ are considered, and are binned in $m_{\ell\ell}$. Each box corresponds to one exclusive signal region. An inclusive signal region is defined by merging all the exclusive signal regions with $m_{\ell\ell}$ below a bin boundary of the 2ℓ signal regions.

$1\ell1T$ signal region : SR–E–$1\ell1T$

The $1\ell1T$ channel targets signal scenarios with very small mass splittings, below a few GeV. Thus a large $E_{\mathrm{T}}^{\mathrm{miss}}$ relative to the p_{T} of the lepton and the track, $E_{\mathrm{T}}^{\mathrm{miss}}/H_{\mathrm{T}}^{\mathrm{lep}} > 30$, is required. The lepton is required to be within 1.0 radians from the $\mathbf{p}_{\mathrm{T}}^{\mathrm{miss}}$ in ϕ, to reduce backgrounds with tracks associated to non-prompt leptons or hadrons.

$m_{\ell\ell}$ binning

After all the selections are applied, the signal regions are binned in $m_{\ell\ell}$, with bin boundaries at $m_{\ell\ell} = 1, 2, 3, 5, 10, 20, 30, 40$, and 60 GeV for the 2ℓ channels, and at $m_{\ell\mathrm{track}} = 0.5, 1, 1.5, 2, 3, 4$, and 5 GeV for the $1\ell1T$ channel. Events in the SR–E–med region with $m_{\ell\ell} > 30$ GeV have minimal sensitivity to the electroweakino signals studied and are not considered. Similarly, events in the SR–E–$1\ell1T$ with $m_{\ell\mathrm{track}} > 5$ GeV are discarded. Figure 6.5 shows the schematic diagram of $m_{\ell\ell}$ bins in the signal regions.

The binned $m_{\ell\ell}$ distributions are used in two different types of statistical test, as explained in Section 9.2. The first test is a search for excesses with minimal model dependence. A single-bin "inclusive signal region" is used for this test. The inclusive signal region is constructed by merging all SR–E–high, SR–E–med, SR–E–low, and SR–E–$1\ell1T$ bins below a $m_{\ell\ell}$ bin boundary of the 2ℓ signal regions. The second type of test is referred to as an exclusion fit, which considers all signal region bins separately in the shape-fit. Each of the box in Figure 6.5 corresponds to one "exclusive signal region".

Chapter 7

Background Estimation

In this chapter, the details of the background estimation method are presented. Most of the contents in this chapter are focused on the backgrounds for the signal regions with two leptons. The overview of the background estimation strategy is described in Section 7.1. The method dedicated to model the reducible backgrounds, which contain at least one fake/non-prompt lepton, is explained in Section 7.2. The background estimation method for the irreducible backgrounds, which consists of processes with two prompt leptons, is described in Section 7.3. The definitions of the validation regions which are used to verify the background modeling are described inSection 7.4. Finally, the background estimation method for the $1\ell 1T$ signal regions is explained in Section 7.5.

7.1 Overview of background estimation strategy

Source of the SM backgrounds in the signal regions with two leptons can be subdivided into two categories: the reducible background from events where at least one of the candidate leptons is fake or non-prompt, and the irreducible background from events that contain two prompt leptons. Figure 7.2 shows a schematic diagram of the background estimation strategy.

Source of the irreducible background is further categorized into three groups; the "top" background from the $t\bar{t}/tW$ processes, the "diboson" background from the $WW/WZ/ZZ$ processes, and the "tau" background from the $Z^{(*)}/\gamma^{*}(\rightarrow \tau\tau)$ + jets process. The number of irreducible background in the signal region is estimated using MC, which are corrected using data. Each of the three major background components have different characteristics, thus are compared and normalized to data separately, in dedicated regions called "control regions".

The reducible background is mainly from events with one prompt lepton and one fake/non-prompt lepton. MC studies have shown that W+jet process dominates the reducible background, where the W-boson decays to a charged lepton and a neutrino, which is observed as prompt lepton plus a large $E_{\mathrm{T}}^{\mathrm{miss}}$. The other fake/non-prompt lepton comes from an extra jet or pile-up contributions, which is difficult to model by MC. Hence, the reducible background yield is estimated using a full data-driven method called fake factor method [148, 149].

Figure 7.1 shows a background component breakdown in three different signal regions, SR–E–high, SR–E–low and SR–E–med. For the SR–E–high (top left) and SR–E–low (top-right) selections, contributions from all the four main sources, top, diboson, tau and the reducible background (fake/non-prompt), are visible and each constitutes an important part of the background. For the SR–E–med selection, the reducible background accounts for most part of the background, followed by the contribution from the tau background.

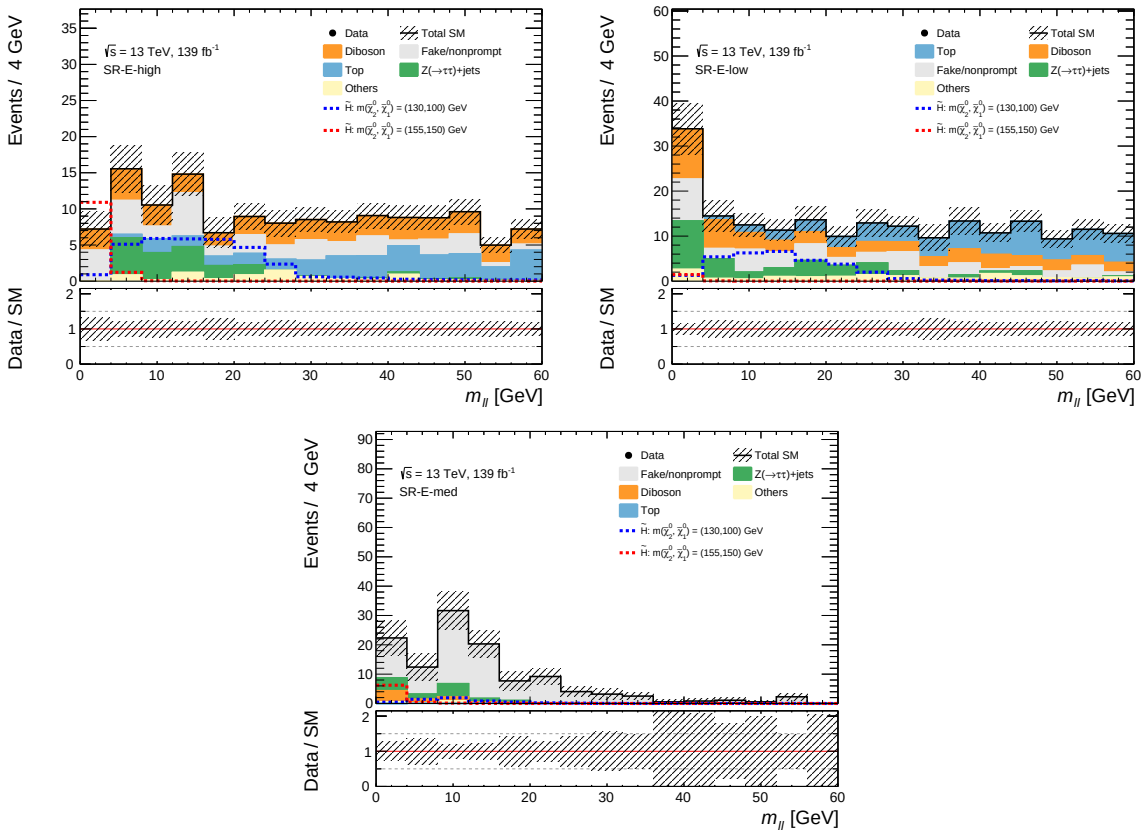

Figure 7.1: The distributions of the invariant mass of the two leptons ($m_{\ell\ell}$) in three different signal regions, SR–E–high (top left), SR–E–low (top right) and SR–E–med (bottom). Signal yields are shown in red and blue dashed lines. The uncertainty bands plotted include all statistical and systematic uncertainties.

Other minor irreducible backgrounds originating from Drell–Yan, triboson production, Higgs boson and top quark pair/single prediction in association with gauge bosons constitute only a small fraction of the total background. Thus their contributions are estimated using the MC samples listed in Table 3.1.

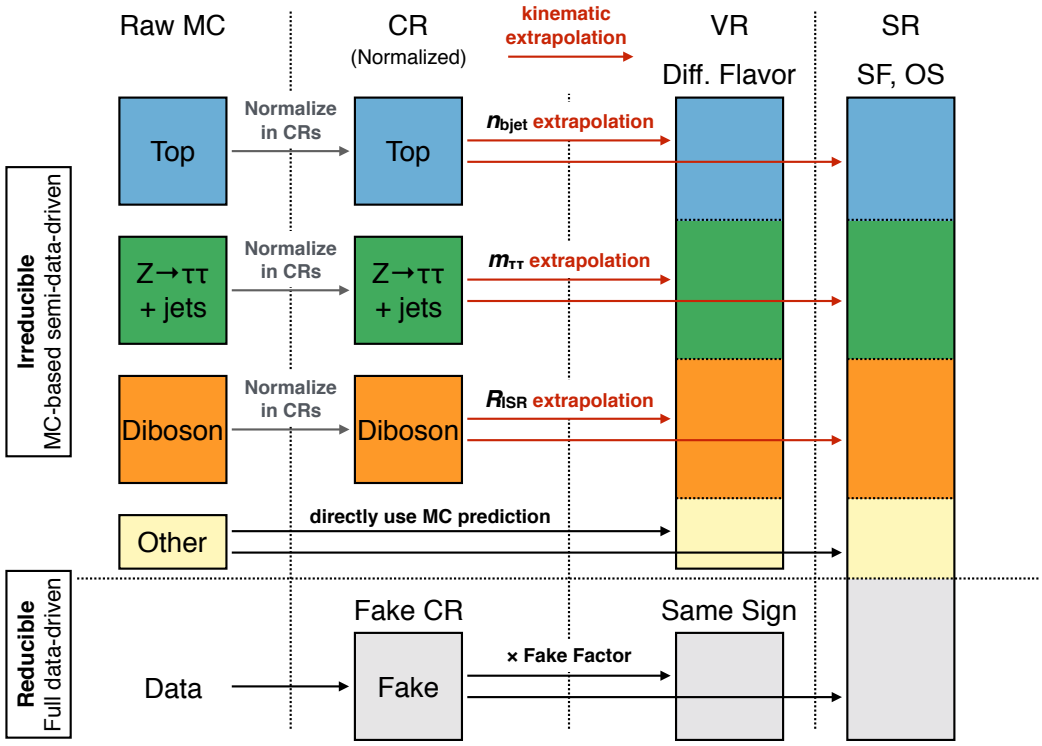

Figure 7.2: A schematic view of the background estimation method for the high-$E_{\mathrm{T}}^{\mathrm{miss}}$ regions. Major irreducible backgrounds with two prompt leptons are estimated using the MC samples, normalized to data in dedicated control regions. Minor irreducible backgrounds are directly derived from MC. The reducible background is estimated using fully data-driven fake factor method. The background prediction is verified in the validation regions, which have similar background composition to the signal regions. A similar strategy is applied to the low-$E_{\mathrm{T}}^{\mathrm{miss}}$ regions.

7.2 Reducible background

The fake factor method is used to estimate the fake/non-prompt lepton background in the two lepton regions. The general idea of this method is explained in Section 7.2.1. The definition of "anti-ID" selection, which plays an important role in the fake factor method, is discussed in Section 7.2.2. The definition of the fake factor measurement region and the measured fake factors are shown in Section 7.2.3. The method to apply the fake factors to events with two leptons is explained in Section 7.2.4,

7.2.1 Fake factor method

The idea of the fake factor method is illustrated in Figure 7.3. In this method, a region enriched with the fake/non-prompt leptons ("measurement region") is selected to measure the probability of a fake/non-prompt lepton to pass all the signal lepton requirements. A fake factor (FF) is defined as

$$FF = \frac{N_{\text{ID}}}{N_{\text{anti-ID}}}, \tag{7.1}$$

where N_{ID} is the number of fake/non-prompt leptons passing all the signal criteria, and $N_{\text{anti-ID}}$ is the number of fake/non-prompt leptons passing an "anti-ID" criteria, which is described in the following paragraphs. In the fake factor method, we often refer to the signal lepton criteria as "ID" criteria. The choice of the anti-ID selection must be orthogonal to the ID criteria. Once the fake factor is measured, we can apply this factor to the number of events in a "fake-enriched signal region" (N_{fake}). The fake-enriched signal region is defined by exactly the same selections as for the signal region, except for the requirements for leptons, where the anti-ID selection is used instead of the ID selection. The final estimation of the number of events in the signal region (N_{exp}) is obtained by

$$N_{\text{exp}} = N_{\text{fake}} \cdot FF = N_{\text{fake}} \cdot \frac{N_{\text{ID}}}{N_{\text{anti-ID}}}. \tag{7.2}$$

In the analysis, the fake factors are measured as a function of lepton p_{T}. This is because the lepton identification and isolation performance is strongly dependent on the lepton p_{T}, thus the fake factors are also expected to be dependent on the lepton p_{T}.

7.2.2 Anti-ID lepton definition

The choice of the anti-ID criteria can be essentially anything that are orthogonal to the ID criteria. However, the origin of the fake lepton is required to be similar between the leptons that pass the ID and the anti-ID criteria. This is because the fake factor method simply applies fake factor weights to events with leptons passing the anti-ID criteria and treat the leptons as the ID leptons. This assumes that the basic kinematics of the events with anti-ID leptons and ID leptons are similar to each other. For example, the fake/non-prompt electrons from photon conversions and heavy-flavor decays would obviously have different kinematics.

The origin of the leptons passing the ID and the anti-ID selections are studied using W+jets MC samples. Figure 7.4 and Figure 7.5 show the origin of the fake/non-prompt leptons in regions similar to the

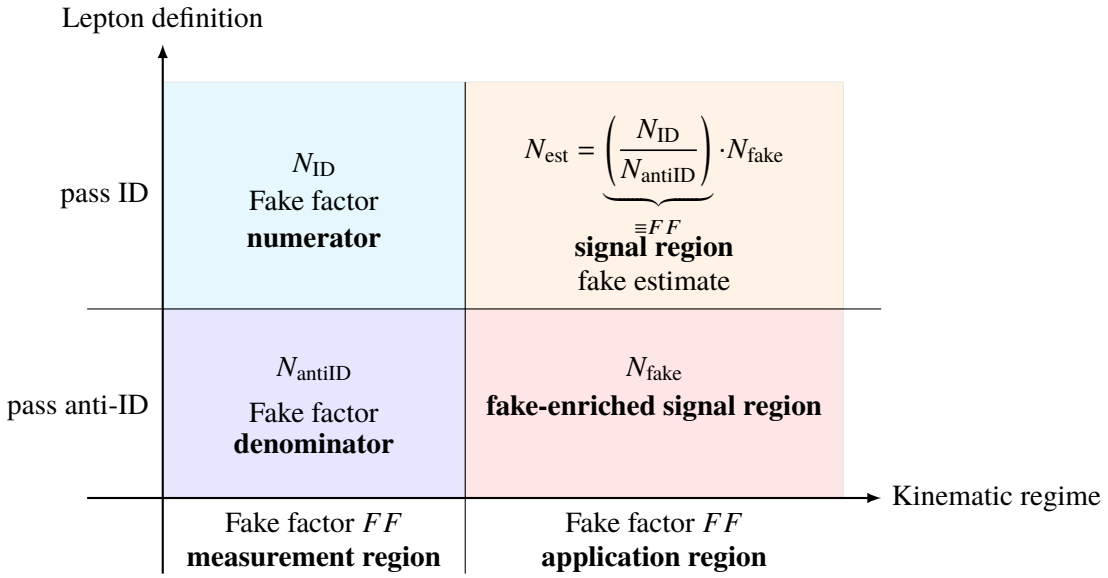

Figure 7.3: Schematic diagram illustrating the fake factor method to estimate the fake lepton contribution in the signal region. The number of events that pass ID (N_{ID}) and anti-ID (N_{antiID}) selections are measured in the measurement region, which are used to compute the fake factor (FF), defined as the ratio between N_{ID} and N_{antiID}. The fake factor is applied to the number of event in the "fake-enriched signal region" (N_{fake}), to get the expected number of events in the signal region N_{est}. The definition of the fake-enriched signal region is exactly the same as the signal region, but the lepton is required to pass anti-ID instead of ID selection.

signal region. Events in this region are required to pass the high-$E_{\text{T}}^{\text{miss}}$ signal region selections, except for cuts on the p_{T} of the sub-leading leptons and $m_{\text{T}}^{\ell_1}$, to gain statistics. The leading lepton is required to match with the lepton from a W-boson decay so that the sub-leading lepton is always a fake/non-prompt lepton. Checks with other regions are also done as summarized in Appendix C.5. The final definitions of the ID and anti-ID selections are shown in Table 7.1.

The origin of the fake/non-prompt electrons passing the final ID and anti-ID selections are shown in Figure 7.4. A large part of fake/non-prompt electrons that pass the ID criteria comes from the "Other" category, which includes hadrons mis-identified as electrons, or electrons from pile-up vertices. The next major source of the fake/non-prompt leptons is the heavy-flavor hadron decays, followed by a non-negligible contribution from photon conversions. The anti-ID electrons are defined to fail at least one of the ID criteria, but are required to pass the *Loose* identification with a hit in the innermost pixel layer (*LooseAndBLayer*). The anti-ID electrons are further required to pass either the *Medium* identification or the isolation. As shown in Figure 7.4, electrons that fail the *LooseAndBLayer* identification have larger contribution from the photon conversion, and thus are excluded from the anti-ID electrons. Similarly, electrons that fail both of the *Medium* identification and the *Gradient* isolation at the same time are dominated by the "Other" categories, and are removed.

Similar studies for muons are shown in Figure 7.5. The fake/non-prompt muons are dominated by the heavy-flavor decays, but there are considerable contributions of light-flavor decays especially at low-p_{T}. The anti-ID muons are defined to fail at least one of the ID criteria, but required to pass either the *FCTightTrackOnly* isolation or the d_0/σ_{d_0} cut. As shown in Figure 7.5, muons that fail these selections at the same time are dominated by the heavy-flavor decays significantly more than those passing the ID

Table 7.1: Summary of anti-ID lepton definitions. ID lepton definitions are also listed for comparison. Baseline selection are applied to both ID and anti-ID leptons. Anti-ID electrons are not allowed to fail the isolation and ID requirements simultaneously. Anti-ID muons are not allowed to fail d_0/σ_{d_0} and isolation requirements simultaneously.

	Electrons	Muons
Baseline	$p_{\mathrm{T}} > 4.5$ GeV $\lvert\eta\rvert < 2.47$ Pass *VeryLoose* identification $\lvert z_0 \sin\theta\rvert < 0.5$ mm	$p_{\mathrm{T}} > 3$ GeV $\lvert\eta\rvert < 2.5$ Pass *LowPt* identification $\lvert z_0 \sin\theta\rvert < 0.5$ mm
ID (Signal)	Pass *Medium* identification $d_0/\sigma_{d_0} < 5$ Pass *Gradient* isolation	– $d_0/\sigma_{d_0} < 3$ Pass *FCTightTrackOnly* isolation
Anti-ID	Fail ID selection Pass *LooseAndBLayer* identification Pass either *Medium* ID or isolation	Fail ID selection – Pass either d_0/σ_{d_0} or isolation

selections. Thus they are removed from the anti-ID definition.

7.2.3 Fake factor measurement region

In our analysis, the fake factors are measured in a data sample collected with single-lepton triggers with low p_{T} threshold. This sample is dominated by multi-jet events with fake/non-prompt leptons, and is referred to as the fake-factor measurement sample. A selection of $m_{\mathrm{T}}^{\ell_1} < 40$ GeV is applied to reduce the contributions from processes with prompt leptons in the measurement sample. The contributions from these processes after the cuts are subtracted using MC simulation.

To make the kinematic phase-space of the measurement region similar to that of the signal regions, the leading-jet p_{T} is required to be greater than 100 GeV. The fake factors are measured separately for electrons and muons. The fake factors are found to have a dependence on the number of b-tagged jets in the events, thus different fake factors are computed in events with and without b-tagged jets. In this section, we focus on the results for events without b-tagged jets. Similar results are obtained for events with b-tagged jets, as shown in Appendix C.3.

For the fake factor measurement, events in data are weighted according to a relevant lepton trigger prescale value. Then the ratio of weighted number of leptons passing the ID and the anti-ID requirements are calculated to obtain the fake factors binned in p_{T}. The MC events are used to subtract the contributions by the prompt leptons, which are scaled to match the yield of the data. The factors applied to the MC events (scale factors) are measured in the region with $m_{\mathrm{T}} > 100$ GeV, where the contribution of the fake/non-prompt leptons is negligible. These factors are measured separately for regions with ID and anti-ID leptons, and also separately with zero or more than one b-tagged jets. The scale factors are also measured using the region with $E_{\mathrm{T}}^{\mathrm{miss}} > 200$ GeV for comparison, which is expected to be dominated by the prompt leptons as well. The scale factors measured in high-m_{T} and high-$E_{\mathrm{T}}^{\mathrm{miss}}$ regions, for both electrons and muons, with and without b-tagged jets, are shown in Table 7.2. The difference of the scale factors are taken into account as a systematic uncertainty. The distributions of m_{T} for ID and anti-ID electrons and

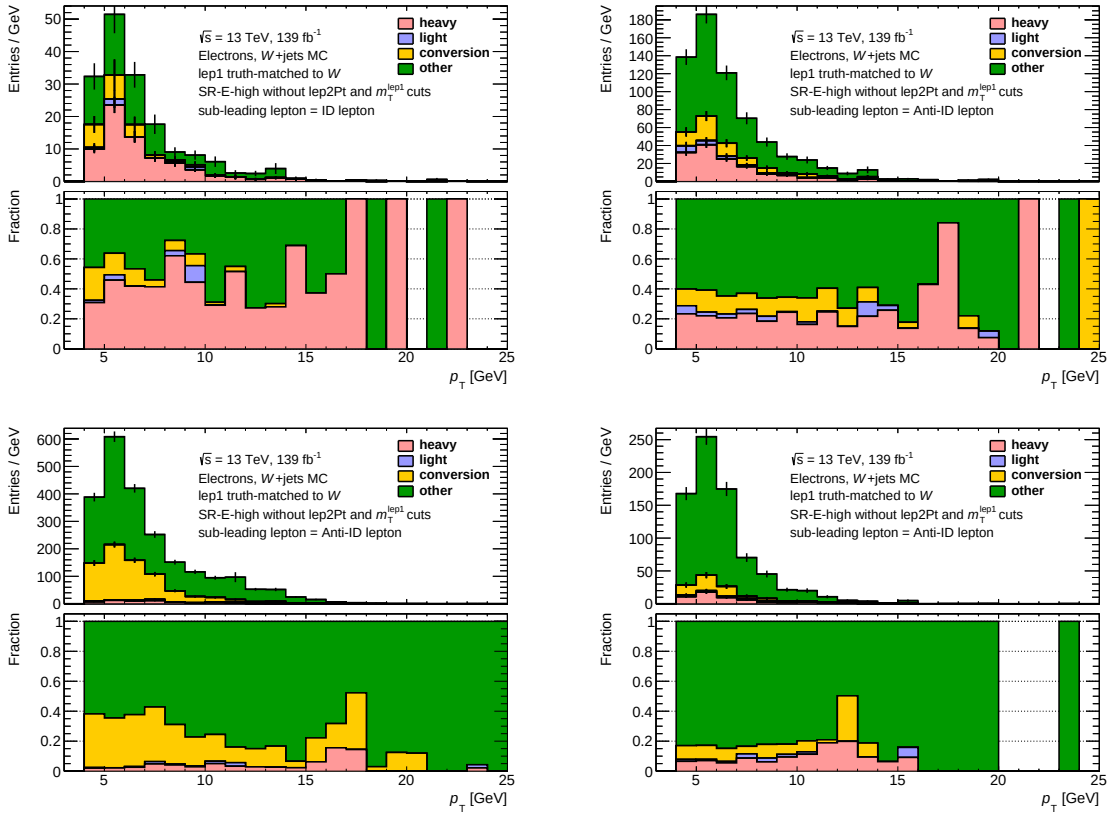

Figure 7.4: Origin of the fake electrons as a function of p_{T}, that (top left) pass the ID selections, (top right) pass the anti-ID selections, (bottom left) fail *LooseAndBLayer* identification (bottom right) fail both *Medium* identification and *Gradient* isolation. The information of the fake origin is taken from the W+jets MC. The red, blue, orange and green entries shows the contribution from the heavy-flavor hadrons, light-flavor hadrons, photon conversion, and other processes. The top panel in each plot shows the number of events in the p_{T} bin, and the bottom panel shows the fraction of each component in the p_{T} bin. Events are required to pass high-$E_{\mathrm{T}}^{\mathrm{miss}}$ signal region selections except for the requirements on the leptons. Cuts on sub-leading lepton p_{T} and $m_{\mathrm{T}}^{\ell_1}$ are also removed to enhance the statistics.

muons in events with exactly zero b-tagged jets are shown in Figure 7.6. The distributions of the p_{T} for ID and anti-ID electrons and muons are shown in Figure 7.7.

The final fake factors as a function of lepton p_{T} are shown in Figure 7.8 and Figure 7.9, for electrons and muons, respectively. The fake factors can only be calculated for leptons with p_{T} larger than the lowest trigger threshold, which is 5 GeV for electrons and 4 GeV for muons. In the analysis, we consider electrons and muons with p_{T} down to 4.5 GeV and 3 GeV, thus the fake factors need to be extrapolated down to these values. This is done by fitting and extrapolating the p_{T} distributions of the numerator and the denominator. An exponential function is used for the fitting, and the fit ranges are chosen to be from 6 to 10 GeV for electrons, and 4.5 to 10 GeV for muons. The lower limits of the fitting ranges are slightly higher than the trigger threshold to avoid the effect from trigger inefficiency near the threshold. The results of the fitting are shown in Figure 7.10 and Figure 7.11, for electrons and muons, respectively. The extrapolated fake factors are included in Figure 7.8 and Figure 7.9.

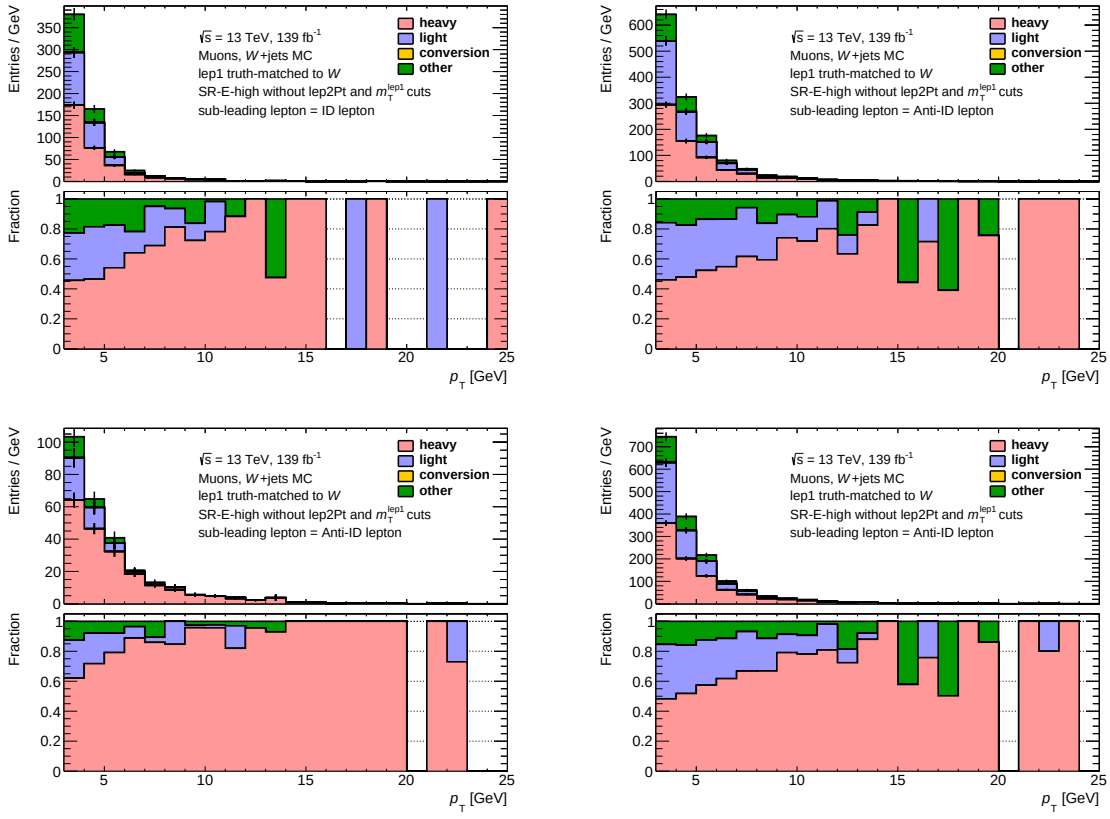

Figure 7.5: Origin of the fake muons as a function of p_{T}, that (top left) pass the ID selections, (top right) pass the anti-ID selections, (bottom left) fail d_0/σ_{d_0} cut and *FCTightTrackOnly* identification (bottom right) fail any of the ID selections The information of the fake origin is taken from the W+jets MC. The red, blue, orange and green entries shows the contribution from the heavy-flavor hadrons, light-flavor hadrons, photon conversion, and other processes. The top panel in each plot shows the number of events in the p_{T} bin, and the bottom panel shows the fraction of each component in the p_{T} bin. Events are required to pass high-$E_{\mathrm{T}}^{\mathrm{miss}}$ signal region selections except for the requirements on the leptons. Cuts on sub-leading lepton p_{T} and $m_{\mathrm{T}}^{\ell_1}$ are also removed to enhance the statistics.

7.2.4 Application of fake factors to 2ℓ analysis

A control data sample for fake the leptons is defined by requiring at least one of the leptons to meet the anti-ID criteria. This sample is enriched in the fake/non-prompt lepton backgrounds and is therefore referred to as the fake/non-prompt control sample. The contributions from processes with two prompt leptons in the fake/non-prompt control sample are subtracted using MC. The leptons in the fake/non-prompt control sample arise from processes similar to those for fake/non-prompt leptons passing the signal region selections, as explained in Section 7.2.2. The fake/non-prompt lepton background prediction in a given region is obtained by applying all the selection requirements except for the signal lepton requirements of that region to the fake/non-prompt control sample, and scaling the observed number of events by the measured fake factor.

Up to here we only discussed the simplified case, where there is at most one anti-ID lepton in a given event. In general, however, processes with multiple fake leptons can enter the signal region, thus events with multiple anti-ID leptons also play a role. Ultimately, the estimation of the reducible background due

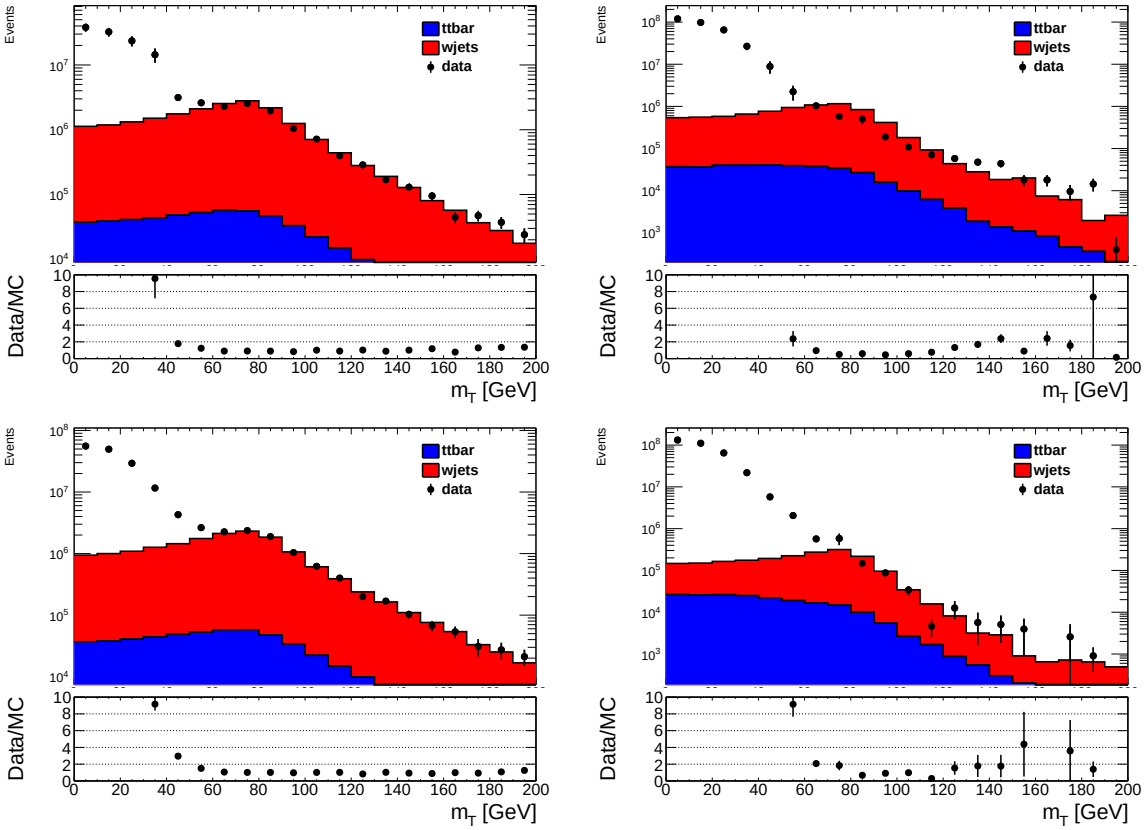

Figure 7.6: The distributions of the m_{T} for electrons (top) and muons (bottom), passing ID (left) and Anti-ID (right) selections, in the fake-factor measurement region with no b-tagged jets. The contribution from events with a prompt lepton is estimated using the MC, and are shown with blue and red histograms for $t\bar{t}$ and W+jets processes, respectively. The MC distribution is scaled to the data in the $m_{\mathrm{T}} > 100$ GeV region. The difference between the data and MC in the low-m_{T} region corresponds to the events with fake/non-prompt lepton.

Table 7.2: The scale factors measured in the regions with ID and Anti-ID leptons,

Region	$m_{\mathrm{T}} > 100$ GeV		$E_{\mathrm{T}}^{\mathrm{miss}} > 200$ GeV	
	Anti-ID	ID	Anti-ID	ID
Electrons, 0 b-jet	6.14 ± 0.44	1.42 ± 0.04	2.30 ± 0.19	1.38 ± 0.30
Electrons, 1 b-jet	2.54 ± 0.22	1.13 ± 0.04	0.85 ± 0.31	0.91 ± 0.09
Muons, 0 b-jet	3.62 ± 0.7	1.32 ± 0.05	6.09 ± 3.91	3.74 ± 0.76
Muons, 1 b-jet	2.90 ± 0.46	1.10 ± 0.05	2.58 ± 1.76	1.42 ± 0.19

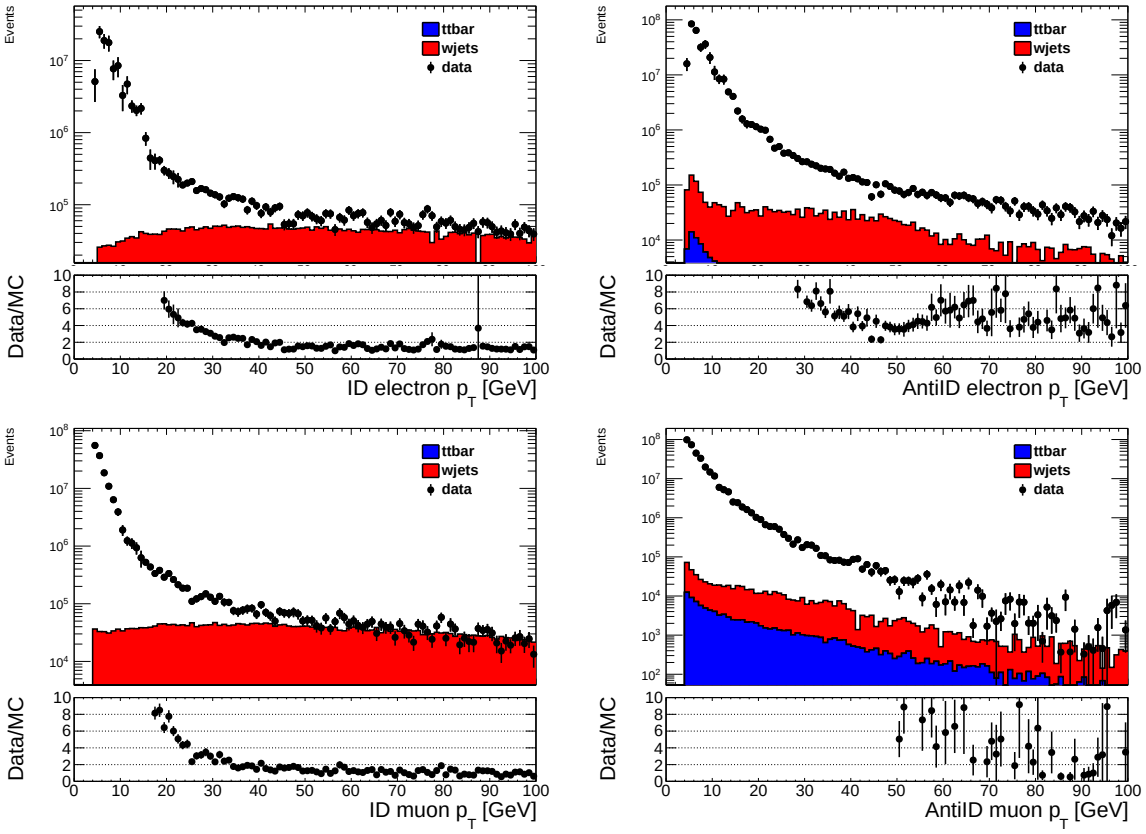

Figure 7.7: The distributions of the p_{T} for electrons (top) and muons (bottom), passing ID (left) and Anti-ID (right) selections, in the fake-factor measurement region with no b-tagged jets. The contribution from events with a prompt lepton is estimated using the MC, and are shown with blue and red histograms for $t\bar{t}$ and W+jets processes, respectively. The MC distribution is scaled to the data in the $m_{\mathrm{T}} > 100$ GeV region, as shown in Figure 7.6. The difference between the data and MC in the low-m_{T} region corresponds to the events with fake/non-prompt lepton.

to the fake leptons is given by

$$N_{TT} - N_{TT}^{RR} = \left[N_{LT} - N_{LT}^{RR}\right] F_1 + \left[N_{TL} - N_{TL}^{RR}\right] F_2 - \left[N_{LL} - N_{LL}^{RR}\right] F_1 F_2, \tag{7.3}$$

where the subscripts shows how the lepton is identified. T and L stands for "Tight" and "Loose" respectively, corresponding to passing ID and anti-ID criteria. The superscript RR refers to the events with two real leptons, which can be subtracted off using the MC. The F_1 and F_2 refer to the fake factors associated to the leading and subleading lepton, respectively. The final term with the negative contribution comes from double-counting of events that contain two fake leptons. The observed N_{TL} includes contribution from two fake leptons that are observed as TL, and the same stands for N_{LT}. Contribution from events with two fake leptons are double-counted thus need to be subtracted. More accurate argument is in Appendix C.4.

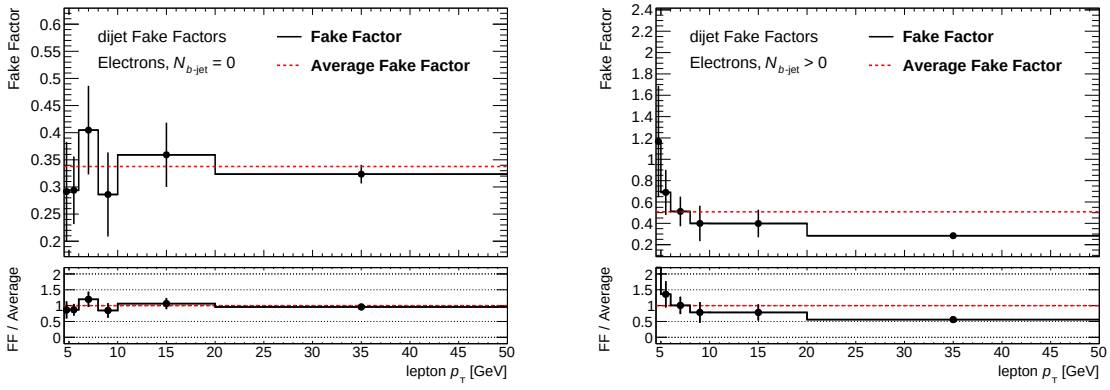

Figure 7.8: Fake factors for electrons computed in events with single-electron prescaled triggers, as a function of electron p_{T} for events with zero b-tagged jets (left) and at least one b-tagged jet (right) in the kinematic region with leading jet $p_{\mathrm{T}} > 100$ GeV and $m_{\mathrm{T}} < 40$ GeV. A red line denotes the average fake factor for electrons over all p_{T} range of the electrons.

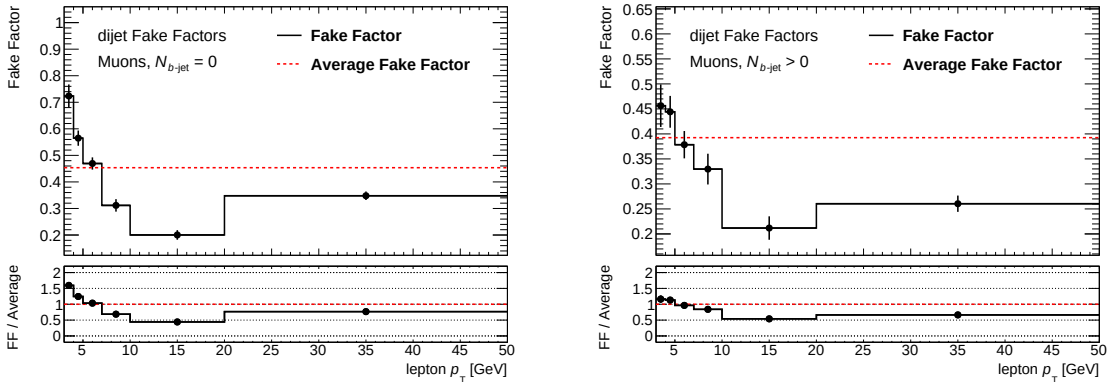

Figure 7.9: Fake factors for muons computed in events with single-muon prescaled triggers, as a function of muon p_{T} for events with zero b-tagged jets (left) and at least one b-tagged jet (right) in the kinematic region with leading jet $p_{\mathrm{T}} > 100$ GeV and $m_{\mathrm{T}} < 40$ GeV. A red line denotes the average fake factor for muons over all p_{T} range of the muons.

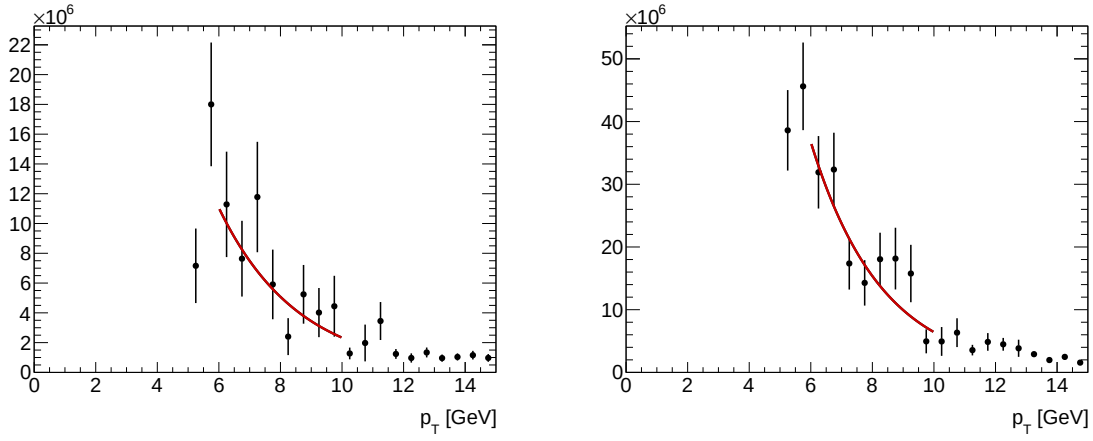

Figure 7.10: The p_{T} distributions of the electrons that pass (left) ID criteria and (right) anti-ID criteria, in fake-factor measurement region with no b-tagged jets. The red line indicates the results of fitting with an exponential function in $p_{\mathrm{T}} \in [6, 10]$ GeV. The fitted exponential functions are extrapolated down to 4.5 GeV to calculate the fake factors in whole p_{T} range.

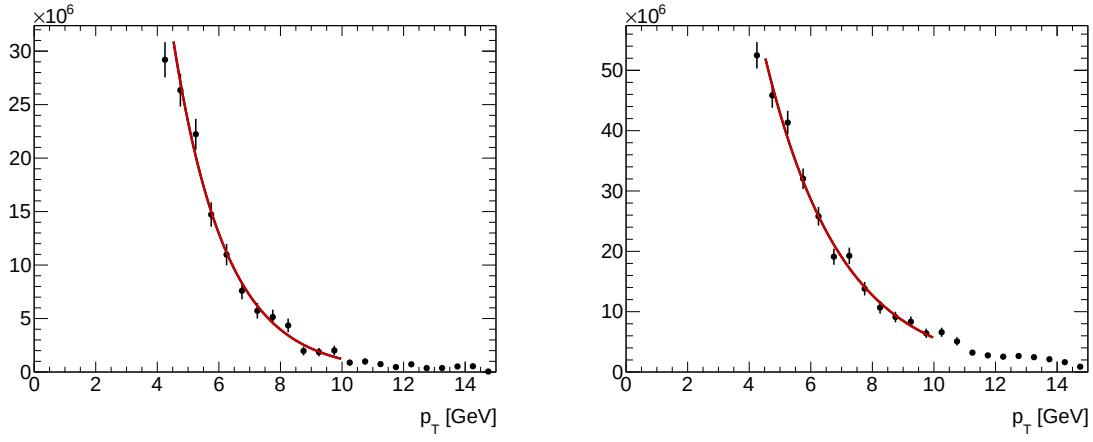

Figure 7.11: The p_{T} distributions of the muons that pass (left) ID criteria and (right) anti-ID criteria, in fake-factor measurement region with no b-tagged jets. The red line indicates the results of fitting with an exponential function in $p_{\mathrm{T}} \in [4.5, 10]$ GeV. The fitted exponential functions are extrapolated down to 3 GeV to calculate the fake factors in whole p_{T} range.

7.3 Irreducible backgrounds

7.3.1 Irreducible background processes

This section briefly explains the source of the major irreducible backgrounds. The $t\bar{t}/tW$ processes are collectively referred to as "top" background, which produces two prompt leptons when both top(s) and W-boson decay leptonically. The neutrinos produced in the decays are observed as large $E_{\mathrm{T}}^{\mathrm{miss}}$. The leptons from the decay of top quarks tend to have high p_{T} (a few tens of GeV), and two leptons are produced from different mother particles in both of the $t\bar{t}$ and tW cases, which make $m_{\ell\ell}$ likely to be larger than a few tens of GeV.

The $WW/WZ/ZZ$ processes are referred to as VV or "diboson" background. Decay modes with two or three prompt leptons are dominant source of the background in the signal regions. The $WW/ZZ \to \ell\ell\nu\nu$ or $WZ \to \ell\ell\ell\nu$ process with one of the leptons not detected due to the limitation of the detector acceptance mainly contributes to this background. The γ^*/Z^* decays produce two correlated leptons with small $m_{\ell\ell}$, while two leptons from W decays would produce relatively large $m_{\ell\ell}$ values. This makes a broad $m_{\ell\ell}$ distribution for the diboson background.

The $Z^{(*)}/\gamma^*(\to \tau\tau)$ + jets background, labeled as "tau" background, enters signal regions when both τ leptons decay leptonically. The neutrinos from the τ decays contribute to a large $E_{\mathrm{T}}^{\mathrm{miss}}$, especially when two τ leptons are collimated. The leptons from the τ decays tend to have lower p_{T} compared to those from the decay of top or on-shell weak bosons, and the collimated τ leptons from $Z^{(*)}/\gamma^*(\to \tau\tau)$ + jets decays make a peak in the $m_{\ell\ell}$ distribution at $m_{\ell\ell} \sim 20 - 30$ GeV.

7.3.2 Kinematical extrapolation method

The major three irreducible backgrounds are estimated based on MC simulations which are normalized to data in dedicated control regions. To constrain the normalization factor for each process independently, the control regions should be enriched with a particular background process. The control regions are also required to have similar kinematic properties to the signal regions, so that the event rates in the signal regions can be predicted by extrapolating the MC distributions. The normalized MC distributions are then verified in validation regions, and extrapolated to the signal regions to give a background estimation. Figure 7.12 shows a schematic diagram of the kinematic extrapolation method. The blue line shows the primary MC estimation, and the red line shows the rescaled MC estimation. The scale factor is determined in a control region, and is extrapolated to the validation region and the signal region. The background prediction is checked in the validation region to verify the extrapolation, before unblinding the signal region.

7.3.3 Control region definitions

Control regions are defined separately for the top, diboson and tau backgrounds. The control regions are also separated in $E_{\mathrm{T}}^{\mathrm{miss}}$, as events in high-$E_{\mathrm{T}}^{\mathrm{miss}}$ and low-$E_{\mathrm{T}}^{\mathrm{miss}}$ regions generally have different kinematics, and also because the mis-modeling of the trigger efficiency in the simulation may lead to different normalization factor depending on $E_{\mathrm{T}}^{\mathrm{miss}}$. Most of the selections applied to the SR–E–high signal regions are applied to the

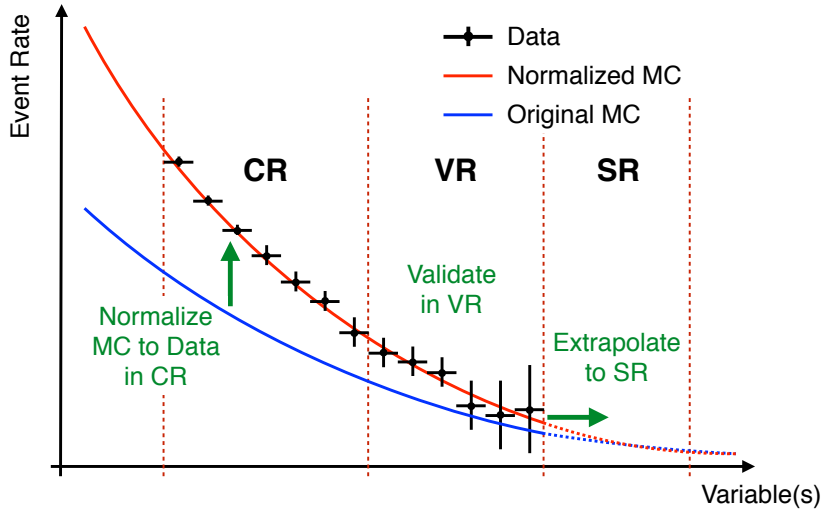

Figure 7.12: Schematic view of kinematic extrapolation method. The MC are normalized to data in a control region, validated in a validation region, and extrapolated to the signal region to estimate the background yield.

Table 7.3: Definitions of control regions ("CR" prefix) used for background estimation in the search, presented relative to the definitions of the corresponding signal regions SR–E–high, SR–E–med and SR–E–low. The 2ℓ preselection criteria from Table 6.2 and selection criteria from Table 6.3 are applied, except for the cuts specified in the table.

Region	Signal region orthogonality	Lepton Flavor	Additional requirements
CRtop–E–high CRtop–E–low	$N^{20}_{b-\text{jet}} \geq 1$	$ee + \mu\mu + e\mu + \mu e$	$R_{\text{ISR}} \in [0.7, 1.0]$, $m_{\text{T}}^{\ell_1}$ removed $E_{\text{T}}^{\text{miss}}/H_{\text{T}}^{\text{lep}}$ and $m_{\text{T}}^{\ell_1}$ removed
CRtau–E–high CRtau–E–low	$m_{\tau\tau} \in [60, 120]$ GeV	$ee + \mu\mu + e\mu + \mu e$	$R_{\text{ISR}} \in [0.7, 1.0]$, $m_{\text{T}}^{\ell_1}$ removed $R_{\text{ISR}} \in [0.6, 1.0]$, $m_{\text{T}}^{\ell_1}$ removed
CRVV–E–high CRVV–E–low	$R_{\text{ISR}} \in [0.7, 0.85]$ $R_{\text{ISR}} \in [0.6, 0.8]$	$ee + \mu\mu + e\mu + \mu e$	$m_{\text{T}}^{\ell_1}$ removed $m_{\text{T}}^{\ell_1} > 30$ GeV, $N_{\text{jets}} \in [1, 2]$, $E_{\text{T}}^{\text{miss}}/H_{\text{T}}^{\text{lep}}$ removed

high-$E_{\text{T}}^{\text{miss}}$ control regions as well. For the low-$E_{\text{T}}^{\text{miss}}$ control regions, similar cuts as the SR–E–low signal regions are applied. Some cuts are reverted or modified to ensure that the control regions are orthogonal to the signal regions and are enriched with the target background process. The low-$E_{\text{T}}^{\text{miss}}$ control regions are also used to constrain the background process entering the SR–E–med signal regions, as they do not have dedicated control regions. Instead, an extra validation region is defined to justify the extrapolation to SR–E–med (described in Section 7.4). The definition of the six control regions used in this analysis are summarized in Table 7.3.

The control regions labeled as CRtop are defined by selecting events with at least one b-tagged jet. The number of events in the control regions is increased by removing the $m_{\text{T}}^{\ell_1}$ selections used in the corresponding signal regions. For the high-$E_{\text{T}}^{\text{miss}}$ top control region, cuts on R_{ISR} are loosened, to further increase the statistics. For the same reason, in the low-$E_{\text{T}}^{\text{miss}}$ top control region (CRtop–E–low), cuts on

Table 7.4: Breakdown of the SM processes in the control regions, before normalization. CR–top, CR–tau, CR–VV corresponds to top, tau and diboson control regions, and the suffix –high and –low indicates the high-$E_{\mathrm{T}}^{\mathrm{miss}}$ and low-$E_{\mathrm{T}}^{\mathrm{miss}}$ control regions. "Purity" row represents the fraction of the target process in the corresponding control region. The errors shown are the statistical plus systematic uncertainties.

Region	CRtop–E–high	CRtop–E–low	CRtau–E–high	CRtau–E–low	CRVV–E–high	CRVV–E–low
Total events	4074.2 ± 655.6	5767.2 ± 941.5	613.6 ± 70.2	2227.2 ± 271.5	705.4 ± 91.6	813.5 ± 109.2
$Z(\rightarrow \tau\tau)$+jets	29.1 ± 7.3	18.8 ± 5.48	506.9 ± 62.0	1911.8 ± 259.9	90.8 ± 15.1	27.8 ± 6.59
Fake/non-prompt	414.8 ± 104.0	238.6 ± 80.8	36.2 ± 30.7	99.8 ± 71.8	74.6 ± 29.7	68.1 ± 18.6
Diboson	130.4 ± 30.5	63.3 ± 15.6	39.2 ± 7.28	101.4 ± 19.3	290.8 ± 63.9	370.2 ± 73.4
$t\bar{t}$, single top	3459.9 ± 646.5	5419.9 ± 937.9	21.3 ± 5.24	80.5 ± 19.9	223.3 ± 56.1	273.5 ± 76.1
Others	39.9 ± 2.96	26.6 ± 2.35	10.0 ± 2.73	33.7 ± 3.06	25.9 ± 2.82	73.9 ± 8.62
Purity	84.9%	94.0%	82.6%	85.8%	41.2%	45.5%

$E_{\mathrm{T}}^{\mathrm{miss}}/H_{\mathrm{T}}^{\mathrm{lep}}$ are removed. The $t\bar{t}/tW$ processes containing two prompt leptons yield same-flavor lepton pairs (ee and $\mu\mu$) at the same rate as for different-flavor pairs ($e\mu$ and μe). This feature is used to enhance the statistical constraining power of the control regions, by selecting events with all possible flavor assignments (ee, $\mu\mu$, $e\mu$, and μe). The high-$E_{\mathrm{T}}^{\mathrm{miss}}$ and low-$E_{\mathrm{T}}^{\mathrm{miss}}$ top control regions have 85% and 94% purities in processes with top quarks, with about 4000 and 5800 expected events in total, respectively. The purities and the numbers of events in the control regions are shown in Table 7.4, which are both found to be sufficient to constrain the normalization factors at reasonable precision.

The tau control regions, denoted by CRtau, are constructed by selecting events satisfying $m_{\tau\tau} \in [60, 120]$ GeV. In both of the high-$E_{\mathrm{T}}^{\mathrm{miss}}$ and low-$E_{\mathrm{T}}^{\mathrm{miss}}$ control regions, the $m_{\mathrm{T}}^{\ell_1}$ cuts are removed and the R_{ISR} cuts are loosened, to increase the statistics. The $Z^{(*)}/\gamma^*(\rightarrow \tau\tau)$ + jets process with two leptons yield same-flavor and different-flavor lepton pairs at the same rate, thus all the flavor combinations are included in the control regions. The tau control regions have the purities of at least 80%, with approximately 600 and 2000 events in high-$E_{\mathrm{T}}^{\mathrm{miss}}$ and low-$E_{\mathrm{T}}^{\mathrm{miss}}$ regions, respectively.

Finally, the diboson control regions, referred to as CRVV, are constructed by modifying the R_{ISR} selection in the corresponding signal regions. In both of the high-$E_{\mathrm{T}}^{\mathrm{miss}}$ and low-$E_{\mathrm{T}}^{\mathrm{miss}}$ control regions, the cut with $m_{\mathrm{T}}^{\ell_1} < 60$ GeV is removed to enhance the number of events, but in the low-$E_{\mathrm{T}}^{\mathrm{miss}}$ control region, a lower cut $m_{\mathrm{T}}^{\ell_1} > 30$ GeV is applied to reduce the contamination of events from the $Z^{(*)}/\gamma^*(\rightarrow \tau\tau)$ + jets process. In addition, a cut on the number of jets, $N_{\mathrm{jets}} \in [1, 2]$ is applied to suppress contribution from the top backgrounds. The diboson control regions allow different-flavor lepton pairs, because the WW process with two leptons in the final state has the same yield for same-flavor and different-flavor events. The purities of the diboson processes in the control regions range from 41 to 45%, with 700–800 events in each control region.

Figure 7.13, Figure 7.14 and Figure 7.15 shows the distributions of the observables in top, tau and diboson control regions, respectively.

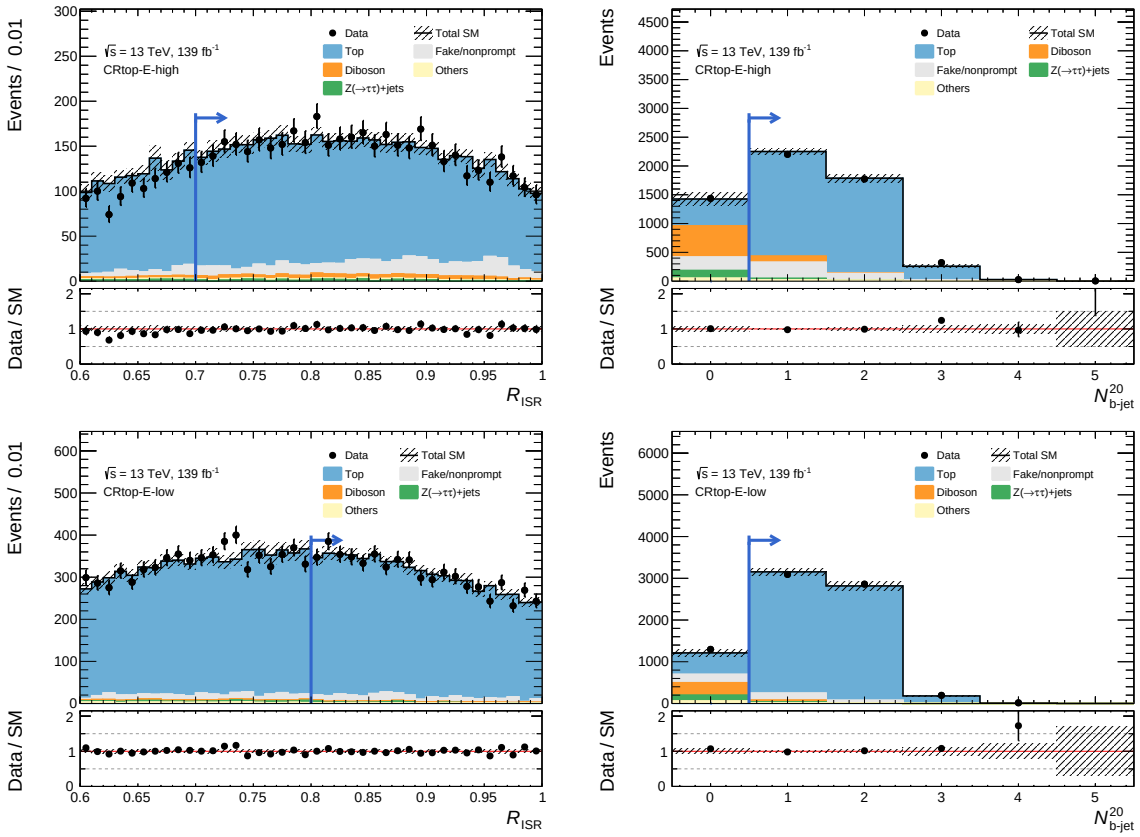

Figure 7.13: The distributions of the R_{ISR} (left) and number of b-tagged jets (right) in CRtop-E-high (top) and CRtop-E-low (bottom). The background expectation is obtained by the background-only fit in all the six control regions. The full event selection of the corresponding regions is applied, except for distributions showing blue arrows, where the requirement on the variable being plotted is removed and indicated by the arrows in the distributions instead. The first (last) bin includes underflow (overflow). The uncertainty bands plotted include all statistical and systematic uncertainties.

7.4 Validation regions

The reducible and irreducible background estimations, obtained by the fake factor method and the MC normalization, are extrapolated to the validation regions, to verify the background estimation methods. Three types of validation regions are defined, as shown in Table 7.5.

The same-sign validation regions, denoted by VRSS, are constructed for each signal region, by selecting events with two leptons with the same electric charge. This region is highly dominated by the reducible backgrounds, as irreducible background processes always have two different-charged leptons, and thus are significantly suppressed by the same-sign requirement. For the reducible backgrounds, the charge of the fake/non-prompt lepton is not relevant to the prompt lepton. Thus the same-sign and opposite-sign events are observed at approximately the same rate, with very similar kinematics. Three different same-sign validation regions, with the suffix "high", "low" and "med" are defined to validate the estimation of the reducible background for the corresponding signal regions. Some cuts are removed or loosened to increase the statistics. For VRSS–high, the R_{ISR} cuts are loosened to $R_{\mathrm{ISR}} \in [0.7, 1.0]$, and cuts on $m_{\mathrm{T}}^{\ell_1}$ and $p_{\mathrm{T}}^{\ell_2}$

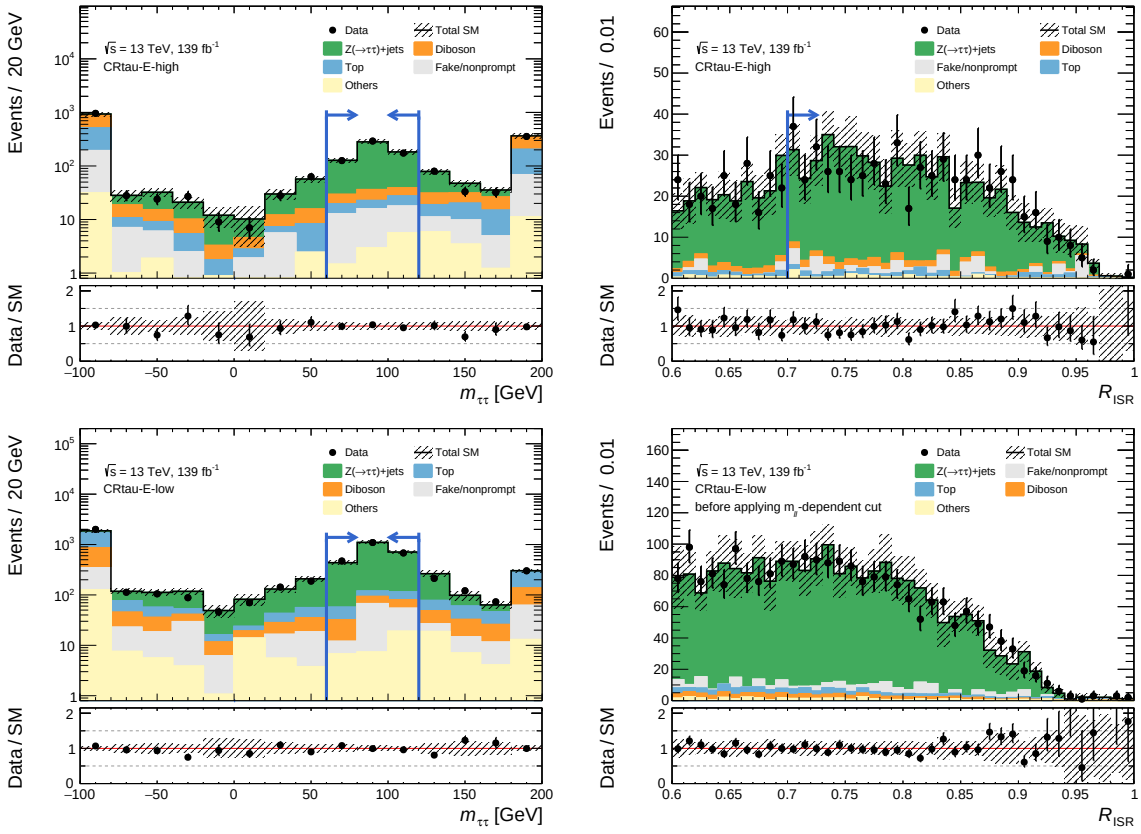

Figure 7.14: The distributions of the $m_{\tau\tau}$ (left) and R_{ISR} (right) in CRtau-E-high (top) and CRtau-E-low (bottom). The background expectation is obtained by the background-only fit in all the six control regions. The full event selection of the corresponding regions is applied, except for distributions showing blue arrows, where the requirement on the variable being plotted is removed and indicated by the arrows in the distributions instead. The first (last) bin includes underflow (overflow). The uncertainty bands plotted include all statistical and systematic uncertainties.

Table 7.5: Definitions of validation regions ("VR" prefix) used to validate the background estimation, presented relative to the definitions of the corresponding signal regions SR–E–high, SR–E–med and SR–E–low. The 2ℓ preselection criteria from Table 6.2 and selection criteria from Table 6.3 are applied, except for the cuts specified in the table.

Region	Signa region orthogonality	Lepton Flavor	Additional requirements
VRSS–E–high	Same sign $\ell^{\pm}\ell^{\pm}$	$ee + \mu e,\ \mu\mu + e\mu$	$R_{\text{ISR}} \in [0.7, 1.0]$, $m_{\text{T}}^{\ell_1}$ and $p_{\text{T}}^{\ell_2}$ removed
VRSS–E–low			$E_{\text{T}}^{\text{miss}}/H_{\text{T}}^{\text{lep}}$, $m_{\text{T}}^{\ell_1}$ and $p_{\text{T}}^{\ell_2}$ removed
VRSS–E–med			–
VRDF–E–high	$e\mu + \mu e$	$e\mu + \mu e$	–
VRDF–E–low			–
VRDF–E–med			–
VRtau–E–med	$m_{\tau\tau} \in [60, 120]$ GeV	$ee + \mu\mu + e\mu + \mu e$	–

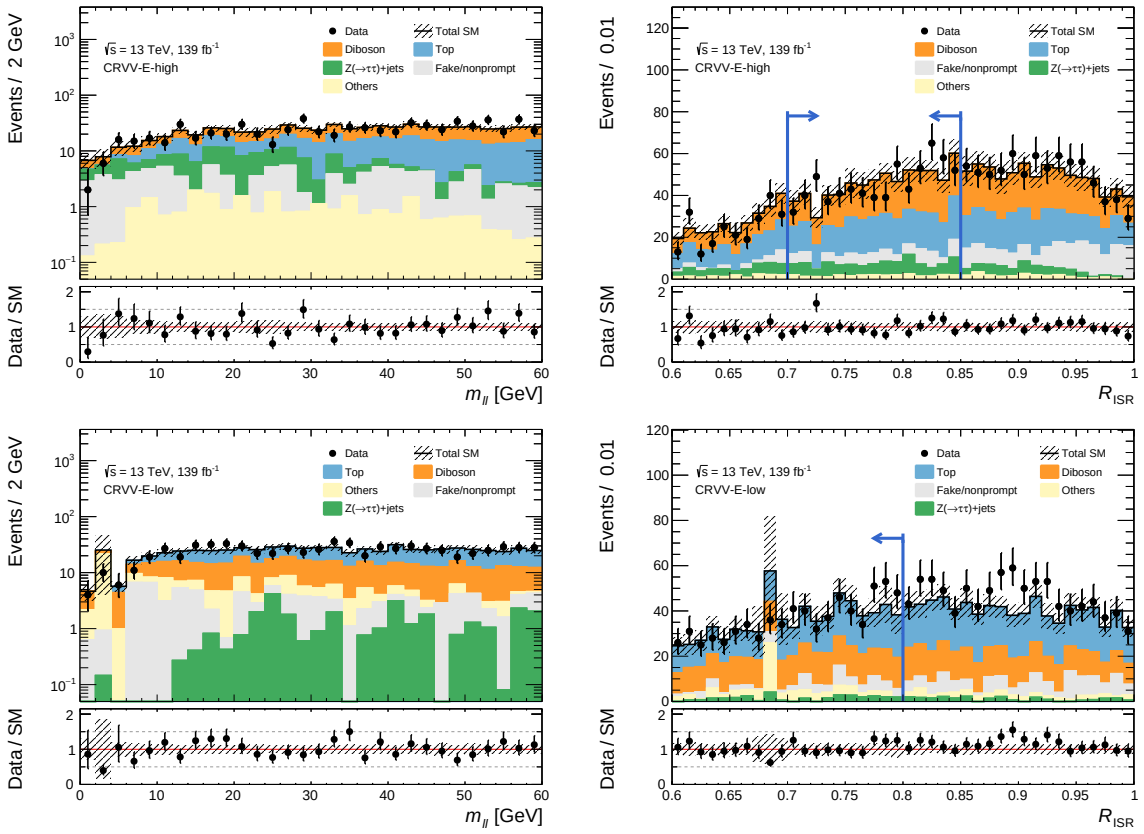

Figure 7.15: The distributions of the $m_{\ell\ell}$ (left) and R_{ISR} (right) in CRVV-E-high (top) and CRVV-E-low (bottom). The background expectation is obtained by the background-only fit in all the six control regions. The full event selection of the corresponding regions is applied, except for distributions showing blue arrows, where the requirement on the variable being plotted is removed and indicated by the arrows in the distributions instead. The first (last) bin includes underflow (overflow). The uncertainty bands plotted include all statistical and systematic uncertainties.

are removed. For VRSS–low, cuts on $E_{\mathrm{T}}^{\mathrm{miss}}/H_{\mathrm{T}}^{\mathrm{lep}}$ and $m_{\mathrm{T}}^{\ell_1}$ are removed. The purity of fake/non-prompt background in the same-sign validation regions is typically above 90%, with the remaining backgrounds originating from the VV processes with the charge of one of the prompt leptons mis-measured.

A different-flavor validation region is defined for each 2ℓ signal region by requiring two different-flavor leptons ($e\mu$ and μe), but keeping the same selections as the corresponding signal region. The relative fractions of each background process are similar in the signal region and the corresponding different-flavor validation region. The different-flavor validation regions are used as the final check of the background estimation, before unblinding the signal regions.

A special validation region is defined to check the compatibility of the irreducible background estimation for the SR–E–med signal region. The dominant source of the irreducible background in this signal region is the $Z^{(*)}/\gamma^*(\rightarrow \tau\tau)$ + jets process. Due to statistical limitation, it is difficult to construct a control region enriched with $Z^{(*)}/\gamma^*(\rightarrow \tau\tau)$ + jets process for the SR–E–med region. MC events are instead normalized in the low-$E_{\mathrm{T}}^{\mathrm{miss}}$ control regions (CR–E–low), and are extrapolated to this signal region. The extrapolation from CRtau–E–low to SR–E–med is checked in an additional validation region, labeled as VRtau–E–med. This validation region is defined by selecting events with $m_{\tau\tau} \in [60, 120]$ GeV, otherwise

applying the same kinematic selections as the SR–E–med region.

The distributions of the validation regions are checked after considering the systematic uncertainties discussed in Chapter 8. The backgrounds are fitted to data in control regions with the systematic uncertainties taken into account, and are extrapolated to the validation regions. The statistical treatment of the fitting procedures are discussed in Chapter 9. The final validation plots after the fitting are shown in Section 10.1.

7.5 Background in the $1\ell 1T$ channel

The background for the $1\ell 1T$ signal regions is dominated by events with fake/non-prompt leptons. Studies with MC samples show that this background mainly comes from the W+ jets process, similar to the 2ℓ reducible background. The lepton and the neutrino from a W decay are observed as one lepton and a significant $E_{\mathrm{T}}^{\mathrm{miss}}$, and additional contribution from jets or pileup vertex constitutes a fake/non-prompt lepton.

The background yield in the $1\ell 1T$ channel is estimated by a simple data-driven procedure. A same-sign region is defined by requiring the same selection as the SR–E–$1\ell 1T$ region, but selecting a pair of a lepton and a track with the same electric charge. The collision data events that enter this same-sign sample region are directly used as the background estimation in SR–E–$1\ell 1T$. This procedure is based on the assumption that the background events are produced with equal rates for the opposite-sign and same-sign events. When the background is purely from the W+jets process and the prompt lepton from W decay and the fake/non-prompt lepton from the jets are not correlated, this procedure would give a good approximation of the background yield. The W+jets MC events are used to test the ratio of the opposite-sign and same-sign events in the signal region. The ratio is found to be compatible with 1.

The assumption is also tested using dedicated validation regions in data. The validation region, denoted by VR–$1\ell 1T$, is defined by requiring the same cuts applied to the $1\ell 1T$ signal region, except for the $\Delta\phi(\mathrm{lep}, \mathbf{p}_{\mathrm{T}}^{\mathrm{miss}})$ cut. Instead of the cut with $\Delta\phi(\mathrm{lep}, \mathbf{p}_{\mathrm{T}}^{\mathrm{miss}}) < 1.0$ applied in the signal region to enhance ISR-like topology, the $\Delta\phi(\mathrm{lep}, \mathbf{p}_{\mathrm{T}}^{\mathrm{miss}}) > 1.5$ cut is required for the validation region to ensure the orthogonality while suppressing the signal contamination. The upper bound on $\Delta R_{\ell\mathrm{track}}$ is removed and the $E_{\mathrm{T}}^{\mathrm{miss}}/H_{\mathrm{T}}^{\mathrm{lep}}$ requirement is loosened, to increase the number of events in the validation region. The distributions of the same-sign and opposite-sign data events in the validation region as functions of p_{T} of the leading lepton and the $E_{\mathrm{T}}^{\mathrm{miss}}$ are shown in Figure 7.16. The ratio is found to be compatible with 1 in both of the distributions.

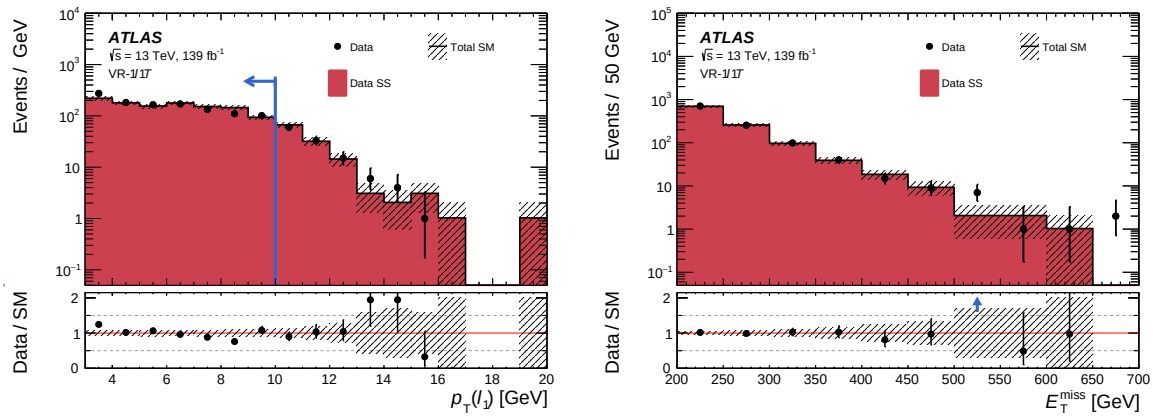

Figure 7.16: The distribution of leading lepton p_{T} (left) and the $E_{\mathrm{T}}^{\mathrm{miss}}$ (right) in the $1\ell 1T$ validation region (VR–$1\ell 1T$). The full event selection of the corresponding regions is applied, except for distributions showing blue arrows, where the requirement on the variable being plotted is removed and indicated by the arrows in the distributions instead. The first (last) bin includes underflow (overflow). The uncertainty bands plotted include all statistical and systematic uncertainties.

Chapter 8

Systematic Uncertainties

Systematic uncertainties are evaluated for all the background and signal samples. The systematic uncertainties considered in this analysis are categorized into four groups; theoretical uncertainties, experimental uncertainties, uncertainties associated with the reducible background estimation, and uncertainties for the $1\ell 1T$ background estimation.

The theoretical uncertainties that affect the yield of the MC simulated events are described in Section 8.1. The dominant experimental uncertainties are explained in Section 8.2. The uncertainties assigned to the estimation of the reducible background are described in Section 8.3. The uncertainties for the background estimation in the $1\ell 1T$ signal region is described in Section 8.4. Finally, the breakdown of the systematic uncertainties assigned to each signal region is shown in Section 8.5.

8.1 Theoretical Uncertainty

8.1.1 Uncertainties on MC parameters

The parameters given at the generation step of the MC samples are varied to assign systematic uncertainties associated with the choice of the parameters. The uncertainties coming from the choice of the Parton Distribution Function (PDF) is calculated by using the other PDFs and evaluating the difference of the yield in each control/validation/signal regions. The MMHT2014 [150] and CT14 [151] PDF sets are compared with our nominal choice (NNPDF [59, 63]), and the difference in the yield is used as uncertainties. Uncertainties in the signal acceptance due to the choice of the PDF are evaluated following the PDF4LHC15 recommendations [152] and account for at most 15% for large $\widetilde{\chi}_2^0$ mass.

The factorization scale μ_F and the renormalization scale μ_R, introduced in Section 3.2, are non-physical theory parameters. The impact on the event yield by the choice of these parameters is evaluated by varying the parameters by a factor of 2 and 0.5 around their nominal values. The uncertainty due to the choice of the strong coupling constant α_s is evaluated by varying the coupling within its uncertainty. These uncertainties are evaluated for the dominant background processes; $t\bar{t}/tW$, $Z^{(*)}/\gamma^*(\rightarrow \tau\tau)$ + jets and VV.

8.1.2 Signal Uncertainties

Uncertainties on the expected yields of the signal events arise from the modeling of the ISR jet in the signal events. The modeling of the ISR at the generator level is tested by using the $Z \rightarrow \mu\mu$ as a proxy for the $E_{\mathrm{T}}^{\mathrm{miss}}$. The yields of the $Z \rightarrow \mu\mu$ events in data are compared with the $Z \rightarrow \mu\mu$ MC events generated

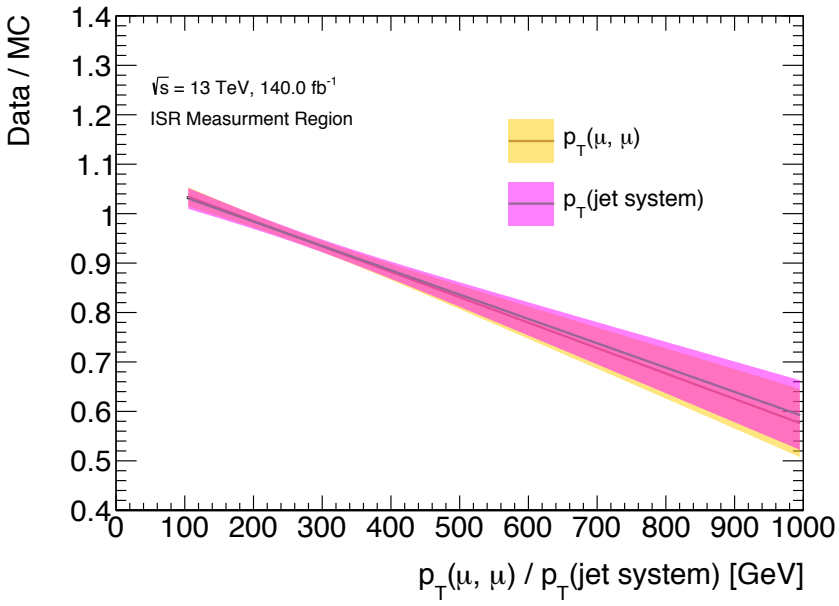

Figure 8.1: The data to MC ratio as a function of sum of the p_{T} of the two leptons (orange) and the p_{T} of the leading jet (magenta) in the $Z \rightarrow \mu\mu$ + jets events [153]. The ratio is smaller in the high p_{T} region, which comes from the mis-modeling of the ISR emission rate in the MC. The bands indicate the errors on the ratio, derived from the fitting error of the ratio.

using the same generation configuration as the signal samples. The four-momenta of the muons are added to the $E_{\mathrm{T}}^{\mathrm{miss}}$ to emulate the p_{T} of the SUSY system in the signal events, and the data to MC ratio (scale factor) is derived as a function of the $E_{\mathrm{T}}^{\mathrm{miss}}$. The scale factor distribution is fitted with a straight line, and the uncertainty on the fitting is used as the systematic uncertainty for the ISR energy. The uncertainties are also derived as a function of the energy of the ISR jet.

The fitted scale factors and uncertainties derived as a function of the $E_{\mathrm{T}}^{\mathrm{miss}}$ and the ISR jet energy are shown in Figure 8.1. The mis-modeling of the $E_{\mathrm{T}}^{\mathrm{miss}}$ and ISR jet energy increase at larger values. The scale factors and the uncertainties as a function of $E_{\mathrm{T}}^{\mathrm{miss}}$ and ISR jet energy are found to be consistent. The impact of the uncertainty is evaluated by varying the scale factor within the uncertainty and comparing the yield of the signal events in the signal regions. The largest uncertainty of approximately 20% are observed for samples with small mass splitting in the high-$E_{\mathrm{T}}^{\mathrm{miss}}$ channels, while in the low-$E_{\mathrm{T}}^{\mathrm{miss}}$ channels and the signals with larger mass splittings have uncertainties ranging from 1% to 10%.

8.2 Experimental Uncertainty

The experimental uncertainties are assigned to cover the mis-modeling of the experimental circumstances in the MC sample. The mis-modeling is often corrected by applying "scale factors", which are obtained by comparing the data and MC. In many cases, the uncertainty on the scale factors is assigned as a systematic uncertainty. The major experimental uncertainties considered in this analysis are explained in this section.

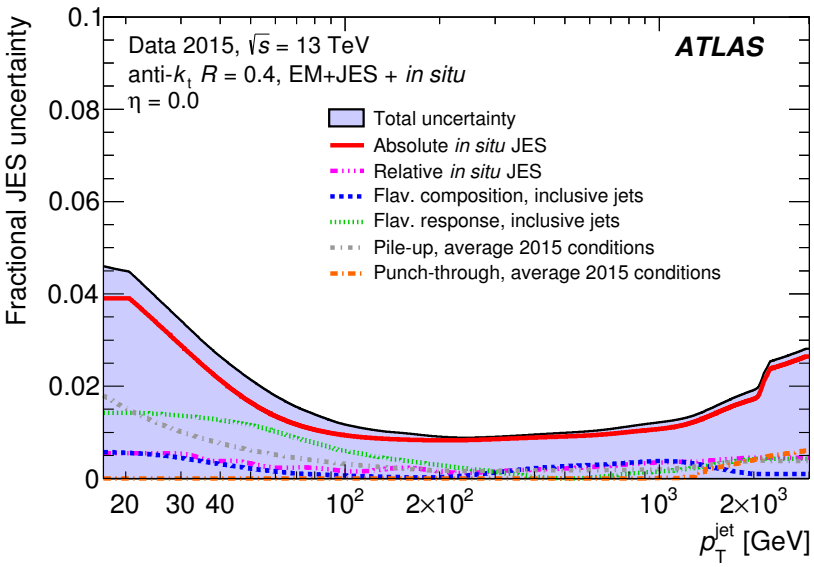

Figure 8.2: Combined uncertainty in the jet energy scale of fully calibrated jets as a function of jet p_{T} at $\eta = 0$. Systematic uncertainty include pile-up, punch-through, and uncertainties propagated from the Z/γ-jet and MJB (absolute in situ JES) and η-intercalibration (relative in situ JES). The flavor composition and response uncertainties assume a quark and gluon composition taken from PYTHIA dijet MC simulation (inclusive jets). [116]

8.2.1 Jets

Jet uncertainties are important in our analysis because the mis-modeling of the energy of the ISR jet can impact on the yield of the background and signal events. Uncertainties on the jet energy scale and resolution are considered in this analysis. Detailed measurements of the jet energy scale/resolution uncertainties are described in Ref. [116]. An overview of the source of the uncertainties is given in the following paragraphs. Additional uncertainties from the Jet Vertex Tagger and the b-tagging efficiency are also considered.

As explained in Section 4.3, the multi-step correction is applied to the reconstructed jets, to scale the energy of the jet to the energy of original quarks/gluons. The uncertainty on this scale conversion is called the jet energy scale uncertainty. Figure 8.2 shows the total jet energy scale uncertainty, as a function of the p_{T} of the jet. The jet energy scale uncertainty dominantly comes from the final step of the correction, the *in-situ* calibration, where the mis-modeling of the jet energy is corrected with the Z/γ+jet or multi-jet events. The uncertainty on this *in-situ* calibration is assigned to cover the difference of event topology, statistical or systematic uncertainties propagated from electrons, muons and photons. The difference on the jet energy scale by the flavor composition, as well as the pile-up effects are also considered and included in the jet energy scale uncertainty. The total uncertainty is largest at low-p_{T} jets: about 4.5 % at 20 GeV, and about 2% in the region with p_{T} larger than 100 GeV.

Uncertainties on the resolution of the jet energy are measured in the dijet events. The final jet energy resolution uncertainty is shown in Figure 8.3. Dominant source of the uncertainty for high p_{T} jets is from *in-situ* measurement. For low-p_{T} jets, the noise term, which mainly come from uncertainties on the pile-up modeling, contributes the most. The total uncertainty is below 1% for the high-p_{T} jets.

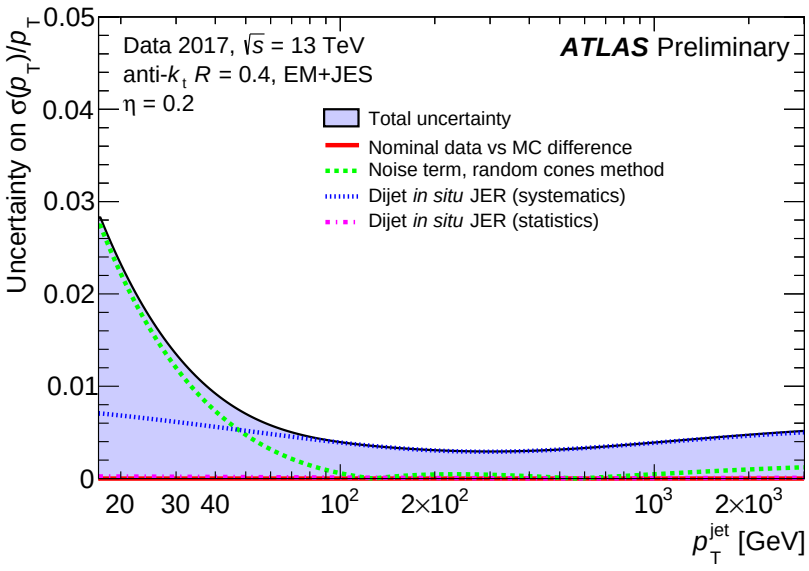

Figure 8.3: The uncertainty on the relative jet energy resolution, defined as the uncertainty on $\sigma(p_{\mathrm{T}})/p_{\mathrm{T}}$, for $\eta = 0.2$ as a function of p_{T} for fully calibrated EM-topo jets. [154]

8.2.2 $E_{\mathrm{T}}^{\mathrm{miss}}$

The systematic uncertainties related to the modeling of the $E_{\mathrm{T}}^{\mathrm{miss}}$ in the simulation are estimated by propagating the uncertainties on the energy and momentum scale of each object used for the calculation. Uncertainties on the resolution and scale of the soft-term (described in Section 4.8) are modeled separately as discussed in Ref. [129].

8.2.3 Leptons

The reconstruction, identification and isolation efficiencies for the leptons, as well as the momentum resolution and scale, are measured and calibrated as explained in Sections 4.4 and 4.5. The $Z \to \ell\ell$ and $J/\psi \to \ell\ell$ events are used in the calibration of the electrons and muons, to compute the scale factors to correct the mis-modeling in the MC. The uncertainties on the scale factors are assigned as systematic uncertainties. The systematic uncertainties are found to be at most a few % for leptons with $p_{\mathrm{T}} > 10$ GeV, and up to 10 % for lower p_{T}.

8.2.4 $E_{\mathrm{T}}^{\mathrm{miss}}$ trigger efficiency

The mis-modeling in the $E_{\mathrm{T}}^{\mathrm{miss}}$ trigger efficiency is corrected by applying scale factors. The scale factors for the $E_{\mathrm{T}}^{\mathrm{miss}}$ trigger efficiency are measured using events collected with single muon triggers. The $E_{\mathrm{T}}^{\mathrm{miss}}$ trigger efficiency is measured by dividing the number of events that fulfilled the $E_{\mathrm{T}}^{\mathrm{miss}}$ trigger condition with the number of all the events. The efficiency is measured as a function of $E_{\mathrm{T}}^{\mathrm{miss}}$ in data and MC, and the data/MC ratio is used as the scale factor to correct the efficiency in the MC. The detailed procedure

Table 8.1: Statistical uncertainty on the fake factor.

Electrons

p_{T} range [GeV]	[4.5, 5]	[5, 6]	[6, 8]	[8, 10]	[10, 20]	[20, ∞]
$N^{20}_{b-\mathrm{jet}} = 0$	33%	22%	20%	26%	15%	5.5%
$N^{20}_{b-\mathrm{jet}} > 0$	46%	30%	26%	40%	30%	9.2%

Muons

p_{T} range [GeV]	[3, 4]	[4, 5]	[5, 7]	[8, 10]	[10, 20]	[20, ∞]
$N^{20}_{b-\mathrm{jet}} = 0$	6.0%	5.1%	4.9%	7.5%	9.0%	4.6%
$N^{20}_{b-\mathrm{jet}} > 0$	9.3%	7.2%	7.2%	9.3%	11%	6.2%

is shown in Appendix E.1. An uncertainty of 5% is assigned to the scale factors, which is used as the systematic uncertainty for the $E_{\mathrm{T}}^{\mathrm{miss}}$ trigger efficiency.

8.2.5 Other experimental uncertainties

MC events do not reproduce the pile-up distribution of the data, thus scale factors are applied to correct the difference. Uncertainties on the scale factor, typically below a few %, are considered in the analysis. The luminosity uncertainty is determined from the measurement by the forward detectors. The total uncertainty on the luminosity is 1.7% in 2015–2018 data.

8.3 Uncertainties on the reducible background

Uncertainties in the fake factor method affect the estimated yield of the fake/non-prompt background. This uncertainty is dominant in the signal regions with small $m_{\ell\ell}$. The uncertainties arise from several different sources, which are explained below.

The statistical limitation in the fake factor measurement region due to the prescale of the low-p_{T} single lepton trigger results in large uncertainty assigned to the fake factor at low-p_{T}. The statistical uncertainty assigned to the fake factor in each measurement p_{T} bins is shown in Table 8.1.

Additional uncertainties are considered to cover the difference in the kinematical distributions between the fake factor measurement region and the signal regions. The size of the uncertainty is determined from the distribution of the fake factor as a function of several variables, as shown in Appendix C.1. For electrons, the fake factors in $N^{20}_{b-\mathrm{jet}} = 0$ regions are found to decrease as the R_{ISR} values get larger. A 40% flat systematic uncertainty is assigned to the electron fake factors to cover this tendency. For muons, there are no significant dependency observed, and 20% flat systematics are assigned to the fake factor to sufficiently cover the difference in kinematic variables.

Systematic uncertainty on the subtraction of the events with prompt leptons is considered when the fake factors are applied to the events in the fake control sample (events with at least one anti-ID leptons). The systematic uncertainty is assigned by varying the prompt subtraction scale factor by 10% up and

Table 8.2: The closure uncertainties applied to the fake factors, derived from the difference in the observed data and the background estimation in fake-rich validation regions. No additional closure uncertainty is assigned for regions shown with "–".

Electrons, High-$E_{\mathrm{T}}^{\mathrm{miss}}$

p_{T} range [GeV]	[4.5, 5]	[5, 6]	[6, 8]	[8, 10]	[10, 20]	[20, ∞]
$N_{b-\mathrm{jet}}^{20} = 0$	–	–	–	51%	–	190%
$N_{b-\mathrm{jet}}^{20} > 1$	34%	6.0%	–	–	–	43%

Electrons, Low-$E_{\mathrm{T}}^{\mathrm{miss}}$

p_{T} range [GeV]	[4.5, 5]	[5, 6]	[6, 8]	[8, 10]	[10, 20]	[20, ∞]
$N_{b-\mathrm{jet}}^{20} = 0$	–	–	–	–	–	36%
$N_{b-\mathrm{jet}}^{20} > 1$	43%	–	–	–	–	47%

Muons, High-$E_{\mathrm{T}}^{\mathrm{miss}}$

p_{T} range [GeV]	[3, 4]	[4, 5]	[5, 7]	[7, 10]	[10, 20]	[20, ∞]
$N_{b-\mathrm{jet}}^{20} = 0$	–	–	–	30%	18%	24%
$N_{b-\mathrm{jet}}^{20} > 1$	19%	–	–	–	10%	34%

Muons, Low-$E_{\mathrm{T}}^{\mathrm{miss}}$

p_{T} range [GeV]	[3, 4]	[4, 5]	[5, 7]	[7, 10]	[10, 20]	[20, ∞]
$N_{b-\mathrm{jet}}^{20} = 0$	–	–	–	18%	11%	–
$N_{b-\mathrm{jet}}^{20} > 1$	28%	–	–	–	15%	5.0%

down. The effect on the final fake background yield is found to be small compared to other systematic uncertainties.

Closure uncertainties are considered to cover any additional mis-modeling on reducible backgrounds that the other uncertainties do not cover. The uncertainties are taken from the difference between the fake estimation and the observed number of events in the same-sign validation region for events with $N_{b-\mathrm{jet}}^{20} = 0$. For events with $N_{b-\mathrm{jet}}^{20} > 0$, the CRtop control region with same-sign requirement is used. The closure uncertainties are measured as a function of p_{T} of the lepton, separately for electrons and muons, high-$E_{\mathrm{T}}^{\mathrm{miss}}$ and low-$E_{\mathrm{T}}^{\mathrm{miss}}$ regions, each p_{T} bins, and $N_{b-\mathrm{jet}}^{20} = 0$ and > 0. The difference between the fake estimation and the observed data is directly used to calculate the uncertainty, except for when the difference is already within other uncertainties. The detailed method is summarized in Appendix C.6. The closure uncertainties assigned in each region are summarized in Table 8.2.

8.4 Uncertainties for the $1\ell 1T$ background

As discussed in Chapter 7, the background predictions in the $1\ell 1T$ signal regions are extracted from the same-sign data. This assumes that the opposite-sign and the same-sign data have exactly the same yield.

In the region with $m_{\ell\mathrm{track}} < 2$ GeV, low-mass resonances can cause higher production rates for

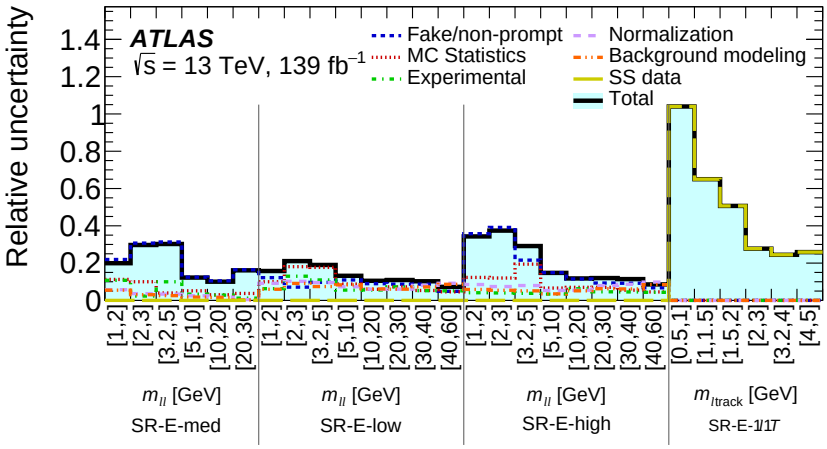

Figure 8.4: The relative systematic uncertainties obtained from the background-only fit in the control regions and the signal regions. The total uncertainty is shown with light-blue histogram. The uncertainty on the *SS data* includes a statistical uncertainty in the same-sign region, used to estimate the background in the SR–E–1ℓ1T region, and the systematic uncertainty. The *MC Statistics* uncertainty originates from the limited size of the MC samples used to model the irreducible background contributions. The *Normalization* uncertainty arises from the use of control regions to normalize the contributions of $t\bar{t}/tW$, $Z^{(*)}/\gamma^*(\rightarrow \tau\tau)$ + jets and WW/WZ backgrounds. The *Background modeling* includes the different sources of theoretical modeling uncertainties on the irreducible backgrounds. All sources of uncertainty affecting the fake/non-prompt background estimate are included under *Fake/non-prompt*. The uncertainties arising from the reconstruction and selection of signal leptons, jets and $E_{\mathrm{T}}^{\mathrm{miss}}$ are included under the *Experimental* category. The individual uncertainties can be correlated and do not necessarily add up in quadrature to the total uncertainty.

opposite sign events compared to the same-sign events. This effect cannot be tested in the MC, thus the ratio of opposite-sign to same-sign event is checked using data in the validation region. The validation region for the 1ℓ1T requires the same selection as the signal region, except for the $\Delta\phi(\mathrm{lep}, \mathbf{p}_{\mathrm{T}}^{\mathrm{miss}})$ cut, where $\Delta\phi(\mathrm{lep}, \mathbf{p}_{\mathrm{T}}^{\mathrm{miss}}) > 1.5$ is required in the validation region (defined in Section 7.5). The opposite-sign to same-sign ratio is measured as a function of $E_{\mathrm{T}}^{\mathrm{miss}}$, and the ratio is found to be consistent with 1 for $E_{\mathrm{T}}^{\mathrm{miss}} > 200$ GeV. A 30% uncertainty is assigned to the ratio, coming from the limited statistics.

In the $m_{\ell\mathrm{track}} > 2$ GeV region, the background is mainly from the W+ jets process. Thus the opposite-sign to same-sign ratio is measured in the W+jets MC sample. The systematics uncertainty extracted from the W+jets MC is 12%, which includes the statistical uncertainty of the MC sample.

8.5 Systematics Uncertainty in Signal Regions

Figure 8.4 illustrates the dominant uncertainties on the expected background yields in the signal regions. The total systematic uncertainties assigned to the 2ℓ signal regions are at most 30 % in the regions with small $m_{\ell\ell}$, and about 15 % in the rest of the signal regions. In most of the 2ℓ signal regions, the systematic uncertainties related to fake/non-prompt background is dominant. In regions with larger $m_{\ell\ell}$, the uncertainties related to the irreducible background estimation and the MC statistical uncertainty also contribute to the total uncertainty. In the 1ℓ1T signal regions, the uncertainties mostly arise from the limited statistics in the same-sign region.

Chapter 9

Statistical treatment

As described in Chapter 7, the major irreducible backgrounds are estimated using MC which are normalized to data in the control regions and extrapolated to the signal regions. The normalization factors are determined in a simultaneous fitting of all the control regions. The systematic uncertainties, explained in Chapter 8, also need to be considered during the fitting procedure to evaluate their impact on the final background yield. The statistical procedure to derive the final background estimation and its uncertainty is explained in this section. The profile likelihood method that we use to compute the background yield with various signal hypotheses is described in Section 9.1. The method of hypothesis tests, to evaluate an excess over the background estimation, or to set an upperlimit on a certain hypothesis, is explained in Section 9.2. The treatment of the systematic uncertainties in the fitting procedure is described in Section 9.3.

9.1 Profile Likelihood

In order to fit the original distribution of the background sample to the observed data, we take a simple maximum likelihood approach. For a set of free parameters $\boldsymbol{\theta}$ which gives background estimation in N independent regions $E = (E_0(\boldsymbol{\theta}), \ldots, E_N(\boldsymbol{\theta}))$, the likelihood of observing $\boldsymbol{x} = (x_0, \ldots, x_N)$ events can be written as

$$L(x;\boldsymbol{\theta}) = \prod_{j=1}^{N} \frac{(E_j(\boldsymbol{\theta}))^{x_j}}{x_j!} e^{-E_j(\boldsymbol{\theta})}, \tag{9.1}$$

which is a simple product of the Poisson distributions. A set of $\boldsymbol{\theta}$ values that best explains the measurements is denoted by $\hat{\boldsymbol{\theta}}$, which can obtained by maximizing the likelihood, i.e.

$$\hat{\boldsymbol{\theta}} = \arg\max_{\boldsymbol{\theta}} L(\boldsymbol{x};\boldsymbol{\theta}). \tag{9.2}$$

In the analysis, the parameters in $\boldsymbol{\theta}$ are derived from a *control measurements*, such that each parameter have a central value and some uncertainties. One example is the scale factor applied to the MC events; the central value of the scale factor and the uncertainty is measured in the calibration, by comparing the data and MC. In our analysis the signal strength μ and the background normalization factors $\boldsymbol{\mu}_B$ are included in the likelihood. The signal strength is the parameter we are most interested in, and therefore are handled differently to other parameters, as described in the following paragraphs. The normalization factors $\boldsymbol{\mu}_B$ are defined for major irreducible background processes, which are also not constrained before the fit. Thu the normalization factors are added to the likelihood formula as free parameters. The parameters included in $\boldsymbol{\theta}$

are not directly of our interest, and are called *nuisance parameters*. The likelihood function becomes

$$L(x;(\mu,\boldsymbol{\mu}_B,\boldsymbol{\theta})) = \prod_{j=1}^{N} \frac{(E_j(\mu,\boldsymbol{\mu}_B,\boldsymbol{\theta}))^{x_j}}{x_j!} e^{-(E_j(\mu,\mu x_B,\boldsymbol{\theta}))} \cdot p(\boldsymbol{\theta}), \tag{9.3}$$

where the expected number of events in j-th region is

$$E_j = \mu s_j(\boldsymbol{\theta}) + b_j(\boldsymbol{\mu}_B,\boldsymbol{\theta}). \tag{9.4}$$

In this Eq. 9.3, we consider N independent measurement regions that are used to constrain the nuisance parameters. The s_j and b_j in Eq. 9.4 are the expected number of signal and background events in region j, respectively. The signal strength μ is a free parameter that scales up/down the signal yield, and the $\boldsymbol{\mu}_B$ are the background normalization factors. The extra $p(\boldsymbol{\theta})$ factor reflects our knowledge on the nuisance parameters. This term works as a "penalty term"; a significant deviation of the nuisance parameter from the central value decreases the value of $p(\boldsymbol{\theta})$, thus decreases the likelihood. The details of the formalization of this term is discussed in Section 9.3. A set of parameters to maximize the likelihood in Eq. 9.3 are given by

$$(\hat{\mu},\hat{\boldsymbol{\mu}}_B,\hat{\boldsymbol{\theta}}) = \arg\max_{\mu,\boldsymbol{\mu}_B,\boldsymbol{\theta}} L(\boldsymbol{x};(\mu,\boldsymbol{\mu}_B,\boldsymbol{\theta})). \tag{9.5}$$

To quantify the significance or to set an upperlimit on the signal strength μ, we use the profile likelihood method [155]. In this method, we *profile out* the signal strength by fixing it to a certain value, and maximize the likelihood function using the other parameters. A set of parameters to minimize the likelihood function for a given μ value are

$$(\hat{\hat{\boldsymbol{\mu}}}_B,\hat{\hat{\boldsymbol{\theta}}}) = \arg\max_{\boldsymbol{\mu}_B,\boldsymbol{\theta}} L(\boldsymbol{x};(\mu,\boldsymbol{\mu}_B,\boldsymbol{\theta})), \tag{9.6}$$

where $\hat{\hat{\boldsymbol{\theta}}}$ denotes the nuisance parameters that maximizes likelihood for the specified μ. For a given fixed μ value, one can define the profile likelihood ratio,

$$\lambda(\mu) = \frac{L(\mu,\hat{\hat{\boldsymbol{\mu}}}_B,\hat{\hat{\boldsymbol{\theta}}})}{L(\hat{\mu},\hat{\boldsymbol{\mu}}_B,\hat{\boldsymbol{\theta}})}. \tag{9.7}$$

The numerator is called the maximum-likelihood estimator, which is a function of μ. The denominator is the maximized likelihood, with the signal strength allowed to float. From the definition of $\lambda(\mu)$, one can see that $0 \leq \lambda \leq 1$, with the value λ close to 1 implying good agreement between the data and the hypothesized value of μ.

9.2 Hypothesis testing

The profile likelihood ratio $\lambda(\mu)$ is often converted to a convenient form

$$q_\mu = -2\ln\lambda(\mu) \tag{9.8}$$

as the basis of a statistical test, referred to as *test statistics*. Higher values of q_μ correspond to increasing incompatibility between the data and the hypothesis. We can define a test of a hypothesized value of μ, by computing the p-value defined as

$$p_\mu = \int_{q_{\mu,obs}}^{\infty} f(q_\mu|\mu)\, dq_\mu \ , \tag{9.9}$$

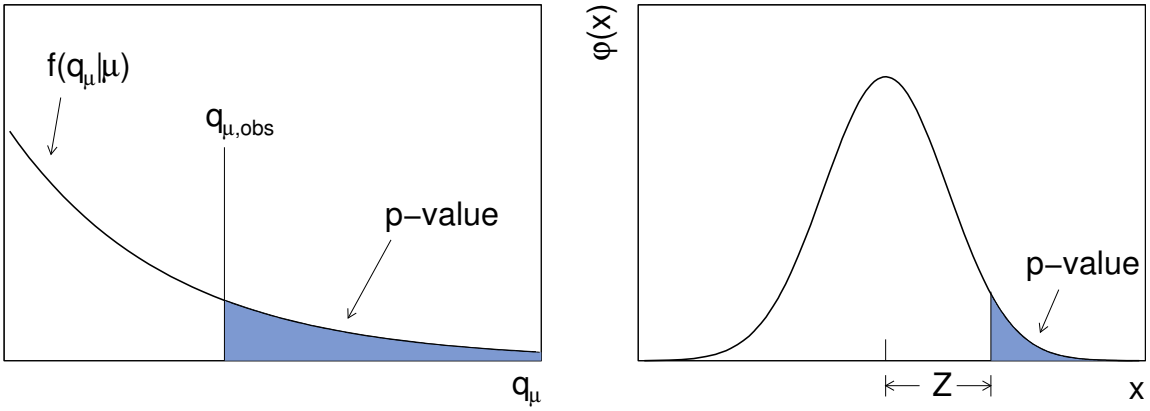

Figure 9.1: Illustration of the relation between the p-value obtained from an observed value of the test statistic q_μ (left). The standard normal distribution $\varphi(x) = (1/\sqrt{2\pi})\exp(-x^2/2)$ showing the relation between the significance Z and the p-value (right).

where $q_{\mu,obs}$ is the observed test statistics, and the $f(q_\mu|\mu)$ is the probability density function of q_μ, assuming a fixed signal strength μ. Figure 9.1 shows the illustration of $f(q_\mu|\mu)$ distribution and the obtained p-value, as well as the relation between the significance Z and the p-value.

For the hypothesis tests, $f(q_\mu|\mu)$ needs to be obtained for each μ assumption. The $f(q_\mu|\mu)$ function can be obtained either by running a number of *toy-experiments*, or from an analytic approximation. In a toy-experiment, we generate a dummy dataset assuming the best-fit nuisance parameters $\hat{\hat{\boldsymbol{\theta}}}$ and normalization factors $\hat{\hat{\boldsymbol{\mu}}}_B$. The fluctuation of the data by the statistical and systematic uncertainties are taken into account to create the dataset. For each generated dataset, we calculate the q_μ. This procedure is repeated until we obtain a smooth distribution of $f(q_\mu|\mu)$. The $f(q_\mu|\mu)$ need to be defined for each of the μ assumptions, and also for every signal model we consider, therefore this procedure requires an enormous amount of computing resource. The alternative is to use an analytic approximation of $f(q_\mu|\mu)$. Wald's approximation [156] transforms the q_μ to an analytic form based on the best-fit signal strength $\hat{\mu}$ and its error. The asymptotic formula based on Asimov dataset [155] is used to obtain $f(q_\mu|\mu)$ from the q_μ. This way, a single fit to obtain $\hat{\mu}$ and its error can be used to immediately obtain the pdf $f(q_\mu|\mu)$, which speeds up the hypothesis test significantly. In this thesis, we take the latter approach.

Discovery test

When a significant excess over the background prediction is observed, a *discovery test*, is performed to claim an discovery. The discovery test is defined as hypothesis test on $\mu = 0$, where a significant excess will be observed as as a small p_0. In high-energy physics field, an evidence of a new particle can be claimed for $p_0 < 0.0027$ which corresponds to 3σ standard deviation. A discovery can be claimed for $p_0 < 6 \times 10^{-7}$, corresponding to 5σ standard deviation.

Upperlimit test

If we observe a background consistent result, we set an upperlimit by performing an *upperlimit test*. In the upperlimit test, signal strength μ are varied from $\hat{\mu}$ up to a certain range, to find a μ value where the model can be excluded with 95% confidence level. Confidence level is calculated based on the ratio of p-values for background-only hypothesis and background plus signal hypothesis [157],

$$CL_s = \frac{CL_{s+b}}{CL_b} = \frac{p_\mu}{p_0}. \tag{9.10}$$

Exclusion test

An *exclusion test* is performed to test if a model can be excluded. In the exclusion test, the signal strength μ is fixed to 1, to calculate $CL_s = p_1/p_0$. The model is excluded with 95% CL when $CL_s < 0.05$ is observed.

9.3 Treatment of systematic uncertainties

The $p(\boldsymbol{\theta})$ function introduced in Eq. 9.3 are added to reflect our knowledge on the nuisance parameters. For each nuisance parameter θ, we have results from a *control measurement* (e.g. calibration) where the central value $\tilde{\theta}$ and its uncertainty σ is determined (e.g. the scale factor and its uncertainty). In other words, from the control measurement, we obtain a Bayesian probability $\rho(\theta|\tilde{\theta})$, which can be understood as the pdf of the true parameter θ, given that we observed $\tilde{\theta}$. In Eq. 9.3, we need $p(\tilde{\theta}|\theta)$, which is the "frequentist" probability of measuring the central value of the nuisance parameter $\tilde{\theta}$ when the truth value is θ. From Bayes' theorem,

$$\rho(\theta|\tilde{\theta}) = p(\tilde{\theta}|\theta) \times \pi(\theta), \tag{9.11}$$

where $\pi(\theta)$ is a *prior density*, which reflects our knowledge on the truth value θ *before* the control measurement. We assume no prior constraint on the truth nuisance parameter value and take a constant $\pi(\theta)$. Thus the distribution of $\rho(\theta|\tilde{\theta})$ can directly be treated as $p(\tilde{\theta}|\theta)$. The systematic uncertainties we consider in this thesis are either given by Gaussian distribution or Gamma distribution. The Gaussian distribution is assumed for most of the systematic uncertainties, where the pdf of the nuisance parameter is given in a form of

$$\rho(\theta|\tilde{\theta}) = p(\tilde{\theta}|\theta) = \frac{1}{\sqrt{2\pi}}\exp(-\frac{(\theta-\tilde{\theta})^2}{2\sigma^2}). \tag{9.12}$$

For the Gamma distribution,

$$\rho(\theta|N) = p(N|\theta) = \frac{\theta^N}{N!}\exp(-\theta), \tag{9.13}$$

where we write $\tilde{\theta} = N$ for readability. A detailed mathematical expression is discussed in Ref. [158]. The final form of $p(\boldsymbol{\theta})$ will be the product of the pdfs of all the nuisance parameters,

$$p(\boldsymbol{\theta}) = \prod_i p(\theta_i|\tilde{\theta}_i). \tag{9.14}$$

This works as a "penalty term" in the likelihood function. In both Eq. 9.12 and Eq. 9.13, a significant deviation of the nuisance parameter θ from the central value $\tilde{\theta}$ leads to $p(\tilde{\theta}|\theta)$ to exponentially decrease. Thus the systematic uncertainties are constrained by this term.

Chapter 10

Results

The results of the search for production of chargino and neutralino is presented in this chapter. The observed data are compared with the expected background in the validation regions, which are shown in Section 10.1. A model-independent hypothesis test is performed to search for a significant excess over the background expectation, in Section 10.2. Finally, the model-dependent interpretation results for the signal scenarios are presented in Section 10.3.

10.1 Background-only fit and the validation region yield

Before unblinding the signal regions, the background estimation is fixed by performing a simultaneous fit using all the control regions, under background-only hypothesis. The data in the six control regions, CRtop, CRtau and CRVV, each for high-$E_{\mathrm{T}}^{\mathrm{miss}}$ and low-$E_{\mathrm{T}}^{\mathrm{miss}}$, are fitted simultaneously to constrain six normalization factors for top, tau and diboson background predictions in high-$E_{\mathrm{T}}^{\mathrm{miss}}$ and low-$E_{\mathrm{T}}^{\mathrm{miss}}$ regions. The systematic uncertainties are taken into account in the fitting, as explained in Section 9.3. The resulting normalization parameters and their errors are presented in Table 10.1.

The background prediction is extrapolated to the validation regions to verify the accuracy of the background modeling. The data in three different types of validation regions introduced in Chapter 7 are compared with the fitted background prediction. The data is found to be in good agreement with the prediction, as shown below.

Figure 10.1 shows a comparison of the data yields with background predictions in the different-flavor validation regions. The $m_{\ell\ell}$ binning is matched to the corresponding signal regions; VRDF–E–high and

Table 10.1: Normalization factors obtained from a background-only fit of the control regions. The uncertainties include statistical and systematic contributions combined.

Backgrounds	$E_{\mathrm{T}}^{\mathrm{miss}}$ region	Normalization Parameters
$t\bar{t}/Wt$	high	1.08 ± 0.20
	low	1.08 ± 0.18
$Z^{(*)}/\gamma^{*}(\rightarrow \tau\tau)$ + jets	high	0.96 ± 0.14
	low	1.02 ± 0.15
VV	high	0.89 ± 0.27
	low	0.69 ± 0.22

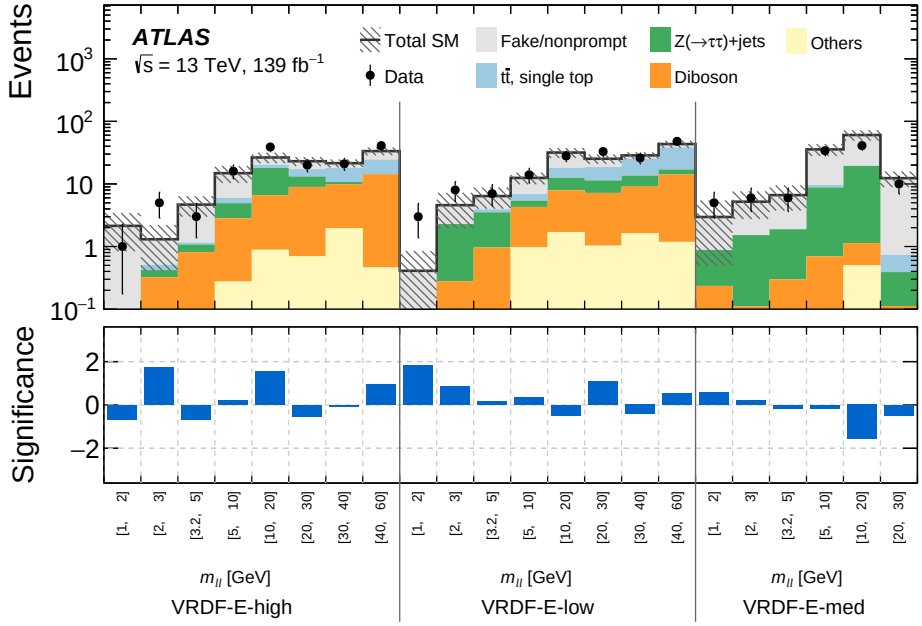

Figure 10.1: Comparison of observed and expected event yields in the different-flavor validation regions after a background-only fit of the control regions. Three different-flavor validation regions are shown, binned in $m_{\ell\ell}$ as the corresponding signal regions. Uncertainties in the background estimates include both the statistical and systematic uncertainties. The bottom panel shows the significance of the difference between the expected and observed yields [147].

VRDF–E–low are separated into eight bins from 1 GeV to 60 GeV, while VRDF–E–med is separated into six bins up to 40 GeV. A good agreement between the data and the background prediction is observed in all the selection categories, with deviations below 2σ. The distributions of ΔR between the two leptons ($\Delta R_{\ell\ell}$) and the p_{T} of the sub-leading lepton ($p_{\mathrm{T}}(\ell_2)$) in different-flavor validation regions are checked, as shown in Figure 10.2, to validate the background expectation at small $\Delta R_{\ell\ell}$ or low-p_{T}, which are generally difficult to model. A good agreement between data and MC simulation is seen in both the shape and the normalization of these variables.

Figure 10.3 shows the distributions of $E_{\mathrm{T}}^{\mathrm{miss}}/H_{\mathrm{T}}^{\mathrm{lep}}$ and M_T^S variables defined in Section 6.3, for events in VRtau–E–med. The VRtau–E–med region is intended to check that the tau background estimation for SR–E–low is also valid for SR–E–med. Thus the variables that separate these two signal regions are checked. A good agreements in both the normalization and the shape of the distributions are found.

Finally, the reducible background predicted by the fake factor method are checked in the same-sign validation regions. Figure 10.4 shows the distributions of $\Delta R_{\ell\ell}$ and $p_{\mathrm{T}}(\ell_2)$ in the same-sign validation regions, VRSS–E–high, VRSS–E–low, and VRSS–E–med, separately. The reducible background prediction from the fake factor method agrees with data, at small p_{T} down to 3 GeV, and small value of $\Delta R_{\ell\ell}$. The discrepancies seen in the p_{T} distributions are taken into account, by adding extra systematic uncertainties as explained in Section 8.3.

The $1\ell 1T$ signal regions have different background estimation method based only on the same-sign data, as described in Section 7.5. The background estimation is directly derived from the number of events with two leptons with same sign. The validation of this method is also explained in Section 7.5, and an

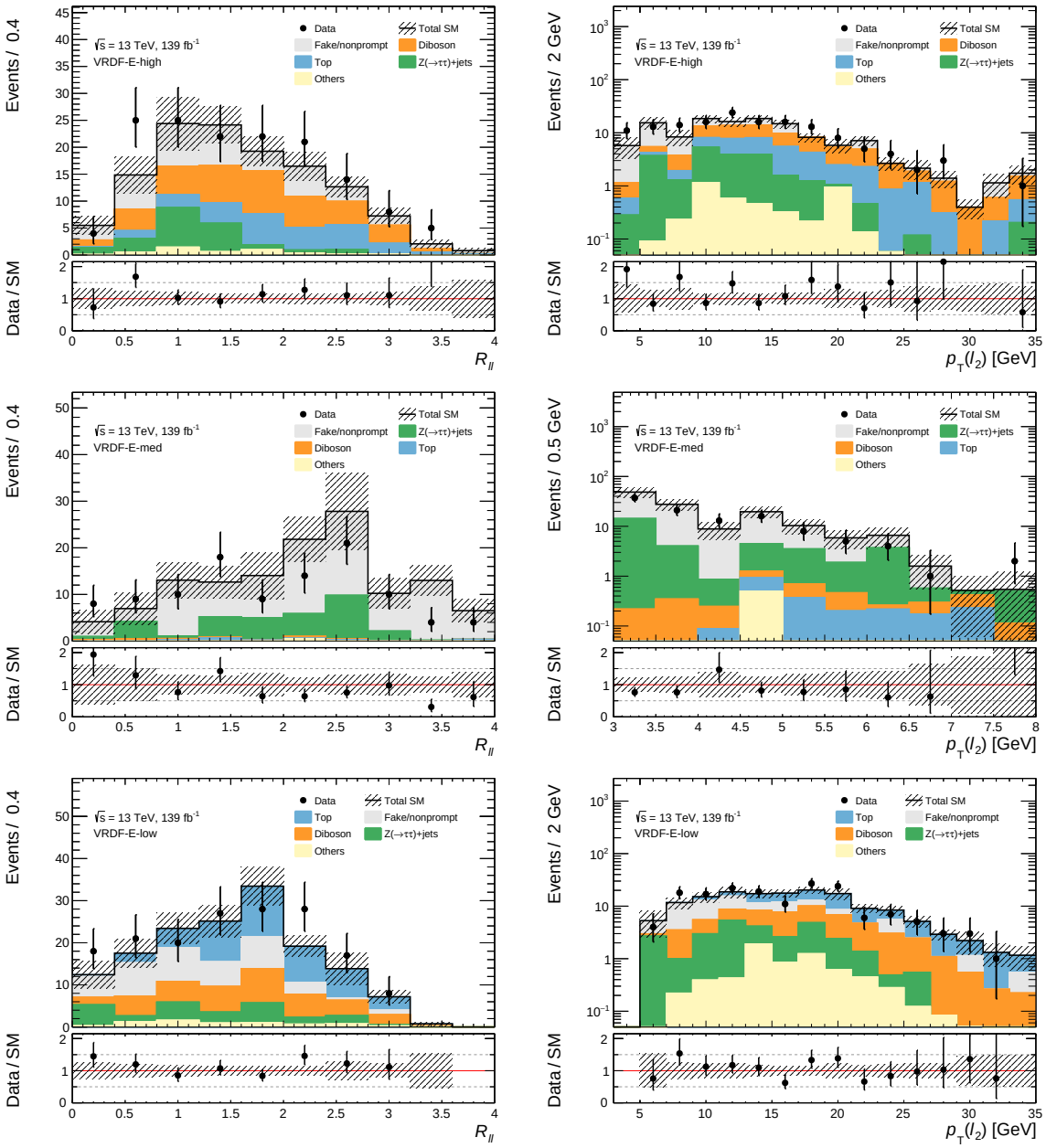

Figure 10.2: The distributions of ΔR between the two leptons (left) and the p_{T} of the sub-leading lepton (right) in the different-flavor validation regions, VRDF–E–high (top), VRDF–E–low (middle) and VRDF–E–med (bottom). The background distributions are fitted using control-regions with background-only hypothesis. The full event selection of the corresponding regions is applied, except for distributions showing blue arrows, where the requirement on the variable being plotted is removed and indicated by the arrows in the distributions instead. The first (last) bin includes underflow (overflow). The uncertainty bands plotted include all statistical and systematic uncertainties.

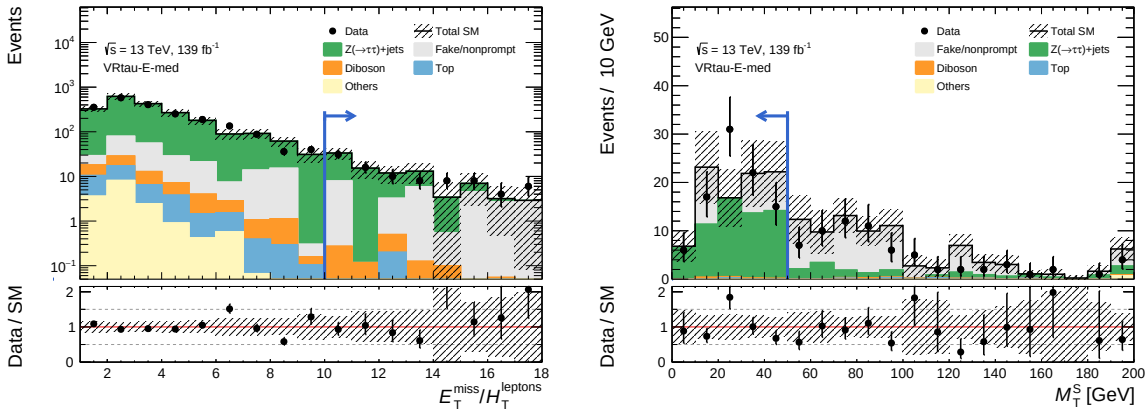

Figure 10.3: The distributions of $E_{\mathrm{T}}^{\mathrm{miss}}/H_{\mathrm{T}}^{\mathrm{lep}}$ and M_T^S in the tau validation region, VRtau-E-med. The background distributions are fitted using control-regions with background-only hypothesis. The full event selection of the corresponding regions is applied, except for distributions showing blue arrows, where the requirement on the variable being plotted is removed and indicated by the arrows in the distributions instead. The first (last) bin includes underflow (overflow). The uncertainty bands plotted include all statistical and systematic uncertainties.

additional systematic uncertainty is assigned to cover the mis-modeling, as explained in Chapter 8. There is no control region to constrain this uncertainty, therefore we do not need to perform the background-only fit. Thus we do not explicitly check the validation region yield for the $1\ell 1T$ signal region here.

After all, the distributions in all the validation regions are found to be consistent with the background expectation, and therefore we proceed to unblinding of the signal region to search for excess over the prediction.

10.2 Model-independent search

The background expectation obtained by a control-region fit with background-only hypothesis are extrapolated to the signal regions, and are compared with the observed data. Model-independent limits are derived using the inclusive signal regions defined in Section 6. The inclusive signal regions are the sum of all the signal regions (2ℓ high/low/med and $1\ell 1T$) with $m_{\ell\ell}$ below an upperlimit. The upperlimit on $m_{\ell\ell}$ for each inclusive signal region is selected from the bin boundaries of the exclusive signal regions, which are 1, 2, 3, 5, 10, 20, 30, 40 and 60 GeV.

The number of observed and expected events, as well as the results of the upperlimit test and discovery test are summarized in Table 10.2, for each inclusive signal region separately. The expected number of events N_{exp} are obtained from background-only fit of the control regions, extrapolated to the signal region. The errors include both the statistical and systematic uncertainties.

The upperlimit on the cross section and observed/expected number of events for the signal events are computed by upperlimit test, described in Section 9.2. Each inclusive signal region is considered one-by-one, to quantify the upperlimit on the number of events above the SM predictions. A hypothetical signal, which yields exactly one event in the inclusive signal region with unconstrained signal strength μ, is used in the hypothesis tests. The signal strength can directly be treated as number of events entering

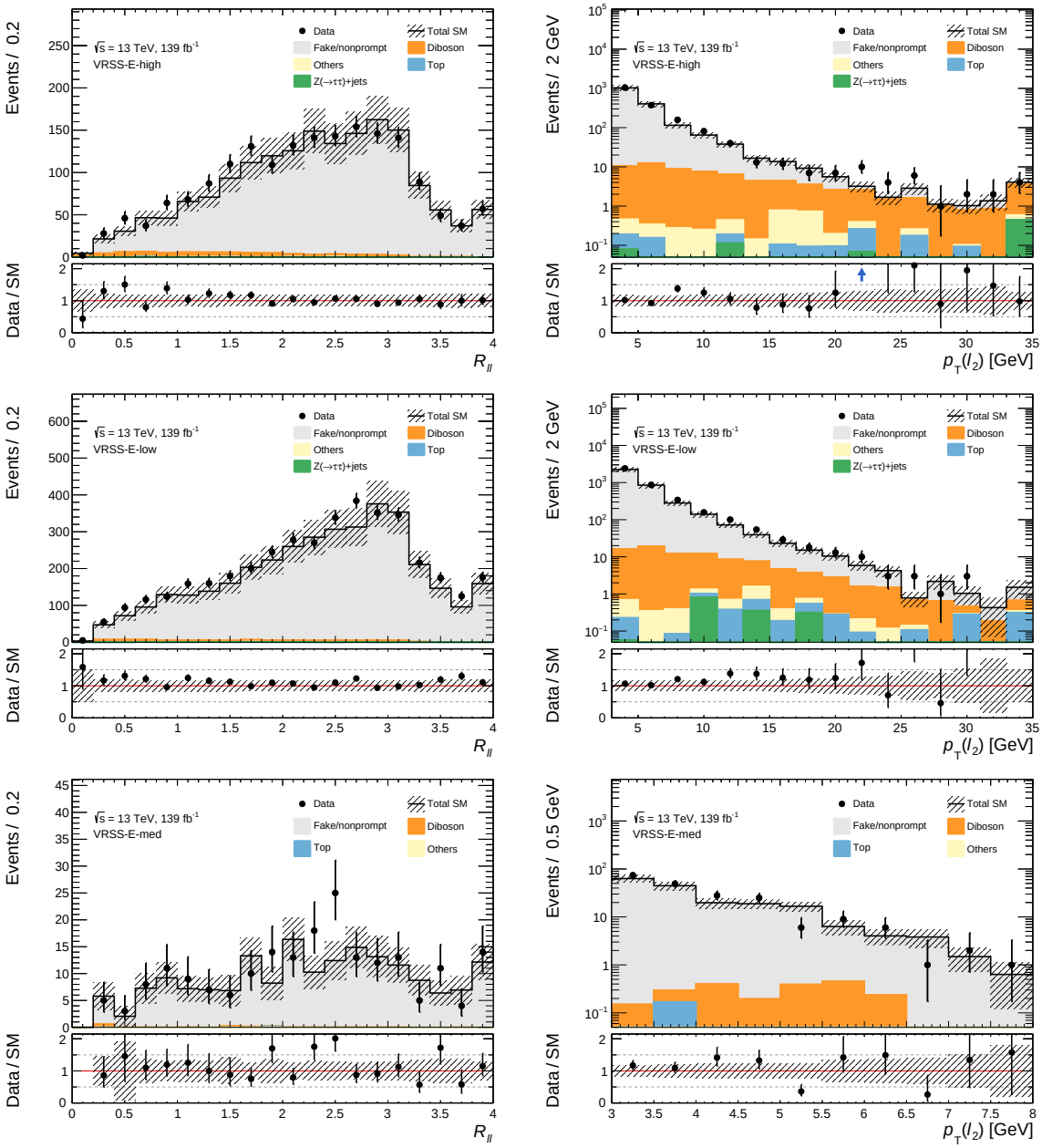

Figure 10.4: The distributions of ΔR between the two leptons (left) and the p_{T} of the sub-leading lepton (right) in the same-sign validation regions, VRSS–E–high (top), VRSS–E–low (middle) and VRSS–E–med (bottom). The background distributions are fitted using control-regions with background-only hypothesis. The full event selection of the corresponding regions is applied, except for distributions showing blue arrows, where the requirement on the variable being plotted is removed and indicated by the arrows in the distributions instead. The first (last) bin includes underflow (overflow). The uncertainty bands plotted include all statistical and systematic uncertainties.

Table 10.2: The results of the model-independent searches in inclusive signal regions. The first column indicates the upper bounds on $m_{\ell\ell}$ in GeV. The next two columns present observed (N_{obs}) and expected (N_{exp}) event yields. The next column shows the observed 95% CL upper limits on the visible cross-section $\left(\langle\epsilon\sigma\rangle^{95}_{\text{obs}}\right)$. The next two columns show the observed $\left(S^{95}_{\text{obs}}\right)$ and expected $\left(S^{95}_{\text{exp}}\right)$ 95% CL upper limit on the number of signal events. The last column indicates the discovery p-value ($p(s=0)$).

Signal Region	N_{obs}	N_{exp}	$\langle\epsilon\sigma\rangle^{95}_{\text{obs}}$ [fb]	S^{95}_{obs}	S^{95}_{exp}	$p(s=0)$
$m_{\ell\ell} < 1$	0	1.0 ± 1.0	0.022	3.0	$3.0^{+1.3}_{-0.0}$	0.50
$m_{\ell\ell} < 2$	46	44 ± 6.8	0.15	21	19^{+7}_{-5}	0.38
$m_{\ell\ell} < 3$	90	77 ± 12	0.29	41	31^{+11}_{-9}	0.18
$m_{\ell\ell} < 5$	151	138 ± 18	0.38	52	43^{+16}_{-11}	0.24
$m_{\ell\ell} < 10$	244	200 ± 19	0.62	86	49^{+26}_{-13}	0.034
$m_{\ell\ell} < 20$	383	301 ± 23	0.95	132	61^{+22}_{-16}	0.0034
$m_{\ell\ell} < 30$	453	366 ± 27	1.04	144	70^{+26}_{-20}	0.0065
$m_{\ell\ell} < 40$	492	420 ± 30	0.96	134	74^{+29}_{-20}	0.027
$m_{\ell\ell} < 60$	583	520 ± 35	0.97	135	84^{+32}_{-23}	0.063

the inclusive signal region. The signal region is fitted simultaneously with the control regions, which are assumed to contain no signal. This way, any excess in the signal region is explained by a large signal strength, resulting in the background estimates effectively constrained only by the background-only fit of the control regions. Upper limits at the 95% confidence level on the observed (expected) number of signal events $S^{95}_{\text{obs (exp)}}$ in each inclusive signal region are shown in Table 10.2. Dividing S^{95}_{obs} by the integrated luminosity 139 fb^{-1} defines the upper limits on the visible cross-sections $\langle\epsilon\sigma\rangle^{95}_{\text{obs}}$. There are some discrepancy between the observed and expected upperlimits, which are checked by discovery tests.

A discovery test on the hypothetical signal is performed for each inclusive signal region, to evaluate the excess of the events over the SM background. A null p-value $p(s=0)$ is calculated for each signal region, which can be understood as the probability of having an event yield greater than or equal to the observed data. The results of the discovery tests are shown in the last column of Table 10.2. Several signal regions have low p-values, with the lowest observed in the $m_{\ell\ell} < 20$ GeV bin with the local p-value 0.0034, corresponding to a significance of 2.7σ. Although the discrepancy is non-negligible in this region, the significance is not large enough to claim a discovery of beyond-SM contribution, and we conclude that the observed events in inclusive signal regions are consistent with the SM predictions. The excess observed at $m_{\ell\ell} < 20$ GeV region is discussed in Chapter 11.

10.3 Model-dependent interpretation

Given the absence of a significant excess, we performed exclusion tests on the Higgsino and Wino/Bino scenarios described in Section 1.2. All the control regions and the signal regions are included to constrain the parameters, to assess the $m_{\ell\ell}$ shape of the signals.

Figure 10.5 shows the comparison of the observed data and the expected background, for all the

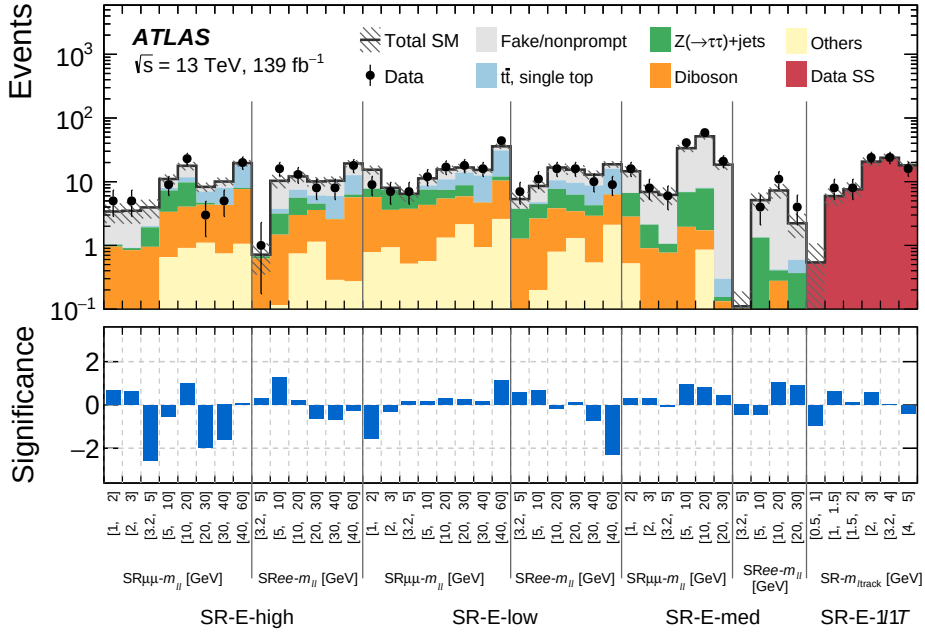

Figure 10.5: Comparison of the observed and the expected event yields in the exclusive signal regions. The background predictions are obtained by fitting all the control regions and the signal regions simultaneously. Uncertainties in the background estimates include both the statistical and systematic uncertainties. The bottom panel shows the significance of the difference between the expected and observed yields [147].

exclusive signal regions. The background expectations are obtained by simultaneously fitting all the control regions and the signal regions with background-only hypothesis. The pulls between the observed data and background prediction in the signal regions are shown in the bottom panel of Figure 10.5, with all the deviations found to be less then 3σ. Tables 10.3 and 10.4 show the detailed breakdown of the background expectation in each signal region compared with the observed data, for the 2ℓ signal regions and the $1\ell 1T$ signal regions.

In the exclusion test, CL_s values defined in Section 9.2 are calculated for $\mu = 1$ hypothesis for each signal assumption independently. The signal scenario is excluded at 95% confidence level when the obtained CL_s value is below 0.05. The signal scenarios are scanned over a 2D plane with the horizontal axis given by the mass of the $\widetilde{\chi}_2^0$ and the vertical axis defined by the difference in mass between the $\widetilde{\chi}_2^0$ and the $\widetilde{\chi}_1^0$. An exclusion contour in this 2D phase-space is defined by smoothly interpolating the region where the signal scenario is excluded at 95% CL.

Limits on the Higgsino scenario

The limits for the Higgsino scenario are set in $m(\widetilde{\chi}_2^0) \times \Delta m$ plane, which are shown in Figure 10.6. The plot on the left shows the final exclusion limits, where the blue dashed line and the red solid line show the expected and observed exclusion contours at 95% CL. The results from the searches at LEP [40] and the previous search in ATLAS [43] are shown in the same plot. The searches at LEP excludes $m(\widetilde{\chi}_1^{\pm}) > 92.4$ GeV for $\Delta m < 3$ GeV and $m(\widetilde{\chi}_1^{\pm}) > 103.5$ GeV for larger Δm. The search presented in this thesis set the most strict limit on the simplified Higgsino scenario, where $\widetilde{\chi}_2^0$ masses below 193 GeV are

Table 10.3: Observed event yields and exclusion fit results with the signal strength parameter set to zero for the exclusive 2ℓ signal regions. Background processes containing fewer than two prompt leptons are categorized as 'Fake/nonprompt'. The category 'Others' contains rare backgrounds from triboson, Higgs boson, and the remaining top-quark production processes listed in Table 1. Uncertainties in the fitted background estimates combine statistical and systematic uncertainties.

	SR bin [GeV]	[1,2]	[2,3]	[3.2,5]	[5,10]	[10,20]	[20,30]	[30,40]	[40,60]
SR–E–high ee	Observed			1	16	13	8	8	18
	Fitted SM events			0.7 ± 0.4	10.3 ± 2.5	12.1 ± 2.2	10.1 ± 1.7	10.4 ± 1.7	19.3 ± 2.5
	Fake/nonprompt			$0.03^{+0.19}_{-0.03}$	6.6 ± 2.7	4.6 ± 2.0	4.0 ± 1.5	4.4 ± 1.6	6.7 ± 2.3
	$t\bar{t}$, single top			$0.01^{+0.06}_{-0.01}$	0.59 ± 0.27	1.9 ± 0.5	1.6 ± 0.4	3.3 ± 0.6	6.4 ± 0.9
	Diboson			0.62 ± 0.23	1.4 ± 0.5	2.3 ± 0.7	2.5 ± 0.7	2.3 ± 0.6	5.4 ± 1.3
	Z($\rightarrow \tau\tau$)+jets			$0.06^{+0.29}_{-0.06}$	1.7 ± 0.7	2.6 ± 1.2	0.93 ± 0.24	0.04 ± 0.04	0.62 ± 0.23
	Others			$0.000^{+0.004}_{-0.000}$	0.12 ± 0.05	0.74 ± 0.18	1.14 ± 0.19	0.29 ± 0.07	0.27 ± 0.14
SR–E–high $\mu\mu$	Observed	5	5	0	9	23	3	5	20
	Fitted SM events	3.4 ± 1.2	3.5 ± 1.3	3.9 ± 1.3	11.0 ± 2.0	17.8 ± 2.7	8.3 ± 1.4	10.1 ± 1.5	19.6 ± 2.3
	Fake/nonprompt	2.4 ± 1.2	2.6 ± 1.4	1.9 ± 1.0	3.1 ± 1.7	6.0 ± 2.8	1.3 ± 0.8	2.0 ± 0.9	1.4 ± 1.3
	$t\bar{t}$, single top	$0.01^{+0.06}_{-0.01}$	$0.01^{+0.06}_{-0.01}$	0.09 ± 0.07	0.67 ± 0.25	2.0 ± 0.5	2.4 ± 0.5	3.7 ± 0.9	10.2 ± 1.7
	Diboson	0.92 ± 0.32	0.84 ± 0.32	0.9 ± 0.4	2.7 ± 0.7	3.1 ± 0.8	3.3 ± 0.8	3.6 ± 0.8	6.6 ± 1.5
	Z($\rightarrow \tau\tau$)+jets	$0.07^{+0.34}_{-0.07}$	$0.06^{+0.34}_{-0.06}$	1.0 ± 0.4	3.9 ± 0.9	5.7 ± 1.6	0.31 ± 0.25	$0.00^{+0.04}_{-0.00}$	0.31 ± 0.16
	Others	$0.032^{+0.035}_{-0.032}$	–	0.025 ± 0.018	0.66 ± 0.33	0.91 ± 0.14	1.10 ± 0.18	0.75 ± 0.16	1.06 ± 0.09
SR–E–med ee	Observed			0	4	11	4		
	Fitted SM events			0.11 ± 0.08	5.1 ± 1.6	7.3 ± 1.9	2.2 ± 0.9		
	Fake/nonprompt			$0.000^{+0.016}_{-0.000}$	3.8 ± 1.3	6.9 ± 2.0	1.6 ± 1.1		
	$t\bar{t}$, single top			$0.00^{+0.05}_{-0.00}$	$0.00^{+0.04}_{-0.00}$	$0.01^{+0.06}_{-0.01}$	$0.23^{+0.25}_{-0.23}$		
	Diboson			0.10 ± 0.05	0.10 ± 0.09	0.28 ± 0.26	$0.02^{+0.13}_{-0.02}$		
	Z($\rightarrow \tau\tau$)+jets			$0.000^{+0.028}_{-0.000}$	1.2 ± 1.2	$0.1^{+0.5}_{-0.1}$	$0.3^{+0.6}_{-0.3}$		
	Others			$0.000^{+0.012}_{-0.000}$	–	–	–		
SR–E–med $\mu\mu$	Observed	16	8	6	41	59	21		
	Fitted SM events	14.6 ± 2.9	6.9 ± 2.1	6.2 ± 1.9	34 ± 4	52 ± 6	18.5 ± 3.2		
	Fake/nonprompt	7.9 ± 3.2	4.8 ± 2.1	5.1 ± 2.0	27 ± 5	44 ± 6	18.2 ± 3.2		
	$t\bar{t}$, single top	$0.01^{+0.06}_{-0.01}$	$0.01^{+0.06}_{-0.01}$	$0.00^{+0.05}_{-0.00}$	$0.12^{+0.13}_{-0.12}$	0.24 ± 0.08	$0.14^{+0.19}_{-0.14}$		
	Diboson	2.3 ± 0.8	0.9 ± 0.4	0.73 ± 0.24	1.9 ± 0.7	0.87 ± 0.26	0.13 ± 0.07		
	Z($\rightarrow \tau\tau$)+jets	3.8 ± 1.8	1.2 ± 0.5	$0.3^{+0.6}_{-0.3}$	4.9 ± 1.6	6.1 ± 2.1	$0.02^{+0.29}_{-0.02}$		
	Others	0.5 ± 0.4	$0.000^{+0.026}_{-0.000}$	0.036 ± 0.015	0.019 ± 0.017	0.9 ± 0.6	–		
SR–E–low ee	Observed			7	11	16	16	10	9
	Fitted SM events			5.3 ± 1.5	8.6 ± 1.8	16.7 ± 2.5	15.5 ± 2.6	12.9 ± 2.1	18.8 ± 2.2
	Fake/nonprompt			1.6 ± 1.1	3.8 ± 1.8	6.2 ± 2.2	5.8 ± 2.3	4.2 ± 1.8	2.8 ± 1.4
	$t\bar{t}$, single top			0.015 ± 0.006	0.32 ± 0.30	2.8 ± 0.6	3.4 ± 1.1	4.5 ± 0.9	9.7 ± 1.5
	Diboson			1.3 ± 0.6	2.4 ± 0.8	3.0 ± 0.7	2.1 ± 0.7	2.4 ± 0.7	4.2 ± 1.0
	Z($\rightarrow \tau\tau$)+jets			2.5 ± 1.1	1.8 ± 0.7	3.9 ± 1.3	2.8 ± 1.0	1.4 ± 0.7	$0.07^{+0.20}_{-0.07}$
	Others			$0.01^{+0.05}_{-0.01}$	0.20 ± 0.05	0.79 ± 0.23	1.3 ± 0.8	0.54 ± 0.09	2.10 ± 0.34
SR–E–low $\mu\mu$	Observed	9	7	7	12	17	18	16	44
	Fitted SM events	15.4 ± 2.4	8.0 ± 1.7	6.5 ± 1.6	11.3 ± 1.9	15.6 ± 2.3	16.7 ± 2.3	15.3 ± 2.0	35.9 ± 3.3
	Fake/nonprompt	7.7 ± 1.9	$0.3^{+0.6}_{-0.3}$	$0.01^{+0.22}_{-0.01}$	2.6 ± 1.3	4.7 ± 1.9	2.8 ± 1.6	2.8 ± 1.6	4.9 ± 2.3
	$t\bar{t}$, single top	$0.00^{+0.04}_{-0.00}$	0.26 ± 0.07	$0.01^{+0.06}_{-0.01}$	1.2 ± 0.5	3.4 ± 0.7	5.1 ± 1.5	7.8 ± 1.3	18.9 ± 2.7
	Diboson	4.9 ± 1.3	2.7 ± 0.7	3.2 ± 0.9	3.8 ± 0.9	4.1 ± 1.0	3.7 ± 0.9	3.8 ± 0.8	7.8 ± 1.6
	Z($\rightarrow \tau\tau$)+jets	2.0 ± 0.7	3.8 ± 1.1	2.7 ± 1.2	3.2 ± 1.1	2.0 ± 1.2	2.9 ± 0.8	$0.01^{+0.27}_{-0.01}$	1.6 ± 0.6
	Others	0.8 ± 0.5	0.9 ± 0.8	0.52 ± 0.24	0.57 ± 0.16	1.32 ± 0.18	2.1 ± 0.4	0.94 ± 0.11	2.60 ± 0.20

Table 10.4: Observed event yields and exclusion fit results with the signal strength parameter set to zero for the exclusive $1\ell 1T$ regions. All backgrounds are determined from the same-sign method. Uncertainties in the fitted background estimates combine statistical and systematic uncertainties.

SR bin [GeV]	[0.5,1.0]	[1.0,1.5]	[1.5,2.0]	[2.0,3.0]	[3.2,4.0]	[4.0,5.0]
Observed	0	8	8	24	24	16
Fitted SM events	0.5 ± 0.5	6.0 ± 1.9	7.6 ± 2.1	20.7 ± 3.4	24 ± 4	18.1 ± 3.1

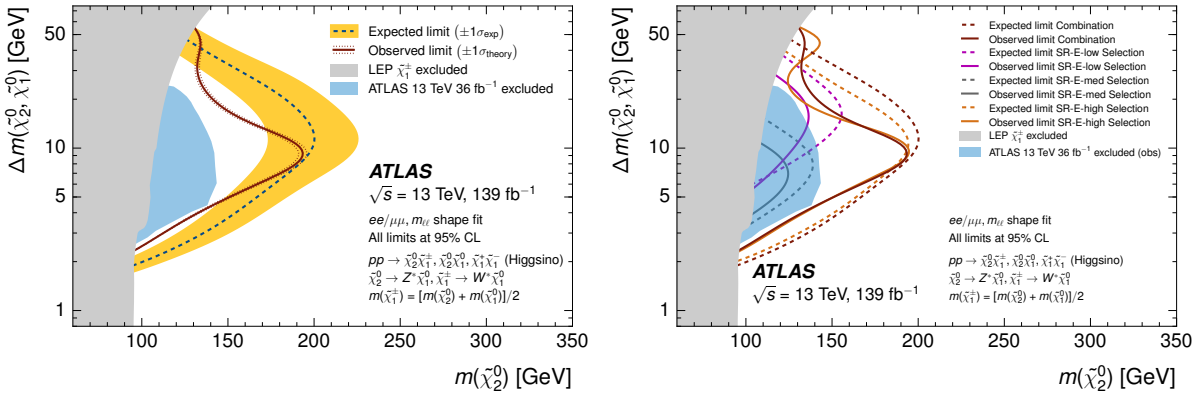

Figure 10.6: Exclusion contours in $m(\tilde{\chi}_2^0) \times \Delta m$ plane, for the simplified Higgsino scenario. (Left) Expected 95% CL exclusion contours (blue dashed line) with $\pm 1\sigma_{\text{exp}}$ (yellow band) from systematic uncertainties and observed limits (red solid line) with $\pm 1\sigma_{\text{theory}}$ (dotted red line) from signal cross-section uncertainties for simplified Higgsino scenarios. (Right) Comparison of the expected (dashed lines) and observed (solid lines) exclusion contours with each signal region. The chargino $\tilde{\chi}_1^{\pm}$ mass is assumed to be halfway between the $\tilde{\chi}_2^0$ and $\tilde{\chi}_1^0$ masses, The gray regions denote the lower chargino mass limit from LEP [40]. The blue regions indicates the limits from ATLAS Run 1 [44, 45] and Run 2 [43].

excluded for mass splittings of 9.3 GeV. At the LEP bound, mass splittings from 2.3 GeV to 55 GeV are excluded.

The plot on the right shows the exclusion contours obtained by using SR–E–high, –low and –med independently. The $1\ell 1T$ region did not have sensitivity for the Higgsino scenario thus the contour is not explicitly shown in the plot, but are included in the combined contours. Most of the exclusion power originates from the SR–E–high signal regions, with added sensitivity provided by the SR–E–low selection at higher mass splittings, and by the SR–E–med selection at smaller mass splittings.

Limits on the Wino/Bino scenarios

The limits for the Wino/Bino scenarios are shown in Figure 10.7, in $m(\tilde{\chi}_2^0) \times \Delta m$ plane. There are two parameter sets for Wino/Bino scenario as explained in Section 3.3, depending on the relative sign of the mass eigenvalues of $\tilde{\chi}_2^0$ and $\tilde{\chi}_1^0$. The plots on the top shows the limits on $m(\tilde{\chi}_2^0) \times m(\tilde{\chi}_1^0) > 0$ assumption, and the plots on the bottom shows the limits on $m(\tilde{\chi}_2^0) \times m(\tilde{\chi}_1^0) < 0$ assumption.

The left plots show the final exclusion limits, where the blue dashed lines and the red solid lines show

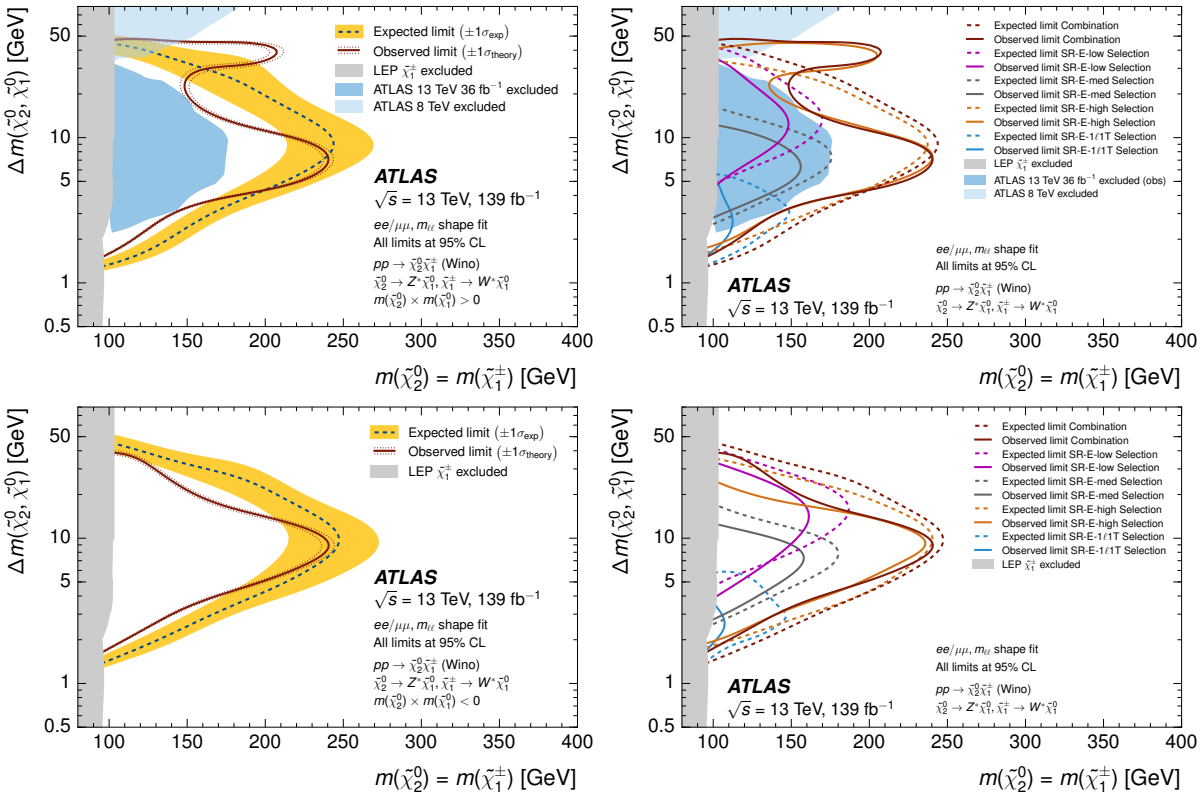

Figure 10.7: Exclusion contours in $m(\tilde{\chi}_2^0)\times\Delta m$ plane, for the simplified Wino/Bino scenario with $m(\tilde{\chi}_1^0)\times m(\tilde{\chi}_2^0) > 0$ assumption (top) and $m(\tilde{\chi}_1^0) \times m(\tilde{\chi}_2^0) < 0$ assumption (bottom). (Left) Expected 95% CL exclusion contours (blue dashed line) with $\pm1\sigma_{\text{exp}}$ (yellow band) from systematic uncertainties and observed limits (red solid line) with $\pm1\sigma_{\text{theory}}$ (dotted red line) from signal cross-section uncertainties for simplified Wino/Bino scenarios. (Right) Comparison of the expected (dashed lines) and observed (solid lines) exclusion contours with each signal region. The chargino $\tilde{\chi}_1^\pm$ mass is assumed to equal to the $\tilde{\chi}_2^0$ mass. The gray regions denote the lower chargino mass limit from LEP [40]. The blue regions indicates the limits from ATLAS Run 1 [44, 45] and Run 2 [43].

the expected and observed exclusion contours at 95% CL. The results from the searches at LEP [40] and the previous search in ATLAS [43] are shown in the same plot. For Wino production, the searches at LEP excludes $m(\tilde{\chi}_1^\pm) > 91.9$ GeV for $\Delta m < 3$ GeV and $m(\tilde{\chi}_1^\pm) > 103.5$ GeV for larger Δm. The search presented in this thesis set the most strict limit on the simplified Wino/Bino scenarios.

For $m(\tilde{\chi}_2^0) \times m(\tilde{\chi}_1^0) > 0$ assumption, $\tilde{\chi}_2^0$ masses below 240 GeV are excluded for mass splittings of 7.0 GeV. At the LEP bound, mass splittings from 1.5 GeV to 46 GeV are excluded. Similarly, for $m(\tilde{\chi}_2^0) \times m(\tilde{\chi}_1^0) < 0$ assumption, $\tilde{\chi}_2^0$ masses below 241 GeV are excluded for mass splittings of 9.0 GeV. At the LEP bound, mass splittings from 1.7 GeV to 39 GeV are excluded. Previous searches at LHC did not test the $m(\tilde{\chi}_2^0) \times m(\tilde{\chi}_1^0) < 0$ case in Wino/Bino scenario, and therefore this is the first exclusion limit set on this scenario by the LHC experiments.

The plots on the right show the exclusion contours obtained by using SR–E–high, –low and –med and $-1\ell1T$ independently. Similar to the Higgsino scenario case, most of the exclusion power originates from the SR–E–high signal regions.

Understanding the shape of the contour

There are some discrepancies between the expected and observed contours that are worth pointing out. We see a common behavior in the shape of the observed exclusion contours for all three scenarios, which are

- weaker limit at $\Delta m < 5$ GeV,
- weaker limit at $\Delta m \in (10, 30)$ GeV,
- stronger limit at $\Delta m \in (40, 60)$ GeV,

compared to the expected exclusion contour. The statement in the last bullet is not visible in the Wino/Bino contour with $m(\widetilde{\chi}_1^0) \times m(\widetilde{\chi}_2^0) < 0$ assumption (bottom plots of Figure 10.7).

The plots on the right shows that the shape of the contour is mostly derived by the contour with the SR–E–high signal regions. Thus the discrepancies can be understood by the excess/deficit of events in the high-$E_{\mathrm{T}}^{\mathrm{miss}}$ signal regions. The excesses or deficits of observed events in the signal regions that are responsible for the discrepancies are found to be

- excess in $\mu\mu$ channel, $m_{\ell\ell} \in [1, 3]$ GeV,
- excess in $\mu\mu$ channel, $m_{\ell\ell} \in [10, 20]$ GeV, and in ee channel, $m_{\ell\ell} \in [5, 10]$ GeV
- deficit in $\mu\mu$ channel, $m_{\ell\ell} \in [20, 40]$ GeV.

The source of the excesses or deficits observed in the high-$E_{\mathrm{T}}^{\mathrm{miss}}$ signal regions are discussed in Section 11. Further studies have shown that all the contours are within 2σ from the expected limit, therefore we conclude that no significant excess is observed in the searches for Higgsino and Wino/Bino production.

Chapter 11

Discussion

The impact of the results shown in the previous chapter and the future prospects of the search are discussed in this chapter. The excesses and deficits observed in the signal regions are examined in Section 11.1. In Section 11.2, the expected gain in the sensitivity by using the Prompt Lepton Tagging method is presented. Finally, the impacts of the results on the Higgsino and Wino/Bino scenarios are discussed in Section 11.3.

11.1 Excess/Deficit follow-up

11.1.1 Excess in the inclusive signal regions

As shown in Section 10.2, an excess of events over background prediction is observed in the inclusive signal region with $m_{\ell\ell} < 20$ GeV, which corresponds to the local significance of 2.7σ. Although the significance is not as large as to claim a discovery of a beyond-SM effect, it is worth trying to understand what can possibly contribute to this excess. The events in the inclusive signal region with $m_{\ell\ell} < 20$ GeV is dominated by events the pass the SR–E–med selection. It is found that the excess in $m_{\mu\mu} \in [5, 20]$ region are the cause of the excess in the inclusive region.

The data in this region are compared to the background prediction, by checking the distributions of several kinematic variables. As a result, a bump in the p_{T} of the leading lepton is found, as shown in Figure 11.1. In the third bin from the left with $p_{\mathrm{T}} \in [8, 9.5]$ GeV, there is a significant excess in the number of events over the background prediction. The background in this region is dominated by the fake/non-prompt events, which are shown with gray histogram. To check the fake/non-prompt background modeling in this p_{T} region, the distribution of the lepton p_{T} is checked in the same-sign validation region. Figure 11.2 shows the distribution of the leading lepton p_{T} in the same-sign validation region, VRSS–E–med. An excess of events is also visible in the same bin, with the ratio of data over prediction about 1.8.

The mis-modeling in the particular p_{T} bin either comes from the mis-measurement of the fake factor itself, or the difference in the fake composition. They are both taken into account as systematic uncertainties, as explained in Section 8.3. The problem is that these systematic uncertainties are only constrained loosely in a discovery fit. This is because the discovery fit only uses the control regions to fit the background distribution, where the events are dominated by irreducible (non-fake) backgrounds.

As a conclusion, we currently understanding that this excess comes from the combination of

- the fake/non-prompt background being under-predicted at certain p_{T} bin, and

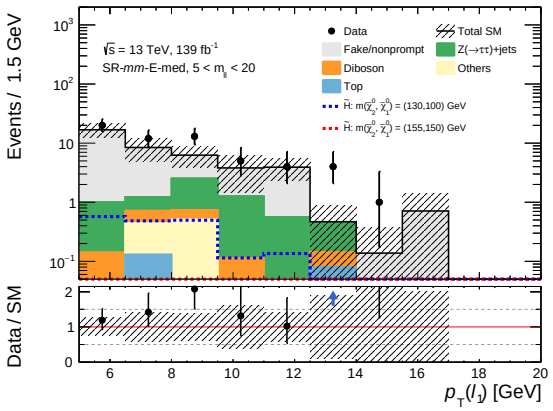

Figure 11.1: The distribution of the p_{T} of the leading lepton in the SR–E–med signal region, for muon channels with $5 < m_{\mu\mu} < 20$ GeV. The bottom panel shows the ratio of the observed data over the SM prediction.

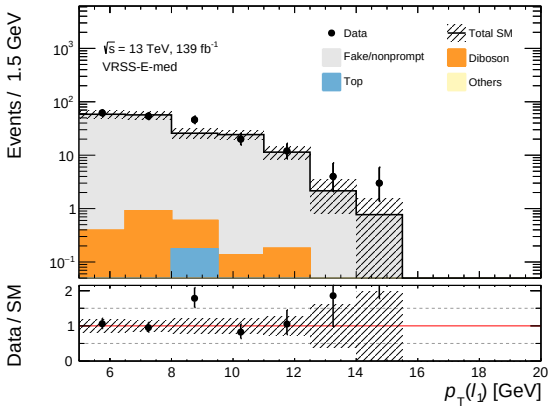

Figure 11.2: The distributions of the p_{T} of the leading leptons in the same sign validation region VRSS–E–med. The bottom panel shows the ratio of the observed data over the SM prediction.

- the fake/non-prompt systematic parameters not constrained in the discovery fit.

Although the excess is not statistically significant in this search, we will need to model the fake background better for the future search. It is also important to constrain the systematic uncertainties related to the fake/non-prompt background in the discovery fit, for example by defining a control region enriched with fake/non-prompt background.

11.1.2 Excesses and deficits in the exclusive signal regions

Excess in regions with small $m_{\ell\ell}$

Excess of events is observed in $m_{\mu\mu} \in [1, 2]$ and $\in [2, 3]$ GeV regions. The background in this region is dominated by the fake/non-prompt processes. The kinematic distributions in these signal regions are studied, and a suspicious behavior is seen in the distribution of ΔR between the two leptons ($\Delta R_{\ell\ell}$), as shown in Figure 11.3.

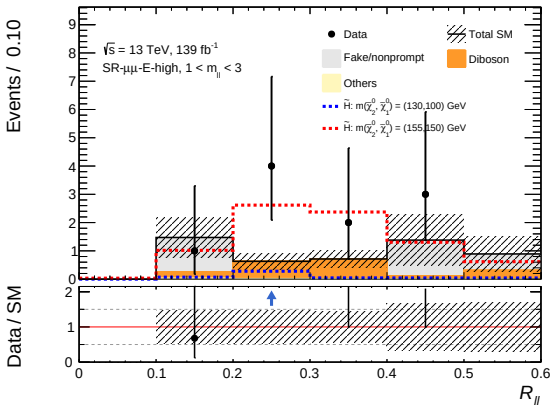

Figure 11.3: The distributions of $\Delta R_{\ell\ell}$ in the SR–E–high signal region, for muon channels with $1 < m_{\ell\ell} < 3$ GeV. The bottom panel shows the ratio of the observed data over the SM prediction.

In the plot, there are some bins with no entries of the fake/non-prompt background. After a detailed study, it is found that this comes from "negative weighted" events in the fake factor method, as explained in Section 7.2.4. The events with two "anti-ID" leptons (leptons not passing the signal criteria) yield a negative contribution in the fake factor method, to avoid double counting of the events (details in Appendix C.4). Out of 17 events with at least one anti-ID lepton, 8 of them had two anti-ID leptons, which is more frequent than in the other signal regions. This can be a statistical fluctuation, but the effects coming from two leptons reconstructed close to each other also contribute. As explained in Section 5.3, a special correction is applied when two leptons are reconstructed close to each other. However, it is not possible to perfectly correct the effect, and could lead to negative yield events enhanced at small $\Delta R_{\ell\ell}$ regions.

We conclude that the excess comes from the limited data events available for estimation of the fake/non-prompt yield, and also potentially from the inevitable effect by two leptons reconstructed close-by. A more sophisticated correction method is necessary to account for this problem.

Other excesses/deficits

The excess of events observed in the high-$E_{\mathrm{T}}^{\mathrm{miss}}$ signal regions with $10 < m_{\mu\mu} < 20$ GeV and $5 < m_{ee} < 10$ GeV is also studied in detail, however there are no apparent mis-modeling in the distribution of the basic kinematic variables ($E_{\mathrm{T}}^{\mathrm{miss}}$, p_{T} of the leptons, ΔR between leptons, etc.). The deficit observed in the high-$E_{\mathrm{T}}^{\mathrm{miss}}$ signal region with $20 < m_{\mu\mu} < 40$ is also studied, but no obvious mis-modeling is found either. Currently, given no implication from the data, we conclude that they are consistent with statistical fluctuations.

11.2 Results using Prompt Lepton Tagging

The Prompt Lepton Tagging method discussed in Section 5.2 is expected to reduce the number of fake/non-prompt background events in the signal regions, with keeping the efficiency for the leptons from the signal process. In this section, the expected exclusion limits using the Prompt Lepton Tagging are shown, and are

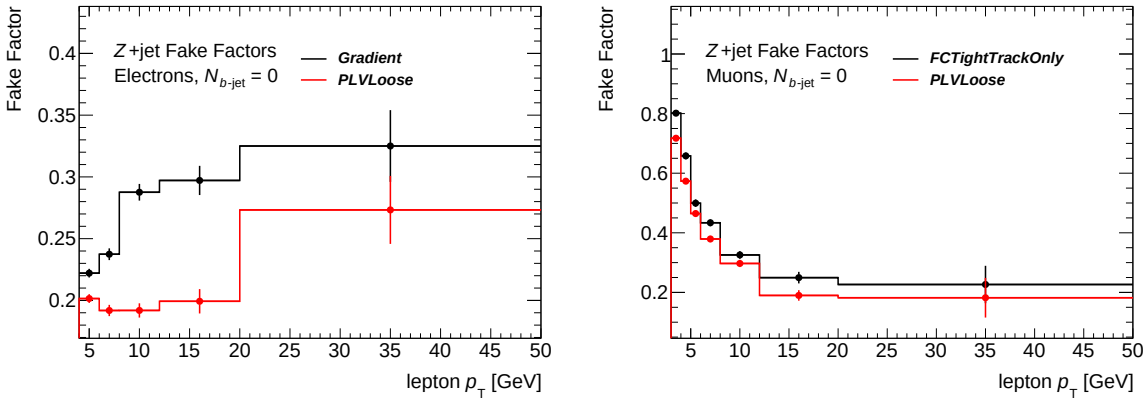

Figure 11.4: The fake factors measured in the Z+jets region with no b-tagged jets as a function of p_{T} of the fake lepton candidate, for electrons (left) and muons (right). The black histogram in each plot shows the fake factors measured using isolation selection in the main analysis, which is the *Gradient* selection for electrons and the *FCTightTrackOnly* selection for muons. The red histogram shows the fake factors measured for the *PLTLoose* selection.

compared with the results presented in Chapter 10, to evaluate the gain by introducing this method. In this section, we refer to the analysis presented in Chapter 10 as "main analysis".

The Prompt Lepton Tagging is intended to substitute the "isolation" cuts on the leptons, which requires the lepton to be isolated from other tracks or clusters in the calorimeter. A new isolation cut *PLTLoose* is defined using the Prompt Lepton Tagging, as described in Section 5.2.4. In the main analysis presented in this thesis, the *Gradient* and *FCTightTrackOnly* selections, defined in Sections 4.4 and 4.5, are applied to electrons and muons, respectively. These are replaced by *PLTLoose* selection, and the expected sensitivity is compared with the results of the main analysis.

In order to introduce the *PLTLoose* selection to the analysis, the fake factors need to be updated. The *PLTLoose* selection is expected to reduce the fake background, thus the fake factors are expected to become lower compared those in the main analysis. The measurement region used in the main analysis is the region enriched with multi-jet events (explained in Section 7.2.3), dominated by events with two jets. The problem in this region is that the statistics is very limited due to the absence of high-p_{T} object that can be used in the trigger to collect the events. The new fake factor is measured in regions dominated by the Z+jets process. In this region, the leptons from the decay of the Z-boson have high p_{T}. The lepton triggers with high p_{T} threshold can be used to efficiently collect the data. The definitions of the anti-ID selection is unchanged from the main analysis.

Figure 11.4 shows the results of the fake factor measurements, for events with no b-tagged jets. The black histograms show the fake factors for the isolation selections used in the main analysis, and the red histograms show the fake factors for the *PLTLoose* selections. The fake factors are smaller when using the *PLTLoose* selections, compared to the original selections in the whole p_{T} range, where about 20% reduction is obtained for electrons, and 10% reduction for muons.

One important observation is that the fake factors in the Z+jets region and in the multi-jet region are not identical. When we compare the fake factors shown with black lines in Figure 11.4 to the fake factors in Figures 7.8 and 7.9, we clearly see that some of the values do not match. For electrons, they are consistent within the statistical uncertainty, although the shapes of the distributions look quite different.

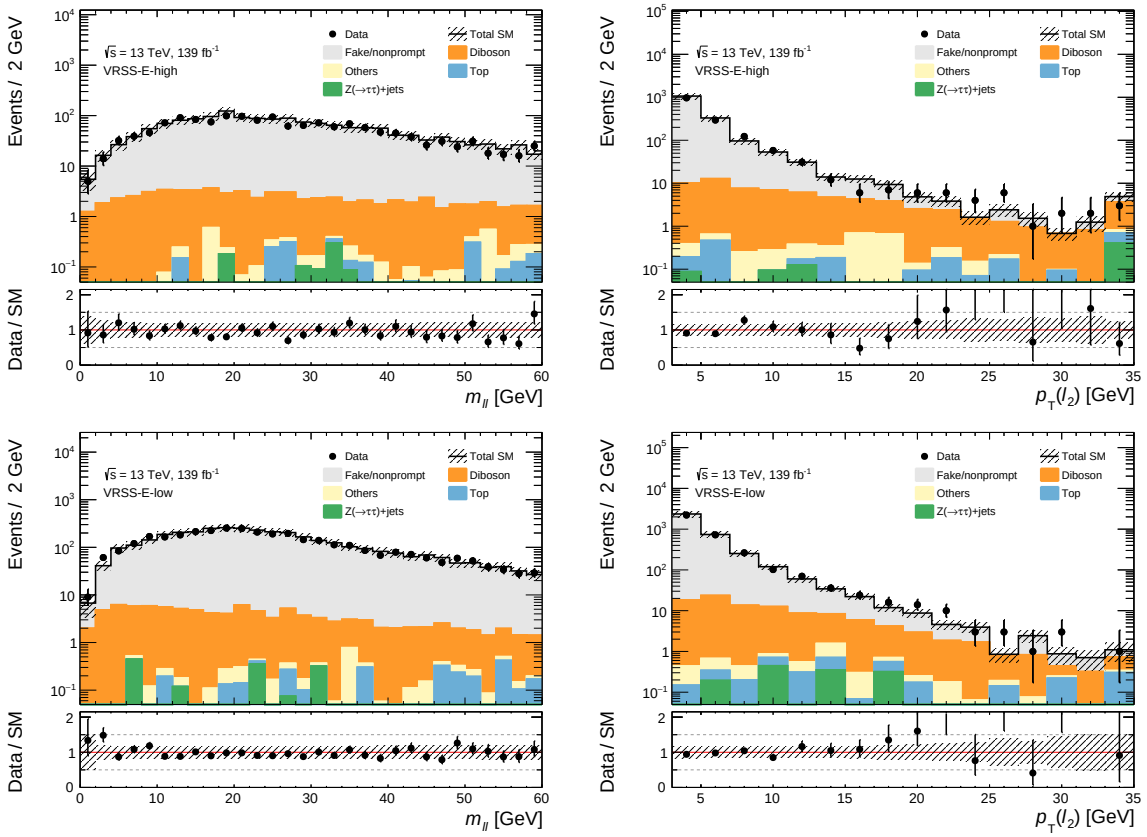

Figure 11.5: The distributions of $m_{\ell\ell}$ (left) and the p_{T} of the sub-leading lepton (right) in the same-sign validation regions, the VR–SS–high (top) and VR–SS–low (bottom) selections. The *PLTLoose* isolation selections are used for the isolation criteria.

For muons, on the other hand, the shape looks consistent but the measured fake factors are generally higher in the Z+jets region. The difference is more evident in the low-p_{T} region, which increases the number of the fake/non-prompt background prediction in regions with small $m_{\ell\ell}$. The source of the difference is not identified yet, but is likely from the difference in the source of the fake/non-prompt events. More studies using the MC samples are needed, but the 40% (20%) uncertainties assigned for electron (muon) fake factors are enough to cover this difference (explained in Section 8.3).

The expected yield of the fake/non-prompt background is updated using the new fake factors, and the shape and the normalization of the background prediction is checked in the same-sign validation regions. Figure 11.5 shows the distributions of mass of the two leptons ($m_{\ell\ell}$) and the sub-leading lepton p_{T} ($p_{\mathrm{T}}(\ell_2)$), for high-$E_{\mathrm{T}}^{\mathrm{miss}}$ and low-$E_{\mathrm{T}}^{\mathrm{miss}}$ validation regions. The observed data agree with the predictions, except for some underestimation at small $m_{\ell\ell}$ values in low-$E_{\mathrm{T}}^{\mathrm{miss}}$ validation region.

Figure 11.6 shows the expected exclusion limits on the Wino/Bino scenario, using the *PLTLoose* selection. The exclusion limits are compared with the expected and the observed limits from the main analysis. The sensitivities to the signals at Δm larger than 20 GeV are improved by introducing the *PLTLoose* selection. This mainly comes from the gain in the lepton isolation efficiency for leptons at low p_{T}. At regions with small Δm, the sensitivity degrades compared to the main analysis. As noted in the previous paragraphs, this is due to the difference of the region to measure the fake factors, and is not

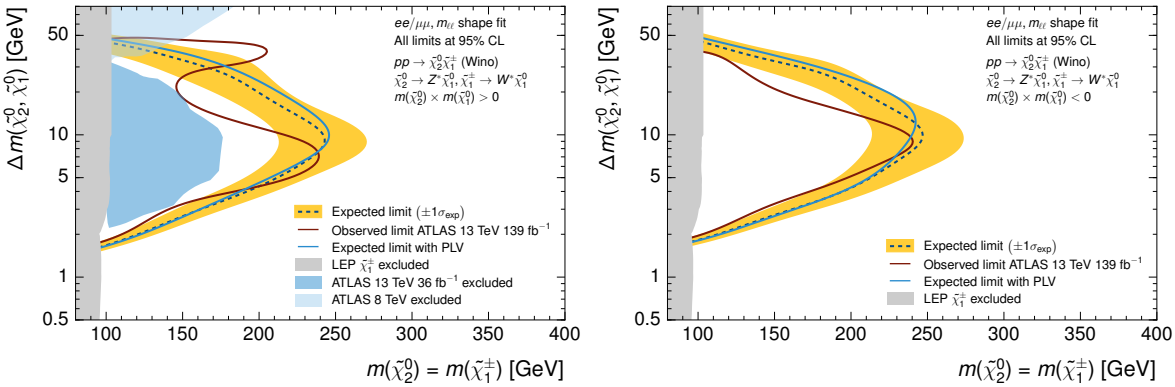

Figure 11.6: Exclusion contours in $m(\tilde{\chi}_2^0)\times\Delta m$ plane, for the simplified Wino/Bino scenario with $m(\tilde{\chi}_1^0)\times m(\tilde{\chi}_2^0) > 0$ assumption (left) and $m(\tilde{\chi}_1^0)\times m(\tilde{\chi}_2^0) < 0$ assumption (right). The expected (observed) limits from the main analysis in this thesis are shown with blue dashed (red solid) lines. The expected limits using *PLTLoose* selection is shown with solid light-blue lines.

directly the consequence of introducing the *PLTLoose* selection. We understand that the fake factors are underestimated in the main analysis, which lead to some excess observed at the signal regions with small $m_{\ell\ell}$. The new fake factors measured in the Z+jets region has larger values, therefore we expect that the excess becomes smaller with the updated fake factor.

Figure 11.7 shows the future sensitivity for the same analysis selections, with 300 fb^{-1} and 3000 fb^{-1} of $\sqrt{s}$ = 13 TeVpp collision. The results are obtained by scaling the background expectation to 300 fb^{-1}or 3000 fb^{-1}, and assuming that we observe exactly the same number of data as the expectation. Note that 3000 fb^{-1}of collision data is expected at high-luminosity LHC, where the center-of-energy is expected to be raised to 14 TeV. This enhances the production cross section of the signal processes, which are not taken into account here. The results with the Prompt Lepton Tagging are compared with the results from the main analysis. Similar behavior is seen as the results for 139 fb^{-1}; the sensitivity gain is seen at medium Δm range, while at small Δm, the sensitivity apparently degrades with the Prompt Lepton Tagging. Again, we emphasize that this is not the direct consequence of introducing the Prompt Lepton Tagging.

11.3 Impacts on the MSSM scenarios

In this section, the exclusion limits obtained for the MSSM with the Higgsino and the Wino/Bino scenarios (introduced in Section 1.2) are compared with some constraints set by other experiments.

11.3.1 Higgsino scenario

Figure 11.8 shows the exclusion contour in $m(\tilde{\chi}_2^0)$–Δm plane, for the analysis presented in this thesis. The same exclusion contour from similar search by CMS using two soft leptons [42] is also shown. Our analysis exclude regions with small mass difference at Δm < 10 GeV, and also at regions with larger Δm, at Δm > 20 GeV. The difference comes from the event selections and the design of the signal regions. Generally, looser selections are applied in our analysis to collect signals with very small Δm (< 5 GeV), whereas

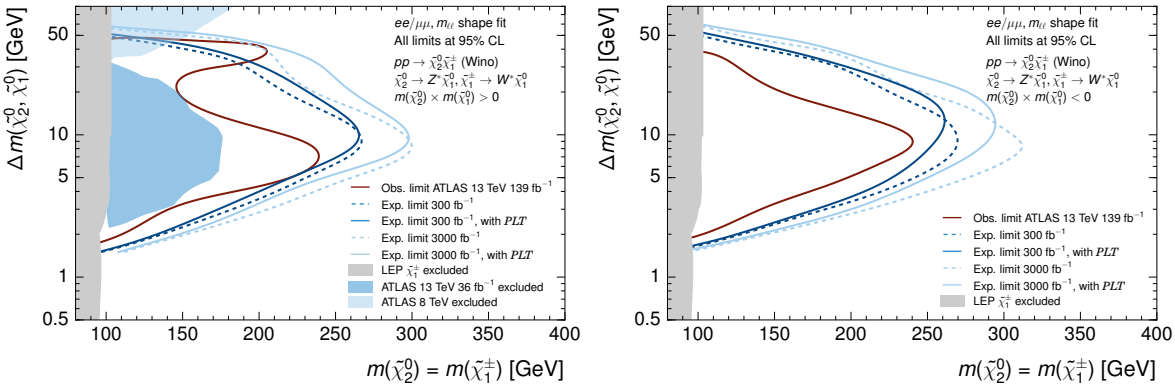

Figure 11.7: Exclusion contours in $m(\tilde{\chi}_2^0) \times \Delta m$ plane, for the simplified Wino/Bino scenario with $m(\tilde{\chi}_1^0) \times m(\tilde{\chi}_2^0) > 0$ assumption (left) and $m(\tilde{\chi}_1^0) \times m(\tilde{\chi}_2^0) < 0$ assumption (right). The observed limits from the main analysis in this thesis are shown with red solid lines. The expected limits using the same selection as the main analysis and using the *PLTLoose* selection are shown with dashed and solid lines, respectively, for 300 fb^{-1}(dark blue) and 3000 fb^{-1}(light blue).

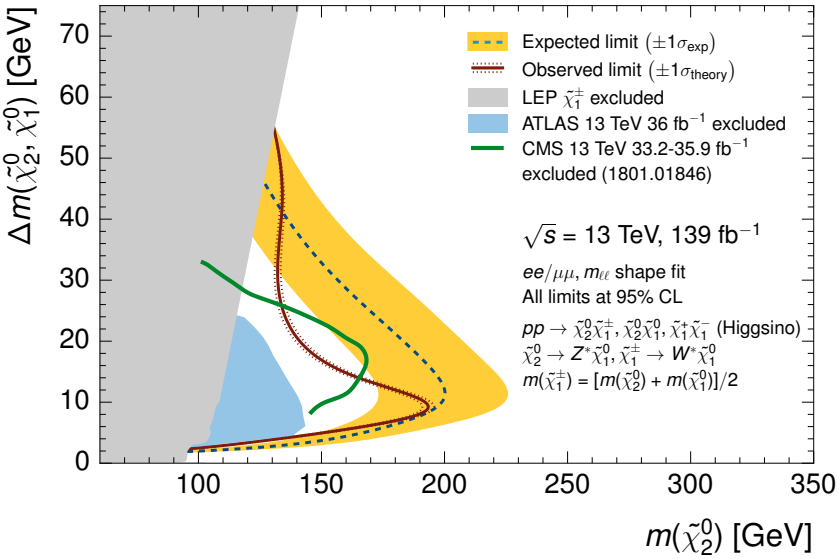

Figure 11.8: Exclusion contours in $m(\tilde{\chi}_2^0) \times \Delta m$ plane, for the simplified Higgsino scenario. The expected and observed limits for the analysis presented in this thesis are shown in dashed blue and solid red lines, respectively. The same limits from the CMS experiment [41] is shown with green solid line.

tighter cuts are applied in the analysis by CMS, which gives optimal sensitivity in the medium Δm range (10–20 GeV). In the future searches for the signals with smaller Δm, which is favored in the Higgsino scenario, the techniques to reconstruct leptons with very low-p_{T} become more important.

In the naturalness point of view, as discussed in Section 1.2.1, a pure Higgsino state with mass < 700 GeV is compatible with 1 % fine tuning, and any other SUSY particles can be much heavier. In this context, the Higgsino can be anywhere in the 2D phase-space in Figure 11.8. Although we set the most strict limits in this region, there are still more phase space to explore the Higgsinos, for example in a future high energy collider [159].

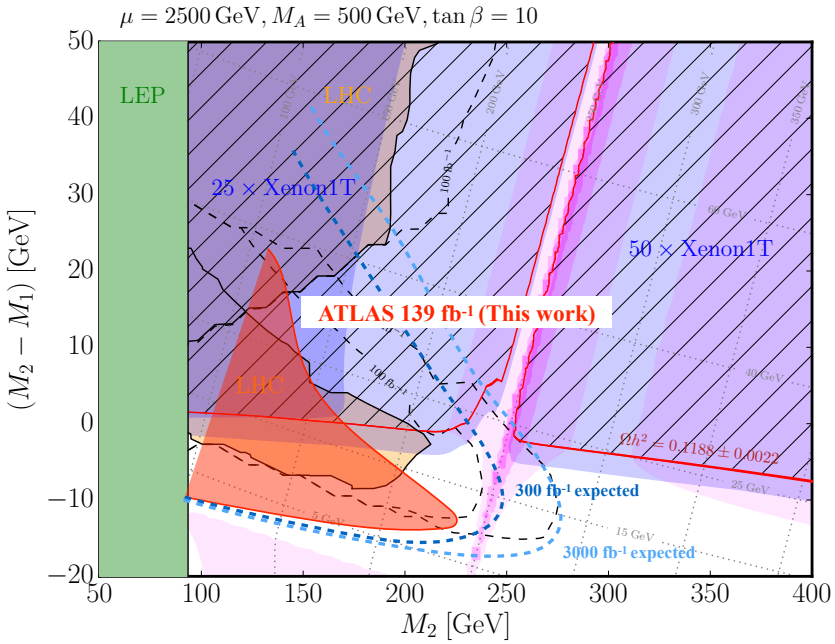

Figure 11.9: The allowed parameter space for the the Wino/Bino scenario in the (M_2, $M_2 - M_1$) plane. The MSSM parameters are set to $|\mu| = 2.5$ TeV, $\tan\beta = 10$ and $M_A = 500$GeV. The exclusion limit obtained for the Wino/Bino scenario is overlayed to the original plot in Ref. [34].

11.3.2 Wino/Bino scenario

The obtained exclusion limits for the MSSM with the simplified Wino/Bino scenario are overlayed to the limits from other experiments, shown in Figure 11.9. Current and projected limits are shown in $M2 \times (M_2 - M_1)$ plane, where the details of each limit is explained in Section 1.2.2, or Ref. [34]. The search presented in this thesis newly excludes the region with small Δm. This region does not reproduce the correct dark matter relic density of the galaxy by itself, but it can account for a part of the dark matter density.

For larger statistics at 3000 fb^{-1}, the search range can extend to the region where the dark matter relic density matches with the neutralinos in the Wino/Bino scenario – at Δm about 25 GeV, and $m(\widetilde{\chi}_1^{\pm})$ about 300 GeV. Further updates in the analysis methods can enhance the sensitivity to regions with medium Δm values, for example by applying the Prompt Lepton Tagging method. The analysis presented in Section 11.2 shows that applying the Prompt Lepton Tagging extends the limit on $m(\widetilde{\chi}_2^0)$ by about 30 GeV at $\Delta m = 25$ GeV. A large phase-space at smaller mass-splitting can also be probed by the future searches by LHC experiments. Other than the collider experiments, this region can only be excluded by XENON1T dark matter direct search with factor of 25 improvements to the result presented in Ref. [36], or Fermi-LAT indirect search with three orders of magnitude improvement from the current limit [39].

Chapter 12

Conclusion

The search for electroweak production of the chargino and neutralino with compressed mass spectra was reported in this thesis. The search used 139 fb^{-1} of $\sqrt{s}$ = 13 TeV proton–proton collision data at the LHC collected by the ATLAS detector. Signals with small mass difference between the lightest two neutralinos ($\widetilde{\chi}_2^0$, $\widetilde{\chi}_1^0$) are targeted in this thesis. Events with two same-flavor, oppositely charged leptons were selected to search for the decay process $\widetilde{\chi}_2^0 \to Z^* \widetilde{\chi}_1^0$, followed by $Z^* \to \ell\ell$. Events were also required to have a significant missing transverse momentum ($E_{\mathrm{T}}^{\mathrm{miss}}$) and a hadronic activity from initial-state radiation. The small mass difference leads to a characteristic peak in the invariant mass of the two leptons ($m_{\ell\ell}$), with the kinematic endpoint at $\Delta m = m(\widetilde{\chi}_2^0) - m(\widetilde{\chi}_1^0)$.

The challenge in this analysis is to reconstruct two leptons from the signal events, which are expected to have small transverse momentum (p_{T}), and are emitted close to each other. To enhance the sensitivity of the search, an algorithm dedicated to reconstruct muons with low-p_{T} was applied. The efficiency to reconstruct muons with $p_{\mathrm{T}} \sim 3$ GeV increased from 40% to 60% with this algorithm. The method to correct the contribution from the leptons reconstructed close-by were also updated.

The selected events were categorized into four signal regions, by the number of high-quality leptons, the size of the $E_{\mathrm{T}}^{\mathrm{miss}}$, and the sum of the p_{T} of the two leptons. Events in each category was binned in $m_{\ell\ell}$ to exploit the characteristic shape in the distribution for the signal process. The number of background events was estimated by using both the Monte Carlo simulated samples and the data. The background processes that include fake or non-prompt leptons from hadron decays were estimated using the data driven method. Other background processes were modeled using the Monte Carlo simulation, which were scaled to data in control regions. Six control regions were defined to normalize the Monte Carlo to data, and seven validation regions were defined to verify the background prediction. All the four categories of signal regions were used to search for excess of events in the range of 1 GeV $< m_{\ell\ell} <$ 60 GeV.

After unblinding, the data were found to be consistent with the predictions from the SM. No signals from the neutralino and chargino production were observed, and thus exclusion limits at 95% CL were set on the $m(\widetilde{\chi}_2^0)$ as functions of the mass difference $\Delta m = m(\widetilde{\chi}_2^0) - m(\widetilde{\chi}_1^0)$, for two scenarios; the Higgsino scenario and the Wino/Bino scenario. For the Higgsino scenario, the lower limits on $m(\widetilde{\chi}_2^0)$ was set at 193 GeV for Δm = 9.3 GeV, and 92.4 GeV for Δm = 2.3 GeV. For the Wino/Bino scenario, two different parameters that produce the same mass spectra were considered. In the first parameter set, the lower limits on $m(\widetilde{\chi}_2^0)$ was set at 240 GeV for Δm = 7.0 GeV and 92.4 GeV for Δm = 1.5 GeV. In the second parameter set, the lower limits on $m(\widetilde{\chi}_2^0)$ was set at 241 GeV for Δm = 9.0 GeV and 92.4 GeV for Δm = 1.7 GeV. The search presented in this thesis sets the most strict limits on both the Higgsino and Wino/Bino scenarios in the simplified MSSM.

The expected limits using the multi-variate analysis technique "Prompt Lepton Tagging" for lepton reconstruction were also examined, and are extrapolated to future sensitivity. The lower limits on

$m(\widetilde{\chi}_2^0)$ were expected to improve by about 15 GeV in the regions with Δm larger than 10 GeV, for both parameter sets in the Wino/Bino scenario. With extrapolating to 3000 fb^{-1}, the exclusion limit extends to $m(\widetilde{\chi}_2^0) > 250$ GeV at $\Delta m = 25$ GeV. The improvement on the limits by applying Prompt Lepton Tagging is about 30 GeV, which makes the search sensitive to the region where the Wino/Bino neutralinos produce correct dark matter density.

Bibliography

[1] Yu. A. Golfand and E. P. Likhtman, *Extension of the Algebra of Poincare Group Generators and Violation of p Invariance*, JETP Lett. **13** (1971) 323, [Pisma Zh. Eksp. Teor. Fiz. **13** (1971) 452] (cit. on p. 1).

[2] J. Wess and B. Zumino, *Supergauge Transformations in Four-Dimensions*, Nucl. Phys. B **70** (1974) 39 (cit. on p. 1).

[3] A. Salam and J. A. Strathdee, *Supersymmetry and Nonabelian Gauges*, Phys. Lett. B **51** (1974) 353 (cit. on p. 1).

[4] P. Fayet, *Supersymmetry and Weak, Electromagnetic and Strong Interactions*, Phys. Lett. B **64** (1976) 159 (cit. on p. 1).

[5] G. R. Farrar and P. Fayet, *Phenomenology of the Production, Decay, and Detection of New Hadronic States Associated with Supersymmetry*, Phys. Lett. B **76** (1978) 575 (cit. on p. 1).

[6] S. P. Martin, *A Supersymmetry Primer*, Adv. Ser. Direct. High Energy Phys. **18** (1998) 1, arXiv: hep-ph/9709356 (cit. on pp. 2, 3, 8, 9).

[7] S. Dimopoulos and D. W. Sutter, *The Supersymmetric flavor problem*, Nucl. Phys. **B452** (1995) 496, arXiv: hep-ph/9504415 [hep-ph] (cit. on p. 4).

[8] ATLAS Collaboration, *Observation of a new particle in the search for the Standard Model Higgs boson with the ATLAS detector at the LHC*, Phys. Lett. B **716** (2012) 1, arXiv: 1207.7214 [hep-ex] (cit. on p. 6).

[9] ATLAS and CMS Collaborations, *Combined Measurement of the Higgs Boson Mass in pp Collisions at $\sqrt{s} = 7$ and 8 TeV with the ATLAS and CMS Experiments*, Phys. Rev. Lett. **114** (2015) 191803, arXiv: 1503.07589 [hep-ex] (cit. on p. 6).

[10] G. 't Hooft and M. J. G. Veltman, *Regularization and Renormalization of Gauge Fields*, Nucl. Phys. **B44** (1972) 189 (cit. on p. 7).

[11] M. E. Peskin and D. V. Schroeder, *An introduction to quantum field theory*, Includes exercises, Westview, 1995, URL: https://cds.cern.ch/record/257493 (cit. on p. 7).

[12] V. C. Rubin and W. K. Ford Jr., *Rotation of the Andromeda Nebula from a Spectroscopic Survey of Emission Regions*, Astrophys. J. **159** (1970) 379 (cit. on p. 7).

[13] V. C. Rubin, N. Thonnard and W. K. Ford Jr., *Rotational properties of 21 SC galaxies with a large range of luminosities and radii, from NGC 4605 /R = 4kpc/ to UGC 2885 /R = 122 kpc/*, Astrophys. J. **238** (1980) 471 (cit. on p. 7).

[14] R. Massey, T. Kitching and J. Richard, *The dark matter of gravitational lensing*, Rept. Prog. Phys. **73** (2010) 086901, arXiv: 1001.1739 [astro-ph.CO] (cit. on p. 7).

[15] D. Clowe et al., *A direct empirical proof of the existence of dark matter*, Astrophys. J. **648** (2006) L109, arXiv: astro-ph/0608407 [astro-ph] (cit. on p. 7).

[16] N. Aghanim et al., *Planck 2018 results. VI. Cosmological parameters*, (2018), arXiv: 1807.06209 [astro-ph.CO] (cit. on p. 7).

[17] L. J. Hall, D. Pinner and J. T. Ruderman, *A natural SUSY Higgs near 125 GeV*, Journal of High Energy Physics **2012** (2012), ISSN: 1029-8479, URL: http://dx.doi.org/10.1007/JHEP04(2012)131 (cit. on pp. 9, 10).

[18] A. Djouadi, J.-L. Kneur and G. Moultaka, *SuSpect: A Fortran code for the supersymmetric and Higgs particle spectrum in the MSSM*, Comput. Phys. Commun. **176** (2007) 426, arXiv: hep-ph/0211331 [hep-ph] (cit. on p. 10).

[19] S. Heinemeyer, W. Hollik and G. Weiglein, *FeynHiggs: A Program for the calculation of the masses of the neutral CP even Higgs bosons in the MSSM*, Comput. Phys. Commun. **124** (2000) 76, arXiv: hep-ph/9812320 [hep-ph] (cit. on p. 10).

[20] *SUSY October 2019 Summary Plot Update*, tech. rep. ATL-PHYS-PUB-2019-044, CERN, 2019, URL: http://cds.cern.ch/record/2697155 (cit. on pp. 9, 10).

[21] C. Cheung, A. L. Fitzpatrick and D. Shih, *(Extra)ordinary gauge mediation*, JHEP **07** (2008) 054, arXiv: 0710.3585 [hep-ph] (cit. on p. 9).

[22] J. Alwall, M.-P. Le, M. Lisanti and J. G. Wacker, *Searching for directly decaying gluinos at the Tevatron*, Phys. Lett. B **666** (2008) 34, arXiv: 0803.0019 [hep-ph] (cit. on p. 9).

[23] J. Alwall, P. Schuster and N. Toro, *Simplified models for a first characterization of new physics at the LHC*, Phys. Rev. D **79** (2009) 075020, arXiv: 0810.3921 [hep-ph] (cit. on p. 9).

[24] D. Alves et al., *Simplified models for LHC new physics searches*, J. Phys. G **39** (2012) 105005, arXiv: 1105.2838 [hep-ph] (cit. on p. 9).

[25] J. A. Casas, J. M. Moreno, S. Robles, K. Rolbiecki and B. Zaldívar, *What is a Natural SUSY scenario?*, JHEP **06** (2015) 070, arXiv: 1407.6966 [hep-ph] (cit. on p. 9).

[26] R. Barbieri and G. F. Giudice, *Upper Bounds on Supersymmetric Particle Masses*, Nucl. Phys. B **306** (1988) 63 (cit. on p. 11).

[27] B. de Carlos and J. A. Casas, *One loop analysis of the electroweak breaking in supersymmetric models and the fine tuning problem*, Phys. Lett. B **309** (1993) 320, arXiv: hep-ph/9303291 (cit. on p. 11).

[28] R. Barbieri and D. Pappadopulo, *S-particles at their naturalness limits*, JHEP **10** (2009) 061, arXiv: 0906.4546 [hep-ph] (cit. on p. 11).

[29] H. Baer, V. Barger and P. Huang, *Hidden SUSY at the LHC: the light higgsino-world scenario and the role of a lepton collider*, JHEP **11** (2011) 031, arXiv: 1107.5581 [hep-ph] (cit. on p. 11).

[30] M. Papucci, J. T. Ruderman and A. Weiler, *Natural SUSY endures*, JHEP **09** (2012) 035, arXiv: 1110.6926 [hep-ph] (cit. on p. 11).

[31] H. Baer, V. Barger, P. Huang, A. Mustafayev and X. Tata, *Radiative natural SUSY with a 125 GeV Higgs boson*, Phys. Rev. Lett. **109** (2012) 161802, arXiv: 1207.3343 [hep-ph] (cit. on p. 11).

[32] S. D. Thomas and J. D. Wells, *Phenomenology of Massive Vectorlike Doublet Leptons*, Phys. Rev. Lett. **81** (1998) 34, arXiv: hep-ph/9804359 [hep-ph] (cit. on p. 11).

[33] A. Djouadi et al., *The Minimal supersymmetric standard model: Group summary report*, 1998, arXiv: hep-ph/9901246 (cit. on p. 11).

[34] L. Roszkowski, E. M. Sessolo and S. Trojanowski, *WIMP dark matter candidates and searches—current status and future prospects*, Rept. Prog. Phys. **81** (2018) 066201, arXiv: 1707.06277 [hep-ph] (cit. on pp. 12, 147).

[35] D. S. Akerib et al., *Results from a search for dark matter in the complete LUX exposure*, Phys. Rev. Lett. **118** (2017) 021303, arXiv: 1608.07648 [astro-ph.CO] (cit. on p. 12).

[36] E. Aprile et al., *First Dark Matter Search Results from the XENON1T Experiment*, Phys. Rev. Lett. **119** (2017) 181301, arXiv: 1705.06655 [astro-ph.CO] (cit. on pp. 11–13, 147).

[37] N. Arkani-Hamed, A. Delgado and G. F. Giudice, *The Well-tempered neutralino*, Nucl. Phys. **B741** (2006) 108, arXiv: hep-ph/0601041 [hep-ph] (cit. on p. 11).

[38] S. Profumo, T. Stefaniak and L. Stephenson Haskins, *The Not-so-well-tempered neutralino*, Phys. Rev. D **96** (2017) 055018, arXiv: 1706.08537 [hep-ph] (cit. on pp. 11, 14).

[39] M. Ackermann et al., *Searching for Dark Matter Annihilation from Milky Way Dwarf Spheroidal Galaxies with Six Years of Fermi Large Area Telescope Data*, Phys. Rev. Lett. **115** (2015) 231301, arXiv: 1503.02641 [astro-ph.HE] (cit. on pp. 11–13, 147).

[40] ALEPH, DELPHI, L3, OPAL Experiments, *Combined LEP Chargino Results, up to 208 GeV for low DM*, LEPSUSYWG/02-04.1, 2002, URL: http://lepsusy.web.cern.ch/lepsusy/www/inoslowdmsummer02/charginolowdm_pub.html (cit. on pp. 11, 13, 15, 16, 135, 137, 138).

[41] A. M. Sirunyan et al., *Search for electroweak production of charginos and neutralinos in multilepton final states in proton-proton collisions at $\sqrt{s}$ = 13 TeV*, JHEP **03** (2018) 166, arXiv: 1709.05406 [hep-ex] (cit. on pp. 11, 13, 146).

[42] CMS Collaboration, *Search for new physics in events with two soft oppositely charged leptons and missing transverse momentum in proton-proton collisions at $\sqrt{s}$ = 13 TeV*, Phys. Lett. B **782** (2018) 440, arXiv: 1801.01846 [hep-ex] (cit. on pp. 11, 13, 17, 145).

[43] ATLAS Collaboration, *Search for electroweak production of supersymmetric states in scenarios with compressed mass spectra at $\sqrt{s}$ = 13 TeV with the ATLAS detector*, Phys. Rev. D **97** (2018) 052010, arXiv: 1712.08119 [hep-ex] (cit. on pp. 16, 41, 135, 137, 138).

[44] ATLAS Collaboration, *Search for direct production of charginos, neutralinos and sleptons in final states with two leptons and missing transverse momentum in pp collisions at $\sqrt{s}$ = 8 TeV with the ATLAS detector*, JHEP **05** (2014) 071, arXiv: 1403.5294 [hep-ex] (cit. on pp. 16, 137, 138).

[45] ATLAS Collaboration, *Search for direct production of charginos and neutralinos in events with three leptons and missing transverse momentum in $\sqrt{s}$ = 8 TeV pp collisions with the ATLAS detector*, JHEP **04** (2014) 169, arXiv: 1402.7029 [hep-ex] (cit. on pp. 16, 137, 138).

[46] G. Aad et al., *The ATLAS Experiment at the CERN Large Hadron Collider*, JINST **3** (2008) S08003 (cit. on p. 18).

[47] L. Evans and P. Bryant, *LHC Machine*, JINST **3** (2008) S08001 (cit. on pp. 18, 19).

[48] S. Chatrchyan et al., *The CMS Experiment at the CERN LHC*, JINST **3** (2008) S08004 (cit. on p. 18).

[49] A. A. Alves Jr. et al., *The LHCb Detector at the LHC*, JINST **3** (2008) S08005 (cit. on p. 18).

[50] K. Aamodt et al., *The ALICE experiment at the CERN LHC*, JINST **3** (2008) S08002 (cit. on p. 18).

[51] C. De Melis, *The CERN accelerator complex. Complexe des accélérateurs du CERN*, (2016), General Photo, URL: http://cds.cern.ch/record/2119882 (cit. on p. 20).

[52] ATLAS Collaboration, *ATLAS Insertable B-Layer Technical Design Report*, ATLAS-TDR-19, 2010, URL: https://cds.cern.ch/record/1291633 (cit. on p. 22), Addendum: ATLAS-TDR-19-ADD-1, 2012, URL: https://cds.cern.ch/record/1451888.

[53] M. Aaboud et al., *Performance of the ATLAS Trigger System in 2015*, Eur. Phys. J. **C77** (2017) 317, arXiv: 1611.09661 [hep-ex] (cit. on p. 34).

[54] ATLAS Collaboration, *Luminosity determination in pp collisions at $\sqrt{s} = 8$ TeV using the ATLAS detector at the LHC*, Eur. Phys. J. C **76** (2016) 653, arXiv: 1608.03953 [hep-ex] (cit. on p. 35).

[55] G. Avoni et al., *The new LUCID-2 detector for luminosity measurement and monitoring in ATLAS*, JINST **13** (2018) P07017 (cit. on p. 35).

[56] ATLAS Collaboration, *LuminosityPublicResultsRun2*, URL: https://twiki.cern.ch/twiki/bin/view/AtlasPublic/LuminosityPublicResultsRun2 (cit. on p. 36).

[57] P. Z. Skands, 'QCD for Collider Physics', *Proceedings, High-energy Physics. Proceedings, 18th European School (ESHEP 2010): Raseborg, Finland, June 20 - July 3, 2010*, 2011, arXiv: 1104.2863 [hep-ph] (cit. on p. 37).

[58] R. D. Ball et al., *Parton distributions from high-precision collider data*, Eur. Phys. J. **C77** (2017) 663, arXiv: 1706.00428 [hep-ph] (cit. on p. 38).

[59] R. D. Ball et al., *Parton distributions for the LHC Run II*, JHEP **04** (2015) 040, arXiv: 1410.8849 [hep-ph] (cit. on pp. 38, 39, 117).

[60] C. Anastasiou, L. J. Dixon, K. Melnikov and F. Petriello, *High precision QCD at hadron colliders: Electroweak gauge boson rapidity distributions at NNLO*, Phys. Rev. D **69** (2004) 094008, arXiv: hep-ph/0312266 (cit. on p. 39).

[61] J. Pumplin et al., *New generation of parton distributions with uncertainties from global QCD analysis*, JHEP **07** (2002) 012, arXiv: hep-ph/0201195 (cit. on pp. 38, 39).

[62] D. de Florian et al., *Handbook of LHC Higgs Cross Sections: 4. Deciphering the Nature of the Higgs Sector*, CERN-2017-002-M (2016), arXiv: 1610.07922 [hep-ph] (cit. on p. 39).

[63] R. D. Ball et al., *Parton distributions with LHC data*, Nucl. Phys. B **867** (2013) 244, arXiv: 1207.1303 [hep-ph] (cit. on pp. 38, 39, 117).

[64] M. Cacciari, M. Czakon, M. Mangano, A. Mitov and P. Nason, *Top-pair production at hadron colliders with next-to-next-to-leading logarithmic soft-gluon resummation*, Phys. Lett. B **710** (2012) 612, arXiv: 1111.5869 [hep-ph] (cit. on p. 39).

[65] M. Czakon and A. Mitov, *NNLO corrections to top-pair production at hadron colliders: the all-fermionic scattering channels*, JHEP **12** (2012) 054, arXiv: 1207.0236 [hep-ph] (cit. on p. 39).

[66] M. Czakon and A. Mitov, *NNLO corrections to top pair production at hadron colliders: the quark-gluon reaction*, JHEP **01** (2013) 080, arXiv: 1210.6832 [hep-ph] (cit. on p. 39).

[67] M. Czakon, P. Fiedler and A. Mitov, *Total Top-Quark Pair-Production Cross Section at Hadron Colliders Through $O(\alpha_S^4)$*, Phys. Rev. Lett. **110** (2013) 252004, arXiv: 1303.6254 [hep-ph] (cit. on p. 39).

[68] M. Czakon and A. Mitov, *Top++: A Program for the Calculation of the Top-Pair Cross-Section at Hadron Colliders*, Comput. Phys. Commun. **185** (2014) 2930, arXiv: 1112.5675 [hep-ph] (cit. on p. 39).

[69] N. Kidonakis, *NNLL resummation for s-channel single top quark production*, Phys. Rev. D **81** (2010) 054028, arXiv: 1001.5034 [hep-ph] (cit. on p. 39).

[70] N. Kidonakis, *Next-to-next-to-leading-order collinear and soft gluon corrections for t-channel single top quark production*, Phys. Rev. D **83** (2011) 091503, arXiv: 1103.2792 [hep-ph] (cit. on p. 39).

[71] R. Frederix, E. Re and P. Torrielli, *Single-top t-channel hadroproduction in the four-flavour scheme with POWHEG and aMC@NLO*, JHEP **09** (2012) 130, arXiv: 1207.5391 [hep-ph] (cit. on p. 39).

[72] N. Kidonakis, *Two-loop soft anomalous dimensions for single top quark associated production with a W- or H-*, Phys. Rev. D **82** (2010) 054018, arXiv: 1005.4451 [hep-ph] (cit. on p. 39).

[73] J. Alwall et al., *The automated computation of tree-level and next-to-leading order differential cross sections, and their matching to parton shower simulations*, JHEP **07** (2014) 079, arXiv: 1405.0301 [hep-ph] (cit. on p. 39).

[74] T. Gleisberg et al., *Event generation with SHERPA 1.1*, JHEP **02** (2009) 007, arXiv: 0811.4622 [hep-ph] (cit. on p. 38).

[75] S. Alioli, P. Nason, C. Oleari and E. Re, *A general framework for implementing NLO calculations in shower Monte Carlo programs: the POWHEG BOX*, JHEP **06** (2010) 043, arXiv: 1002.2581 [hep-ph] (cit. on p. 39).

[76] ATLAS Collaboration, *Multi-Boson Simulation for* 13 *TeV ATLAS Analyses*, ATL-PHYS-PUB-2017-005, 2017, URL: https://cds.cern.ch/record/2261933 (cit. on p. 39).

[77] ATLAS Collaboration, *ATLAS simulation of boson plus jets processes in Run 2*, ATL-PHYS-PUB-2017-006, 2017, URL: https://cds.cern.ch/record/2261937 (cit. on p. 39).

[78] ATLAS Collaboration, *Studies on top-quark Monte Carlo modelling with Sherpa and MG5_aMC@NLO*, ATL-PHYS-PUB-2017-007, 2017, URL: https://cds.cern.ch/record/2261938 (cit. on p. 39).

[79] ATLAS Collaboration, *A study of different colour reconnection settings for Pythia8 generator using underlying event observables*, ATL-PHYS-PUB-2017-008, 2017, URL: https://cds.cern.ch/record/2262253 (cit. on p. 39).

[80] ATLAS Collaboration, *Modelling of the $t\bar{t}H$ and $t\bar{t}V(V = W, Z)$ processes for $\sqrt{s} = 13$ TeV ATLAS analyses*, ATL-PHYS-PUB-2016-005, 2016, URL: https://cds.cern.ch/record/2120826 (cit. on p. 39).

[81] ATLAS Collaboration, *The Pythia 8 A3 tune description of ATLAS minimum bias and inelastic measurements incorporating the Donnachie–Landshoff diffractive model*, ATL-PHYS-PUB-2016-017, 2016, URL: https://cds.cern.ch/record/2206965 (cit. on p. 39).

[82] A. D. Martin, W. Stirling, R. S. Thorne and G. Watt, *Parton distributions for the LHC*, Eur. Phys. J. C **63** (2009) 189, arXiv: 0901.0002 [hep-ph] (cit. on p. 39).

[83] D. J. Lange, *The EvtGen particle decay simulation package*, Nucl. Instrum. Meth. A **462** (2001) 152 (cit. on p. 39).

[84] ATLAS Collaboration, *The ATLAS Simulation Infrastructure*, Eur. Phys. J. C **70** (2010) 823, arXiv: 1005.4568 [physics.ins-det] (cit. on p. 39).

[85] S. Agostinelli et al., *GEANT4 - a simulation toolkit*, Nucl. Instrum. Meth. A **506** (2003) 250 (cit. on p. 39).

[86] E. Richter-Was, D. Froidevaux and L. Poggioli, *ATLFAST 2.0 a fast simulation package for ATLAS*, (1998) (cit. on p. 39).

[87] P. Artoisenet, R. Frederix, O. Mattelaer and R. Rietkerk, *Automatic spin-entangled decays of heavy resonances in Monte Carlo simulations*, JHEP **03** (2013) 015, arXiv: 1212.3460 [hep-ph] (cit. on p. 40).

[88] T. Sjöstrand et al., *An introduction to PYTHIA 8.2*, Comput. Phys. Commun. **191** (2015) 159, arXiv: 1410.3012 [hep-ph] (cit. on p. 40).

[89] M. M. Muhlleitner, A. Djouadi and M. Spira, *Decays of supersymmetric particles: The Program SUSY-HIT*, Acta Phys. Polon. B **38** (2007) 635, arXiv: hep-ph/0609292 [hep-ph] (cit. on p. 40).

[90] U. De Sanctis, T. Lari, S. Montesano and C. Troncon, *Perspectives for the detection and measurement of supersymmetry in the focus point region of mSUGRA models with the ATLAS detector at LHC*, Eur. Phys. J. C **52** (2007) 743, arXiv: 0704.2515 [hep-ex] (cit. on pp. 40, 41).

[91] B. C. Allanach et al., *SUSY Les Houches Accord 2*, Comput. Phys. Commun. **180** (2009) 8, arXiv: 0801.0045 [hep-ph] (cit. on p. 41).

[92] B. Fuks, M. Klasen, S. Schmiemann and M. Sunder, *Realistic simplified gaugino-higgsino models in the MSSM*, Eur. Phys. J. C **78** (2018) 209, arXiv: 1710.09941 [hep-ph] (cit. on p. 41).

[93] W. Beenakker et al., *The Production of charginos/neutralinos and sleptons at hadron colliders*, Phys. Rev. Lett. **83** (1999) 3780, arXiv: hep-ph/9906298 (cit. on p. 41), Erratum: Phys. Rev. Lett. **100** (2008) 029901.

[94] J. Debove, B. Fuks and M. Klasen, *Threshold resummation for gaugino pair production at hadron colliders*, Nucl. Phys. B **842** (2011) 51, arXiv: 1005.2909 [hep-ph] (cit. on p. 41).

[95] B. Fuks, M. Klasen, D. R. Lamprea and M. Rothering, *Gaugino production in proton-proton collisions at a center-of-mass energy of* 8 *TeV*, JHEP **10** (2012) 081, arXiv: 1207.2159 [hep-ph] (cit. on p. 41).

[96] B. Fuks, M. Klasen, D. R. Lamprea and M. Rothering, *Precision predictions for electroweak superpartner production at hadron colliders with Resummino*, Eur. Phys. J. C **73** (2013) 2480, arXiv: 1304.0790 [hep-ph] (cit. on p. 41).

[97] J. Fiaschi and M. Klasen, *Neutralino-chargino pair production at NLO+NLL with resummation-improved parton density functions for LHC Run II*, Phys. Rev. D **98** (2018) 055014, arXiv: 1805.11322 [hep-ph] (cit. on p. 41).

[98] G. Bozzi, B. Fuks and M. Klasen, *Threshold Resummation for Slepton-Pair Production at Hadron Colliders*, Nucl. Phys. B **777** (2007) 157, arXiv: hep-ph/0701202 [hep-ph] (cit. on p. 41).

[99] B. Fuks, M. Klasen, D. R. Lamprea and M. Rothering, *Revisiting slepton pair production at the Large Hadron Collider*, JHEP **01** (2014) 168, arXiv: 1310.2621 [hep-ph] (cit. on p. 41).

[100] J. Fiaschi and M. Klasen, *Slepton pair production at the LHC in NLO+NLL with resummation-improved parton densities*, JHEP **03** (2018) 094, arXiv: 1801.10357 [hep-ph] (cit. on p. 41).

[101] C. Borschensky et al., *Squark and gluino production cross sections in pp collisions at* $\sqrt{s} = 13, 14, 33$ *and* 100 *TeV*, Eur. Phys. J. C **74** (2014) 3174, arXiv: 1407.5066 [hep-ph] (cit. on p. 41).

[102] ATLAS Collaboration, *Performance of the ATLAS track reconstruction algorithms in dense environments in LHC Run 2*, Eur. Phys. J. C **77** (2017) 673, arXiv: 1704.07983 [hep-ex] (cit. on p. 44).

[103] A. Rosenfeld and J. Faltz, *Sequential Operations in Digital Picture Processing*, J. ACM **13** (1996) 471 (cit. on p. 44).

[104] R. Frühwirth, *Application of Kalman Filtering to Track and Vertex*, Nucl. Instrum. Meth. A **262** (1987) 444 (cit. on p. 44).

[105] ATLAS Collaboration, *A neural network clustering algorithm for the ATLAS silicon pixel detector*, JINST **9** (2014) P09009, arXiv: 1406.7690 [hep-ex] (cit. on p. 44).

[106] ATLAS Collaboration, *Performance of primary vertex reconstruction in proton–proton collisions at* $\sqrt{s}$ = 7 *TeV in the ATLAS experiment*, ATLAS-CONF-2010-069, 2010, URL: https://cds.cern.ch/record/1281344 (cit. on p. 45).

[107] F. Meloni, *Primary vertex reconstruction with the ATLAS detector*, JINST **11** (2016) C12060 (cit. on p. 45).

[108] R. Fruhwirth, W. Waltenberger and P. Vanlaer, *Adaptive vertex fitting*, J. Phys. **G34** (2007) N343 (cit. on p. 45).

[109] ATLAS Collaboration, *Vertex Reconstruction Performance of the ATLAS Detector at* $\sqrt{s}$ = 13 *TeV*, ATL-PHYS-PUB-2015-026, 2015, URL: https://cds.cern.ch/record/2037717 (cit. on p. 46).

[110] ATLAS Collaboration, *Vertex performance in 2018 data*, https://atlas.web.cern.ch/Atlas/GROUPS/PHYSICS/PLOTS/IDTR-2018-006/ (cit. on p. 46).

[111] ATLAS Collaboration, *Topological cell clustering in the ATLAS calorimeters and its performance in LHC Run 1*, Eur. Phys. J. C **77** (2017) 490, arXiv: 1603.02934 [hep-ex] (cit. on p. 45).

[112] ATLAS Collaboration, *Muon reconstruction performance of the ATLAS detector in proton–proton collision data at* $\sqrt{s}$ = 13 *TeV*, Eur. Phys. J. C **76** (2016) 292, arXiv: 1603.05598 [hep-ex] (cit. on pp. 46, 52, 53, 56, 57).

[113] J. Illingworth and J. Kittler, *A Survey of the Hough Transform*, Comput. Vision Graph. Image Process. **44** (1988) 87, ISSN: 0734-189X, URL: http://dx.doi.org/10.1016/S0734-189X(88)80033-1 (cit. on p. 46).

[114] M. Cacciari, G. P. Salam and G. Soyez, *The anti-*k_t *jet clustering algorithm*, JHEP **04** (2008) 063, arXiv: 0802.1189 [hep-ph] (cit. on p. 47).

[115] M. Cacciari, G. P. Salam and G. Soyez, *FastJet user manual*, Eur. Phys. J. C **72** (2012) 1896, arXiv: 1111.6097 [hep-ph] (cit. on p. 47).

[116] ATLAS Collaboration, *Jet energy scale measurements and their systematic uncertainties in proton–proton collisions at* $\sqrt{s}$ = 13 *TeV with the ATLAS detector*, Phys. Rev. D **96** (2017) 072002, arXiv: 1703.09665 [hep-ex] (cit. on pp. 47, 119).

[117] M. Cacciari and G. P. Salam, *Pileup subtraction using jet areas*, Phys. Lett. **B659** (2008) 119, arXiv: 0707.1378 [hep-ph] (cit. on pp. 47, 48).

[118] ATLAS Collaboration, *Jet energy measurement with the ATLAS detector in proton–proton collisions at* $\sqrt{s}$ = 7 *TeV*, Eur. Phys. J. C **73** (2013) 2304, arXiv: 1112.6426 [hep-ex] (cit. on p. 47).

[119] ATLAS Collaboration, *Tagging and suppression of pileup jets with the ATLAS detector*, ATLAS-CONF-2014-018, 2014, URL: https://cds.cern.ch/record/1700870 (cit. on pp. 48, 57).

[120] ATLAS Collaboration, *Forward Jet Vertex Tagging: A new technique for the identification and rejection of forward pileup jets*, ATL-PHYS-PUB-2015-034, 2015, URL: https://cds.cern.ch/record/2042098 (cit. on pp. 48, 56).

[121] ATLAS Collaboration, *Commissioning of the ATLAS high performance b-tagging algorithms in the 7 TeV collision data*, ATLAS-CONF-2011-102, 2011, URL: https://cds.cern.ch/record/1369219 (cit. on p. 48).

[122] G. Piacquadio and C. Weiser, *A new inclusive secondary vertex algorithm for b-jet tagging in ATLAS*, Journal of Physics: Conference Series **119** (2008) 032032, URL: https://doi.org/10.1088%2F1742-6596%2F119%2F3%2F032032 (cit. on p. 48).

[123] H. Drucker and C. Cortes, 'Boosting Decision Trees', *Proceedings of the 8th International Conference on Neural Information Processing Systems*, NIPS'95, MIT Press, 1995 479 (cit. on p. 48).

[124] ATLAS Collaboration, *Performance of b-jet identification in the ATLAS experiment*, JINST **11** (2016) P04008, arXiv: 1512.01094 [hep-ex] (cit. on pp. 48, 57).

[125] ATLAS Collaboration, *Optimisation of the ATLAS b-tagging performance for the 2016 LHC Run*, ATL-PHYS-PUB-2016-012, 2016, URL: https://cds.cern.ch/record/2160731 (cit. on pp. 48, 57).

[126] ATLAS Collaboration, *Improved electron reconstruction in ATLAS using the Gaussian Sum Filter-based model for bremsstrahlung*, ATLAS-CONF-2012-047, 2012, URL: https://cds.cern.ch/record/1449796 (cit. on p. 49).

[127] ATLAS Collaboration, *Electron and photon performance measurements with the ATLAS detector using the 2015-2017 LHC proton–proton collision data*, (2019), arXiv: 1908.00005 [hep-ex] (cit. on pp. 49, 50, 57).

[128] ATLAS Collaboration, *Measurement of the photon identification efficiencies with the ATLAS detector using LHC Run 2 data collected in 2015 and 2016*, Eur. Phys. J. C **79** (2019) 205, arXiv: 1810.05087 [hep-ex] (cit. on pp. 54, 57).

[129] ATLAS Collaboration, E_T^{miss} *performance in the ATLAS detector using 2015–2016 LHC pp collisions*, ATLAS-CONF-2018-023, 2018, URL: https://cds.cern.ch/record/2625233 (cit. on pp. 54, 55, 120).

[130] ATLAS Collaboration, *Performance of pile-up mitigation techniques for jets in pp collisions at* $\sqrt{s} = 8$ *TeV using the ATLAS detector*, Eur. Phys. J. C **76** (2016) 581, arXiv: 1510.03823 [hep-ex] (cit. on p. 56).

[131] ATLAS Collaboration, *Early Inner Detector Tracking Performance in the 2015 Data at* $\sqrt{s} = 13$ *TeV*, ATL-PHYS-PUB-2015-051, 2015, URL: https://cds.cern.ch/record/2110140 (cit. on pp. 56, 57).

[132] *Identification of very-low transverse momentum muons in the ATLAS experiment*, tech. rep. ATL-PHYS-PUB-2020-002, CERN, 2020, URL: https://cds.cern.ch/record/2710574 (cit. on p. 60).

[133] ATLAS Collaboration, *Evidence for the associated production of the Higgs boson and a top quark pair with the ATLAS detector*, Phys. Rev. D **97** (2018) 072003, arXiv: 1712.08891 [hep-ex] (cit. on p. 64).

[134] ATLAS Collaboration, *Identification of Jets Containing b-Hadrons with Recurrent Neural Networks at the ATLAS Experiment*, ATL-PHYS-PUB-2017-003, 2017, URL: https://cds.cern.ch/record/2255226 (cit. on pp. 65, 66).

[135] A. Graves, 'Supervised Sequence Labelling with Recurrent Neural Networks', *Studies in Computational Intelligence*, 2008 (cit. on p. 65).

[136] F. Chollet et al., *Keras*, https://keras.io, 2015 (cit. on p. 65).

[137] ATLAS Collaboration, *Optimisation and performance studies of the ATLAS b-tagging algorithms for the 2017-18 LHC run*, ATL-PHYS-PUB-2017-013, 2017, URL: https://cds.cern.ch/record/2273281 (cit. on p. 66).

[138] A. Hoecker et al., *TMVA - Toolkit for Multivariate Data Analysis*, 2007, arXiv: physics/0703039 [physics.data-an] (cit. on p. 66).

[139] S. Chen, personal communication (cit. on p. 81).

[140] Y. Wei, personal communication (cit. on p. 81).

[141] ATLAS Collaboration, *Performance of the ATLAS Trigger System in 2015*, Eur. Phys. J. C **77** (2017) 317, arXiv: 1611.09661 [hep-ex] (cit. on p. 88).

[142] ATLAS Collaboration, *Missing Energy Trigger Public Results*, URL: https://twiki.cern.ch/twiki/bin/view/AtlasPublic/MissingEtTriggerPublicResults (cit. on p. 89).

[143] K. Griest and D. Seckel, *Three exceptions in the calculation of relic abundances*, Phys. Rev. D **43** (1991) 3191 (cit. on p. 91).

[144] H. Baer, A. Mustafayev and X. Tata, *Monojet plus soft dilepton signal from light higgsino pair production at LHC14*, Phys. Rev. D **90** (2014) 115007, arXiv: 1409.7058 [hep-ph] (cit. on pp. 91, 163).

[145] A. Barr and J. Scoville, *A boost for the EW SUSY hunt: monojet-like search for compressed sleptons at LHC14 with 100 fb^{-1}*, JHEP **04** (2015) 147, arXiv: 1501.02511 [hep-ph] (cit. on pp. 91, 163).

[146] P. Jackson and C. Rogan, *Recursive jigsaw reconstruction: HEP event analysis in the presence of kinematic and combinatoric ambiguities*, Phys. Rev. D **96** (2017) 112007, arXiv: 1705.10733 [hep-ph] (cit. on pp. 92, 93, 165).

[147] R. D. Cousins, J. T. Linnemann and J. Tucker, *Evaluation of three methods for calculating statistical significance when incorporating a systematic uncertainty into a test of the background-only hypothesis for a Poisson process*, Nucl. Instrum. Meth. A **595** (2008) 480, arXiv: physics/0702156 [physics.data-an] (cit. on pp. 95, 130, 135).

[148] ATLAS Collaboration, *Measurement of the WW cross section in $\sqrt{s} = 7$ TeV pp collisions with the ATLAS detector and limits on anomalous gauge couplings*, Phys. Lett. B **712** (2012) 289, arXiv: 1203.6232 [hep-ex] (cit. on p. 97).

[149] ATLAS Collaboration, *Prospects for Higgs boson searches using the $H \to WW^{(*)} \to \ell\nu\ell\nu$ decay mode with the ATLAS detector at* 10 *TeV*, ATL-PHYS-PUB-2010-005, 2010, URL: https://cds.cern.ch/record/1270568 (cit. on p. 97).

[150] L. A. Harland-Lang, A. D. Martin, P. Motylinski and R. S. Thorne, *Parton distributions in the LHC era: MMHT 2014 PDFs*, Eur. Phys. J. **C75** (2015) 204, arXiv: 1412.3989 [hep-ph] (cit. on p. 117).

[151] S. Dulat et al., *New parton distribution functions from a global analysis of quantum chromodynamics*, Phys. Rev. **D93** (2016) 033006, arXiv: 1506.07443 [hep-ph] (cit. on p. 117).

[152] J. Butterworth et al., *PDF4LHC recommendations for LHC Run II*, J. Phys. G **43** (2016) 023001, arXiv: 1510.03865 [hep-ph] (cit. on p. 117).

[153] M. Holzbock, personal communication (cit. on p. 118).

[154] ATLAS Collaboration, *Jet energy resolution in 2017 data and simulation*, https://atlas.web.cern.ch/Atlas/GROUPS/PHYSICS/PLOTS/JETM-2018-005/ (cit. on p. 120).

[155] G. Cowan, K. Cranmer, E. Gross and O. Vitells, *Asymptotic formulae for likelihood-based tests of new physics*, Eur. Phys. J. C **71** (2011) 1554, arXiv: 1007.1727 [physics.data-an] (cit. on pp. 125, 126), Erratum: Eur. Phys. J. C **73** (2013) 2501.

[156] A. Wald, *Tests of Statistical Hypotheses Concerning Several Parameters when the Number of Observations is Large*, American Mathematical Society, 1943, URL: https://books.google.co.jp/books?id=igL7xgYxsJEC (cit. on p. 126).

[157] T. Junk, *Confidence level computation for combining searches with small statistics*, Nucl. Instrum. Meth. A **434** (1999) 435, ISSN: 0168-9002, URL: http://dx.doi.org/10.1016/S0168-9002(99)00498-2 (cit. on p. 127).

[158] *Procedure for the LHC Higgs boson search combination in Summer 2011*, tech. rep. CMS-NOTE-2011-005. ATL-PHYS-PUB-2011-11, CERN, 2011, URL: https://cds.cern.ch/record/1379837 (cit. on p. 127).

[159] M. Saito, R. Sawada, K. Terashi and S. Asai, *Discovery reach for wino and higgsino dark matter with a disappearing track signature at a 100 TeV pp collider*, Eur. Phys. J. **C79** (2019) 469, arXiv: 1901.02987 [hep-ph] (cit. on p. 146).

[160] Z. Han, G. D. Kribs, A. Martin and A. Menon, *Hunting quasidegenerate Higgsinos*, Phys. Rev. D **89** (2014) 075007, arXiv: 1401.1235 [hep-ph] (cit. on p. 163).

[161] C. G. Lester and D. J. Summers, *Measuring masses of semi-invisibly decaying particles pair produced at hadron colliders*, Phys. Lett. B **463** (1999) 99, arXiv: hep-ph/9906349 (cit. on p. 167).

[162] A. Barr, C. Lester and P. Stephens, *A variable for measuring masses at hadron colliders when missing energy is expected; m_{T2}: the truth behind the glamour*, J. Phys. G **29** (2003) 2343, arXiv: hep-ph/0304226 (cit. on p. 167).

[163] ATLAS Collaboration, *Precision measurement and interpretation of inclusive W^+, W^- and Z/γ^* production cross sections with the ATLAS detector*, Eur. Phys. J. C **77** (2017) 367, arXiv: 1612.03016 [hep-ex] (cit. on p. 182).

Appendix A

Prompt Lepton Tagger studies

A.1 Prompt Lepton Tagging working point performance

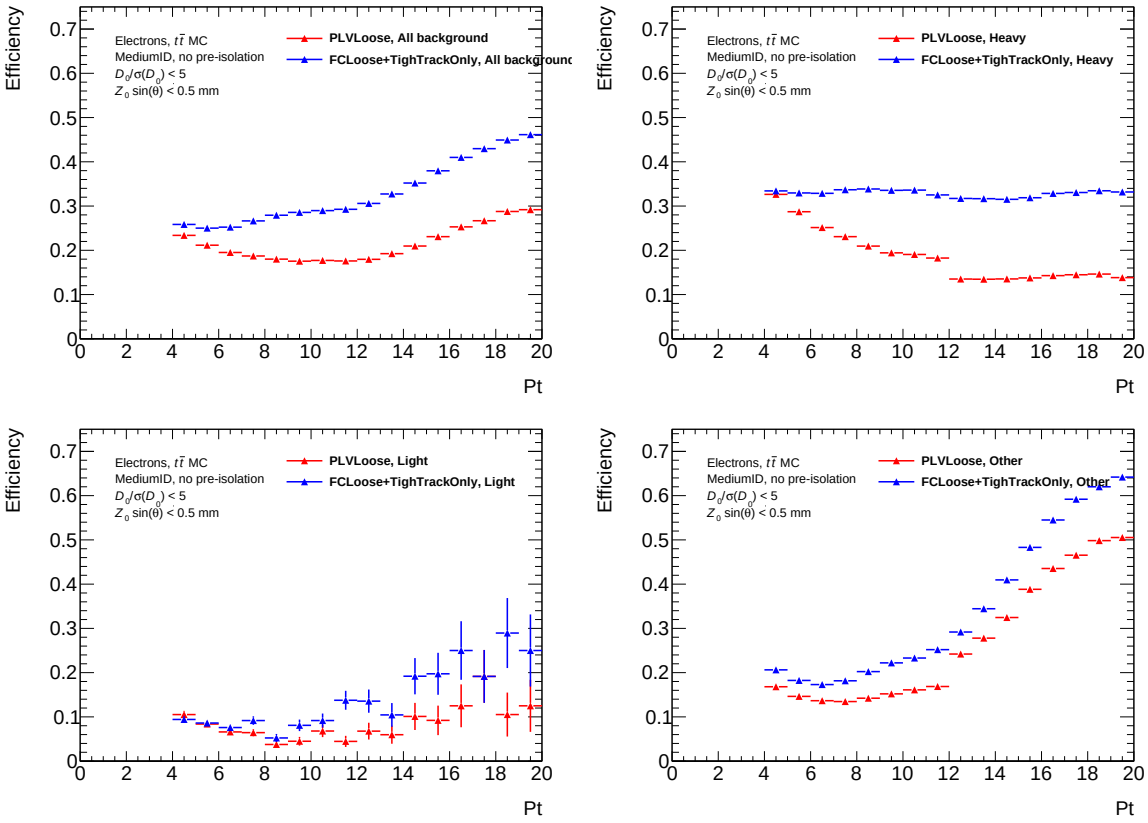

Figure A.1: Background efficiencies for electronss *PLTLoose*, separated by different background sources. Efficiencies are measured with $t\bar{t}$ MC samples.

A.2 PLT calibration

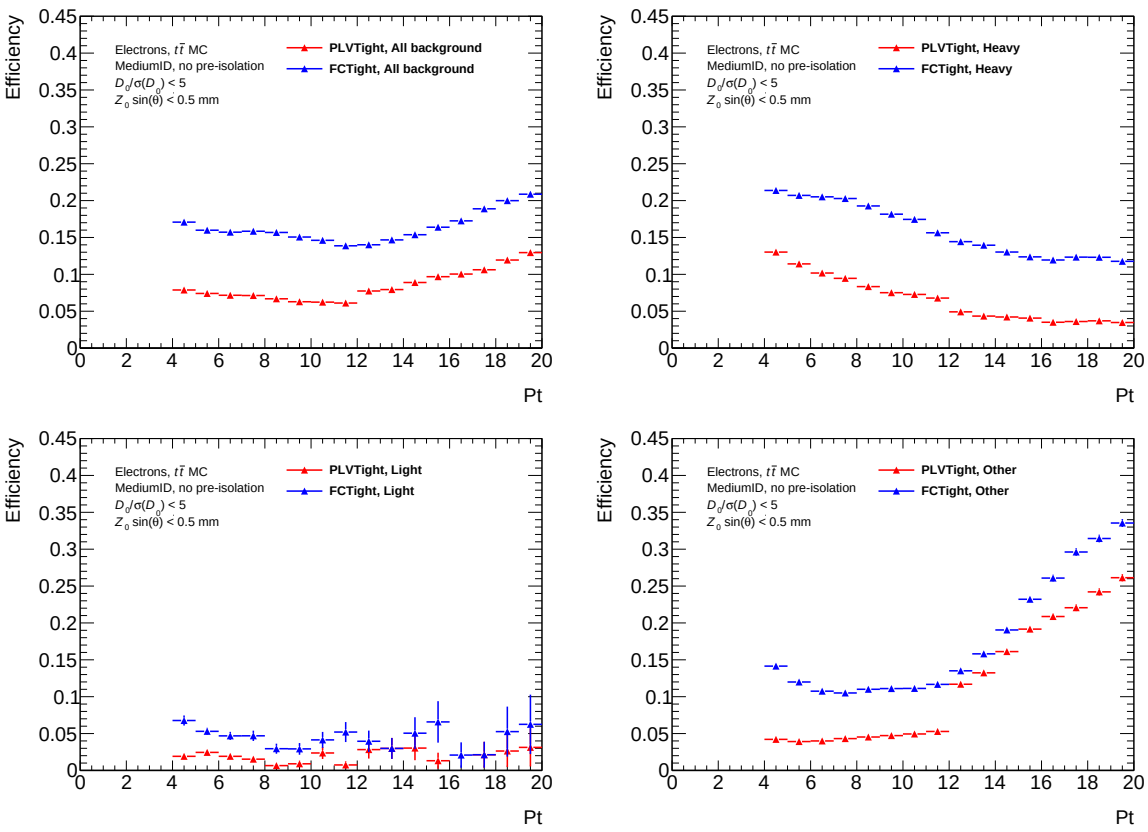

Figure A.2: Background efficiencies for electrons *PLTTight*, separated by different background sources. Efficiencies are measured with $t\bar{t}$ MC samples.

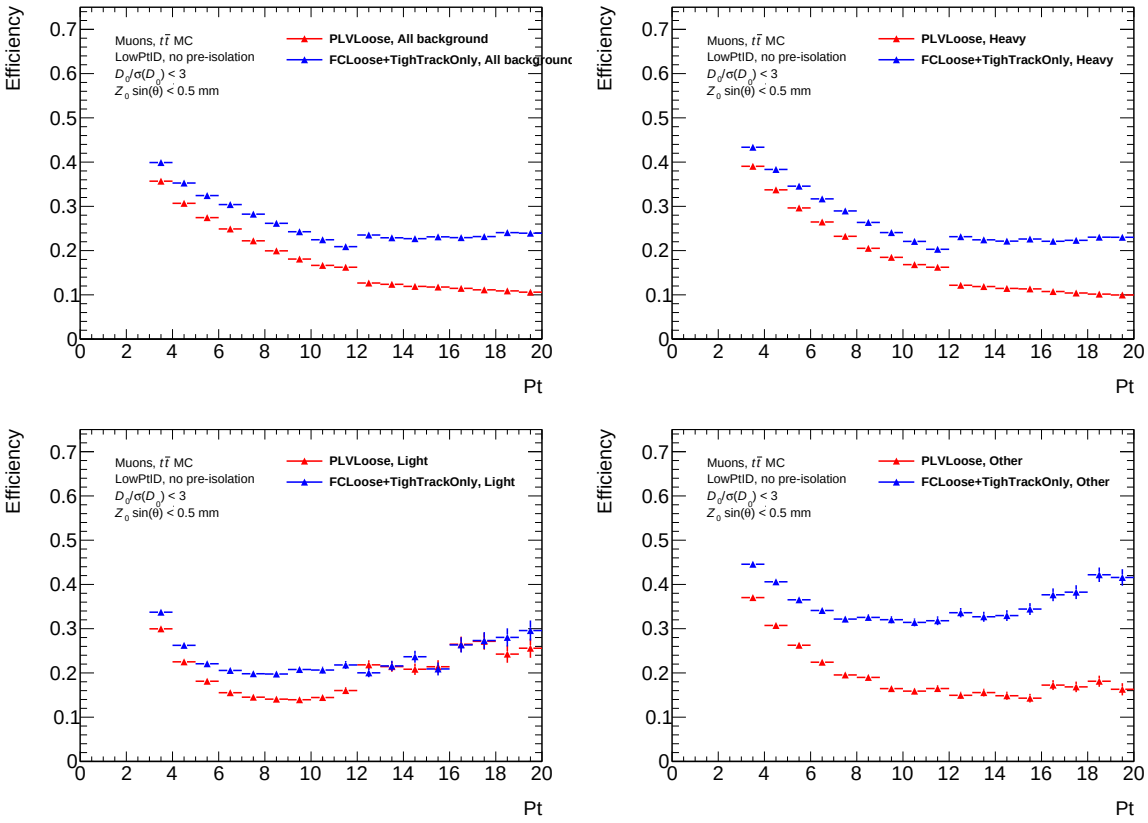

Figure A.3: Background efficiencies for muons *PLTLoose*, separated by different background sources. Efficiencies are measured with $t\bar{t}$ MC samples.

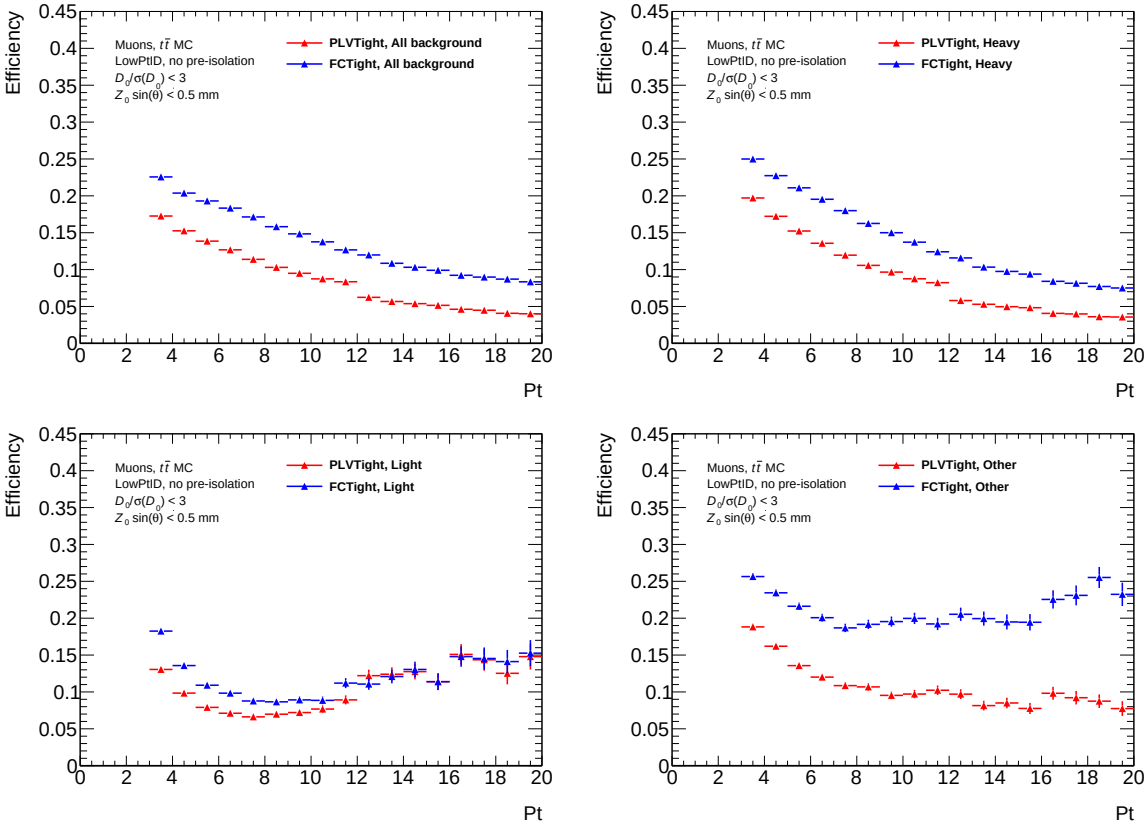

Figure A.4: Background efficiencies for muons *PLTTight*, separated by different background sources. Efficiencies are measured with $t\bar{t}$ MC samples.

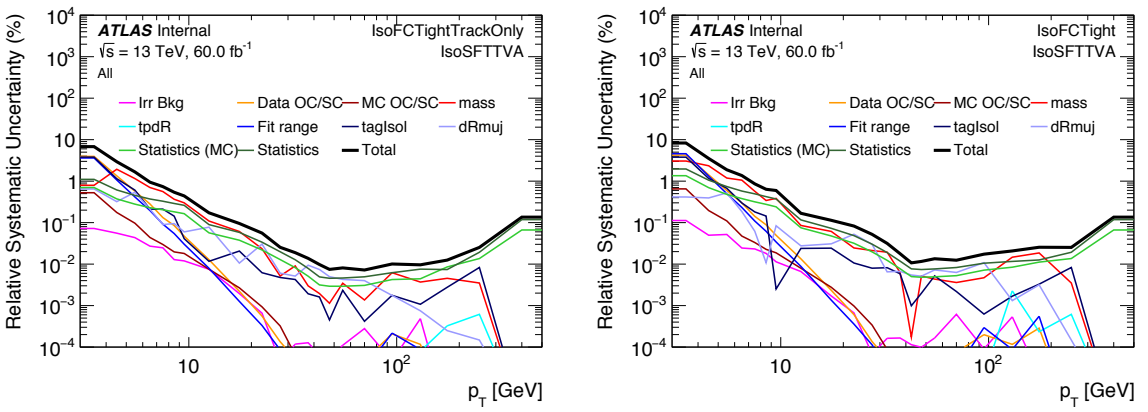

Figure A.5: Systematic uncertainty breakdown for muons *PLTLoose* and *PLTTight* for 2018 data (60 fb).

Appendix B

Discriminating variable details

B.1 $m_{\tau\tau}$ calculation

Various definitions of $m_{\tau\tau}$ exist in the literature to resolve the kinematic ambiguities due to immeasurable neutrino momenta by imposing assumptions on the underlying process. This analysis primarily follows Refs. [144, 145, 160].

In the $Z \to \tau\tau$ process where both taus undergo leptonic decays $\tau \to \ell\nu_\ell\nu_\tau$, only the missing transverse momentum $\mathbf{p}_{\mathrm{T}}^{\mathrm{miss}}$ and 4-momenta of the two leptons p_{ℓ_i} from the i-th tau are observable, where $i = \{1, 2\}$ label the tau decay chains. The reconstruction relies on the large boost of the taus, decaying from the Z recoiling off hadronic activity. This boost ensures the daughter leptons and neutrinos are nearly collinear, so the 4-momentum of the neutrino system p_{ν_i} from the i-th tau defined by $p_{\nu_i} = p_{\nu_{\ell_i}} + p_{\nu_{\tau_i}}$, is well approximated as a rescaling of the visible lepton momenta $p_{\nu_i} \simeq \xi_i p_{\ell_i}$, where ξ_i is a scalar to be determined. The i-th tau 4-momentum is the sum of the daughter lepton and neutrino system $p_{\tau_i} = p_{\ell_i} + p_{\nu_i}$. Then the τ momentum is a rescaling of the observable lepton momenta p_{ℓ_i}

$$p_{\tau_i} = (1 + \xi_i) p_{\ell_i} \equiv f_i p_{\ell_i}, \tag{B.1}$$

where $f_i \equiv 1 + \xi_i$. To solve for the two unknown scalars ξ_i, one constrains the neutrino momenta using the missing transverse momentum [1] as Ref. [145] prescribes Equation (6.9) assumes the lepton–invisible colinearity limit $p_{\nu_i} \simeq \xi_i p_{\ell_i}$ and comprises two independent constraints in the transverse plane for the two unknown scalars ξ_i. This is solved by performing 2×2 matrix inversion in for example the x-y transverse plane

$$\begin{pmatrix} \xi_1 \\ \xi_2 \end{pmatrix} = \frac{1}{p_x^{\ell_1} p_y^{\ell_2} - p_x^{\ell_2} p_y^{\ell_1}} \begin{pmatrix} p_x^{\mathrm{miss}} p_y^{\ell_2} - p_x^{\ell_2} p_y^{\mathrm{miss}} \\ p_y^{\mathrm{miss}} p_x^{\ell_1} - p_x^{\mathrm{miss}} p_y^{\ell_1} \end{pmatrix}. \tag{B.2}$$

Assuming highly boosted taus such that $m_{\tau_i}^2 \simeq 0$, the di-tau invariant mass squared is then given by

$$m_{\tau\tau}^2 = \left(p_{\tau_1} + p_{\tau_2}\right)^2 \simeq 2 p_{\ell_1} \cdot p_{\ell_2} (1 + \xi_1)(1 + \xi_2). \tag{B.3}$$

An important feature of $m_{\tau\tau}^2$ in Equation (6.6) is not only that it can go negative, but also in an asymmetric way such that the absolute value of the negative range of values $\left(m_{\tau\tau}^2\right)^-$ are qualitatively distinct from those of the positive range $\left(m_{\tau\tau}^2\right)^+$

$$\left(m_{\tau\tau}^2\right)^+ \neq \left|\left(m_{\tau\tau}^2\right)^-\right|. \tag{B.4}$$

[1] An alternative way to constrain $f_i \equiv 1 + \xi_i$ is by assuming the tau momenta balance the hadronic recoil as CMS [**CMS-PAS-SUS-16-025**] do: $-\mathbf{p}_{\mathrm{T}}^{\mathrm{hadronic}} = f_1 \mathbf{p}_{\mathrm{T}}^{\ell_1} + f_2 \mathbf{p}_{\mathrm{T}}^{\ell_2}$, where $\mathbf{p}_{\mathrm{T}}^{\mathrm{hadronic}}$ is the transverse projection of the vectorial sum of the jet momenta.

A naïve square root does not capture this feature. Negative values of $m^2_{\tau\tau}$ arise when the assumption of lepton–invisible colinearity fails for the underlying process. Mathematically, this happens when either (but not both) $f_i \equiv 1 + \xi_i < 0$ with $E_{\mathrm{T}}^{\mathrm{miss}} > \left|\mathbf{p}_{\mathrm{T}}^{\ell_i}\right|$. allowing them to direct probe the electroweak structure of the underlying process, facilitating signal and background discrimination. Physically, this occurs when one of the lepton momenta is smaller in magnitude and points in the opposite hemisphere to the missing transverse momentum $\mathbf{p}_{\mathrm{T}}^{\mathrm{miss}}$ (or equivalently, the same hemisphere as the hadronic activity $\mathbf{p}_{\mathrm{hadronic}}$). Therefore, this lepton's momentum must be inverted in direction when rescaling to obtain an estimate of the tau momentum that balances the hadronic recoil. This happens rarely for highly boosted leptonic $Z \to \tau\tau$ decays when lepton–invisible colinearity largely holds. By contrast, this occurs with greater frequency when the leptons and missing transverse momenta originate from less boosted heavy parent particles, such as the WW background or $\tilde{\ell}\tilde{\ell}$ signal where the leptons can decay nearly back-to-back. In these cases, $m^2_{\tau\tau}$ is merely interpreted as a variable that can discriminate against leptons originating from $Z \to \tau\tau$.

To construct a variable with mass dimension 1 while properly capturing the information encoded across the full range of $m^2_{\tau\tau} \in [-\infty, \infty]$, the signed square root is a natural operation

$$m_{\tau\tau}\left(p_{\ell_1}, p_{\ell_2}, \mathbf{p}_{\mathrm{T}}^{\mathrm{miss}}\right) = \begin{cases} \sqrt{m^2_{\tau\tau}} & m^2_{\tau\tau} \geq 0, \\ -\sqrt{\left|m^2_{\tau\tau}\right|} & m^2_{\tau\tau} < 0. \end{cases} \tag{B.5}$$

This prescription maintains a one-to-one map to $m^2_{\tau\tau}$ and its distinct behaviour at negative values, despite introducing a discontinuity at $m_{\tau\tau} = 0$ GeV. Equation (6.5) defines the $m_{\tau\tau}$ variable used in this analysis.

B.2 Recursive Jigsaw Variables

As discussed, the search for compressed signals is experimentally difficult because of the soft final state decay products and little missing energy. However, the fact that the $\widetilde{\chi}^0_1$ gains very little momenta from the electroweakino decays leads to other useful correlations that are exploited for the higgsino signals. If the di-$\widetilde{\chi}^0_1$ system gains all its p_T by recoiling against a system of ISR jets, it will have a strong correlation with the momenta of the ISR system. To zeroth order (in the momenta of electroweakino decay products) the correlation between $E_{\mathrm{T}}^{\mathrm{miss}}$ and ISR is proportional to the ratio of the $\widetilde{\chi}^0_1$ and $\widetilde{\chi}^{\pm}_1$ masses. The same relationship exists if the intermediate particle is a $\widetilde{\chi}^0_2$.

We can exploit these features by using an event analysis strategy based on Recursive Jigsaw Reconstruction (RJR), a general scheme for analyzing high energy collision events, as described in detail in Ref. [**rjr-note**]. It provides a way to derive new kinematic observables that are often especially useful where typical variable choices are less effective. RJR also implements algorithms that assist with object assignment, when there are several identical objects in a final state. These algorithms can overcome kinematic ambiguities as well, which arise if there is information missing in an event due to the presence of invisible particles. Specifically, we address the use of RJR in the case of ISR-assisted $E_{\mathrm{T}}^{\mathrm{miss}}$ signals.

In compressed cases, one is not necessarily looking for a signature of invisible particles with large momenta (although this is, ultimately, how we observe the presence of invisible particles through $E_{\mathrm{T}}^{\mathrm{miss}}$). Rather, one searches for a signature of the presence of massive invisible particles. In the cases discussed here, the invisible particles must receive their momenta from a source other than their parents, namely some other object recoiling against the parent system. One such source is initial-state radiation (ISR), or

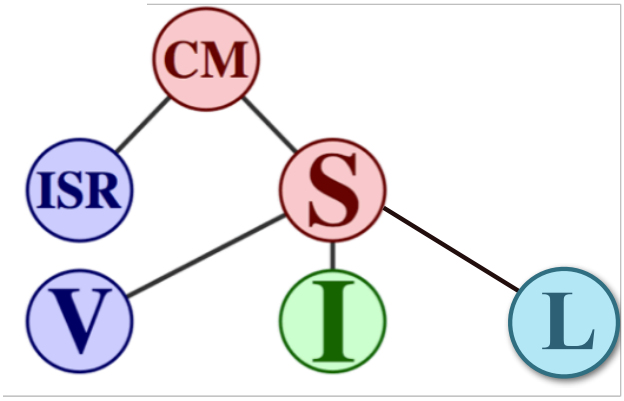

Figure B.1: Decay tree corresponding to ISR-assisted $E_{\mathrm{T}}^{\mathrm{miss}}$ strategy. [146]

strong emmissions coming from the interacting partons, which kick the entire parent particle system in the transverse plane. If invisible particles have significant mass (relative to the other decay products coming from the parents) they will absorb a larger fraction of this momentum.

The first step of an RJR-based analysis is to impose a decay tree on the events we wish to analyze. While this decay tree can specify each expected final state object and all the intermediate states of the decay, we choose a more generic tree, as shown in Figure 6.3. The RJR method described here uses four frames, or groups of final state particles: the ISR, invisible, visible, and dedicated lepton systems. The ISR frame is needed to give momentum to the system of interest. This system of interest, called the sparticle or S frame, can then be categorized into two subsequent decay groups. One is the collection of particles that are visible in the detector (V frame), and one or more invisible particles (I frame) which escape detection, leaving only a transverse imbalance of momenta in the event. The center of mass frame (CM frame) is then the sum of the reconstructed or missing objects, sparticles and accompanying particles. Each of these four frames is identified by a four-vector sum of all particles, which can then be evaluated in any of the frames implicitly defined by the decay tree.

To impose this decay tree on an event, we must fill in the four vectors of our four final frames, which are I, V, L, and and ISR. To start, the leptons are placed in the L frame by default. We then move to the I frame, by making choices/guesses for any missing pieces of information required to assign a four-vector to each state. We interpret the vectorial $E_{\mathrm{T}}^{\mathrm{miss}}$ reconstructed in each event as the transverse momentum of I, evaluated in the lab frame. This leaves two four-vector components unspecified: these can be expressed as the mass of I and its longitudinal momentum in the lab frame. For the first, we choose $m_I = 0$; while this isn't necessarily a correct assignment (certainly not for signals with massive invisible particles) it is a convenient one that we find does not prevent us from resolving the kinematic effect we hope to observe. For the second, we purposefully ignore the longitudinal momentum of all the objects we reconstruct, resulting in an exclusively transverse view of the event.

Once the I frame is decided upon, we must next assign all other reconstructed objects to either the V or ISR frame. This is done with a jigsaw rule, which is a generic algorithm that resolves any combinatoric ambiguities associated with frame assignment. In the case of ISR-assisted $E_{\mathrm{T}}^{\mathrm{miss}}$ signals, we choose to group objects together which are closest in phase-space in the lab transverse plane (flying in the same direction) by minimizing the masses M_{ISR} and M_S simultaneously over all the choices of object assignment. There

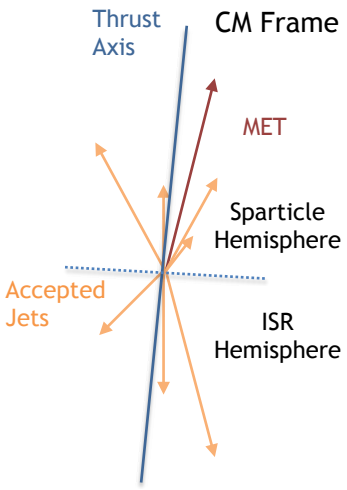

Figure B.2: Diagram of an event, where the calculation of a thrust axis allows for the designation of two distinct hemispheres. All objects can be categorized into one of these hemispheres, which become the S frame (if the $E_{\mathrm{T}}^{\mathrm{miss}}$ vector is present) or the ISR frame.

is no unique way to accomplish this (one could minimize the sum of masses, the sum of masses squared, the product of masses, etc.), so we can think of this minimization in two different ways. The first is that we are simply performing an exclusive two-jet re-clustering, using transverse mass as a distance metric and treating the $E_{\mathrm{T}}^{\mathrm{miss}}$ as just another jet. The second is that minimizing M_{ISR} and M_S is equivalent to maximizing the amount of back-to-back p_T of the two systems. Specifically, in the CM frame:

$$M_{CM} = \sqrt{M_{ISR}^2 + (p_{ISR}^{CM})^2} + \sqrt{M_S^2 + (p_S^{CM})^2} \tag{B.6}$$

where $p_{ISR}^{CM} = p_S^{CM}$ are the momenta of the two systems, equal in magnitude and opposite in direction in the CM frame. Regardless of how we partition objects between ISR and V, the total mass M_{CM} is constant in each event. This means that by maximizing $p_{ISR/S}^{CM}$ we are, in effect, simultaneously minimizing M_{ISR} and M_S.

We can think of maximizing back-to-back p_T as calculating the thrust axis, which can then be used to divide the event into two hemispheres. The hemisphere that contains the $E_{\mathrm{T}}^{\mathrm{miss}}$ is thus the sparticle S frame, and the other hemisphere must be the ISR frame. Figure B.2 provides a diagram of this hemispherical separation along the thrust axis, showing how all of the objects in the event will then fall into one of the two frames.

After this frame assignment, all objects are in one of the three final state frames, and there is a full kinematic description of the decay tree in the transverse plane. From here, it is possible to analyze events by building unique jigsaw variables and using these to discriminate signal from background. Due to our planned ignorance of the longitudinal momentum in each event, the masses of the different states are actually transverse masses.

B.3 $m_{\mathrm{T2}}^{m_\chi}$

The 'stransverse' mass [161, 162] is a functional of the two leptons' momenta p_{ℓ_1}, p_{ℓ_2}, the $\mathbf{p}_{\mathrm{T}}^{\mathrm{miss}}$ and invisible particle mass hypothesis χ. This variable serves an analogous role for sleptons as $m_{\ell\ell}$ does for Higgsinos. The values of this variable from is kinematically bounded by the mass splitting of the hypothesised slepton signal $m(\tilde{\ell}) - m(\widetilde{\chi}_1^0)$, if the hypothesis invisible particle mass is set to the LSP mass $m(\widetilde{\chi}_1^0)$.

The $m_{\mathrm{T2}}^{m_\chi}$ variable is defined as an extremisation over the variable $\mathbf{q}_{\mathrm{T}}$, which is the sum of the immeasurable missing transverse momentum vectors $\mathbf{p}_{\mathrm{T}}^{\chi,i}$ of each decaying invisible particle $\mathbf{q} = \mathbf{p}_{\mathrm{T}}^{\chi,1} + \mathbf{p}_{\mathrm{T}}^{\chi,2}$

$$m_{\mathrm{T2}}^{m_\chi}\left(p_{\ell_1}, p_{\ell_2}, \mathbf{p}_{\mathrm{T}}^{\mathrm{miss}}; m_\chi\right) = \min_{\mathbf{q}_{\mathrm{T}}}\left(\max\left[m_{\mathrm{T}}\left(\mathbf{p}_{\mathrm{T}}^{\ell_1}, \mathbf{p}_{\mathrm{T}}^{\mathrm{miss}}, \chi\right), m_{\mathrm{T}}\left(\mathbf{p}_{\mathrm{T}}^{\ell_2}, \mathbf{p}_{\mathrm{T}}^{\mathrm{miss}} - \mathbf{q}_{\mathrm{T}}, \chi\right)\right]\right), \tag{B.7}$$

where $\mathbf{p}_{\mathrm{T}}^{\ell_i}$ is the transverse momentum of the i-th lepton, $\mathbf{p}_{\mathrm{T}}^{\mathrm{miss}}$ the missing transverse momentum. The square of the transverse mass m_{T} is defined by

$$m_{\mathrm{T}}\left(\mathbf{p}_{\mathrm{T}}^{\ell}, \mathbf{q}_{\mathrm{T}}, m_\chi\right) = \sqrt{m_\ell^2 + m_\chi^2 + 2\left(E_{\mathrm{T}}^{\ell} E_{\mathrm{T}}^{q} - \mathbf{p}_{\mathrm{T}}^{\ell} \cdot \mathbf{q}_{\mathrm{T}}\right)}. \tag{B.8}$$

For the pair of semi-invisible particles of the slepton signal, $m_{\mathrm{T2}}^{m_\chi}$ is always less than the parent slepton mass $m(\tilde{\ell})$ when the hypothesis invisible mass is set to the neutralino mass of $m_\chi = m_{\tilde{\chi}_1^0}$ of the underlying process. This defines the lower kinematic endpoint of the variable. By requiring $m_{\mathrm{T2}}^{m_\chi} < m_{\tilde{\ell}}$, various masses scenarios in the slepton–neutralino plane can be probed. The background processes do not necessary satisfy this, given their invisible particles are effectively massless (neutrinos). In particular for a given slepton mass, the variable becomes more effective as the mass splitting decreases because the signal events become more concentrated in a narrower window of m_{T2}.

The shape of the m_{T2} distribution has a mild dependence on the hypothesis mass m_χ. For the purpose of this analysis, the target slepton masses are of order 100 to 200 GeV. A choice of $m_\chi = 100$ GeV is set for this analysis, motivated by the neutralino–slepton masses probed by this analysis.

This is in contrast with many non-compressed multilepton searches, which set $m_\chi = 0$ GeV. When using this choice, the slepton signals have a less prominent shape than $m_\chi = 100$ GeV. This variable is not used for the Higgsino interpretation.

Appendix C

Fake Factor

C.1 Electron Fake Factor additional plots

The specific trigger applied to each range in electron p_{T} was chosen to narrow the effect of the trigger turn-on and still maintain good statistics. For data taken in 2015 and 2016, `HLT_e5_lhvloose` trigger is required for electron p_{T} 5 – 11 GeV, `HLT_e10_lhvloose_L1EM7` is required for electron p_{T} 11 – 18 GeV, `HLT_e15_lhvloose_L1EM13VH` is required for electron p_{T} 18 – 23 GeV, and `HLT_e20_lhvloose` is required for electron $p_{\mathrm{T}} > 23$ GeV. For data taken in 2017, `HLT_e5_lhvloose_nod0` trigger is required for electron p_{T} 5 – 13 GeV, `HLT_e12_lhvloose_nod0_L1EM10VH` is required for electron p_{T} 13 – 18 GeV, `HLT_e17_lhvloose_nod0` is required for electron p_{T} 18 – 23 GeV, and `HLT_e20_lhvloose_nod0` is required for electron $p_{\mathrm{T}} > 23$ GeV. Finally, for data taken in 2018, `HLT_e5_lhvloose_nod0` trigger is required for electron p_{T} 5 – 11 GeV, `HLT_e10_lhvloose_nod0_L1EM7` is required for electron p_{T} 11 – 18 GeV, `HLT_e15_lhvloose_nod0_L1EM7` is required for electron p_{T} 18 – 23 GeV, and `HLT_e20_lhvloose_nod0` is required for electron $p_{\mathrm{T}} > 23$ GeV.

A summary of these triggers and their corresponding p_{T} ranges is shown in Table C.1.

In addition to p_{T}, fake factors as functions of other variables are also inspected to check for significant trends:

- fake factors as a function of electron $|\eta|$ are shown in Figure C.1,
- fake factors as a function of leading jet p_{T} are shown in Figure C.2,

Trigger	2015/2016 p_{T} range [GeV]	2017 p_{T} range [GeV]	2018 p_{T} range [GeV]
`HLT_e5_lhvloose`	5–11	–	–
`HLT_e10_lhvloose_L1EM7`	11–18	–	–
`HLT_e15_lhvloose_L1EM13VH`	18–23	–	–
`HLT_e20_lhvloose`	>23	–	–
`HLT_e5_lhvloose_nod0`	–	5–13	5–11
`HLT_e12_lhvloose_nod0_L1EM10VH`	–	13–18	–
`HLT_e17_lhvloose_nod0`	–	18–23	–
`HLT_e20_lhvloose_nod0`	–	>23	–
`HLT_e10_lhvloose_nod0_L1EM7`	–	–	11–18
`HLT_e15_lhvloose_nod0_L1EM7`	–	–	18–23
`HLT_e20_lhvloose_nod0`	–	–	> 23

Table C.1: Single-electron triggers used for fake factor computation and their corresponding p_{T} range for different years.

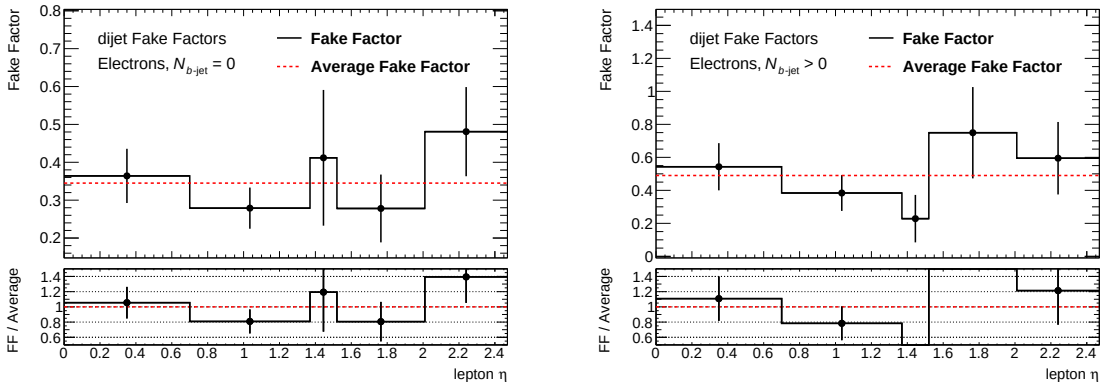

Figure C.1: Electron fake factors computed from single-electron prescaled triggers as a function of electron $|\eta|$ for events with zero b-tagged jets (left) and at least one b-tagged jet (right) in the kinematic region with leading jet $p_{\mathrm{T}} > 100$ GeV and $m_{\mathrm{T}} < 40$ GeV. A red line denotes the average electron fake factor.

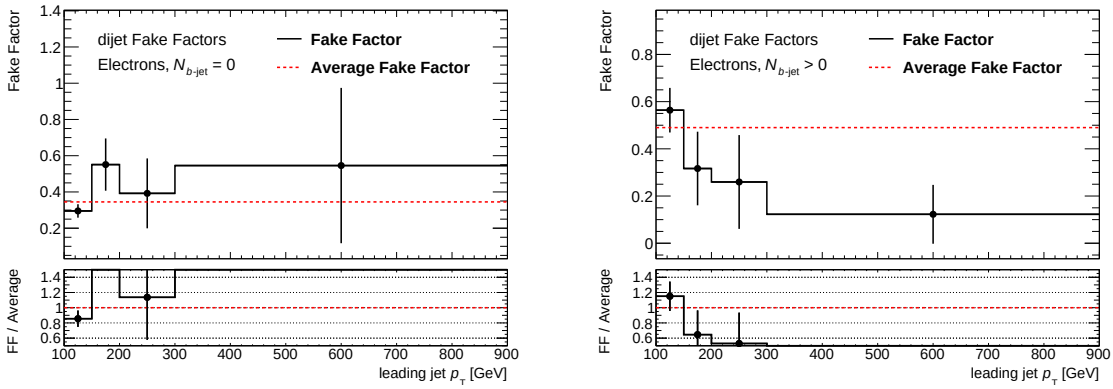

Figure C.2: Electron fake factors computed from single-electron prescaled triggers as a function of the leading jet p_{T} for events with zero b-tagged jets (left) and at least one b-tagged jet (right) in the kinematic region with leading jet $p_{\mathrm{T}} > 100$ GeV and $m_{\mathrm{T}} < 40$ GeV. A red line denotes the average electron fake factor.

- fake factors as a function of $\Delta\phi(j_1, \mathbf{p}_{\mathrm{T}}^{\mathrm{miss}})$ are shown in Figure C.3,
- fake factors as a function of jet multiplicity are shown in Figure C.4,
- fake factors as a function of $\langle\mu\rangle$ are shown in Figure C.5.
- fake factors as a function of R_{ISR} are shown in Figure C.6.

C.2 Muon Fake Factors additional plots

The specific trigger applied to each range in lepton p_{T} was chosen to reduce the effect of the trigger turn on and maintain good statistics. For data taken in 2015 and 2016, `HLT_mu4` trigger is required for muon p_{T} 4 – 11 GeV, `HLT_mu10` is required for muon p_{T} 11 – 15 GeV, `HLT_mu14` is required for muon

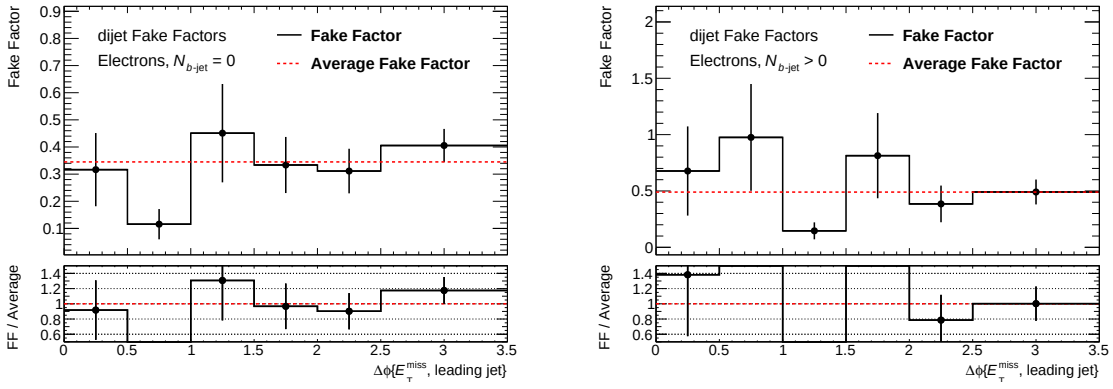

Figure C.3: Electron fake factors computed from single-electron prescaled triggers as a function of $\Delta\phi(j_1, \mathbf{p}_{\mathrm{T}}^{\mathrm{miss}})$ for events with zero b-tagged jets (left) and at least one b-tagged jet (right) in the kinematic region with leading jet $p_{\mathrm{T}} > 100$ GeV and $m_{\mathrm{T}} < 40$ GeV. A red line denotes the average electron fake factor.

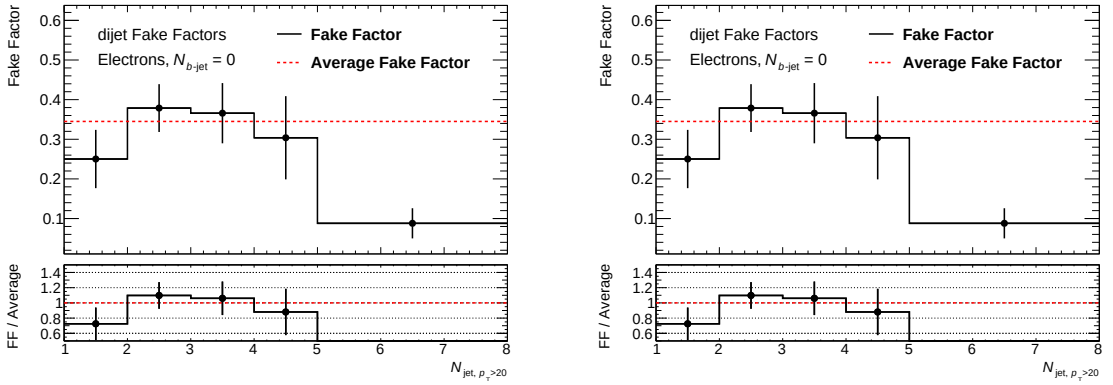

Figure C.4: Electron fake factors computed from single-electron prescaled triggers as a function of the jet multiplicity for events with zero b-tagged jets (left) and at least one b-tagged jet (right) in the kinematic region with leading jet $p_{\mathrm{T}} > 100$ GeV and $m_{\mathrm{T}} < 40$ GeV. A red line denotes the average electron fake factor.

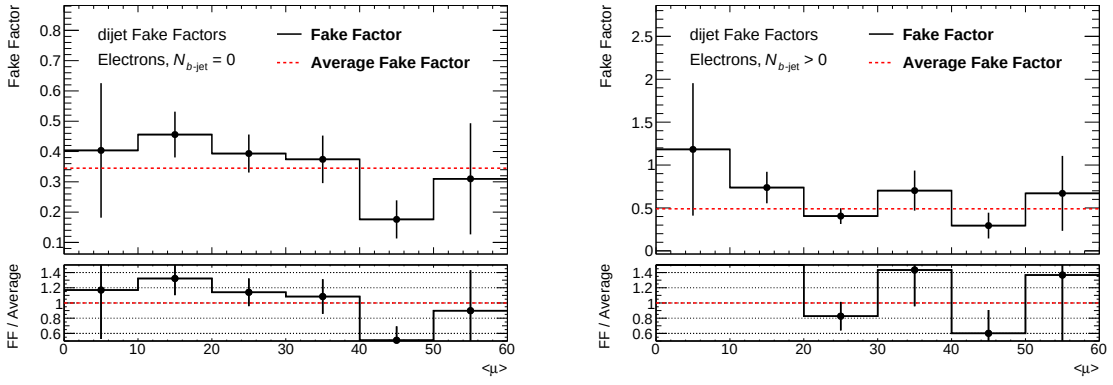

Figure C.5: Electron fake factors computed from single-electron prescaled triggers as a function of $\langle\mu\rangle$ for events with zero b-tagged jets (left) and at least one b-tagged jet (right) in the kinematic region with leading jet $p_{\mathrm{T}} > 100$ GeV and $m_{\mathrm{T}} < 40$ GeV. A red line denotes the average electron fake factor.

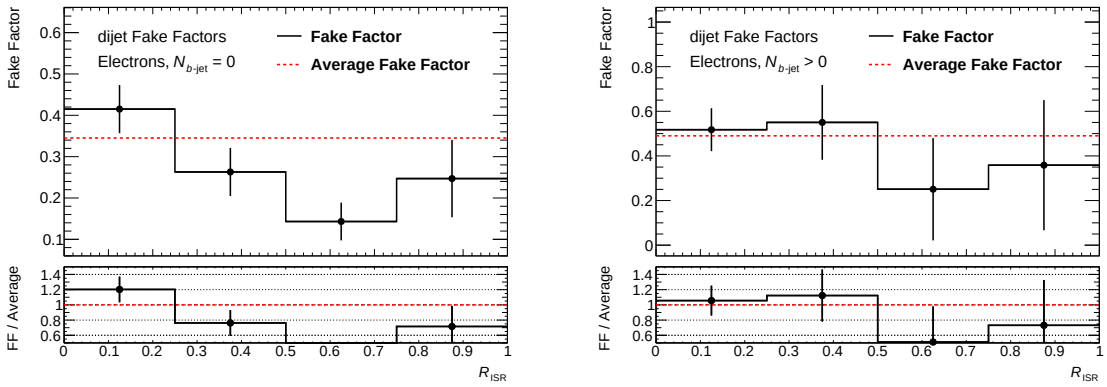

Figure C.6: Electron fake factors computed from single-electron prescaled triggers as a function of R_{ISR} for events with zero b-tagged jets (left) and at least one b-tagged jet (right) in the kinematic region with leading jet $p_{\mathrm{T}} > 100$ GeV and $m_{\mathrm{T}} < 40$ GeV. A red line denotes the average electron fake factor.

Trigger	2015/2016 p_{T} range [GeV]	2017/2018 p_{T} range [GeV]
HLT_mu4	4 –11	4 –11
HLT_mu10	11–15	–
HLT_mu10_idperf	–	11 – 15
HLT_mu14	15–20	> 15
HLT_mu18	> 20	–

Table C.2: Single-muon triggers used for fake factor computation and their corresponding p_{T} range for different years.

p_{T} 15 – 20 GeV, and HLT_mu18 is required for muon $p_{\mathrm{T}} > 20$ GeV. For data taken in 2017 and 2018, HLT_mu10_idperf trigger is used to replace the HLT_mu10 trigger for muons in the same range of p_{T}. Additionally, since no HLT_mu18 trigger is available in 2017 or 2018 data, the HLT_mu14 trigger is required for muon p_{T}> 15 GeV . A summary of the considered muon triggers and their corresponding p_{T} ranges is shown in Table C.2.

In addition to p_{T}, fake factors as functions of other variables are also inspected to check for significant trends:

- fake factors as a function of muon $|\eta|$ are shown in Figure C.7,
- fake factors as a function of leading jet p_{T} are shown in Figure C.8,
- fake factors as a function of $\Delta\phi(j_1, \mathbf{p}_{\mathrm{T}}^{\mathrm{miss}})$ are shown in Figure C.9,
- fake factors as a function of jet multiplicity are shown in Figure C.10,
- fake factors as a function of $\langle\mu\rangle$ are shown in Figure C.11.
- fake factors as a function of R_{ISR} are shown in Figure C.12.

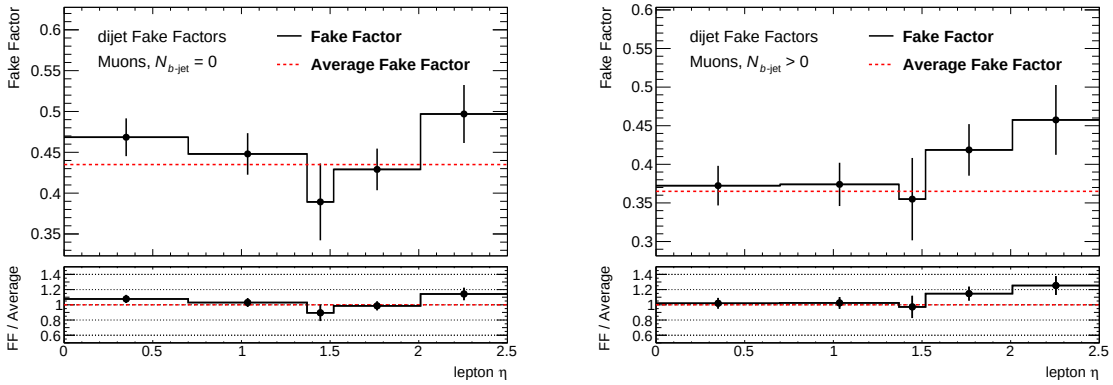

Figure C.7: Muon fake factors computed from single-muon prescaled triggers as a function of muon $|\eta|$ for events with zero b-tagged jets (left) and at least one b-tagged jet (right) in the kinematic region with leading jet $p_{\mathrm{T}} > 100$ GeV and $m_{\mathrm{T}} < 40$ GeV. A red line denotes the average muon fake factor.

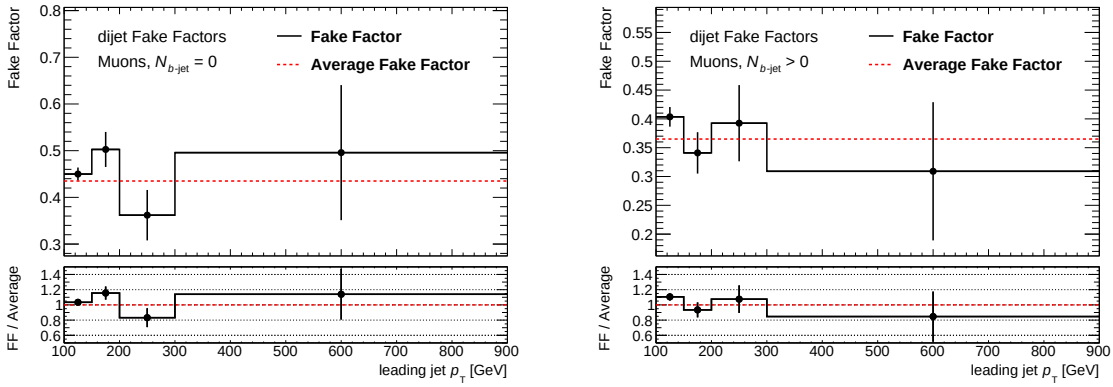

Figure C.8: Muon fake factors computed from single-muon prescaled triggers as a function of the leading jet p_{T} for events with zero b-tagged jets (left) and at least one b-tagged jet (right) in the kinematic region with leading jet $p_{\mathrm{T}} > 100$ GeV and $m_{\mathrm{T}} < 40$ GeV. A red line denotes the average muon fake factor.

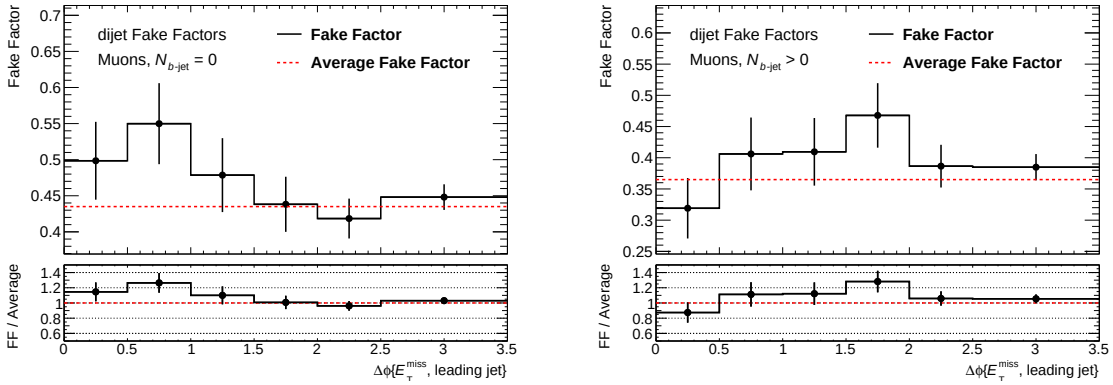

Figure C.9: Muon fake factors computed from single-muon prescaled triggers as a function of $\Delta\phi(j_1, \mathbf{p}_{\mathrm{T}}^{\mathrm{miss}})$ for events with zero b-tagged jets (left) and at least one b-tagged jet (right) in the kinematic region with leading jet $p_{\mathrm{T}} > 100$ GeV and $m_{\mathrm{T}} < 40$ GeV. A red line denotes the average muon fake factor.

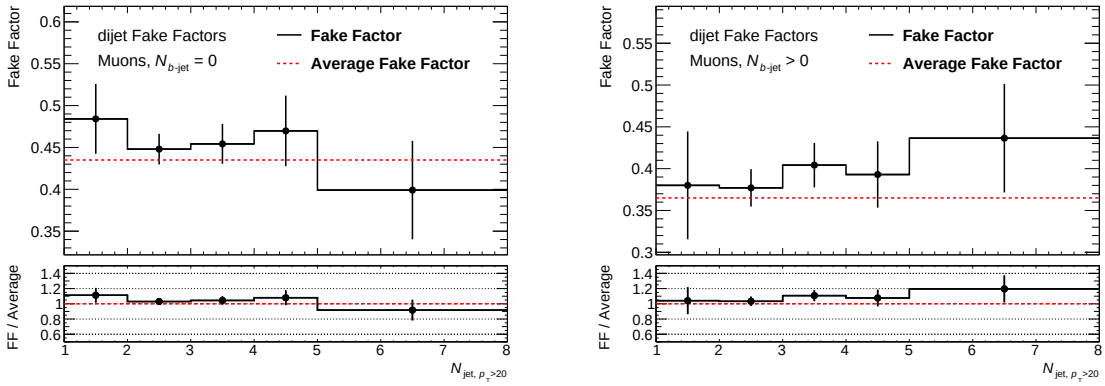

Figure C.10: Muon fake factors computed from single-muon prescaled triggers as a function of the jet multiplicity for events with zero b-tagged jets (left) and at least one b-tagged jet (right) in the kinematic region with leading jet $p_{\mathrm{T}} > 100$ GeV and $m_{\mathrm{T}} < 40$ GeV. A red line denotes the average muon fake factor.

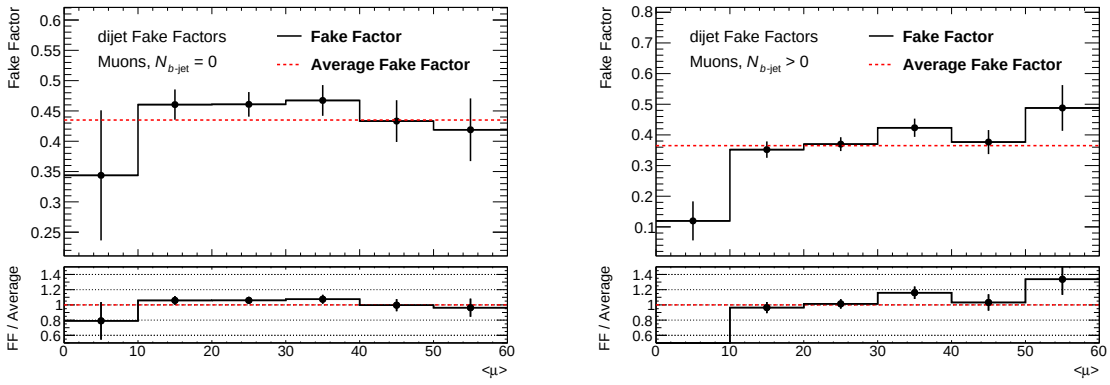

Figure C.11: Muon fake factors computed from single-muon prescaled triggers as a function of $\langle\mu\rangle$ for events with zero b-tagged jets (left) and at least one b-tagged jet (right) in the kinematic region with leading jet $p_{\mathrm{T}} > 100$ GeV and $m_{\mathrm{T}} < 40$ GeV. A red line denotes the average muon fake factor.

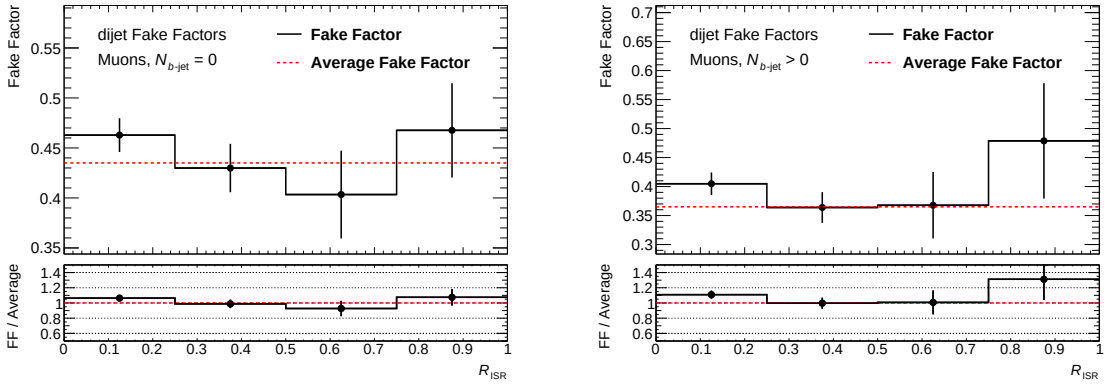

Figure C.12: Muon fake factors computed from single-muon prescaled triggers as a function of R_{ISR} for events with zero b-tagged jets (left) and at least one b-tagged jet (right) in the kinematic region with leading jet $p_{\mathrm{T}} > 100$ GeV and $m_{\mathrm{T}} < 40$ GeV. A red line denotes the average muon fake factor.

C.3 Fake factor measurement for events with b-jets

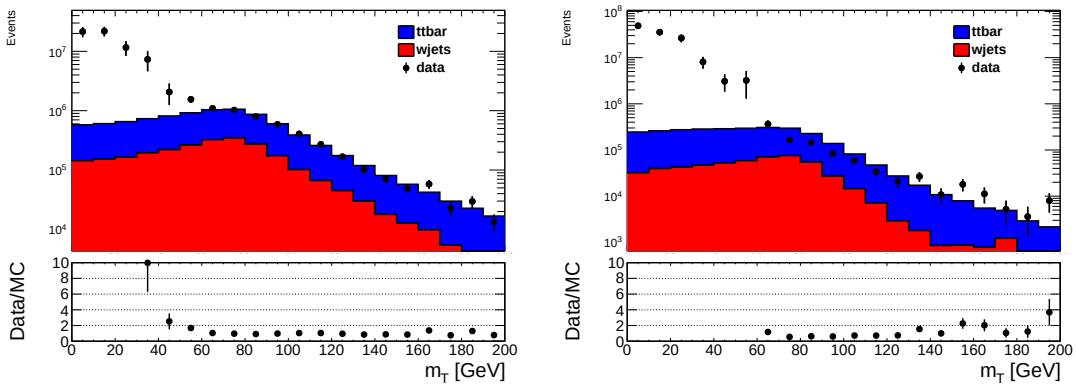

Figure C.13: The $E_{\mathrm{T}}^{\mathrm{miss}}$ (left) and m_{T} (right) distributions for numerator (top) and denominator (bottom) electrons in the prescaled single-lepton-trigger sample for events with one or more b-tagged jets. MC has been scaled to the data in the $m_{\mathrm{T}} > 100$ GeV region.

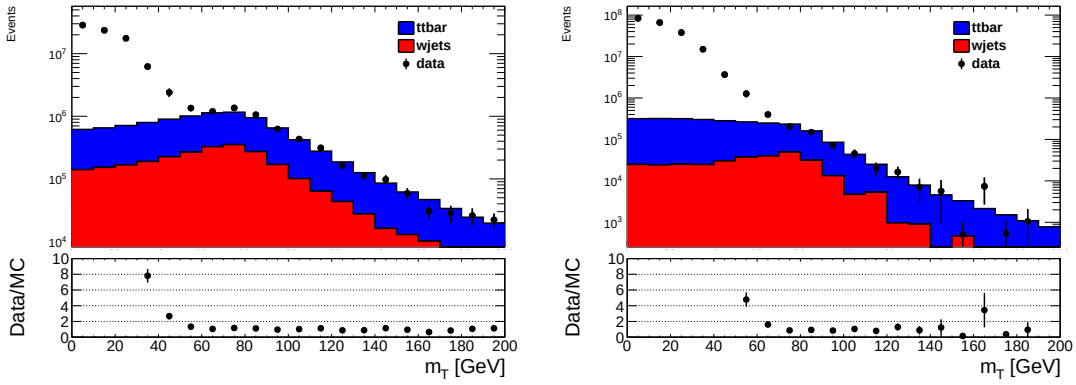

Figure C.14: The $E_{\mathrm{T}}^{\mathrm{miss}}$ (left) and m_{T} (right) distributions for numerator (top) and denominator (bottom) muons in the prescaled single-lepton-trigger sample for events with one or more b-tagged jets. MC has been scaled to the data in the $m_{\mathrm{T}} > 100$ GeV region.

C.4 Fake factor application in 2 lepton region

$$N_{\mathrm{TT}}^{\mathrm{All}} = N_{\mathrm{TT}}^{\mathrm{FR}} + N_{\mathrm{TT}}^{\mathrm{RF}} + N_{\mathrm{TT}}^{\mathrm{FF}}. \tag{C.1}$$

Now, by applying fake factor F, one can estimate number of fake lepton passing tight criteria from number passing loose criteria. For example,

$$\begin{aligned} N_{\mathrm{TT}}^{\mathrm{FR}} &= N_{\mathrm{LT}}^{\mathrm{FR}} \cdot F_1, \\ N_{\mathrm{TT}}^{\mathrm{RF}} &= N_{\mathrm{TL}}^{\mathrm{RF}} \cdot F_2, \\ N_{\mathrm{TT}}^{\mathrm{FF}} &= N_{\mathrm{LL}}^{\mathrm{FF}} \cdot F_1 F_2. \end{aligned} \tag{C.2}$$

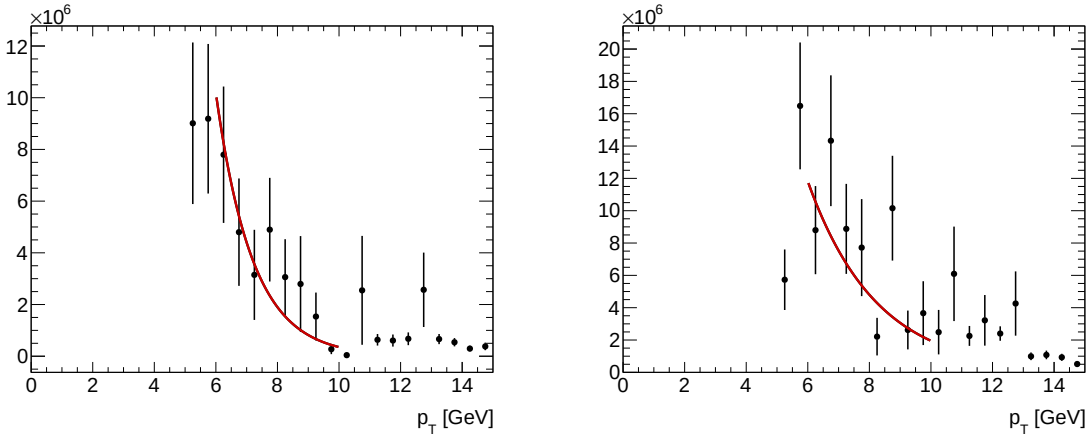

Figure C.15: Exponential fits to the numerator (top) and denominator (bottom) electron p_{T} distributions used for the fake factor extrapolation. Events with exactly zero b-tagged jets are shown on the left, while events with at least one b-tagged jet are shown on the right.

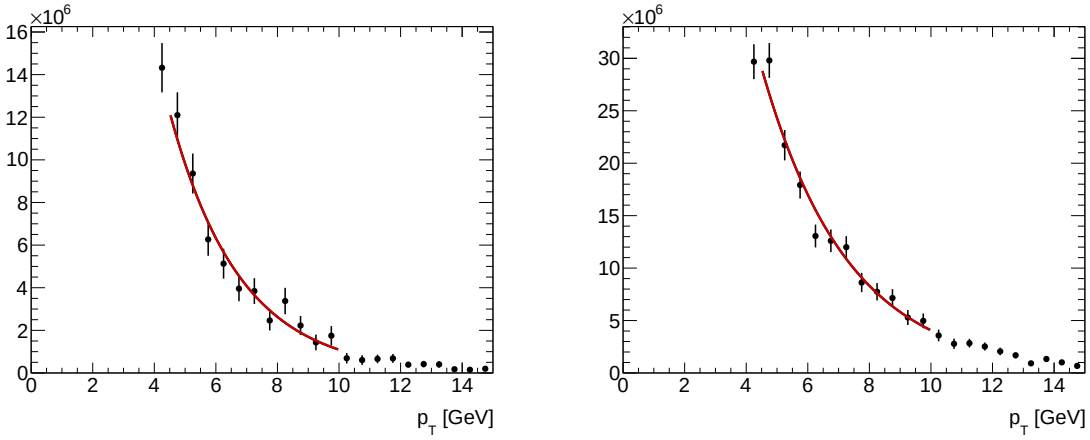

Figure C.16: Exponential fits to the numerator (top) and denominator (bottom) muon p_{T} distributions used for the fake factor extrapolation. Events with exactly zero b-tagged jets are shown on the left, while events with at least one b-tagged jet are shown on the right.

$$
\begin{aligned}
N_{\mathrm{LT}}^{\mathrm{All}} &= N_{\mathrm{LT}}^{\mathrm{FR}} + N_{\mathrm{LT}}^{\mathrm{RF}} + N_{\mathrm{LT}}^{\mathrm{FF}} \\
N_{\mathrm{TT}}^{\mathrm{All}} &= N_{\mathrm{TT}}^{\mathrm{FR}} + N_{\mathrm{TT}}^{\mathrm{RF}} + N_{\mathrm{TT}}^{\mathrm{FF}} \\
N_{\mathrm{LL}}^{\mathrm{All}} &= N_{\mathrm{LL}}^{\mathrm{FR}} + N_{\mathrm{LL}}^{\mathrm{RF}} + N_{\mathrm{LL}}^{\mathrm{FF}}
\end{aligned}
\tag{C.3}
$$

$$
N_{\mathrm{T,\,T}} = N_{\mathrm{L,\,T}} \cdot F_1 + N_{\mathrm{T,\,L}} \cdot F_2 - N_{\mathrm{L,\,L}} \cdot F_1 F_2 \tag{C.4}
$$

C.5 Fake origin studies

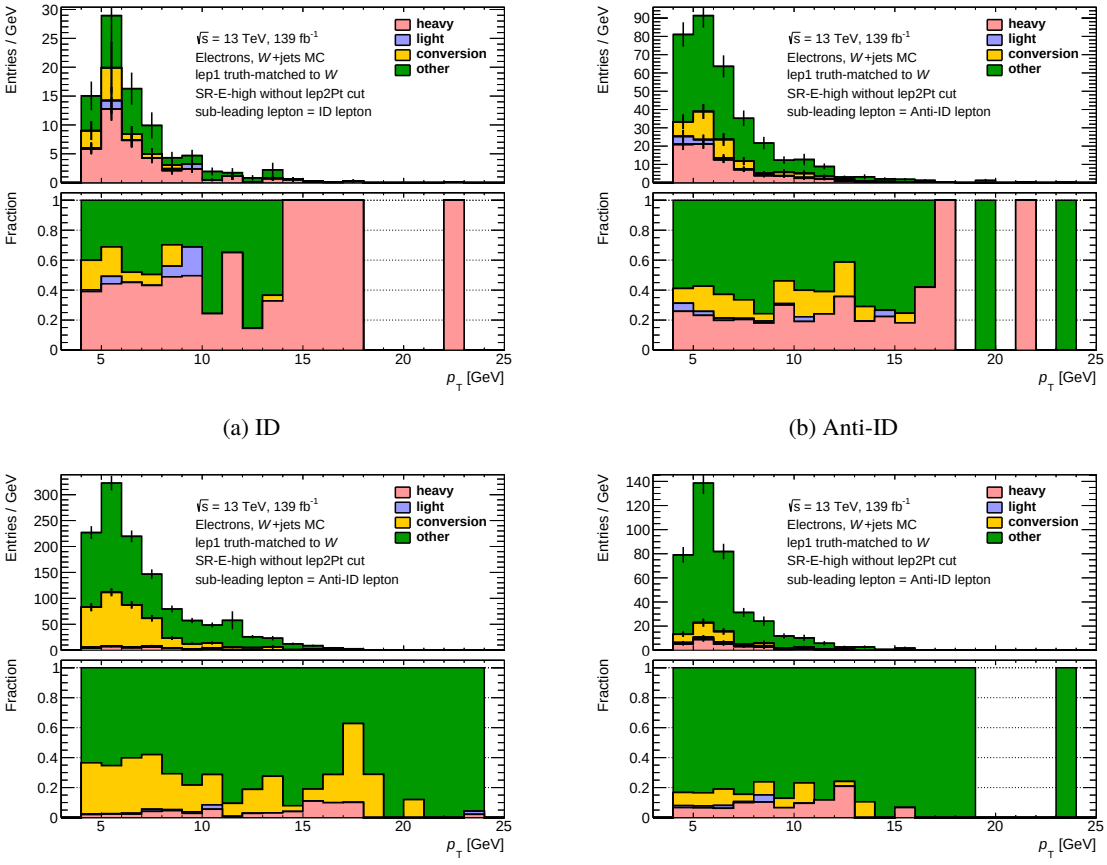

(a) ID

(b) Anti-ID

(c) Fail LooseAndBLayer ID

(d) Fail both MediumID and Gradient isolation

Figure C.17: Origin of electron fake lepton in ID and Anti-ID region. MC origin information are taken from W+jets MC. Events are required to pass SR-E-high except for the cuts on sub-leadintglepton p_{T}.

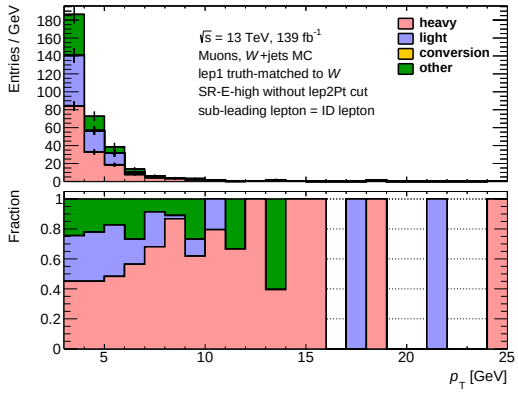

(a) ID

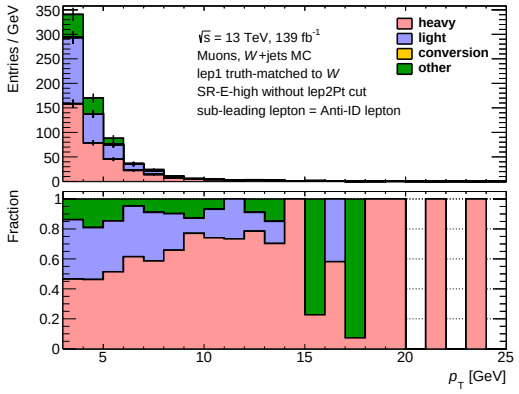

(b) Anti-ID

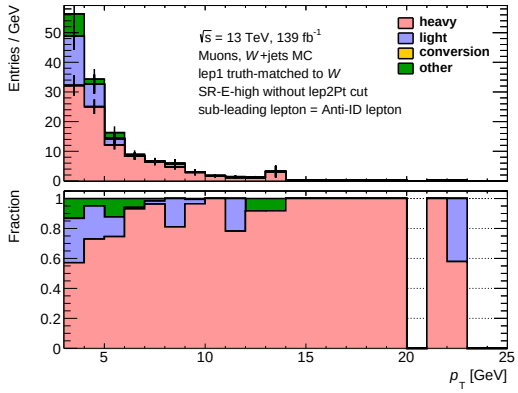

(c) Fail d_0/σ_{d_0} cut and FCTightTrackOnly isolation

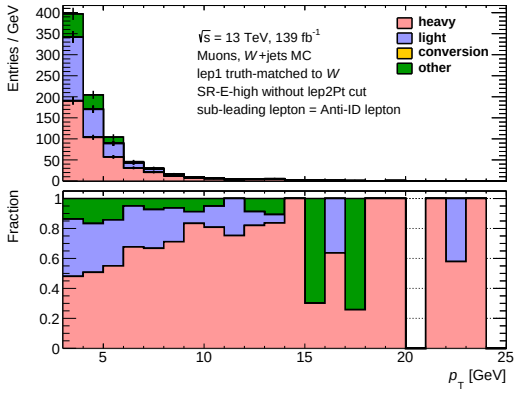

(d) Fail ID (inclusive)

Figure C.18: Origin of muon fake lepton in ID and Anti-ID region. MC origin information are taken from W+jets MC. Events are required to pass SR-E-high except for the cuts on sub-leadintglepton p_{T}.

C.6 Fake factor closure systematic

This section will discuss how the fake factor closure systematic was derived.

As our same-sign validation region is very pure in fake leptons, a systematic uncertainty can be derived based on the extent of non-closure between the fake lepton estimate and the data. Events in which the subleading lepton is an electron (muon) are used to assess the closure systematic on the electron (muon) fake factors. Since the subleading contribution to VR-SS is due to diboson processes, we apply the diboson normalization factors obtained from the background-only fits in order to have a more direct assessment of our fake lepton modeling for events with zero b-tagged jets. Bins where the data central value is within 1 sigma of the fake lepton estimate are assigned a closure uncertainty of zero, while the closure uncertainty on the other bins is chosen to be x, where x is the value necessary for the total systematic uncertainty to cover the data for the given bin. Put differently, the RMS over the other variations is computed, and this RMS is added in quadrature with x. This total is then compared with the data central value, and this x can be determined. In each of the regions that follow, we do not apply any $m_{\ell\ell}$-dependent cut on the subleading lepton p_{T} since this cut is designed to mitigate the contributions from fake/non-prompt leptons.

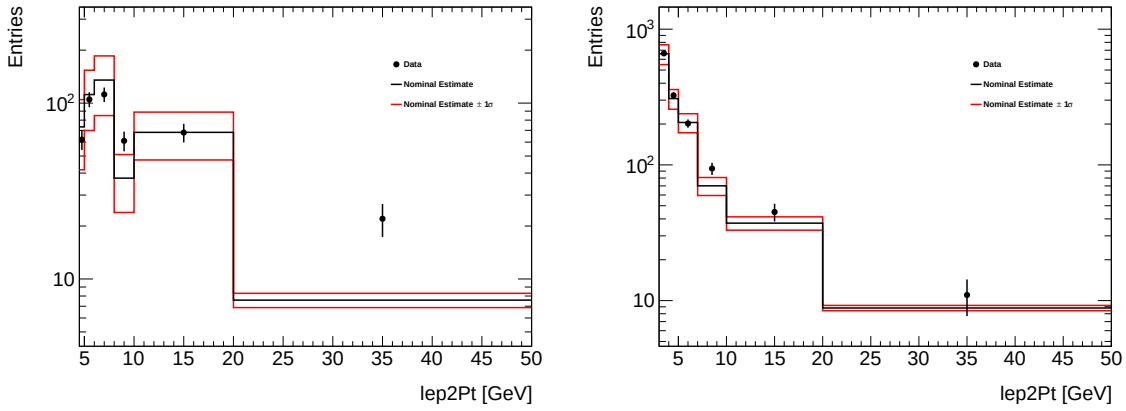

(a) $ee + \mu e$ channel

(b) $\mu\mu + e\mu$ channel

Figure C.19: Data compared with the fake lepton estimate in high-MET VR-SS for the $ee + \mu e$ channel (left) and the $\mu\mu + e\mu$ channel (right). This is used to calculate the closure systematic.

Figure C.19 and Figure C.20 show the agreement between the data and the estimated background in the high-MET and low-MET VR-SS, respectively. Ultimately, these are used to assign the following closure uncertainties for events with zero b-tagged jets:

- Electrons ($E_{\mathrm{T}}^{\mathrm{miss}} > 200$ GeV):
  - 51% for 8 GeV $< p_{\mathrm{T}} <$ 10 GeV
  - 190% for $p_{\mathrm{T}} > 20$ GeV
- Muons ($E_{\mathrm{T}}^{\mathrm{miss}} > 200$ GeV):
  - 30% for 7 GeV $< p_{\mathrm{T}} <$ 10 GeV
  - 18% for 10 GeV $< p_{\mathrm{T}} <$ 20 GeV
  - 24% for $p_{\mathrm{T}} > 20$ GeV
- Electrons ($E_{\mathrm{T}}^{\mathrm{miss}} < 200$ GeV):
  - 36% for $p_{\mathrm{T}} > 20$ GeV
- Muons ($E_{\mathrm{T}}^{\mathrm{miss}} < 200$ GeV):
  - 18% for 7 GeV $< p_{\mathrm{T}} <$ 10 GeV
  - 11% for 10 GeV $< p_{\mathrm{T}} <$ 20 GeV

Since the fake factors are binned in the number of b-tagged jets, the closure uncertainties are derived separately for events with at least one b-tagged jet. The same methodology is used but we instead look at same-sign events in CR-top. Figure C.21 and Figure C.22 show the agreement between the data and the estimated background in same-sign high-MET and same-sign low-MET CR-top, respectively. Ultimately, these are used to assign the following closure uncertainties for events with at least one b-tagged jet:

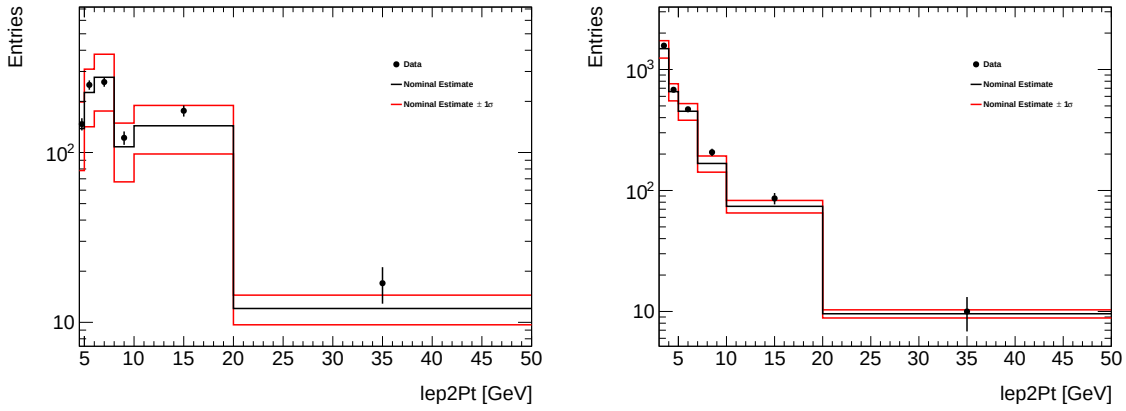

(a) $ee + \mu e$ channel

(b) $\mu\mu + e\mu$ channel

Figure C.20: Data compared with the fake lepton estimate in low-MET VR-SS for the $ee + \mu e$ channel (left) and the $\mu\mu + e\mu$ channel (right). This is used to calculate the closure systematic.

- Electrons ($E_{\mathrm{T}}^{\mathrm{miss}} > 200$ GeV):
  - 34% for 4.5 GeV $< p_{\mathrm{T}} <$ 5 GeV
  - 6% for 5 GeV $< p_{\mathrm{T}} <$ 6 GeV
  - 43% for $p_{\mathrm{T}} > 20$ GeV
- Muons ($E_{\mathrm{T}}^{\mathrm{miss}} > 200$ GeV):
  - 19% for 3 GeV $< p_{\mathrm{T}} <$ 4 GeV
  - 10% for 10 GeV $< p_{\mathrm{T}} <$ 20 GeV
  - 34% for $p_{\mathrm{T}} > 20$ GeV
- Electrons ($E_{\mathrm{T}}^{\mathrm{miss}} < 200$ GeV):
  - 43% for 4.5 GeV $< p_{\mathrm{T}} <$ 5 GeV
  - 47% for $p_{\mathrm{T}} > 20$ GeV
- Muons ($E_{\mathrm{T}}^{\mathrm{miss}} < 200$ GeV):
  - 28% for 3 GeV $< p_{\mathrm{T}} <$ 4 GeV
  - 15% for 10 GeV $< p_{\mathrm{T}} <$ 20 GeV
  - 5% for $p_{\mathrm{T}} > 20$ GeV

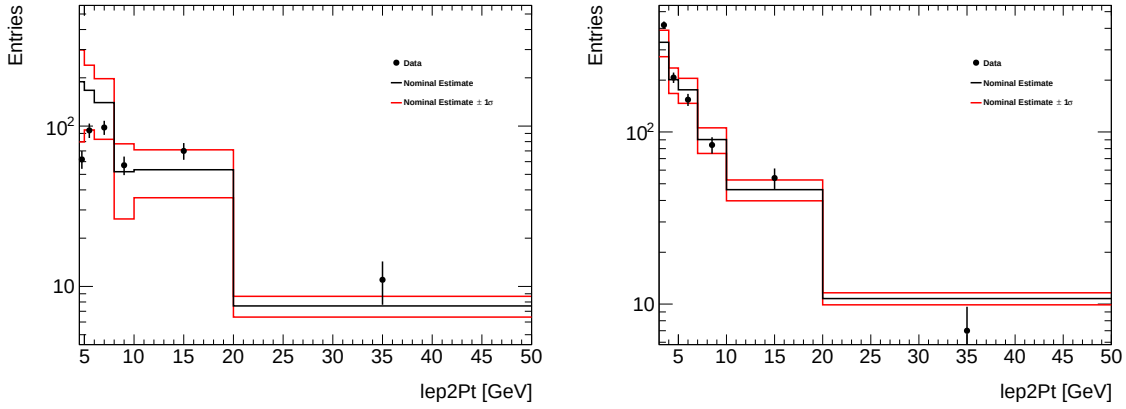

(a) $ee + \mu e$ channel (b) $\mu\mu + e\mu$ channel

Figure C.21: Data compared with the fake lepton estimate in high-MET CR-top-SS for the $ee + \mu e$ channel (left) and the $\mu\mu + e\mu$ channel (right). This is used to calculate the closure systematic.

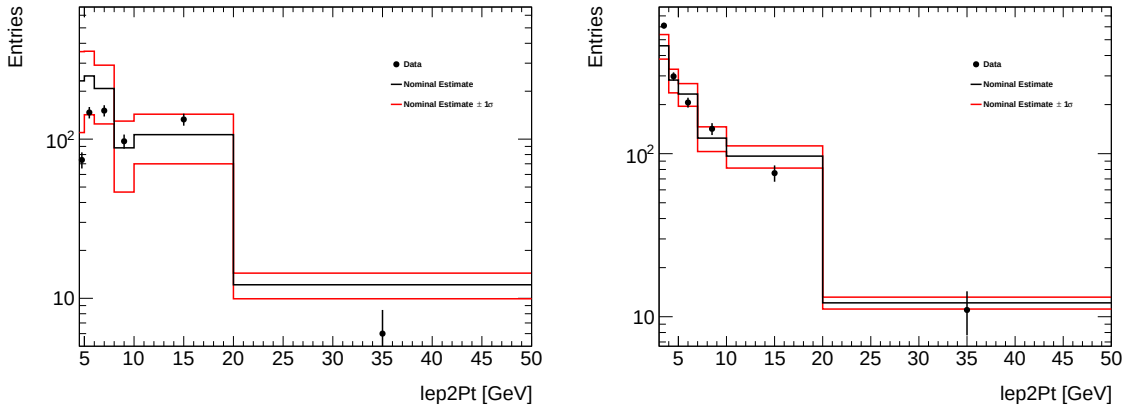

(a) $ee + \mu e$ channel (b) $\mu\mu + e\mu$ channel

Figure C.22: Data compared with the fake lepton estimate in low-MET CR-top-SS for the $ee + \mu e$ channel (left) and the $\mu\mu + e\mu$ channel (right). This is used to calculate the closure systematic.

Appendix D

$1\ell 1T$ analysis

D.1 Backgournd estiation validation for $1\ell 1T$ region

The main source of background in the 1L+1T selection is due to combinatory events, where a random track is associated with a real lepton. This fake contribution dominated particularly at very low momentum of the lepton and the track. For this reason it has been decided to use a completely data driven technique to estimate the background.

The strategy is to use events with the lepton and the track with the same sign of the charge (SS events) as a proxy for the events with opposite charge. For this combinatorial background, the track charge is not correlated with the lepton charge. Thus, there is the same probability that the couple lepton-track could have opposite sign or same sign.

The verify the SS=OS hypothesis, a Control Region is defined where we can look at the ratio between the SS and OS events in data with no signal contribution. The region is defined by requiring $m_{\ell\text{track}} > 5$ GeV and $E_{\mathrm{T}}^{\mathrm{miss}}/(p_{\mathrm{T}}^{lep} + p_{\mathrm{T}}^{track}) < 30$, such that the targeted signals at low Δm are not present. The ratio of OS over SS events as a function of both the lepton and track p_{T} and η is shown in figure D.1. As it can be seen at low p_{T}, where the signal region is defined, the ratio is consistent with one, while at increasing p_{T} the ratio is higher that one. Inside the red lines, which show the kinematics relevant in the signal region, the average ratio is: 1.05 ± 0.02.

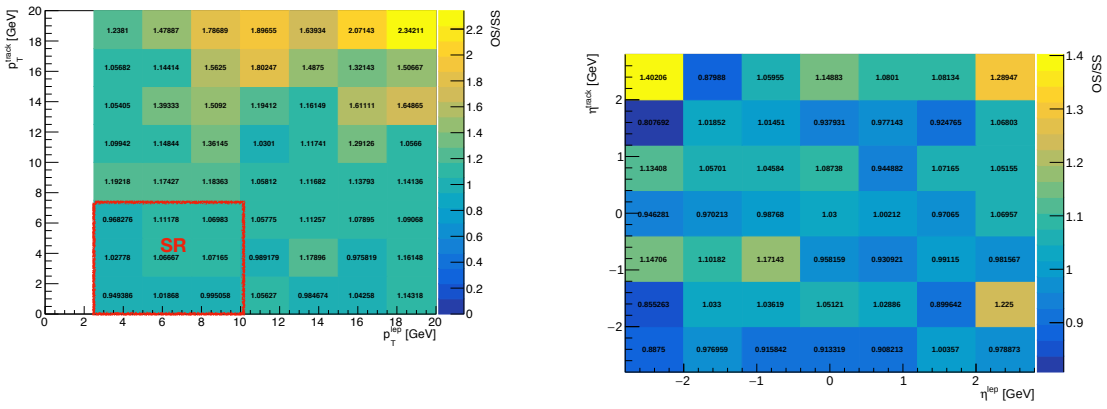

Figure D.1: Ratio of OS over SS events as a function of the lepton and track p_{T} (left) and η (right) in the one lepton + one track channel.

In figure D.2 we show a comparison between SS and OS data as a function of $E_{\mathrm{T}}^{\mathrm{miss}}/(p_{\mathrm{T}}^{lep} + p_{\mathrm{T}}^{track})$

for 2015+2016 data, 2017 data, and 2018 data, normalized to 1, after requirements of $m_{\ell\text{track}} > 5$ GeV and $p_{\mathrm{T}}^{lep/track} < 10$ GeV. The plot indicates the SS=OS equality does not depend on $E_{\mathrm{T}}^{\mathrm{miss}}/H_{\mathrm{T}}^{\mathrm{lep}}$ or data-taking year.

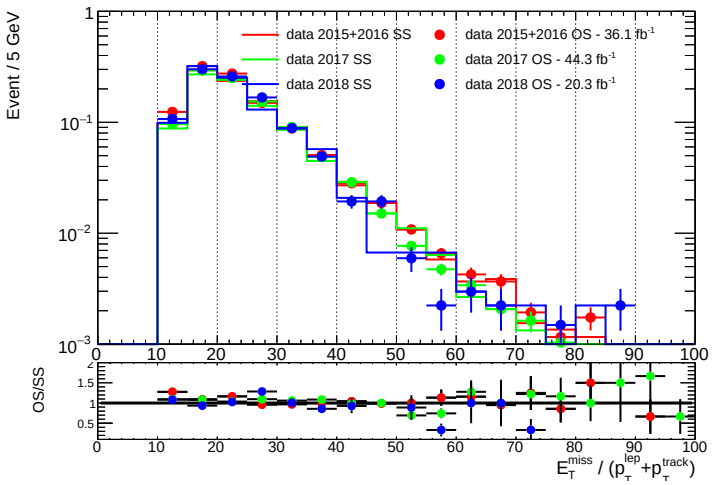

Figure D.2: Ratio of OS over SS events as a function of $E_{\mathrm{T}}^{\mathrm{miss}}/(p_{\mathrm{T}}^{lep} + p_{\mathrm{T}}^{track})$ divided by year in the one lepton + one track channel. The distributions are normalized to 1.

Figure D.3 shows the dependency of the OS/SS ratio as a function of η. Except at very high η where the statistic is rather low, the ratio is consistent with 1.

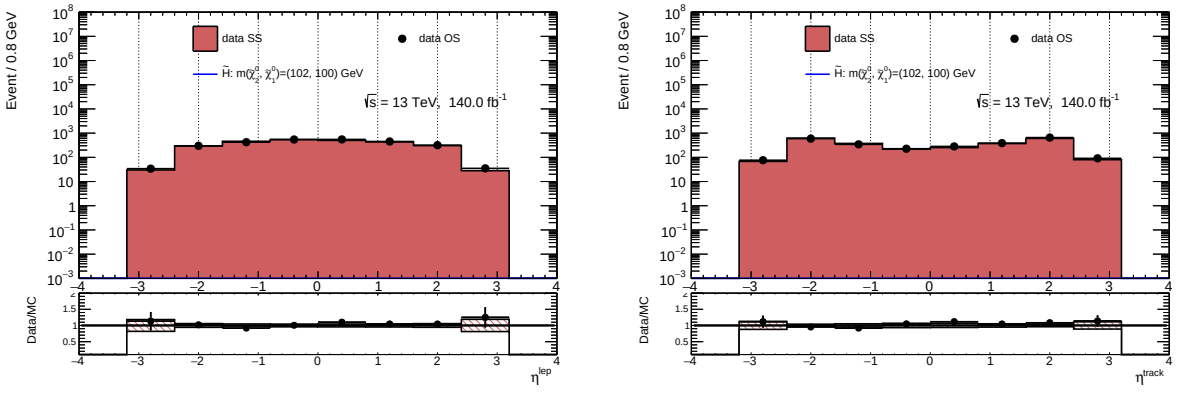

Figure D.3: Ratio of OS over SS events as a function of η for the lepton (left) and the track (right), asking $E_{\mathrm{T}}^{\mathrm{miss}}/(p_{\mathrm{T}}^{lep} + p_{\mathrm{T}}^{track}) < 30$ and $m_{\ell\text{track}} > 5$ GeV, $E_{\mathrm{T}}^{\mathrm{miss}} > 200$ GeV, $p_{\mathrm{T}}^{track} < 5$ GeV, and $p_{\mathrm{T}}^{lep} < 10$ GeV

An additional check is done to verify the different contribution from plus and minus charged leptons. Figure D.4 shows the ratio between events with SS lepton-track pairs with a positive and negative lepton as a function of both lepton and track p_{T}. The number of evens with a positive charge are more than the one with a negative one by a factor ~ 1.6, which is compatible with the ratio of the cross section of W^+ over W^- [163]. Instead figure D.5 (left) shows as a function of the track p_{T} the ratio of events with a positive charged tracks over negative charged one, while the lepton is in both cases positively charged. In figure D.5 (right) is the same plot but with negative charged lepton. In both these cases the ratio is close to one in the region of interest for this analysis ($p_{\mathrm{T}}^{track} < 10$ GeV), meaning that again most of the background tracks

are not correlated to the lepton, even if there are more positive charged leptons. In all of these plots we require at least one jet with a $p_{\mathrm{T}}^{jet} > 100$ GeV, $E_{\mathrm{T}}^{\mathrm{miss}} > 180$ GeV, and $\Delta\phi(\mathrm{lep}, \mathbf{p}_{\mathrm{T}}^{\mathrm{miss}}) > 1.5$.

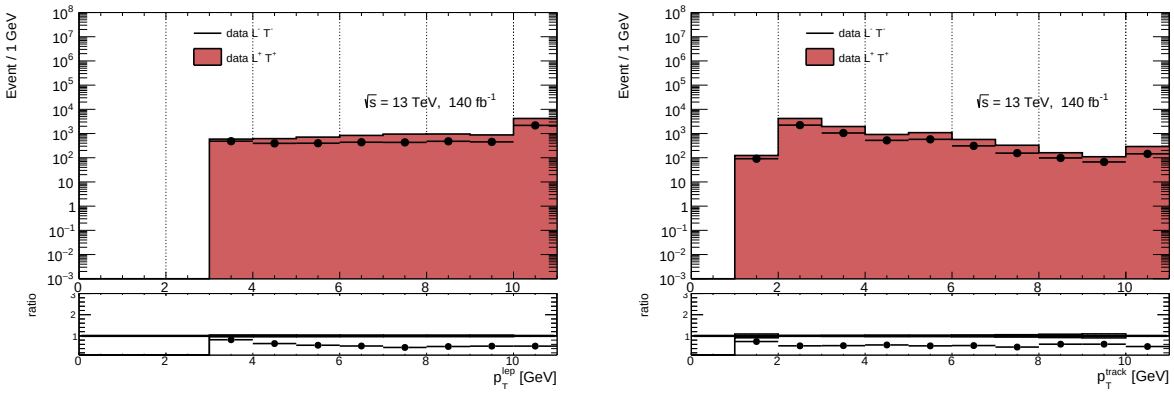

Figure D.4: Ratio of plus charged lepton-track pair over negative charged lepton-track pair as a function of lepton p_{T} (left) and track p_{T} (right) in the one lepton + one track channel. Requiring at least one jet with a $p_{\mathrm{T}}^{jet} > 100$ GeV, $E_{\mathrm{T}}^{\mathrm{miss}} > 180$ GeV, and $\Delta\phi(\mathrm{lep}, \mathbf{p}_{\mathrm{T}}^{\mathrm{miss}}) > 1.5$.

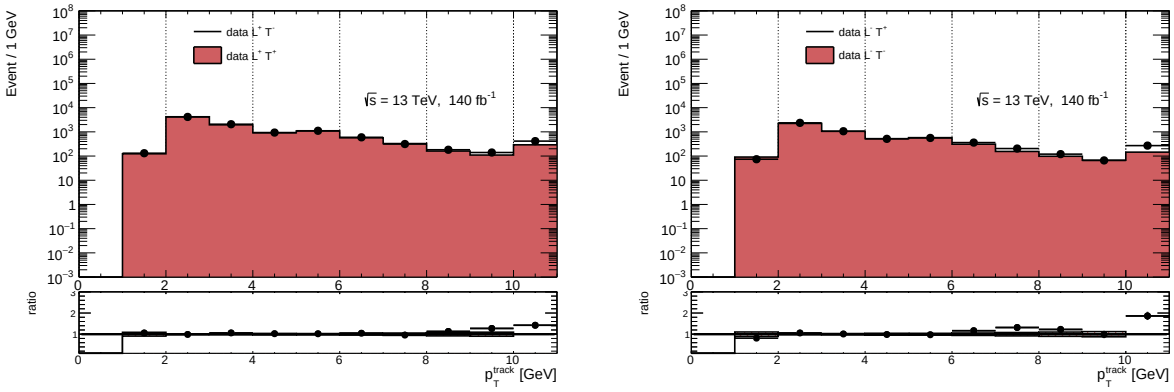

Figure D.5: Ratio of events with plus charged and minus charged tracks with a plus (right) or minus (right) charged lepton, as a function of the track p_{T} in the one lepton + one track channel. Requiring at least one jet with a $p_{\mathrm{T}}^{jet} > 100$ GeV, $E_{\mathrm{T}}^{\mathrm{miss}} > 180$ GeV, and $\Delta\phi(\mathrm{lep}, \mathbf{p}_{\mathrm{T}}^{\mathrm{miss}}) > 1.5$.

We conclude that it is possible to consider the SS events as a good proxy for the OS background in the signal region. We also checked that the prompt contribution in the SS region is negligible, meaning that the SS data can be used directly as an estimate of the OS fake background, with no need to subtract processes with two prompt leptons. Sherpa diboson samples of $\nu\nu$, ν, and are used for this check. In figure D.6 we show the contribution of these backgrounds in the SS region at preselection level, as a function of $E_{\mathrm{T}}^{\mathrm{miss}}/(p_{\mathrm{T}}^{lep} + p_{\mathrm{T}}^{track})$. We conclude that the prompt contribution can be ignored.

Finally it is checked the contribution to the background from the signal itself. Figure D.7 shows the $m_{\ell\mathrm{track}}$ distribution for different signal samples in the SR for both OS and SS contribution, while table D.1 shows the integral of these distributions (normalized to 140 fb^{-1}). It is possible to see that the SS contribution is small, especially where the OS signal is dominant.

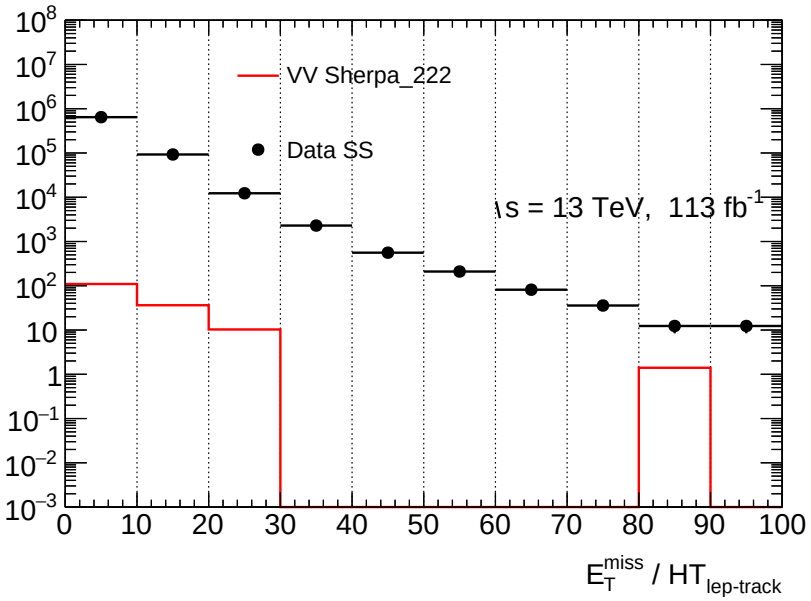

Figure D.6: Diboson prompt contribution at preselection level.

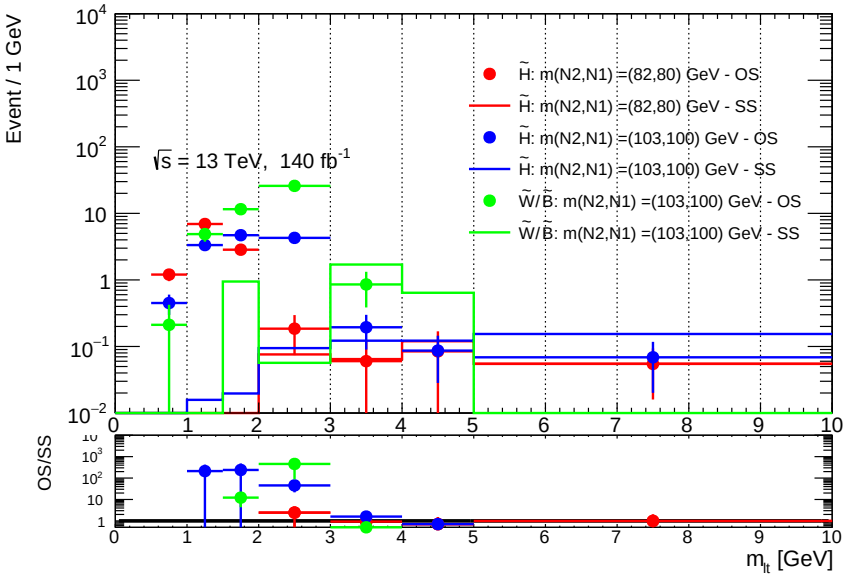

Figure D.7: OS and SS events $m_{\ell\text{track}}$ distribution for signal samples in the SR The bottom box shows the OS/SS ratio.

Sample	OS events	SS events
$\tilde{H}$ $(m(\tilde{\chi}_2^0), m(\tilde{\chi}_1^0))$ = (82, 80) GeV	11.36 ± 0.72	0.32 ± 0.10
$\tilde{H}$ $(m(\tilde{\chi}_2^0), m(\tilde{\chi}_1^0))$ = (103, 100) GeV	13.12 ± 0.75	0.53 ± 0.15
$\tilde{W}/\tilde{B}$ $(m(\tilde{\chi}_2^0), m(\tilde{\chi}_1^0))$ = (103, 100) GeV	43.38 ± 3.50	3.35 ± 0.99

Table D.1: Yields for OS and SS signal events in the SR, normalized to 140 fb^{-1}

Appendix E

$E_{\mathrm{T}}^{\mathrm{miss}}$ trigger scale factors

E.1 General Concept

As the inclusive $E_{\mathrm{T}}^{\mathrm{miss}}$-triggers are not fully efficient below 200 GeV, dedicated SFs have to bee derived to account for any mis-modeling in simulation for the low-$E_{\mathrm{T}}^{\mathrm{miss}}$ selection. In general $E_{\mathrm{T}}^{\mathrm{miss}}$-trigger SFs are to a large extend phase-space dependent, so they have to be measured in a selection that is as close as possible to the baseline analysis.

To measure the efficiencies for $E_{\mathrm{T}}^{\mathrm{miss}}$-triggers an unbiased sample of events is needed. This can be accomplished by using events selected by single-muon triggers as muons are not taken into account in the $E_{\mathrm{T}}^{\mathrm{miss}}$ calculation on HLT level. The efficiency ϵ can then be measured in this sample via

$$\epsilon = \frac{\text{\# events selected by single-muon trigger \&\& by } E_{\mathrm{T}}^{\mathrm{miss}} \text{ trigger}}{\text{\# events selected by single-muon trigger}} \tag{E.1}$$

Equation E.1 can be evaluated in several $E_{\mathrm{T}}^{\mathrm{miss}}$ bins to check how the trigger efficiency evolves with $E_{\mathrm{T}}^{\mathrm{miss}}$, which is usually plotted in a turn-on curve.
In the approach presented here, a specific $E_{\mathrm{T}}^{\mathrm{miss}}$ flavor, $E_{\mathrm{T},\,\mu\,\mathrm{invis}}^{\mathrm{miss}}$, is used that assumes the muons to be invisible to the detector. $E_{\mathrm{T},\,\mu\,\mathrm{invis}}^{\mathrm{miss}}$ is closer to the online $E_{\mathrm{T}}^{\mathrm{miss}}$ seen on HLT level and thus should give smoother turn-on curves as online and offline reference are more similar.
The trigger SFs are both measured and later applied with respect to this specific $E_{\mathrm{T}}^{\mathrm{miss}}$ flavor $E_{\mathrm{T},\,\mu\,\mathrm{invis}}^{\mathrm{miss}}$.

The SFs are calculated by dividing the measured efficiencies in data by the ones measured on MC and a fit of the resulting ratio with an error function F

$$F(x) = 0.5 \cdot \left[1 + Erf\left(\frac{x - p_0}{\sqrt{1p_1^2}}\right)\right] \tag{E.2}$$

The parameter p_0 in F can be related to the trigger threshold, while p_0 reflects the size of the turn-on region.

After the fit, F can be evaluated at the value of $E_{\mathrm{T},\,\mu\,\mathrm{invis}}^{\mathrm{miss}}$ to get the $E_{\mathrm{T}}^{\mathrm{miss}}$-trigger SF for the event.

MR	trigger matched μ	$n_{\text{Lep}}^{\text{sig}}$	$m_{\ell\ell}$	$m_{\ell\ell}$	$m_{\ell\ell}$	n_{jets}	$p_{\text{T}}(j_1)$	$p_{\text{T}}(j_2)$
cut value	>= 1	== 2	[1, 60] GeV	]3, 3.2[GeV	]9, 10[GeV	>= 2	> 100	> 26

Table E.1: Definition of the measurement region for the $E_{\text{T}}^{\text{miss}}$-trigger SFs.

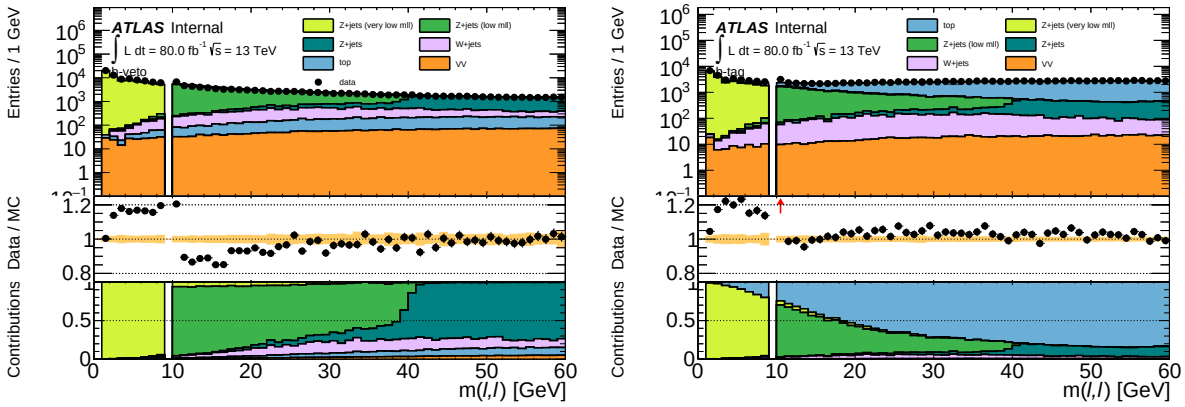

Figure E.1: Distributions of $m_{\ell\ell}$ in the measurement region for b-veto (left) and b-tagged (right) events.

E.2 Measurement Region

To retrieve valid SFs for the analysis it is important to perform the measurement in a phase-space as close as possible to the one used in the analysis. This means that the measurement region has exactly 2 signal leptons with one of them a muon that is trigger-matched to the single muon trigger firing the event. Other baseline leptons in the event are vetoed as well as the $J\psi$ and Υ resonances by inverted window cuts on $m_{\ell\ell}$. A cut on the leading jet p_{T} brings the selection further towards the baseline analysis.
As SUSY5 has to be used for this study, additional requirements on the number of jets and the subleading jet p_{T} have to be applied to account for a skimming on derivation level for MC.
The selection is summarized in Table E.1.
Lastly, the is separated into a b-veto and b-tagged region as the SFs are found to be different in these phase-spaces.

The $m_{\ell\ell}$ distributions of the b-veto and b-tag region are shown in Figure E.1. As expected, the former is dominated by $Z \to \ell\ell$ while the latter is dominated by $t\bar{t}$ events. The underestimation of the data by simulation at $m_{\ell\ell}$ below 10 GeV can be—at least partially—explained by some missing $Z \to \ell\ell$ samples at very low $m_{\ell\ell}$, because these samples have not been available for MC16a.
For that reason, the current measurements have been additionally restricted to $m_{\ell\ell} > 10$GeV. The missing samples have been requested in MC16a and will be included in further iterations of the measurements.

E.3 Efficiency Measurements

The measured efficiencies for all considered inclusive $E_{\text{T}}^{\text{miss}}$-triggers are shown in Figure E.2. Generally, the turn-on region is a bit larger in the b-tagged case, which means the trigger is fully efficient at larger

$E^{\text{miss}}_{\text{T, }\mu\text{ invis}}$ values.

In most cases the measurement of the efficiencies work fine. In some cases the measurements are limited by statistics, especially for triggers that ran only a short amount of time as lowest unprescaled trigger and in the b-veto region, as such events have in general low $E^{\text{miss}}_{\text{T}}$.

E.4 Fitting of the SFs

The fits of the ratios of the data and MC trigger efficiencies using the function F defined by Equation E.2 is shown in Figure E.3. A χ^2-fit taking into account the range $[70,\ 300]$ GeV on $E^{\text{miss}}_{\text{T, }\mu\text{ invis}}$ is used.

All fits converge and give reasonable results with adequate values of χ^2/ NDF that are noted on the plots.

E.5 Closure Test

In order to validate the technical implementation of retrieving and applying the SFs a closure test has been performed. For this check, the efficiencies are measured again with the SFs, that have been retrieved before, applied on simulation. If everything works as intended data and MC efficiencies should then be the same. This is the case as shown for HLT_xe110_pufit_L1XE55 in Figure E.4 as an example.

E.6 'Proof of Concept' Check

The SFs are measured and applied with respect a particular $E^{\text{miss}}_{\text{T}}$ flavor $E^{\text{miss}}_{\text{T, }\mu\text{ invis}}$. To check if the SFs are also valid for the baseline $E^{\text{miss}}_{\text{T}}$ definition used in the analysis, the efficiencies are also measured with respect to the nominal $E^{\text{miss}}_{\text{T}}$ and the efficiencies in data and MC are compared with and without applying (still with respect to $E^{\text{miss}}_{\text{T, }\mu\text{ invis}}$) the SFs.
This is shown in Figure E.5. In the b-tag case, the SFs clearly increase the agreement between the efficiencies in data and MC, but in the b-veto case, the SFs seem to over-correct the MC efficiency between 100 and 150 GeV a bit. This is under study but might be an effect due to statistics as the uncertainty in MC are quite large in this regime and might be improved by adjusting the binning.

E.7 $m_{\ell\ell}$ Dependence of the Efficiencies

To check the $m_{\ell\ell}$ dependence of the measured trigger efficiencies, the measurements have been performed in three different regions that are based on the selected defined in Table E.1 but differ in the $m_{\ell\ell}$ range under consideration:

low $m_{\ell\ell}$: $m_{\ell\ell}[10, 60]$ GeV

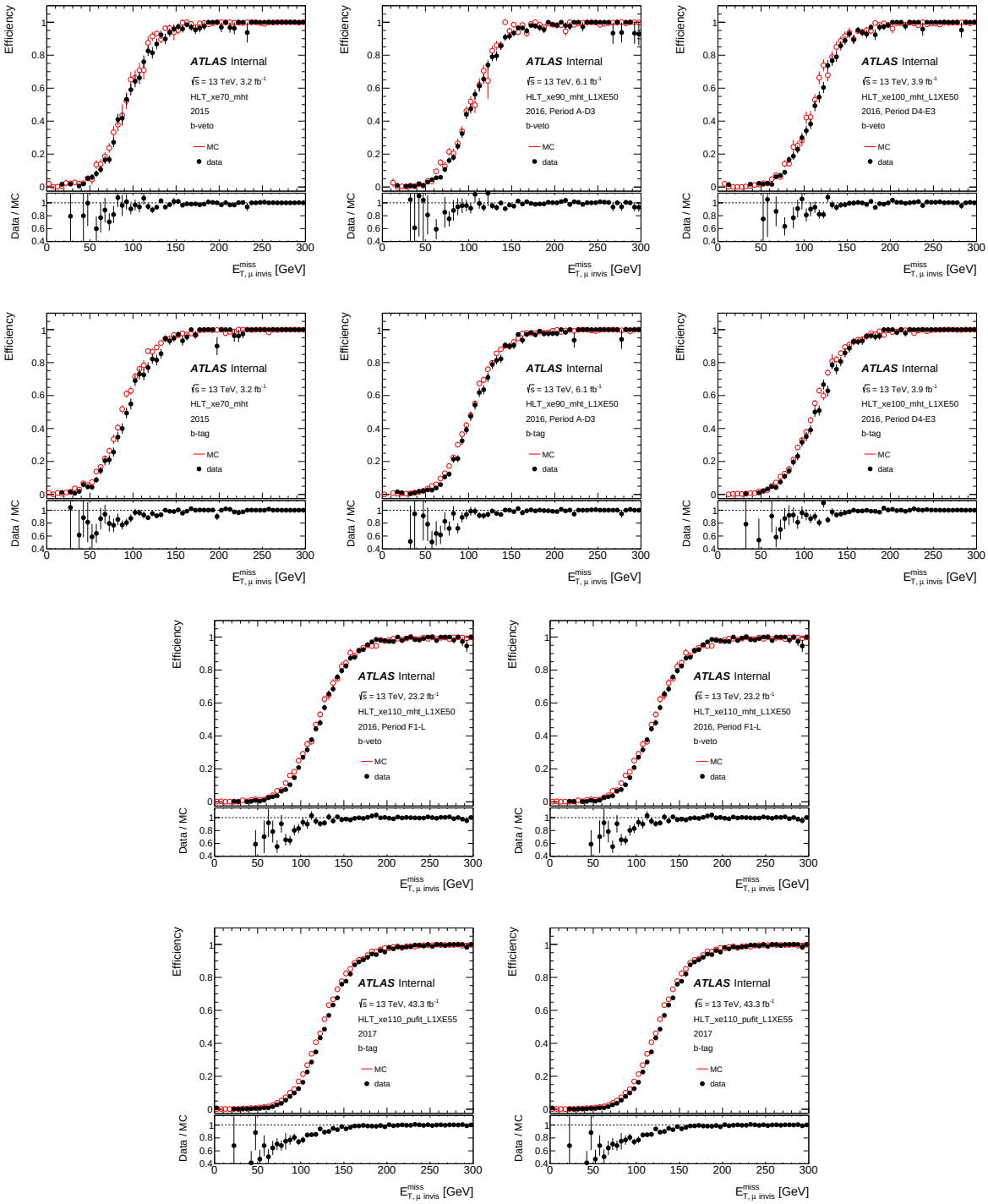

Figure E.2: Efficiencies of $E_{\mathrm{T}}^{\mathrm{miss}}$-triggers that have been run in Run 2 in the b-veto (first and third row) and in the b-tag region (second and last row).

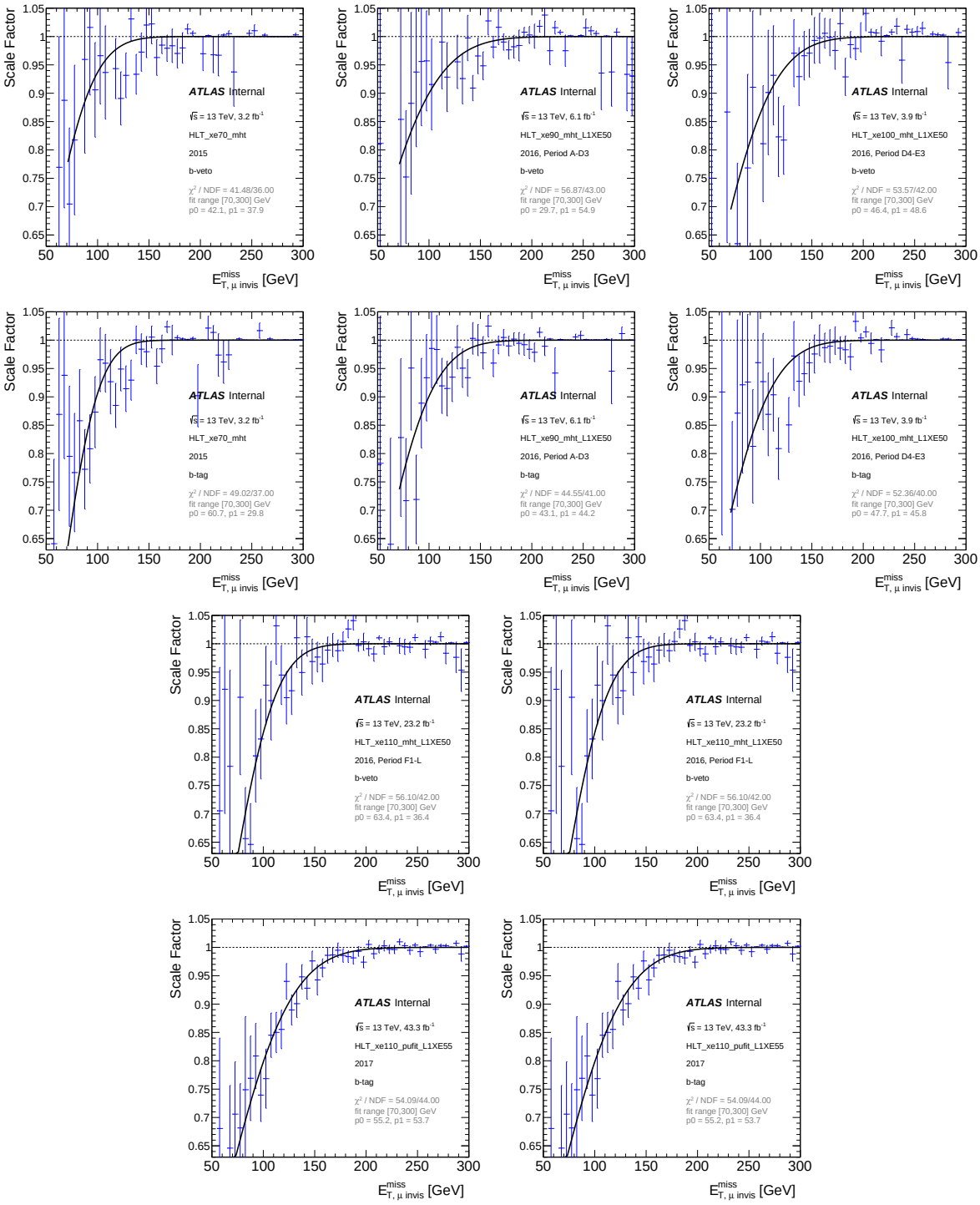

Figure E.3: Fit of the SFs for the $E_{\mathrm{T}}^{\mathrm{miss}}$-trigger efficiencies in the b-veto (first and third row) and in the b-tag region (second and last).

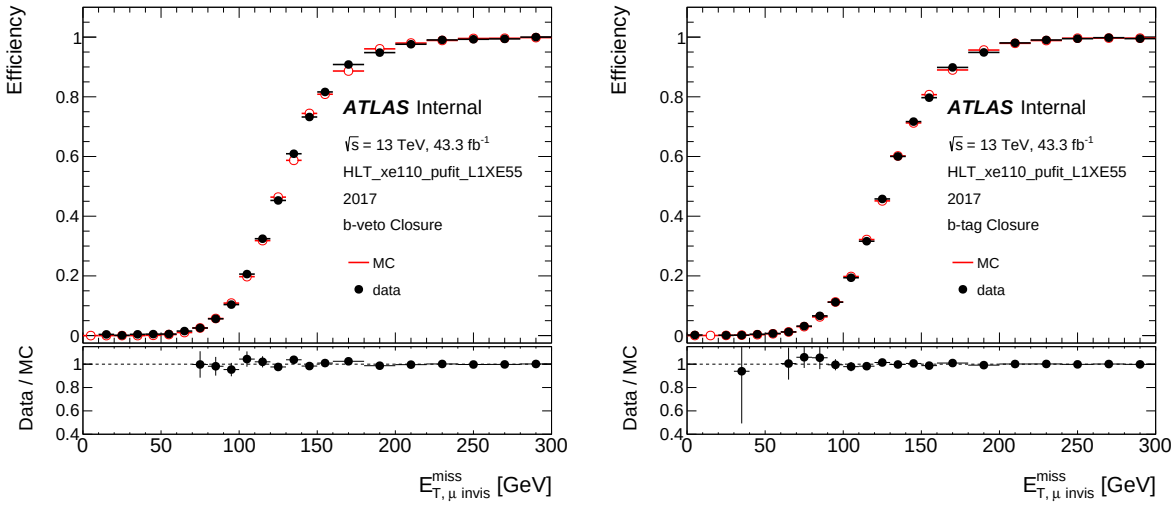

Figure E.4: Closure test of the SFs for HLT_xe110_pufit_L1XE55 the for b-veto (left) and -tagged (right) events.

medium $m_{\ell\ell}$: $m_{\ell\ell}[60, 110]$ GeV

high $m_{\ell\ell}$: $m_{\ell\ell}[110, \infty]$ GeV

Figure E.6 shows the efficiencies separately for the Zjets, ttbar and diboson background, splitted into b-tag and b-veto events and the three $m_{\ell\ell}$ regimes. No strong dependence of the efficiencies on $m_{\ell\ell}$ is observed. Furthermore the efficiencies of the background processes are also found to be compatible with each other.

E.8 Application of the SFs on Signal Events

The trigger efficiency in an example signal point (evaluated at preselection level of the baseline analysis) is also shown in Figure E.6. The trigger efficiency in signal is notably larger than in the backgrounds. This is most likely due to the clean ISR topology in the signal events with real sources of $E_{\mathrm{T}}^{\mathrm{miss}}$. In the backgrounds there is potentially more jet activity (ttbar) or no real source of $E_{\mathrm{T}}^{\mathrm{miss}}$ (Zjets) that may lead to larger discrepancy between the online and offline calculation of $E_{\mathrm{T}}^{\mathrm{miss}}$. The plots indicate that the efficiency in signal roughly agrees with the efficiencies in background when evaluating the latter at a value with additional 10 GeV. So the SF for this value is taken retrieving the SFs for signal. The difference in the SF to the "nominal" one is then added as additional uncertainty for the signal.

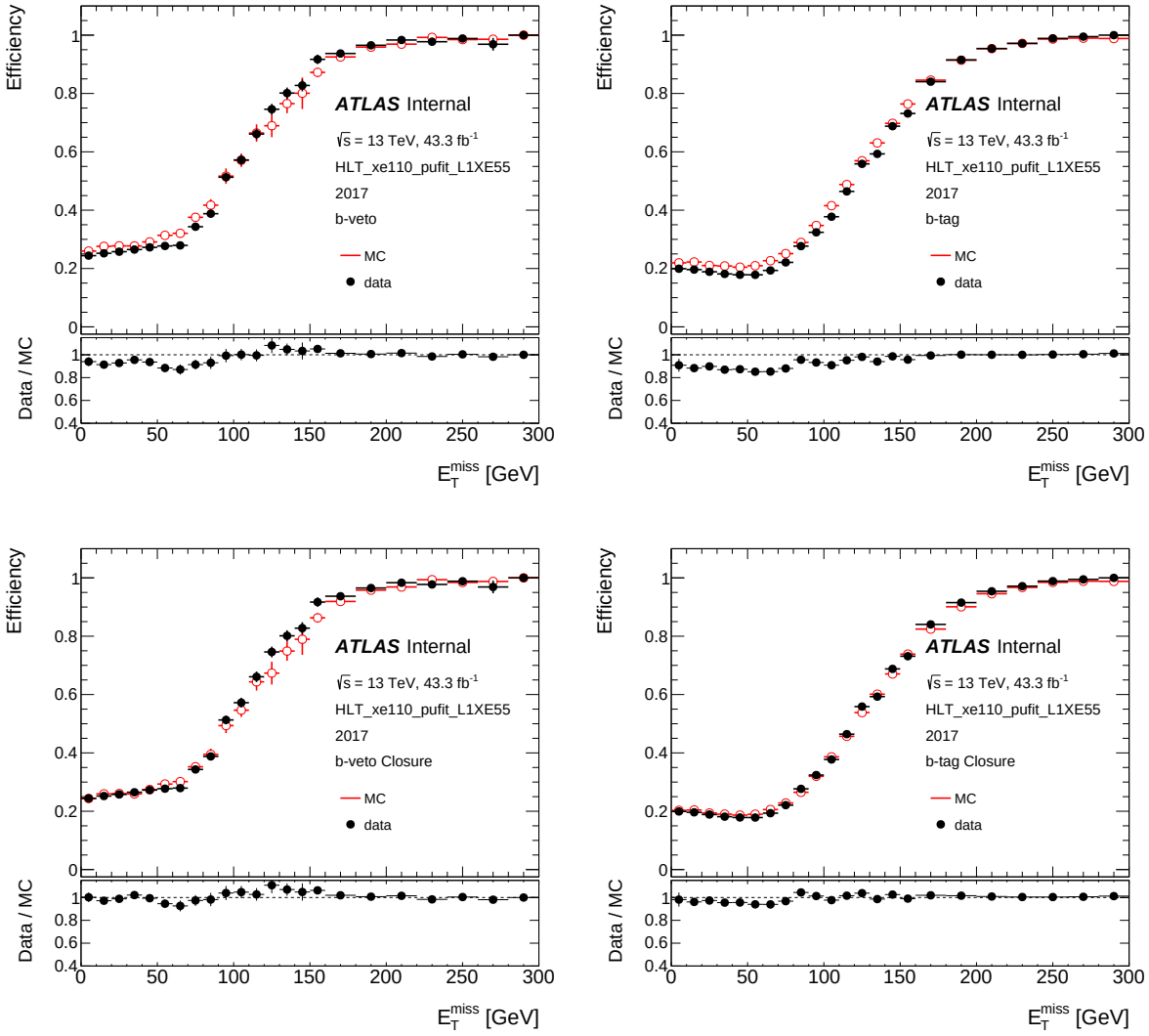

Figure E.5: Comparison of the trigger efficiencies for HLT_xe110_pufit_L1XE55 with respect to the nominal $E_{\mathrm{T}}^{\mathrm{miss}}$ without (top) and with (bottom) applying the SFs for b-veto (left) and -tagged (right) events.

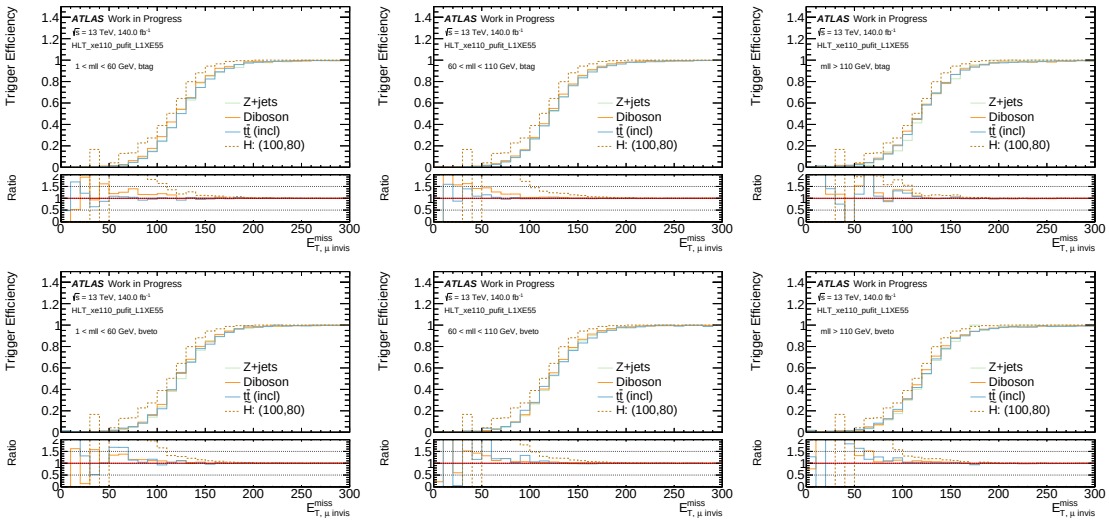

Figure E.6: Comparison of the trigger efficiencies for HLT_xe110_pufit_L1XE55 in different $m_{\ell\ell}$ regimes for b-tag (upper row) and b-vet (lower row) events. The plot shows the efficiencies separately for the Zjets, diboson and ttbar background. For comparison, the signal efficiency of one higgsino signal point at preselection level of the baseline analysis is also shown.

Appendix F

Limits on benchmark models

F.1 Upperlimit on signal cross section

Table F.1: Upper limits on observed (expected) Higgsino simplified model signal cross section.

$m(\tilde{\chi}_2^0)$ [GeV]	$m(\tilde{\chi}_2^0) - m(\tilde{\chi}_1^0)$ [GeV]	σ^{95}_{obs} [pb]	$\sigma^{95}_{\text{obs}}/\sigma_{\text{theory}}$	σ^{95}_{exp} [pb]	$\sigma^{95}_{\text{exp}}/\sigma_{\text{theory}}$
100.0	40.0	11.510	0.512	10.637	0.473
100.0	20.0	6.148	0.384	3.379	0.211
101.5	1.5	155.910	13.571	83.337	7.254
102.0	2.0	24.640	2.171	13.848	1.220
103.0	3.0	8.977	0.809	4.407	0.397
105.0	5.0	3.261	0.307	2.459	0.231
110.0	10.0	1.879	0.197	1.794	0.188
110.0	30.0	8.872	0.704	5.150	0.409
115.0	15.0	3.362	0.392	2.019	0.235
120.0	20.0	4.697	0.645	2.378	0.327
120.0	60.0	9.654	0.718	17.542	1.305
120.0	40.0	7.078	0.702	7.327	0.727
126.5	1.5	171.284	33.494	104.194	20.375
127.0	2.0	27.262	5.379	14.947	2.949
128.0	3.0	8.577	1.724	4.270	0.858
130.0	30.0	6.085	0.953	4.019	0.629
130.0	5.0	2.924	0.609	2.050	0.427
135.0	10.0	1.404	0.319	1.444	0.328
140.0	40.0	5.383	1.012	5.664	1.065
140.0	15.0	3.062	0.755	1.698	0.419
140.0	60.0	12.030	1.789	12.832	1.908
145.0	20.0	4.004	1.073	1.995	0.534
152.0	2.0	32.004	12.167	17.577	6.682
153.0	3.0	7.940	3.064	3.966	1.531
155.0	30.0	5.136	1.613	3.204	1.006
155.0	5.0	2.945	1.171	2.014	0.800
160.0	60.0	6.643	1.756	10.280	2.717
160.0	10.0	1.258	0.552	1.208	0.530
165.0	40.0	3.903	1.427	4.431	1.620
165.0	15.0	2.309	1.060	1.330	0.610
170.0	20.0	3.416	1.681	1.665	0.819
178.0	3.0	9.055	6.094	5.150	3.466
180.0	30.0	3.234	1.823	2.380	1.342
180.0	5.0	2.514	1.736	1.842	1.271
185.0	10.0	1.180	0.867	1.089	0.801
190.0	40.0	2.951	1.896	3.707	2.382
190.0	15.0	2.064	1.615	1.186	0.928
195.0	20.0	2.984	2.482	1.407	1.170
202.0	2.0	52.724	57.164	33.754	36.597
203.0	3.0	7.744	8.493	4.482	4.916
205.0	5.0	2.917	3.273	2.048	2.297
210.0	10.0	1.022	1.212	0.984	1.168
215.0	15.0	2.010	2.521	1.106	1.387
220.0	20.0	2.794	3.701	1.330	1.761
230.0	30.0	2.678	3.951	1.927	2.842
230.0	5.0	2.798	4.846	1.976	3.422
235.0	10.0	1.050	1.914	0.931	1.696
240.0	40.0	2.325	3.803	2.675	4.375
240.0	15.0	2.050	3.928	1.041	1.995
253.0	3.0	9.997	25.235	5.787	14.608
255.0	5.0	2.767	7.116	1.936	4.980
260.0	10.0	1.109	2.989	0.976	2.631
265.0	15.0	1.821	5.142	0.963	2.720
270.0	20.0	2.527	7.459	1.148	3.388
280.0	30.0	2.382	7.699	1.585	5.124
290.0	40.0	1.590	5.604	2.212	7.797
81.5	1.5	146.768	5.530	74.963	2.825
82.0	2.0	23.390	0.895	13.171	0.504
83.0	3.0	11.313	0.446	5.544	0.219
85.0	5.0	4.021	0.168	3.297	0.138
90.0	10.0	2.541	0.122	2.285	0.110
95.0	15.0	4.149	0.228	2.538	0.139

Table F.2: Upper limits on observed (expected) wino–bino ($m(\tilde{\chi}_2^0) \times m(\tilde{\chi}_1^0) > 0$) simplified model signal cross section $\sigma^{95}_{\text{obs (exp)}}$.

$m(\tilde{\chi}_2^0)$ [GeV]	$m(\tilde{\chi}_2^0) - m(\tilde{\chi}_1^0)$ [GeV]	σ^{95}_{obs} [pb]	$\sigma^{95}_{\text{obs}}/\sigma_{\text{theory}}$	σ^{95}_{exp} [pb]	$\sigma^{95}_{\text{exp}}/\sigma_{\text{theory}}$
100.0	60.0	61.571	2.717	56.879	2.510
100.0	40.0	18.504	0.817	18.418	0.813
100.0	25.0	12.643	0.558	7.709	0.340
100.0	15.0	7.372	0.325	3.481	0.154
100.0	10.0	3.002	0.132	2.034	0.090
100.0	5.0	1.462	0.065	1.764	0.078
100.0	3.0	7.245	0.320	3.165	0.140
100.0	2.0	11.985	0.529	5.951	0.263
100.0	1.5	34.967	1.543	14.950	0.660
100.0	1.0	1854.464	81.834	1246.846	55.021
125.0	25.0	7.585	0.756	4.921	0.490
125.0	15.0	5.944	0.592	2.618	0.261
125.0	10.0	2.393	0.238	1.523	0.152
125.0	5.0	1.203	0.120	1.419	0.141
125.0	3.0	6.869	0.685	3.078	0.307
125.0	2.0	15.507	1.545	6.896	0.687
125.0	1.5	41.469	4.132	17.074	1.701
125.0	60.0	25.831	2.574	32.446	3.233
125.0	40.0	6.124	0.610	9.900	0.987
125.0	35.0	6.822	0.680	7.815	0.779
125.0	30.0	7.956	0.793	6.612	0.659
150.0	40.0	3.912	0.755	6.559	1.266
150.0	35.0	3.610	0.697	5.545	1.070
150.0	30.0	4.437	0.856	4.373	0.844
150.0	25.0	5.428	1.048	3.682	0.711
150.0	15.0	4.256	0.821	1.875	0.362
150.0	10.0	1.705	0.329	1.210	0.233
150.0	5.0	1.257	0.243	1.440	0.278
150.0	3.0	6.807	1.314	2.895	0.559
150.0	2.0	17.226	3.325	7.552	1.458
150.0	1.5	54.544	10.528	21.253	4.102
150.0	60.0	22.879	4.416	21.172	4.087
175.0	60.0	12.048	4.080	13.481	4.565
175.0	40.0	2.674	0.906	4.490	1.520
175.0	35.0	2.772	0.938	3.800	1.287
175.0	30.0	3.170	1.073	3.476	1.177
175.0	25.0	3.791	1.284	2.780	0.941
175.0	15.0	3.507	1.188	1.610	0.545
175.0	10.0	1.358	0.460	1.061	0.359
175.0	5.0	1.265	0.428	1.427	0.483
175.0	3.0	8.096	2.741	4.513	1.528
175.0	2.0	30.877	10.455	20.316	6.879
200.0	60.0	6.903	3.819	8.646	4.784
200.0	40.0	1.786	0.988	3.649	2.019
200.0	35.0	2.019	1.117	3.380	1.870
200.0	30.0	1.711	0.947	2.254	1.247
200.0	25.0	3.005	1.663	2.204	1.219
200.0	15.0	3.297	1.824	1.413	0.782
200.0	10.0	1.455	0.805	1.030	0.570
200.0	5.0	1.063	0.588	1.383	0.765
200.0	3.0	7.984	4.417	4.423	2.447
200.0	2.0	46.096	25.504	29.089	16.094
225.0	60.0	6.135	5.266	7.173	6.156
225.0	40.0	1.540	1.321	3.074	2.638
225.0	25.0	2.266	1.945	1.882	1.615
225.0	15.0	2.670	2.291	1.243	1.067
225.0	10.0	1.202	1.032	0.934	0.801
225.0	5.0	1.357	1.165	1.519	1.304
225.0	3.0	10.143	8.705	5.511	4.730
225.0	2.0	51.247	43.985	33.626	28.861
250.0	40.0	1.320	1.686	2.627	3.357
250.0	15.0	2.907	3.715	1.234	1.577
250.0	10.0	1.294	1.654	0.892	1.140
250.0	5.0	1.538	1.966	1.607	2.053
250.0	3.0	10.944	13.986	5.944	7.596
275.0	40.0	1.055	1.942	2.185	4.024
275.0	25.0	1.997	3.677	1.474	2.714
275.0	15.0	2.606	4.799	1.118	2.059
275.0	10.0	1.302	2.397	0.878	1.617
275.0	5.0	1.494	2.752	1.609	2.963
275.0	3.0	11.537	21.246	6.359	11.709
300.0	25.0	2.021	5.223	1.464	3.783
300.0	15.0	14.930	38.584	8.193	21.173
300.0	10.0	1.187	3.069	0.869	2.246
300.0	5.0	1.799	4.648	1.708	4.415
325.0	25.0	1.855	6.580	1.478	5.244
325.0	15.0	2.590	9.188	1.099	3.897
325.0	10.0	1.153	4.091	0.808	2.866
325.0	5.0	1.748	6.201	1.775	6.295
90.0	5.0	1.444	0.042	1.837	0.054
90.0	3.0	8.323	0.244	3.820	0.112
90.0	2.0	12.354	0.362	6.062	0.178
90.0	1.5	28.504	0.836	12.450	0.365
90.0	1.0	509.654	14.952	738.911	21.678

Table F.3: Upper limits on observed (expected) wino–bino ($m(\tilde{\chi}_2^0) \times m(\tilde{\chi}_1^0) < 0$) simplified model signal cross section $\sigma^{95}_{\text{obs (exp)}}$.

$m(\tilde{\chi}_2^0)$ [GeV]	$m(\tilde{\chi}_2^0) - m(\tilde{\chi}_1^0)$ [GeV]	σ^{95}_{obs} [pb]	$\sigma^{95}_{\text{obs}}/\sigma_{\text{theory}}$	σ^{95}_{exp} [pb]	$\sigma^{95}_{\text{exp}}/\sigma_{\text{theory}}$
100.0	60.0	61.045	2.694	46.400	2.048
100.0	40.0	25.937	1.145	17.238	0.761
100.0	25.0	12.807	0.565	6.068	0.268
100.0	15.0	4.476	0.198	2.874	0.127
100.0	10.0	2.123	0.094	2.060	0.091
100.0	5.0	2.869	0.127	2.083	0.092
100.0	3.0	7.388	0.326	3.218	0.142
100.0	2.0	15.131	0.668	7.197	0.318
100.0	1.5	66.737	2.945	28.439	1.255
100.0	1.0	1924.194	84.911	1440.274	63.557
125.0	25.0	7.842	0.781	4.116	0.410
125.0	15.0	4.412	0.440	2.341	0.233
125.0	10.0	1.793	0.179	1.520	0.151
125.0	5.0	2.519	0.251	1.670	0.166
125.0	3.0	7.410	0.738	3.368	0.336
125.0	2.0	19.013	1.895	8.286	0.826
125.0	1.5	77.573	7.730	32.099	3.199
125.0	60.0	26.266	2.617	32.510	3.240
125.0	40.0	9.517	0.948	11.270	1.123
125.0	35.0	12.576	1.253	7.928	0.790
125.0	30.0	12.755	1.271	6.317	0.629
150.0	40.0	7.257	1.401	7.242	1.398
150.0	35.0	7.644	1.475	6.470	1.249
150.0	30.0	7.533	1.454	4.151	0.801
150.0	25.0	6.082	1.174	3.227	0.623
150.0	15.0	3.112	0.601	1.629	0.314
150.0	10.0	1.305	0.252	1.204	0.232
150.0	5.0	2.276	0.439	1.504	0.290
150.0	3.0	6.762	1.305	2.885	0.557
150.0	2.0	20.864	4.027	8.760	1.691
150.0	1.5	100.117	19.324	37.482	7.235
150.0	60.0	19.048	3.677	24.621	4.752
175.0	60.0	11.493	3.892	16.381	5.547
175.0	40.0	6.080	2.059	5.822	1.971
175.0	35.0	7.153	2.422	4.159	1.408
175.0	30.0	5.809	1.967	3.403	1.152
175.0	25.0	5.187	1.756	2.546	0.862
175.0	15.0	2.286	0.774	1.346	0.456
175.0	10.0	0.988	0.335	1.069	0.362
175.0	5.0	1.941	0.657	1.405	0.476
175.0	3.0	7.361	2.492	4.243	1.437
175.0	2.0	43.248	14.644	27.893	9.445
200.0	60.0	8.847	4.895	13.439	7.436
200.0	40.0	3.609	1.997	4.873	2.696
200.0	35.0	5.947	3.290	4.143	2.292
200.0	30.0	4.214	2.331	2.836	1.569
200.0	25.0	4.369	2.417	2.094	1.159
200.0	15.0	1.932	1.069	1.115	0.617
200.0	10.0	1.054	0.583	0.978	0.541
200.0	5.0	1.865	1.032	1.439	0.796
200.0	3.0	7.818	4.326	4.418	2.444
200.0	2.0	69.745	38.589	43.265	23.938
225.0	60.0	6.894	5.917	9.793	8.405
225.0	40.0	3.519	3.021	4.707	4.040
225.0	25.0	3.523	3.024	1.904	1.635
225.0	15.0	2.033	1.745	1.147	0.984
225.0	10.0	0.853	0.732	0.896	0.769
225.0	5.0	1.976	1.696	1.388	1.191
225.0	3.0	8.748	7.508	5.004	4.295
225.0	2.0	54.503	46.778	36.444	31.279
250.0	40.0	3.136	4.007	4.035	5.157
250.0	15.0	1.847	2.360	1.013	1.295
250.0	10.0	0.865	1.106	0.828	1.058
250.0	5.0	2.115	2.703	1.472	1.881
250.0	3.0	8.880	11.348	5.086	6.500
275.0	40.0	3.079	5.670	3.453	6.359
275.0	25.0	2.952	5.436	1.452	2.674
275.0	15.0	1.602	2.950	0.870	1.601
275.0	10.0	0.936	1.724	0.827	1.523
275.0	5.0	1.972	3.631	1.388	2.555
275.0	3.0	9.608	17.693	5.395	9.935
300.0	25.0	2.798	7.232	1.355	3.503
300.0	15.0	11.173	28.874	6.541	16.905
300.0	10.0	0.990	2.558	0.896	2.316
300.0	5.0	2.041	5.274	1.366	3.531
325.0	25.0	2.237	7.936	1.352	4.796
325.0	15.0	1.648	5.846	0.883	3.131
325.0	10.0	0.801	2.841	0.712	2.527
325.0	5.0	2.143	7.602	1.474	5.228
90.0	5.0	2.643	0.078	2.200	0.065
90.0	3.0	7.945	0.233	3.745	0.110
90.0	2.0	14.646	0.430	6.934	0.203
90.0	1.5	30.403	0.892	13.231	0.388
90.0	1.0	509.654	14.952	738.911	21.678